FLOW CONTROL USING TRAVELING WAVES

A Dissertation

by

AMIR MAHDI AKBARZADEH

Submitted to Graduate and Professional School of
Texas A&M University
in partial fulfillment of the requirements for the degree of

DOCTOR OF PHILOSOPHY

Chair of Committee,	Iman Borazjani
Committee Members,	Reza Sadr
	Sharath Girimaji
	Diego A. Donzis
Head of Department,	Guillermo Aguilar

December 2021

Major Subject: Mechanical Engineering

ABSTRACT

Flow separation is the detachment of boundary layer from a surface, which is associated with aerodynamic loss. In this work, the feasibility of controlling flow separation by backward (toward downstream) traveling waves is studied using large-eddy simulations (LES) of traveling waves (1) within an incompressible turbulent channel to investigate the impact of traveling wave parameters such as wave speed and wave steepness, (2) on an inclined plate and suction side of a NACA0018 airfoil at stall angle of attack where the flow is massively separated, and (3) within a compressible wavy turbulent channel. For (3), an LES framework for compressible flow is developed and combined with the curvilinear immersed boundary (CURVIB) method. Both incompressible and compressible frameworks are validated. The incompressible framework is validated for a fully developed turbulent channel, a pitching airfoil, two-dimensional inclined plate, and an NREL PHASE VI wind turbine. The compressible framework is validated by performing simulations for isotropic decay, subsonic and supersonic turbulent channel, and shock diffraction by a cylinder. The results of the simulations of actuated airfoil and plate reveal that low-amplitude backward traveling waves can postpone stall. Moreover, it is found for the first time that traveling waves are more effective than other types of oscillations, e.g., standing waves and pitching motion, in delaying stall because traveling waves can directly increase the axial momentum of the fluid in addition to triggering boundary layer instabilities, which occurs in all type of flow control with periodic excitation. In addition to the axial momentum, the traveling waves increase the lateral velocity of the fluid near the surface, which tends to separate the flow. The scalings of axial force and lateral velocity, which depend on amplitude, wavelength and frequency, were derived analytically using elongated body theory (EBT). Based on the scalings and the results, in contrast to common belief, wave speed (the main parameter for the axial force) is not the only parameter for flow reattachment, and amplitude, wavelength and frequency individually can impact flow separation by triggering instabilities or increasing the lateral velocity.

DEDICATION

To My love, Mahin, and my parents.

ACKNOWLEDGMENTS

I would like to express my sincere gratitude to my advisor, Professor Iman Borazjani for his excellent guidance, patience, and support through this endeavor, without whom this work would have not been possible. I am grateful to the members of my doctoral committee, Professors Sharath Girimaji, Reza Sadr, Dorrin Jarrahbashi, and Diego Donzis whose comments have greatly improved this work. I owe a great deal of gratitude my wife for her support and love, to my parents for devoting their lives to me, and to my brothers for their kind support. This work was supported by National Science Foundation [NSF: CAREER grant CBET 1453982], and the computational resources were provided by Texas A&M High-Performance Research Computing Center (HPRC).

CONTRIBUTORS AND FUNDING SOURCES

Contributors

This work was supported by a dissertation committee consisting of Professor Iman Borazjani (advisor) and Reza Sadr of the Department of mechanical engineering and Professors Girimaji and Donzis of the Department of Aerospace engineering. The Overset framework used for modeling wind turbine flow in chapter 5 is partly developed by MohammadAli Hedayat, former PhD student of the lab. All other work conducted for the dissertation was completed by the student independently.

Funding Sources

This work was supported by National Science Foundation [NSF: CAREER grant CBET 1453982], and the computational resources were provided by Texas A&M High-Performance Research Computing Center (HPRC).

NOMENCLATURE

AOA	Angle of Attack
C_L	Lift Coefficient
C_D	Drag Coefficient
C_f	Skin Friction Coefficient
C_p	Pressure Coefficient
C_s	Smagorinsky Constant
μ_t	Eddy Viscosity
ν	Kinematic Viscosity
μ	Dynamic Viscosity
ρ	Density
λ	Wavelength
f	frequency
s	Wave steepness
u_τ	Friction Velocity
p	Pressure
Re	Reynolds Number
τ	Turbine Shaft Torque
CFD	Computational Fluid Dynamics
FSI	Fluid-structure Interaction
FSI	Immeresed Boundary Method
LES	Large Eddy Simulation
NS	Navier-Stokes

DNS	Direct Numerical Simulation
RANS	Reynolds-averageed Navier-Stokes
CURVIB	Curvilinear immersed boundary method
ALE	Arbitrary Lagrangian Eulerian
WENO	Weigthed Essentially Non-Oscillatory
HPRC	High Performance Computing Center

TABLE OF CONTENTS

Page

LIST OF FIGURES

FIGURE Page

LIST OF TABLES

TABLE Page

1. INTRODUCTION AND MOTIVATION

Flow separation or boundary layer separation is the detachment of a boundary layer from a surface into a wake. Flow separation is associated with aerodynamic loss and decrease of energy efficiency. To solve this problem, several techniques have been used to remove flow separation, referred as flow control, in engineering applications. Flow control strategies can be classified based on the mechanism of reattachment into: (i) direct injection of momentum to the boundary layer, e.g., steady blowing [5, 6], or (ii) indirect transfer of momentum by periodic excitations, e.g., by surface morphing [7], zero net mass flux synthetic jets [8], etc., which trigger flow instabilities that form large coherent structures (LCS) to entrain high momentum fluid into the near-wall flow. The surface morphing is the most recent flow control method which is energy efficient, using light, low-power piezoelectric actuators [8, 9] which can create low-amplitude oscillations. The main objective of this study is to numerically investigate controlling flow separation by surface deformations in the form of traveling waves (Fig. 1.1), which have been created experimentally [10]. The main hypothesis to be tested in this work is that traveling waves perform better than pure periodic excitations because they can inject momentum (generate thrust) and also trigger flow instability.

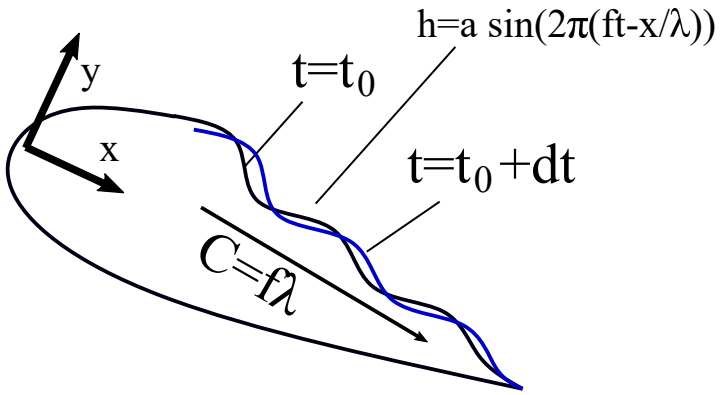

Figure 1.1: The schematic of backward traveling wave, in which wave propagates from the leading edge towards the trailing edge. Reprinted from [183]

1.1 Flow control

Since separation is associated with significant performance losses, its mitigation becomes important. Flow control is a technique introduced to reduce flow separation which can be applied by both passive and active devices. From this perspective, flow control is classified into passive and active flow control. In this section, we briefly review passive and active flow control methods.

1.1.1 Passive flow control

The main advantage of passive control is that they do not require any additional power. Vortex generators (VG) and boundary layer trips are the most popular passive flow control techniques. In vortex generator technique, the VGs act similar to a surface roughness and intensify the boundary layer instabilities which leads to transition to turbulence.

The earlier transition to turbulence increases the boundary layer momentum and consequently reduces flow separation. The vortex generators and surface roughness has been used in different flight regimes, including subsonic, transonic, and supersonic flight. Mueller and Batil (1982) found an improvement in the lift-curve slope of a NACA 663-018 airfoil at Re = 40,000 by using surface roughness. Vortex generators has also been found to have a positive effect on low Re airfoil performance (Lin, 2002; Kerho et al., 1993; Manolesos and Voutsinas, 2015).

The surface roughness has also been used for supersonic flow control. The main effects of surface roughness on supersonic flight vehicles are to increase skin drag coefficient and to promote boundary layer transition to turbulence, which increases the heat transfer coefficient. However, if the roughness size is large enough, the surface roughness might generate shock waves [11] that significantly influence the boundary layer characteristics, increase drag by wave drag, and increase heat transfer. For example, Ekoto et al. [12] observed strong compressibility effects at Mach 2.9 when the roughness was in the form of diamond-shaped elements. They found that these strong compressibility effects had a significant effect on the turbulent flow statistics, such as the Reynolds stress.

The drawback of passive control is that it cannot adapt to changing flow conditions. Although

Gopalarathnam et al. [13] found that trips have a net drag benefit, the performance of this flow control method was only optimum for a given flight condition. Similarly, while VGs were found to improve performance at certain conditions, they have also been found to exhibit a drag penalty at others [14]. In fact, VGs were most suitable when the separation location was fixed so they could be optimally positioned upstream of this location [15]. Due to these drawbacks, several active flow control methods have been proposed which will be briefly reviewed in section 1.1.2.

1.1.2 Active flow control

Active flow control requires additional power but they are aerodynamically harmless when they are inactive, e.g., at low angle of attack (AOA). Various active flow control techniques such as steady blowing [16, 5, 6], periodic suction and blowing [17, 18, 19, 20, 21, 22], and surface morphing [23, 24, 25, 26, 27] have been applied to delay stall. These flow control techniques have been studied experimentally [23, 8, 9, 22] and numerically using different turbulence modeling approaches such as direct numerical simulation (DNS) [28, 29], large eddy simulation (LES) [30, 31, 32], and Reynolds-Averaged-Navier-Stokes (RANS) [31]. Steady blowing and suction blowing are among the early active flow control methods. These methods are capable of improving performance, but complex auxiliary compressors and plumbing result in a high power consumption [17]. Seifert et al. [18] replaced a periodic jet with a constant blowing jet and could achieve 84% power saving. These periodic jets, increase the boundary layer momentum by triggering the boundary layer instabilities without directly increasing the boundary momentum like constant blowing. Another active flow control method is morphing which is defined as changing the shape of an airfoil using flaps and slats or vibrating its surface.

The morphing can be employed in several forms, including trailing edge flaps (TEF) [33, 27, 34, 25], leading edge flaps (LEF) [26, 35, 24], and suction side vibrations [36, 23, 28, 29, 37]. The leading edge and trailing edge flaps conventionally work based on adapting the shape of an airfoil by changing either the radius of the leading edge or the camber of the trailing edge [38]. Typically, changing the shape of an airfoil requires large deformations which can be done by servomotors. In contrast to TEF and LEF, morphing by surface vibrations, which is referred to

as surface morphing hereafter, can be performed using light, low-power piezoelectric actuators [8, 9]. In the following sections, recent work on surface morphing with a focus on traveling wave morphing will be reviewed.

1.1.2.1 Surface morphing

Surface morphing is a modern energy efficient flow control method that can be deployed using light, low-power piezoelectric actuators [8, 9, 10] which can create low-amplitude oscillations. Flow control via surface morphing has been investigated in several studies [28, 29, 37, 36]. Munday et al. [36, 39] reported up to 60% decrease in flow separation. Recently, Jones et al. [23] reported a delay in the onset of stall by morphing the suction side of a NACA4415 airfoil in which the fibers of piezoelectric materials covered about 80% of the whole suction side. In these studies, the oscillations of the surface were in the form of a standing wave [23] or a simple vibration [36], which accelerates the fluid adjacent to the surface along its normal direction. These types of surface morphing reduce flow separation by triggering the boundary layer instability and increasing the mixing of high momentum fluid of the separated shear layer to the low momentum fluid of the reverse flow zone [23, 18], similar to other periodic excitation methods. Nevertheless, the morphing can increase the boundary layer momentum directly if the surface vibrations are in the form of backward (opposite direction to the forward motion of an airfoil, i.e., toward downstream) traveling waves (Fig. 1.1) because traveling waves can increase the fluid momentum along their propagation direction [4, 40, 41], e.g., backward traveling waves, in which the wave is propagated from the leading edge toward the trailing edge, can increase the streamwise momentum. This enhancement of the streamwise momentum by backward traveling waves has also been observed in aquatic swimmers [42] which will be further discussed in sections 1.1.2.2 and 4.2.3.

1.1.2.2 Bio-inspired active flow control

Flow control has been observed in nature by flying animals and aquatic swimmers. In nature, the hovering wings of bats and insects can improve flow attachment, e.g., the leading edge vortex (LEV) created on the leading edge of their wings becomes stable [43, 44, 45, 46]. The stabil-

ity of LEV, which is due to the wings rotational acceleration [47], can enhance the aerodynamic performance and postpone the stall.

In addition to the flying animals, flow over aquatic swimmer's wavy bodies remains attached [48, 42, 45] as they generate high amplitudes backward traveling waves on their bodies. The reason for flow attachment on aquatic swimmers' bodies is the creation of backward traveling waves which increases the fluid chordwise momentum in the vicinity of their bodies.

1.1.2.3 Traveling wave morphing for flow control

Traveling waves create the propulsion force (thrust) of the aquatic swimmers [42, 49]. Several studies have investigated the propulsion mechanism and force generation by these waves. Wu [50] and Lighthill [40] analytically investigated the propulsion characteristics of a plate undergoing an undulatory motion to understand the basic principle of fish swimming hydrodynamics. Lighthill [40] proposed elongated body theory (EBT), in which the instantaneous lift of an undulating slender body (low thickness) is scaled with the added mass force (reactive force). The produced reactive force by the undulation generates a thrust that increases as wave speed ($C = \lambda f$) is increased. It also predicts zero net lateral force (perpendicular force to the body) as the flow is assumed potential which remains periodic. Furthermore, the investigations of Taneda [51] and Triantafyllou [42] also, show that traveling waves reattach the flow on wavy surfaces. Taneda [51] experimentally observed that when the wave speed is less than flow speed ($C < U$), the flow separates from the first crest of the horizontal plate, but it becomes attached when it is more than the flow speed, i.e., ($C > U$). These visualizations were confirmed by simulations for a turbulent channel flow [4]. They also reported that turbulence intensity reduces by the increase in C/U. Traveling waves have also been used for controlling flow separation over bluff bodies. For example, Wu et al. [52] controlled the flow separation of a circular cylinder by employing a traveling wave over the cylinder. Musgrave and Tarazaga [53] controlled flow separation over an airfoil by employing spanwise traveling waves.

These observations reveal that backward traveling wave deformations might be more effective than other types of morphing as they can increase the fluid momentum directly by accelerating the

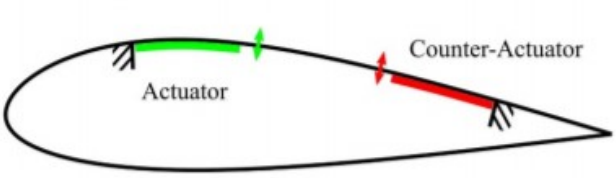

Figure 1.2: The schematic of traveling wave generation by the piezoelectric actuators.

flow along axial direction [4, 42, 54] and in indirectly by triggering the boundary layer instabilities similar to standing wave morphing.

Nevertheless, the experimental creation of traveling waves is a difficult problem but possible using piezoelectric actuators. To understand the experimental challenges, first a two-mode excitation traveling wave generation mechanism developed by Olivett et al. [10] is explained. Two-mode excitation generates traveling waves by mixing two adjacent longitudinal vibrational modes of the morphing surface along in transverse deflection. The concept of morphing wings created by Olivett et al. [10] is demonstrated in Fig. 1.2. The mechanism is driven by two sets of actuators. The actuators in the leading edge generate a bending wave that propagates toward the trailing edge. The counter-actuators are driven at the same frequency, but offset phase, and eliminate reflection at the boundary, therefore removing the possibility of standing wave formation. Nevertheless, these waves are not pure traveling waves. In fact, they are a combination of traveling waves and standing waves [10] because the waves in finite media still reflect at the trailing edge which result in creation of standing waves [55].

Due to the complexity of the creation of these traveling waves, the performance of traveling waves needs to be tested numerically. To apply these waves in complex engineering applications, first, the effects of traveling waves on the physics of the turbulent boundary layer need to be understood. To achieve this aim, the role of different parameters of traveling waves on reducing flow separation and turbulence statistics are studied in sections 4.1 and 6 with our numerical framework. Later, the feasibility of applying surface deformations to control flow separation needs to be tested on highly separated flows, e.g., inclined plates and airfoils. Therefore, we have investi-

gated the impacts of different parameters of surface deformations, i.e., frequency, amplitude, and wavelength on flow separation of a plate and NACA18 airfoil at high angles of attack in sections 4.2 and 4.3, respectively. After controlling flow separation on airfoils and plates via traveling wave oscillations, we investigate the effect of pitching oscillations on the performance of a phase VI wind turbine (chapter 5). Simulations of flow over the wind turbine are more complicated than flow over airfoils because the turbine blade has a more complicated geometry, e.g., large span to chord ratio (≈ 10) and twist angle, and also it has a periodic rotary motion. Finally, the effect of wavy surface and traveling waves are studied for turbulent compressible boundary layers by our developed compressible framework in §6.

The above-mentioned simulations are performed using our LES curvilinear sharp-interface immersed boundary (CURVIB) method framework. The morhing flow control problems need to handle turbulent flows interacting with moving surfaces. In our framework, the moving surfaces are handled with a sharp-interface immersed boundary method. To model turbulent compressible flows a dynamic LES model is added to the framework. More details about numerical method for surface morphing is described in 1.2 and our framework is explained in detail in chapter 2.

1.2 Numerical methods for surface morphing flow control

Computational fluid dynamics (CFD) is a proper tool to handle these problems because it can provide sufficient data about the underlying physics, e.g., pressure and velocity of the fluid surrounding the moving surface, and it can handle complex surface motions such as undulation which their experimental creation is still complicated. To handle the surface morphing flow control problem, the CFD framework needs to be capable of handling (i) moving solid surfaces surrounded by the fluid and (ii) turbulent flows. The problems involving moving surface (boundary) can generally be classified into (a) boundary conforming or interface tracking and (b) non-boundary conforming or interface capturing methods. More information about these methods will be provided in section 1.2.1. The turbulent flows involved with morphing wings can be modeled with three approaches (a) direct numerical simulation (DNS), (b) Reynolds averaged Navier-Stokes (RANS), and (c) large-eddy simulation (LES). These turbulence modeling approaches for morphing flow

control are discussed in 1.2.2. Later, the LES modeling which has been used and developed for surface morphing flow control will be described in §1.2.3.

1.2.1 Handling moving surface

The problems involving moving surface (boundary) are classified into (a) boundary conforming or interface tracking and (b) non-boundary conforming or interface capturing methods. In the following sections, different methods for handling moving boundaries will be reviewed with a focus on sharp-interface immersed boundary method that has been used in this work.

1.2.1.1 Boundary conforming methods

The boundary conforming techniques can keep a high resolution near moving boundaries more efficiently, but suffer from highly skewed grids when deformations are large [56]. Such methods have been applied to simulate flows with moving boundaries [57, 58, 59], but typically require remeshing for large deformations. The most well-known boundary conformed methods are arbitrary Lagrangian Eulerian *(ALE)* [60, 61, 62] a. The *ALE* method can track complex geometries and be used in fluid-structure-interaction problems. However, *ALE* is a computationally expensive method since the mesh needs to be updated [63]. ALE has been applied in many engineering and bioengineering applications. Here, we name few studies in which ALE has been used. It has been used in aeroelastic applications, e.g, in modeling flow over bridges [64], flapping of flexible wings with nonlinear elasticity [65, 66], and parachute inflation [67]. In biological flows, flow over mechanical heart valves and mitral heart valve [68, 69, 70, 71, 72, 73, 74] are modeled.

1.2.1.2 Non-conforming methods

In non-boundary conforming methods, which are also called Eulerian methods, the moving boundary moves over a fixed background mesh, i.e., does not conform to the moving boundary and there is no mesh deformation. One of the main non-boundary conforming methods is the immersed boundary method (*IBM*) [75, 76, 56] which can be implemented in different ways such as the Brinkman penalization [77], cut-cell, [78, 79], direct forcing [80, 81], and sharp-interface immersed boundary method [82, 1], among others.

1.2.1.3 Immersed boundary method

Immersed boundary method was first introduced by Peskin [83, 84, 85, 86] for modeling cardiovascular flow. In this method, generally, a boundary condition is imposed, typically in the form of a forcing term, to model the effect of moving boundaries [83, 56]. Based on the implementation of the boundary condition the immersed boundary method can be classified as a diffused interface method and sharp interface method [87]. In the diffuse interface method, the forcing term is distributed over several grid nodes in the vicinity of the immersed boundary, but in the sharp interface method the forcing term is applied (explicitly or implicitly) only on the nodes adjacent to the moving boundary. The diffuse interface methods require excessive resolution near the boundary because the force distribution smeared the effect of boundaries over several grid nodes. To overcome this problem, these methods are being combined with adaptive mesh refinement [88, 89, 90].

Sharp interface methods can be classified as direct forcing, and cut cell methods [87, 56]. In direct forcing method, a forcing term [91] is added directly to the right hand side of N-S. This forcing term is applied to satisfy the no-slip boundary condition on the interface. Later Fadlun et al. [92] modified this method by enforcing the effect of forcing directly to the velocity and pressure of fluid near the interface by using ghost nodes. The ghost nodes are nodes in the solid that have at least one neighbor node in the fluid. In this approach, the velocity and pressure of the ghost nodes are interpolated such that the no-slip boundary condition is applied on the moving boundary. Later Gilmanov et al. [82] developed a hybrid incompressible Cartesian/immersed boundary method, in which the velocity and pressure of the fluid nodes adjacent to the boundary are reconstructed using an interpolation along the normal direction of the interface. This method has been later extended for curvilinear coordinates [1, 2] and is now called as CURVIB (curvilinear immersed boundary).

1.2.1.4 Curvilinear immersed boundary (CURVIB)

The CURVIB has been developed for more than a decade and has been validated extensively [1, 45]. It has been used for different applications, including biological flows such as aquatic locomotion [46, 93, 94, 95], cardiovascular flows [1, 96, 97, 98, 99, 100, 97, 101, 102], and aneurysm

blood flow [103, 104], and rheological flow [105, 106]. This method (CURVIB) has also been used for modeling turbulent flow over rotating blades, e.g. hydrokinetic turbines [107]. Recently, Hedayat and Borazjani [108] added an overset to the framework for reducing the computational cost of simulations with large solid motions, e.g., wind turbine simulation. In this study, CURVIB is used for handling moving surfaces (Fig. 1.1) interacting with surrounding fluid in surface morphing flow control problems.

Recently, Borazjani [109] extended the CURVIB framework for laminar compressible flows interacting with immersed boundaries. In this framework, the inviscid fluxes of compressible flow equations in curvilinear coordinates are discretized with a third-order weighted essentially nonoscillatory (WENO) scheme and it has been validated against experimental measurements and shown to be between second- and third-order-accurate in the presence of immersed boundaries. Nevertheless, the framework was not suitable for modeling turbulent flows because third-order WENO is very dissipative and therefore cant be used for turbulent flows. Therefore, in this work, we added LES modeling for handling turbulent compressible flows. More detailed background about the WENO scheme and LES of compressible flows is provided in §1.2.4, and velocity and flux reconstruction in CURVIB is described in detail in §2.3.

1.2.2 Turbulence modeling for flow control

DNS is the only method in which turbulence is not modeled but the full Navier Stokes (NS) equations are solved. Solving full NS equations requires resolving the smallest length scale, i.e., the Kolmogorov scale which decreases as $Re^{-3/4}$. Therefore, DNS computational costs increase with Re^3, which limits its applications. Even though the computational power of supercomputers has increased considerably in recent years, DNS is still restricted to moderate Reynolds numbers. Therefore, most of the DNS studies on flow control with surface morphing are performed for Reynolds numbers ranging from 5000 to 60,000 [28].

Due to the high cost of DNS, RANS, LES, and hybrid RANS-LES are more popular for high Reynolds number flows, e.g., flow control problems. In the RANS modeling, which is the least expensive turbulence modeling, the Reynolds closure stresses are modeled to solve the Reynolds

averaged equations to determine the mean velocity [110]. The Reynolds averaged models can typically be categorized into: (i) turbulent viscosity model, and (ii) Reynolds stress model which is known to be more accurate [111]. RANS is the most popular method at high Reynolds flow simulations, e.g., flow over wind turbines $Re >^{6}$ [112, 113, 114], and it has been used for active flow control of high speed morphing wings [115, 116, 117]. Nevertheless, in the flow control problems, the large-scale dynamics needs to be properly captured because it may contain large regions of highly unsteady separated flow that are not in turbulent equilibrium [32]. For example, Large-coherent structures (LCS) which can significantly influence flow separation might be present. These LCSs might break due to unsteady forcing or triggering the unsteady shear layer and result in the generation of additional small-scale structures and transitional flowfield. Since RANS models cannot handle this unsteadiness and transitions they are not suitable for flow control problems. In contrast to RANS, LES can handle these difficulties. In LES modeling, the filtered velocity field which represents the large turbulent motion is solved and the effect of small scales on the large scale motion is modeled. High resolution LES, LES without wall modeling, can resolve the viscous sub-layer boundary layer and capture the effect of unsteady large coherent structures. Therefore, LES is the most suitable approach for modeling active flow control problems [32] with $Re < 200,000$ because it is computationally less expensive than DNS, and it is more appropriate than RANS for unsteady and transitional flows. However, LES will be computationally expensive at high Reynolds number, for example, a LES with $Re \approx 10^{7}$ requires 10^{11} grid points [118], and a hybrid model is preferred at those range of Reynolds numbers.

Nevertheless, LES has been used extensively in active flow control at low Reynolds number flows. Wang et al. [119] Dandois et al. [120], Asgari and Tadjfar [121] used LES for synthetic jet flow control. Abdesssemed [122], Rizzetta et al. [123], Shide et al. [124], [125], Garmann and Visbal [126], Ogunka et al. [127], and Bonnet [128] performed surface morphing flow control with LES.

1.2.3 Large-eddy simulation (LES)

The LES modeling is first introduced by *Smagorinsky* [129] to model atmospheric flows. In these models, the small scale motions are modeled as dissipation explicitly by subgrid-scale stress (SGS) terms. Based on his model, several subgrid-stress models were developed, including the dynamic Smagorinsky model [130, 131] and the mixed model [132]. The SGS model has two major drawbacks. The first one is that the SGS flow is considered to be homogeneous isotropic far from the wall, while it has been shown that SGS flow is not ideally homogeneous far from the wall [133]. The second problem is choosing a proper test filter in finite volume and finite element approaches [133]. Nevertheless, the SGS models have been used extensively in turbulent homogeneous, wall bounded flows and showed a good performance in flows involving complex geometries with low order schemes, e.g., second-order central [94] and fourth-order central schemes [134]. The other popular LES method is implicit LES, which has been used extensively in finite volume and finite element approaches. In these models, the subgrid-stress term are computed implicitly by artificial dissipation [135, 133] introduced by intrinsic nonlinear high-frequency filters built into the convection discretization. These models require high order schemes and are not suitable for problems involving immersed boundaries due to the difficulty associated with high order schemes near the immersed boundary. Recently, by the new progress in machine learning and artificial intelligence, data-driven models have been proposed [136]. In this approach, the closure term which is appeared by filtered Navier-Stokes is modeled using data-driven methods. The closure term is estimated from previous DNS data using machine learning algorithms [136]. These models are novel and have only been tested for homogeneous and simple wall-bounded flows and their capability for handling complex flows is not confirmed.

For these reasons, the sub-grid scale models are used for LES modeling of flows involving immersed boundaries in this work. Our incompressible framework utilize a dynamic Smagrinsky model [45] with a second-order central scheme for handling turbulent flows involving immersed boundaries. In this work, we have first, validated the model by turbulent channel simulations (§3) and later we used it for traveling wave flow control problem (§4) and wind turbine problem (§5).

For compressible flows, we have developed a new framework that models SGS based on the model proposed by Moin et al. [137] and Vreman [138].

1.2.4 LES of compressible flows

Applying LES models for compressible flows is a more complicated task than incompressible flows due to the modeling of complicated SGS terms coming from the energy equation and the presence of shock waves at high-speed flows. Modeling shock turbulence interaction is challenging because it requires special schemes to accurately capture shock waves as well as resolve turbulent fluctuations. To solve this problem, two approaches are proposed: (i) high order scheme with ILES, and (ii) hybrid schemes. Implicit compressible LES models are similar to the incompressible ones, i.e., the SGS terms are implicitly modeled by high frequency filters. In these models, usually, a high order ($O > 5$) weighted essentially non-oscillatory (WENO) schemes [139, 140] is deployed for grid discretization. High-order WENO schemes are used to calculate the inviscid fluxes with high order accurate conservative fluxes in smooth regions and resolve shock and contact discontinuity profiles monotonically with a Riemann solver [141]. However, low-order WENO schemes ($O < 5$) are dissipative and are not suitable for LES modeling because their dissipative nature may dominate the dissipation from the subgrid-scale modeling. The issue of high dissipation of low-order ($O = 3$) WENO schemes can be solved by hybridizing WENO with a central or compact scheme [142, 143]. By this approach, inviscid fluxes in smooth regions are computed by the central scheme, and the discontinuity is handled with WENO. The transition between schemes is typically performed by switch functions that act like a shock sensor [144, 143]. By using hybrid models, SGS can be modeled explicitly far from the shock discontinuity, and the computational stencil will be reduced which makes it a proper choice for problems associated with immersed boundaries. In fact, a third-order WENO and a central scheme has a small stencil (3 to 5, for second order and fourth-order central schemes, respectively), which reduces the computational cost and alleviates the numerical implementation near the immersed boundary.

Recently, Borazjani [109] has developed a compressible framework in the context of CURVIB [1] that properly solves laminar compressible problems involving immersed boundaries. To model

turbulent compressible flows using this framework, we developed a hybrid scheme that incorporates the third-order WENO with a fourth-order skew-central scheme. Moreover, for modeling the SGS terms, we added a dynamic SGS [137, 138] into our framework. The developed compressible LES is described in detail in §6.2. The framework has been validated in §3. First, LES is validated against DNS results by simulations of decaying isotropic turbulent flow, which is a key turbulent feature for calibrating phenomenological turbulence models. Afterwards, it has been tested for wall bounded flows by modeling turbulent channel flow. The final validation is performed to investigate the capability of our hybrid scheme immersed boundary framework for shock capturing by performing 2D simulations of the diffraction of a moving shock by a circular cylinder. Finally, the simulation of wavy channels and traveling wave channels are performed in section 6.

2. NUMERICAL METHODS *

This chapter is organized as follows: In section 2.1 we present the governing equations used to solve turbulent incompressible flows in a non-inertial frame of reference along with the LES modeling used in the context of general curvilinear coordinates. In section 2.2 we describe the dynamic sub-grid scale LES method. Finally, the sharp-interface immersed boundary method is reviewed in §2.3.

2.1 LES of Incompressible flows in overset-CURVIB

The equations governing the flow are three-dimensional filtered unsteady incompressible continuity and Navier-Stokes equations. The governing equations are first written in an inertial frame in the context of curvilinear coordinates (ξ_i: $i = 1$ to 3) and then transformed version in the non-inertial-frame curvilinear coordinates.

The filtered Navier-Stokes equations in curvilinear coordinates $\xi^i = \xi^i(x, y, z)$, are as follows in tensor notation ($i, j, m, q = 1, 2, 3$):

$$J\frac{\partial U^i}{\partial \xi^i} = 0, \tag{2.1}$$

$$\frac{\partial U^i}{\partial t} = \xi^i_j\Big(\frac{\partial}{\partial \xi_n}(U^n u_j) - \frac{\partial}{\partial \xi_q}(\frac{\xi^q_j}{J}p) + \frac{1}{Re}\frac{\partial}{\partial \xi_q}(\frac{g^{qm}}{J}\frac{\partial u_j}{\partial \xi^m}) - \frac{\xi^q_m}{J}\frac{\tau_{jm}}{\xi^q} + \frac{f_j}{J}\Big). \tag{2.2}$$

Here, $J = |\partial(\xi^1, \xi^2, \xi^3)/\partial(x_1, x_2, x_3)|$ is the determinant of the Jacobian of the transformation $\xi^j_m = \partial\xi^j/\partial x_m$; g^{qm} is the contravariant metric of the transformation, $g^{qm} = \xi^q_j\xi^m_j$; p is the filtered non-dimensional pressure; $Re = U^*H^*/\nu^*$ is the Reynolds number where ν^* is the kinematic viscosity of the fluid; $U^q = u_m\xi^q_m/J$ is the non-dimensional contravariant velocity of the fluid, f_j is a constant value added to RHS only along the streamwise direction to enforce a constant flow

*Part of This chapter is reprinted with permission from "Large eddy simulations of a turbulent channel flow with a deforming wall undergoing high steepness traveling waves" by A.M. Akbarzadeh and I. Boazjani, 2019 Physics of Fluid 31 (12), 125107, copyright [2019] by authors.

rate [145] for turbulent channel flow studies, and τ_{jm} is the sub-grid scale (SGS) stress tensor for LES. The details of derivations of the governing equations in CURVIB can be found in previous studies [2, 146, 1].

To reduce the computational cost of problems with overset grids that contain solid objects with large deformation, e.g., wind turbine simulation, Eq. 2.2 are transformed to a non-inertial frame of reference by Borazjani et al. [146]. Figure 2.1 illustrates the position and orientation of a grid in inertial and non-inertial coordinates relative to each other.

Let t, x_i' and x_i ($i = 1, 2, 3$) denote time, Cartesian coordinates of the inertial and non-inertial frame, respectively, as shown in Fig. 2.1. Here, (') denotes the inertial parameter. Pressure and non-inertial Cartesian velocity is denoted by p and $\mathbf{u}$, respectively, (italic variables are scalar while the Boldface variables are vectors). The non-inertial velocity $\mathbf{u}$ is obtained by rotating the inertial velocity by an orthogonal rotation tensor $\mathbf{Q}$ as follows using a tensor notation

$$u_q = Q_{qr} u_r' \tag{2.3}$$

The frame velocity is $\mathbf{v}$, and it is composed of a rotation velocity ($\mathbf{w}$) and translational velocity (u^{ctr})

$$v_i = w_i + u_i^{ctr} \tag{2.4}$$

$$w_i = \epsilon_{ilm} \Omega_l X_m^{int} \tag{2.5}$$

where $u_q^{ctr} = u_q^{ctr}(t)$ and $\Omega_q = \Omega_q(t)$ are the translational and rotational velocity of the non-inertial frame, respectively, relative to the inertial frame. X_q^{int} is a component of the position vectors in the inertial reference frame. By using a curvilinear transformation $\xi_i(x_1, x_2, x_3)$, $i = 1, 2, 3$, based on the hybrid staggered/non-staggered approach [2], the continuity and momentum equations in a non-inertial frame of reference are formulated as follows in a tensor notation [146] (see appendix

?? for the derivation):

$$J\frac{\partial}{\partial \xi^r}(U^r) = 0 \tag{2.6}$$

$$\frac{\partial U^r}{\partial t} = \frac{\xi_q^r}{J}\Big(\frac{\partial u_q}{\partial t}\Big) = \frac{\xi_q^r}{J}\Big(- C_1(u_q) - C_2(w_q) - G_q(p) + (\frac{1}{Re} + \nu_t)D(u_q)\Big) \tag{2.7}$$

where ν_t is the eddy viscosity, C_1, C_2, G, and D are the convective, gradient, and viscous operators in curvilinear coordinates

$$C_1(*) = J\frac{\partial}{\partial \xi^r}\Big[\Big(U^r - V^r\Big) * \Big], \tag{2.8}$$

$$C_2(*) = J\frac{\partial}{\partial \xi^r}\Big[U^r * \Big], \tag{2.9}$$

$$G_q(*) = J\frac{\partial}{\partial \xi^r}\Big(\frac{\xi_q^r}{J} * \Big), \tag{2.10}$$

$$D(*) = J\frac{\partial}{\partial \xi^r}\Big(\frac{g^{rm}}{J}\frac{\partial}{\partial \xi^m} * \Big), \tag{2.11}$$

where U^q and V^q are the contravariant velocity components, which are correlated with the Cartesian velocity components as follows:

$$U^r = u_q\frac{\xi_q^r}{J},\ and\, V^r = v_q\frac{\xi_q^r}{J} \tag{2.12}$$

2.1.1 Subgrid-scale large-eddy simulation

The filtered Navier-Stokes equations solved in LES (Eq. 2.2) are obtained by decomposing the velocity into resolved and unresolved components and integrating the Navier-Stokes equations over a spatial filter. By applying the spatial filter, a subgrid-stress term (τ_{ij}) appears in the momentum equations (Eq.2.2) which is modeled using the dynamic Smagorinsky sub-grid scale (SGS) model [147, 129] as follows:

$$\tau_{jm} - \tau_{nn}\delta_{jm} = C_s\Delta^2|\bar{S}|\bar{S}_{jm} \tag{2.13}$$

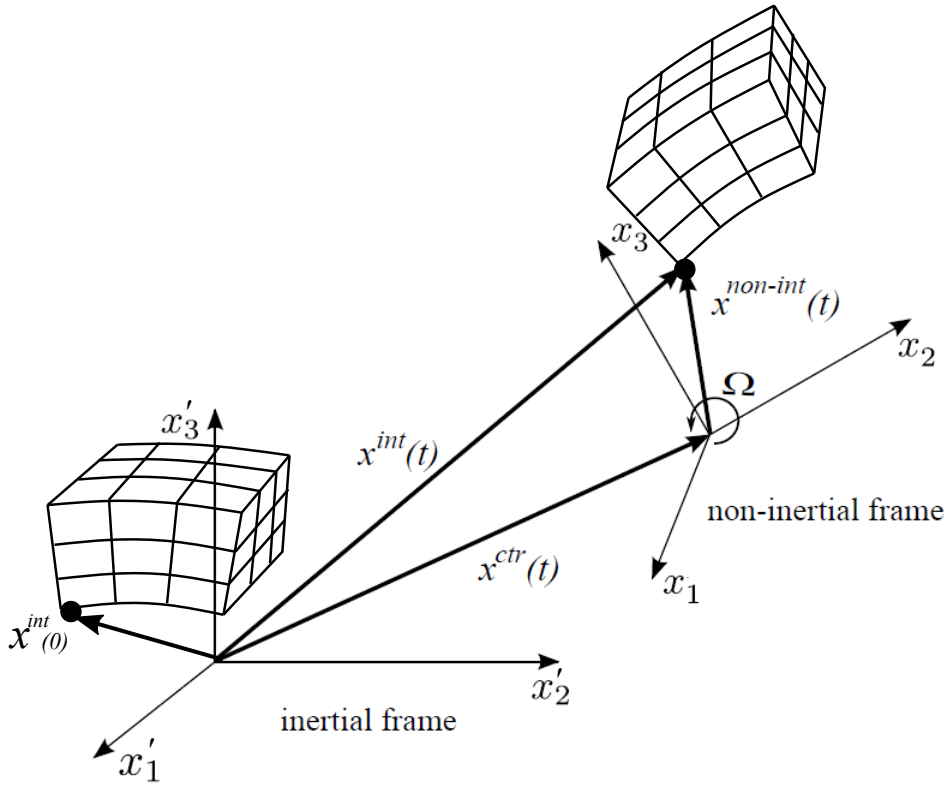

Figure 2.1: schematic position and orientation of a curvilinear grid in a non-inertial frame and an inertial frame where x^{int}, $x^{non-int}$ and x^{ctr} are the coordinate vectors in inertial frame, non-inertial frame and origin of non-inertial frame in inertial coordinate.

where, the left hand side is same as ν_t in Eq.2.7, δ_{jm} is Kronecker delta, overbar denotes the grid filtering, S_{jm} is the strained-rate tensor, $|S| = 0.5\sqrt{\bar{S}_{mn}\bar{S}_{mn}}$, $\Delta = (J^{-1/3})$ is the filter size and C_s is Smagorinsky constant computed by the curvilinear version [148] of the dynamic Smagorinsky model proposed by Lilly et al. [131] as follows

$$C_s = \frac{< L_{im} M_{jn} g^{mn} >}{< M_{im} M_{jn} g^{mn} >} \tag{2.14}$$

where $<>$ signifies spatial averaging which is typically employed in the homogeneous direction, $M_{ij} = -2(\widehat{\Delta}^2|\widehat{\bar{S}}|\widehat{\bar{S}}_{ij} - \Delta^2|\widehat{\bar{S}|\bar{S}_{ij}})$ and $L_{ij} = (\widehat{\Delta}^2|\widehat{\bar{S}}|\widehat{\bar{S}_{ij}} - \Delta^2|\widehat{\bar{S}|\bar{S}_{ij}})$ is resolved turbulent stress. Herein, the caret symbol ($\widehat{}$) is the test filter [147] which has a length of three grid size in each direction. Note that all the terms of Eqn. (2.2) are grid filtered. The sub-grid stress tensor (Eqn. 2.13) is computed once at the beginning of each iteration. The details of the implementation of this method in curvilinear coordinate are similar to the previous publications [107, 45].

2.1.2 Solution of the Navier Stokes

The convective and viscous terms are discretized with a second-order hybrid staggered/non-staggered central scheme in space. The above equations are advanced in time using a fractional step method on curvilinear grids [2]. The momentum equations (Eqs.2.7) is discretized in time in a fully implicit manner using a second-order backward difference scheme:

$$\frac{3\boldsymbol{U}^{(*)} - 4\boldsymbol{U}^{(n)} + \boldsymbol{U}^{(n-1)}}{2\Delta t} = RHS(\boldsymbol{U}^{(*)}, \boldsymbol{u}^{(*)}, p^{(n)}) \tag{2.15}$$

where $\boldsymbol{U}$, $\boldsymbol{u}$, and p are the contravariant velocity, Cartesian velocity, and pressure, respectively. n denotes the time level and RHS is the right hand side of Eq. 2.7. Equation 2.15 is solved implicitly using a Newton-Krylov method to obtain the intermediate fluxes $U^{(*)}$. However, these fluxes are not divergence-free and need to be corrected to satisfy the continuity Eq.2.6. This correction is made by using the projection method in which the Poisson equation is solved. This method can be written for our problem in curvilinear coordinates as follows:

$$p^{n+1} = p^n + \phi, \tag{2.16}$$

where ϕ is the correction term that can be obtained by solving the Poisson Eq. as follows:

$$-\frac{\partial}{\partial \xi_r}(\frac{\xi_q^r}{J} G_q(\phi)) = \frac{3}{2\Delta t}\frac{\partial}{\partial \xi_r} U_r^* \tag{2.17}$$

where, the Poisson equation for the pressure correction (ϕ) is solved using flexible GMRES with multigrid as a preconditioner to obtain divergence-free solution [2]. By solving the presssure correction terms, the divergence-free fluxes are obtained as follows:

$$U^{n+1} = U^* + \frac{2\Delta t}{3}\frac{\xi_q^r}{J} G_q(\phi), \tag{2.18}$$

The solver is fully parallelized using MPI and PETSc libraries [149].

2.2 LES of compressible flows in CURVIB

In this section, the LES framework developed for solving turbulent flows is presented. First, the governing equations in a generalized curvilinear coordinates are presented. Afterwards, the deployed LES and numerical solution are provided.

2.2.1 Governing equations

The governing equations for the filtered compressible flow in curvilinear coordinates $\xi^q (m, p, q, r = 1, 2, 3$ and repeated indices imply summation) are as follows:

$$\frac{1}{J}\frac{\partial \mathbf{Q}}{t} + \frac{\partial}{\partial \xi^q}(\mathbf{F}^q - \mathbf{F}_v^q) = \mathbf{G}, \tag{2.19}$$

where Q is the variable vector, $\mathbf{F^q}$ and $\mathbf{F_v^q}$ are the filtered inviscid and viscous flux vectors, respectively:

$$Q = \begin{bmatrix} \bar{\rho} \\ \bar{\rho}\tilde{u}_1 \\ \bar{\rho}\tilde{u}_2 \\ \bar{\rho}\tilde{u}_3 \\ \bar{\rho}E \end{bmatrix} \mathbf{F}^q = \frac{1}{J} \begin{bmatrix} \bar{\rho}\tilde{U}^q \\ \bar{\rho}\tilde{u}_1\tilde{U}^q + \xi^q_{x_1}\bar{p} \\ \bar{\rho}\tilde{u}_2\tilde{U}^q + \xi^q_{x_2}\bar{p} \\ \bar{\rho}\tilde{u}_3\tilde{U}^q + \xi^q_{x_3}\bar{p} \\ (\bar{\rho}E + \bar{p})\tilde{U}^q \end{bmatrix} \mathbf{F}^q_v = \frac{1}{J} \begin{bmatrix} 0 \\ \xi^q_{x_r}(\tilde{\sigma}_{1r} - \tau_{1r}) \\ \xi^q_{x_r}(\tilde{\sigma}_{2r} - \tau_{2r}) \\ \xi^q_{x_r}(\tilde{\sigma}_{3r} - \tau_{3r}) \\ \xi^q_{x_r}(\tilde{K}_r) \end{bmatrix} G = \begin{bmatrix} 0 \\ 0 \\ 0 \\ f_3 \\ -\alpha - \beta + \epsilon + \bar{\rho}\tilde{u}_3 f_3 \end{bmatrix} \tag{2.20}$$

where the overbar denotes a filter operation, which commutes with the partial derivatives. The tilde filter represents the Favre filter operation, which is defined as $\tilde{u} = \overline{\rho u}/\bar{\rho}$, where ρ is density, $\tilde{u}_p$ $(p = 1, 2, 3)$ is the p^{th} component of the filtered Cartesian velocity, E is the total energy per unit mass, $J = |\partial(\xi^1, \xi^2, \xi^3)/\partial(x_1, x_2, x_3)|$ is the determinant of the Jacobian of the transformation, $\xi^q_{x_r}$, $\tilde{U}^q = \tilde{u}_r\xi^q_{x_r}$ is the contravariant velocity, $\tilde{p} = (\gamma - 1)(\bar{\rho}E - 0.5\bar{\rho}\tilde{u}_r\tilde{u}_r)$ is filtered pressure, γ is the ratio of the specific heats, $\tilde{\sigma}_{rm} = \bar{\mu}(\xi^p_{x_m}\frac{\partial\tilde{u}_r}{\partial\xi^p} + \xi^p_{x_r}\frac{\partial\tilde{u}_m}{\partial\xi^p}) - \frac{2}{3}\mu\xi^p_{x_k}\frac{\partial\tilde{u}_k}{\partial\xi^p}\delta_{rm}$ is the filtered shear stress tensor in curvilinear coordinates, μ is the dynamic viscosity, δ_{rm} is the Kronecker delta tensor, $K_r = \gamma\mu Pr^{-1}\xi^p_{x_r}\partial(E - \frac{1}{2}\tilde{u}_m\tilde{u}_m)/\partial\xi^p + \tilde{u}_p\tilde{\sigma}_{rp}$, Pr is the Prandtl number. Here, τ_{rm} is the subgrid stress tensor (SGS) of the momentum equation, and f_3 is a source term, which is nonzero in turbulent channel simulation added to keep the mass flux of the channel constant.

2.2.2 Subgrid-scale LES of compressible flows

To date, subgrid-scale models have been used extensively to model turbulent flows in different turbulent regimes such as isotropic turbulent flows [150, 151], wall flows [147, 152, 153], and shock wave turbulence interaction [154, 155, 156, 124]. The LES model of this study is employed based on subgrid-scale models of Vreman et al. [138, 137], which is similar to its incompressible version [129]. The SGS term (τ_{ij}) is modeled by the dynamic model proposed by Moin et al.[137]

as follows:

$$\tau_{ij} = \frac{2}{3} C_I \bar{\rho} \Delta^2 |\tilde{S}|^2 \delta_{ij} - 2 C_s \bar{\rho} \Delta^2 |\tilde{S}| (\tilde{S}_{ij} - \frac{1}{3} \tilde{S}_{mm} \delta_{ij}), \tag{2.21}$$

where the first term is the isotropic term of the SGS, $S_{ij} = 0.5(\xi^m_{x_j} \frac{\partial \tilde{u}_i}{\partial \xi^m} + \xi^m_{x_i} \frac{\partial \tilde{u}_j}{\partial \xi^m})$, and $|S| = \sqrt{2 S_{ij} S_{ij}}$, and the second term is the eddy viscosity term. Here, C_s is the Smagorinsky constant that can be modeled dynamically [137] or be a constant value ($C_s = 0.01$) similar to the values used for incompressible flows. However, the term C_I can be modeled dynamically [137] or assumed to be $C_I = 0.06$ [138]. Here, C_s is computed by the dynamic model proposed by Moin et al.[137] as follows:

$$Cs = \frac{< [\widehat{\rho \bar{\rho} v_k v_l} - (1/\widehat{\rho})(\widehat{\rho v_k} \widehat{\rho v_l}) S_{kl}] - \frac{1}{3} S_{mm} (\widehat{\rho v_j v_j} - (1/\widehat{\rho})(\widehat{\rho v_j} \widehat{\rho v_j})) >}{< -2 \widehat{\rho} \widehat{\Delta}^2 |\widehat{S}| (\widehat{S_{kl}} S_{kl} - \frac{1}{3} \widehat{S_{mm}} S_{jj}) + 2 \Delta^2 (\widehat{\rho |S| S_{kl}} S_{kl} - \frac{1}{3} \widehat{\rho |S| S_{mm}} S_{jj}) >} \tag{2.22}$$

where $<>$ signifies spatial averaging which is typically employed in the homogeneous direction, and if flow is not homogeneous it will be averaged in a cube of $3 \times 3 \times 3$ cells.

Based on the model proposed by Vreman et al. [138], the subgrid-terms in the energy equations have the following form in curvilinear coordinates:

$$\begin{aligned} \alpha &= \tilde{u}_i \xi^m_j \frac{\partial (\bar{\rho} \tau_{ij})}{\partial_{\xi^m}} \\ \beta &= \xi^m_{x_j} \frac{\partial ((\overline{p u_j} - \bar{p} \tilde{u}_j)(\gamma - 1))}{\partial \xi^m} \\ \epsilon &= \overline{\sigma_{ij} \xi^m_{x_j} \frac{\partial u_i}{\partial \xi^m}} - \bar{\sigma}_{ij} \xi^m_{x_j} \frac{\partial \tilde{u}_i}{\partial \xi^m}, \end{aligned} \tag{2.23}$$

where α is the turbulent stress term on the scalar level that is calculated conveniently from $\bar{\tau}$ (Eq. 2.21). β is the pressure-velocity subgrid-term, and ϵ is subgrid-scale turbulent dissipation. Here, the effect of pressure dilatation is ignored as it has been shown previously [138] that it has minor effect on the energy term. Herein, β and ϵ are modeled with a simple eddy-viscosity model proposed by Vreman et al. [138] as follows:

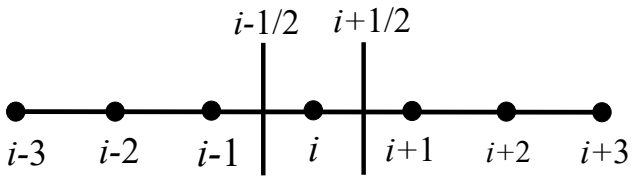

Figure 2.2: 1D computational scheme for computing fluxes, 6 points stencil is used for central fluxes and 5 points stencil are used for WENO fluxes.

$$\beta = -\xi_j^n \frac{\partial \left(\frac{\rho \nu_t}{(\gamma-1)PrM^2} \xi_j^m \frac{\partial T}{\partial \xi^m} \right)}{\partial_{\xi^n}} \tag{2.24}$$

$$\epsilon = C_\epsilon \rho \frac{\sqrt{3/4\nu_t |S|}^{\frac{3}{2}}}{\Delta} \tag{2.25}$$

where $T = \gamma M^2 p/\rho$ is the fluid temperature and $C_\epsilon = 0.6$.

2.2.3 Solution of the compressible Navier Stokes

Here, the viscous terms are discretized with a second-order central scheme, and the convective terms are discretized by a hybrid WENO-central scheme. The hybridization is applied using a switch function that smoothly transforms from a fourth order skew-central scheme to a third order WENO scheme [140] in the vicinity of the shock by a switch function proposed by Wu and Zhao [144]. The detail of the discretization of the convective flux is described for the 1D version ($q = 1$) of eqn. 2.19 for simplicity as follows:

$$\frac{\partial \mathbf{F}_i}{\partial \xi} = \left(\frac{\hat{\mathbf{F}}_{i+1/2} - \hat{\mathbf{F}}_{i-1/2}}{\Delta \xi} \right), \tag{2.26}$$

where i denotes cell center location, and $i \pm 1/2$ denotes cell interface location, where the fluxes are computed. The flux $\mathbf{F_{i+1/2}}$ in a hybrid scheme is

$$\hat{\mathbf{F}}_{i+1/2} = \sigma_{i+1/2} \mathbf{F}_{i+1/2}^{central} + (1 - \sigma_{i+1/2}) \mathbf{F}_{i+1/2}^{WENO} \tag{2.27}$$

where $\sigma_{i+1/2}$ is the switch function, $\mathbf{F}^{central}_{i+1/2}$ and $\mathbf{F}^{WENO}_{i+1/2}$ are the central and WENO convective fluxes, respectively. $\mathbf{F}^{central}_{i+1/2}$ for a given convective term such as $(vw)_{(i+1/2)}$, where (v, w) can be $(\rho u_1, U^1)$ or $(\xi^1_{x_1}, p)$, is calculated with a fourth-order skew-central as follows [157]:

$$\begin{aligned}(vw)_{i+1/2} = \frac{1}{12}\left(-v_{i+2}w_{i+2} + 7v_{i+1}w_{i+1} + 7v_i w_i - v_{i-1}w_{i-1}\right) + \\ \frac{1}{3}\left(\frac{1}{2}(v_{i+1}w_{i+1} + v_i w_i) - \frac{1}{4}(v_{i+1} + w_i)(v_{i+1} + w_i)\right)\end{aligned} \tag{2.28}$$

The third-order WENO flux in the context of CURVIB is provided by Borazjani [109] based on the work of Shu et al. [140]. The WENO fluxes are approximated by a Lax-Friedrichs flux to avoid oscillations near the shock [140]:

$$\begin{aligned}F^{WENO}_{i+1/2} &= F_{LF}(Q^-_{i+1/2}, Q^+_{i+1/2}) \\ &= 1/2(F^-_{i+1/2} + F^+_{i+1/2}) - 1/2\alpha((Q^+_{i+1/2} - Q^-_{i+1/2})\end{aligned} \tag{2.29}$$

where $Q^{\pm}_{i+\frac{1}{2}}$ are obtained by the WENO reconstruction, $F^{\pm}_{i+\frac{1}{2}}$ are the exact fluxes based on the reconstructed parameters ($Q^{\pm}_{i+\frac{1}{2}}$), and $\alpha = Max(\lambda^-_{i+\frac{1}{2}}, \lambda^+_{i+\frac{1}{2}})$ is the maximum eigenvalue of the Jacobian $\partial F/\partial Q$. The maximum eigenvalue is $\lambda^q = |\sqrt{g^{qq}/, \gamma p/\rho}| + |U^q|$, where $g^{qq} = \xi^q_{x1}\xi^q_{x1} + \xi^q_{x2}\xi^q_{x2} + \xi^q_{x3}\xi^q_{x3}$. More details on WENO reconstruction can be found in Borazjani [109].

Here, we employed the switch function proposed by Wu and Zhao [144]. The switch function has a value ranging from 0 ($3rd$ order WENO) to 1 ($4th$ order skew-central). The switch function is defined at half points ($i + 1/2$) as follows:

$$\sigma_{i+1/2} = \frac{1}{2}\frac{tanh(\frac{3(r_{i+1/2} - r_d)}{max(r_d, |r_{i+1/2} - r_d|)})}{tanh(3)} + \frac{1}{2}, \tag{2.30}$$

where $r_{i+1/2} = min(r_i, r_{i+1})$, and r_i is obtained as follows:

$$r_i = \frac{|2\Delta f_{i+1/2}\Delta f_{i-1/2}| + \epsilon}{(\Delta f_{i+1/2})^2 + (\Delta f_{i-1/2})^2 + \epsilon}, \tag{2.31}$$

where $\Delta f_{i+1/2} = f_{i+1} - f_i$, $\epsilon < 10^{-10}$ is a small number to avoid divide by zero. Note that the 3^{rd}

order accuracy of the WENO and 4^{th} of the central scheme is only obtained on uniform grids. For non-uniform grids the order of accuracy of this discretization will be 2^{nd} order due to the 2^{nd} order accurate calculation of the metric of the transformation $\xi^q_{x_r}$. For non-periodic boundary conditions and points adjacent to the immersed nodes, the inviscid fluxes are constructed from second-order central and third-order ENO due to lower stencil near those points [109].

The governing equations (Eq.2.19) are advanced in time using a third-order Runge-Kutta method at each grid point similar to the immersed boundary method for compressible flows (without turbulence) [109].

2.3 Sharp-interface immersed boundary method

The boundaries of the solid objects, which can undergo any arbitrary motion, are handled using the sharp-interface immersed boundary (IB) method. This method is described in detail in previous publications [1, 2], however, to complete this section, a brief description of our sharp-interface immersed boundary method is given. In this method, the background grid is fixed and

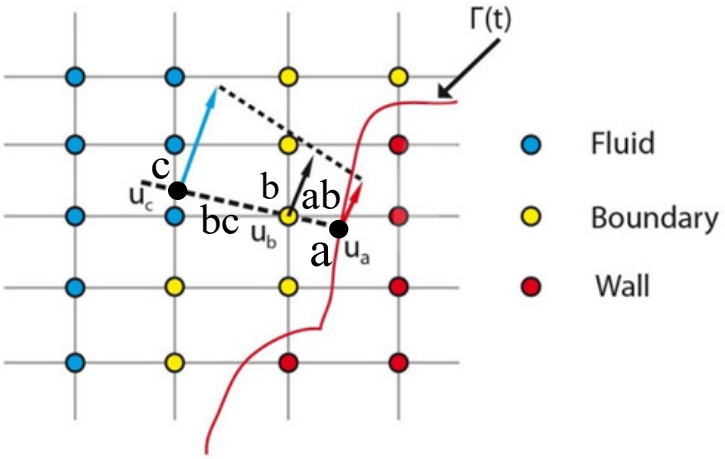

Figure 2.3: The schematic of the sharp-interface immersed boundary method [1]. The velocity at the boundary nodes are reconstructed along the normal direction [2].

does not move with the boundaries. The solid boundaries are discretized by the triangular mesh and placed as a sharp-interface IB over the fixed background grid. However, to explain the immersed

boundary method more clearly, a 2D schematic of the immersed boundary is presented in Fig. 2.3. The background grid nodes are classified into solid (red), fluid (blue) and IB nodes (yellow) by an efficient ray-tracing algorithm [1]. The grid nodes inside the immersed boundary (solid nodes) are blanked out, while the variables, p, u, and ρ (compressible flow) on the nodes that are exterior to, but adjacent to, the immersed boundary, i.e., IB nodes, are reconstructed using an interpolation along the normal to the boundary [82]. The classification of the grid nodes is performed once in the whole simulation for the cases with static boundaries and once in each time step for the moving boundaries. The method is fully validated for flows with moving boundaries [158, 1, 159, 160], and has been used in different applications [161, 103, 162, 161, 163, 164].

2.3.1 Immersed boundary reconstruction

The interpolation is similar for the both incompressible and compressible solver. The interpolation along the normal direction imposes a no-slip boundary condition on the solid wall which can be applied with different methods based on the flow regime and wall unit grad spacing (y^+) along the wall normal. For turbulent flows with a high Reynolds number, a wall function is required if $y^+ > 5$ for the immersed points, otherwise the velocity of the immersed points can be reconstructed with a linear interpolation [165]. The interpolation equations are explained here using Fig. 2.3. By assuming the velocity at points a, b, and c are $\mathbf{u_a}$, $\mathbf{u_b}$ and $\mathbf{u_c}$, the goal is reconstructing $\mathbf{u_b}$ by $\mathbf{u_c}$ and $\mathbf{u_a}$. The velocities can be decomposed into a normal and tangential term, e.g., $\mathbf{u_a} = u_a^n\mathbf{n} + u_a^t\mathbf{t}$, where $\mathbf{n}$ and $\mathbf{t}$ superscripts denote the normal and tangential, respectively. The normal term is obtained by a linear interpolation as follows:

$$u_b^n = \frac{|ab|u_c^n + |bc|u_a^n}{|ac|} \tag{2.32}$$

where $|ab|$, $|bc|$, and $|ac|$ are the distance of those points. The above equation is applied for any flow regime and Re, and a similar relation can be used for estimating u_b^t when the viscous sublayer is resolved [165].

$$u_b^t = \frac{|ab|u_c^t + |bc|u_a^t}{|ac|} \tag{2.33}$$

Here, when viscous sublayer is not resolved, two types of wall functions are used, i.e., the log-law wall model and a wall shear stress balance model [166]. For the log law model, first the friction velocity $u_\tau = \sqrt{(\tau_w/\rho)}$ is obtained by solving the three following equations:

$$y_c^+ = u_\tau |ac|/\nu \tag{2.34}$$

$$u_c^+ = (u_c^t - u_a^t)/u_\tau \tag{2.35}$$

$$u_c^+ = \frac{1}{\kappa} ln(y_c^+) + B \tag{2.36}$$

where $\kappa = 0.42$ and $B = 5.2$. These three equations are solved with an iterative method. After, calculating u_τ, u_b^+ is calculated as follows

$$y_b^+ = u_\tau |ab|/\nu \tag{2.37}$$

$$u_b^+ = \begin{cases} y_b^+ \quad \text{if} \quad y_b^+ < 11.0 \\ \frac{1}{\kappa} ln(y_c^+) + B \quad \text{if} \quad y_b^+ \geq 11.0 \end{cases} \tag{2.38}$$

$$u_b^t = u_a^t + u_b^+ u_\tau \tag{2.39}$$

After calculating u_b^+, the physical velocity can easily be calculated by adding the wall velocity This model works properly when the flow is attached and the boundary layer is turbulent. However, it is not suitable for more complex flows such as separated and transition flow. For these types of flows, a wall stress balanced model is more suitable, where the velocity is estimated as follows [107]:

$$u_b^t = \frac{\int_0^{|ab|} 1/(\nu + \nu_t) dl}{\int_0^{|ac|} 1/(1/Re + \nu_t) dl} (u_c^t - u_a^t) + u_a^t \tag{2.40}$$

where

$$\tau_t = \frac{1}{\int_0^{|ac|} \frac{dl}{\nu+\nu_t}} (u_c^t - u_a^t) \tag{2.41}$$

where ν_t is the eddy viscosity near the wall which is modeled with a near-wall damping model as follows:

$$\nu_t/\nu = \frac{1}{\kappa}(y_b^+)(1.0 - e^{-y^+}) \tag{2.42}$$

Equations 2.41 and 2.42 are solved with a Newton iterative method to calculate (u_τ).

For both compressible and incompressible solver, the pressure at immersed point needs to be calculated. The pressure of immersed point (p_b) is same as the fluid points p_c when the surface is stationary because of zero pressure gradient near wall. When the wall is moving, the effect of surface motion on pressure is calculated by adding surface acceleration along normal to the surface $\frac{du_a^n}{dt}$:

$$p_b = p_c + \rho \frac{du_a^n}{dt}. \tag{2.43}$$

For compressible flows, the density should be reconstructed as well based on the type of the boundary condition which can be Dirichlet or Neumann. For example, an isothermal wall imposes a Dirichlet boundary condition for the immersed boundary, i.e., T_a, temperature of solid surface at point (a) remains constant. Consequently, the temperature at point b can be computed using a linear interpolation similar to velocity

$$T_b = \frac{|ba|T_c + |bc|T_a}{|ac|}. \tag{2.44}$$

The density of immersed point can be computed conveniently by using the state equation:

$$\rho_b = p_b/(RT_b). \tag{2.45}$$

Now, with the computed velocity, pressure and density, the energy term (ρE) can easily be com-

puted.

3. VALIDATION *

In this chapter, the validations for LES of incompressible and compressible flows are reported in §3.1 and §3.2, respectively. Part of these studies are now published in Akbarzadeh & Borazjani [167, 158, 127].

3.1 Incompressible LES

This section is organized as follows: The validation for incompressible channel flow is presented in 3.1.1 which is published in Akbarzadeh and Borazjani [167]. The validations for an inclined plate is presented in 3.1.2 that is published now in Akbarzadeh and Borazjani [158], and section 3.1.3 demonstrates the validation of our framework for a pitching airfoil published in Akbarzadeh and Borazjani [158].

3.1.1 Incompressible turbulent channel

Two types of validations are performed here: First, the validation for a turbulent boundary layer for a channel with smooth (flat) walls are presented in §3.1.1.1. Afterwards, the validations are performed for a wavy channel in 3.1.1.2 to ensure our framework can handle separated turbulent boundary layer as well.

3.1.1.1 Turbulent channel with flat walls

The simulations were performed for a turbulent channel with $Re = UH/\nu = 10,000$, defined based on the channel half width (H), mean bulk velocity (U), and kinematic viscosity (ν). Figure 3.1a shows the simulation set-up. The mesh is cuboid and two walls are placed in the fluid domain as immersed boundaries. The simulations of flat channel are performed with two grids that their details are provided in Table 3.1. The simulation with the coarse grid is performed with a Cabot wall modeling. The simulations of the wavy channel are performed with grid 2 in which the grid spacing is kept constant in the vicinity of the wave, i.e., at $-1.2 < y < -0.8$

*Part of this chapter is reprinted from "Large eddy simulations of a turbulent channel flow with a deforming wall undergoing high steepness traveling waves" by A.M. Akbarzadeh and I. Boazjani, 2019 Physics of Fluid 31 (12), 125107

Table 3.1: The details of grids of the simulations. Grid 1 (coarse) and 2 (fine) are used for grid sensitivity study in the flat channel. Grid 2 is used for wavy channel as well.

grid	N_x	N_y	N_z	Δx_{min}	Δy_{min}	Δz_{min}
1	48	48	48	0.0652	0.016	0.1308
2	61	201	361	0.0331	0.0041	0.0110

the grid spacing is ($\delta y = 0.0042$) as expressed in Table 3.1 and Fig. 3.1b,c. The wall normal resolution ($\delta y = 0.0042$) is equivalent to $y^+ = u_\tau^* \delta y^* / \nu^* = 2.5$ which is enough for reconstructing the velocity of the IB nodes with a linear interpolation [165]. The non-dimensional time step ($\delta t = \delta t^* U^* / H^*$) is set to $\delta t = 0.004$ for the flat wall and wavy channel with grid 2, respectively. The corresponding Courant-Friedrichs-Lewy (CFL=$U^* \delta t^* / \Delta z^{*_{min}}$) number for the flat and wavy simulations is 0.35. The time step of the motionless channel corresponds to the time-step in wall unit of $\delta t^+ = \delta t^* u_\tau^{*^2} / \nu^* = 0.13$ which is sufficient for capturing the turbulence statistics [168]. The boundary conditions along streamwise (z), and spanwise (x) directions. The averaging for the flat channel simulations is performed from the time $t = 250H/U$ at which the flow is statistically stationary for a duration of $t = 220H/U$. The averaging for the motionless wavy channel simulations are performed after $t = 85H/U$ and the averaging is performed for $t = 75H/U$.

Figure 3.2a shows the mean normalized streamwise velocity profile ($\bar{u}_z^+ = \bar{u}_z / u_\tau$) compared with the DNS study of Lee and Moser [169]. The flat channel flow study is performed for a coarse grid (grid 1) and a fine grid (grid 2), as shown in Fig. 3.2. The normalized streamwise velocity for both grids follow the log region reasonably though there is a small discrepancy near the wall for the coarse grid due to a lower grid resolution near the wall (Fig. 3.1c). In addition, the profile of normalized turbulent kinetic energy ($q = 0.5(u_x^{'2} + u_y^{'2} + u_z^{'2})$: $u_j' = u_j - \bar{u}_j$ is velocity fluctuation) is plotted in Fig. 3.2b.

3.1.1.2 Turbulent channel with wavy walls

The results of validations for separated flow over a wavy channel are presented in Fig. 3.3. Here, the goal is validating the immersed-boundary LES for separated flows by simulating the

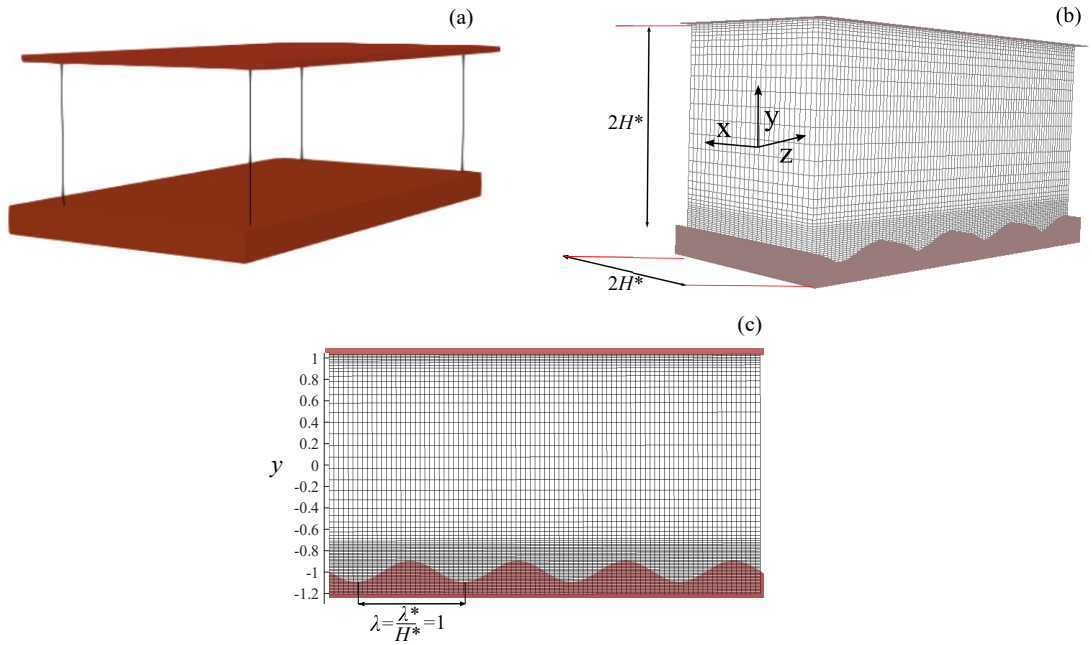

Figure 3.1: Flow simulation set-up: (a) 3D flat channel, (b) 3D wavy channel, and (c) 2D view of the simulation grid and the wavy channel wall. The fluid is discretized with a cartesian grid whose resolution increases near the walls. The wavy bottom wall is discretized with triangular elements and placed as an immersed body onto the background mesh. Every third and fourth points, respectively, are shown in y and z directions for the background grid. Reprinted from [167].

separated flow over a wavy sinusoidal channel, which is placed as an immersed boundary in the fluid domain. The results of these simulations are compared to the LES of Henn and Skyes [170] and the experiment of Buckles et al. [171]. In this simulation, the lower wall has a sinusoidal wavy deformation $y = s\lambda\ sin(2\pi z/\lambda)$: h: is lower wall displacement, the wave steepness is $s = a/\lambda = 0.1$, a is the wave amplitude and λ is the wavelength. The channel streamwise length is $L = 2\lambda$, channel spanwise length is λ, channel height is $2H = \lambda$, and Reynolds number is $HU/\nu = 5300$. In this validation study, the time-averaged spanwise-averaged profile of the wall pressure p_w, i.e., the pressure of the closest immersed nodes to the wall, and streamwise velocity (u_z) over the crest and trough of the wave are plotted in Fig. 3.3a,b,c, respectively. To validate the results, the velocity and pressure are normalized similar to the previous simulations and experiments [170, 171]. The velocity is normalized with the streamwise bulk velocity U_b^*,

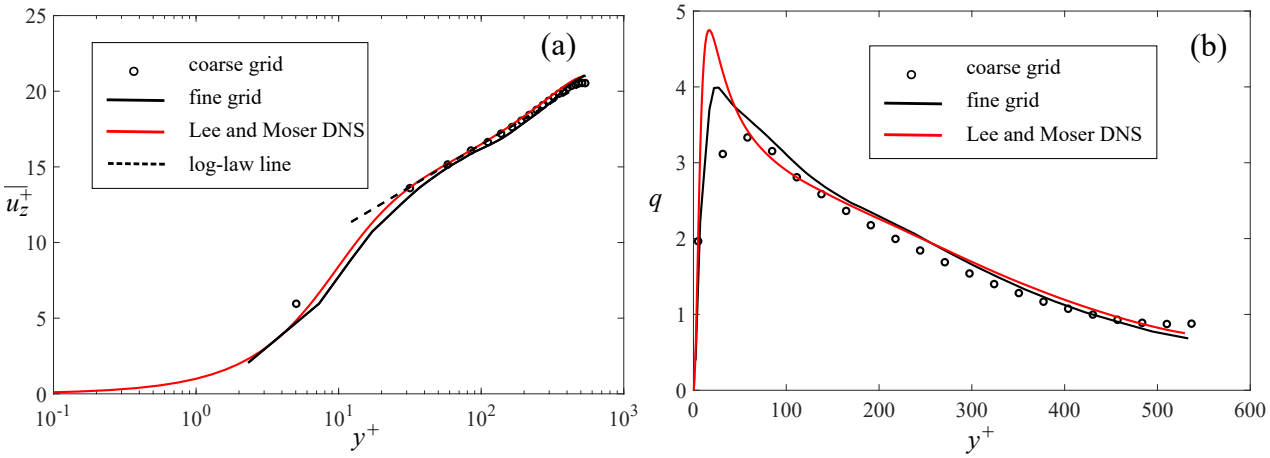

Figure 3.2: Validation for a fully developed turbulent flat channel. (a): Mean streamwise velocity profile. (b): Profile of the normalized turbulent kinetic energy along the channel vertical axis. Reprinted from [167].

which is defined with a normalizing depth equal to the minimum channel depth ($2H - a$) rather than the mean channel depth $2H$. The bulk velocity (U_b) is defined as follows [171]

$$U_b = \frac{1}{2H - a} \int_h^{2H} \overline{u_z} dy, \tag{3.1}$$

Similarly, wall pressure (p_w) is nondimensionalized with $\frac{1}{2}\rho U_b^2$, where ρ is the density. This definition of the bulk velocity (U_b) is used to compare the velocity and pressure of this study to the previous work [170, 171]. Figure 3.3a demonstrates that the computed wall pressure is in good agreement with the previous numerical observation [170] and experimental measurements [171]. The pressure over the downslope and trough of the wave agrees well with the experiment, while there is a small discrepancy (under-prediction) near the uphill. The profile of mean streamwise velocity at both sections ($z = 0$ and $z = 0.5\lambda$) approximately matches the experimental one as shown in Fig. 3.3b,c. In both streamwise sections (crest and trough of the wave), the maximum velocity is about 1.2 at $y = 1.2$ from the wavy wall. In fact, it is deviated toward the flat wall as the momentum of the fluid near the wavy wall has reduced. In Fig. 3.3c, the magnitude of reverse flow on the trough of the wave is approximately equal to the value observed in the experiment.

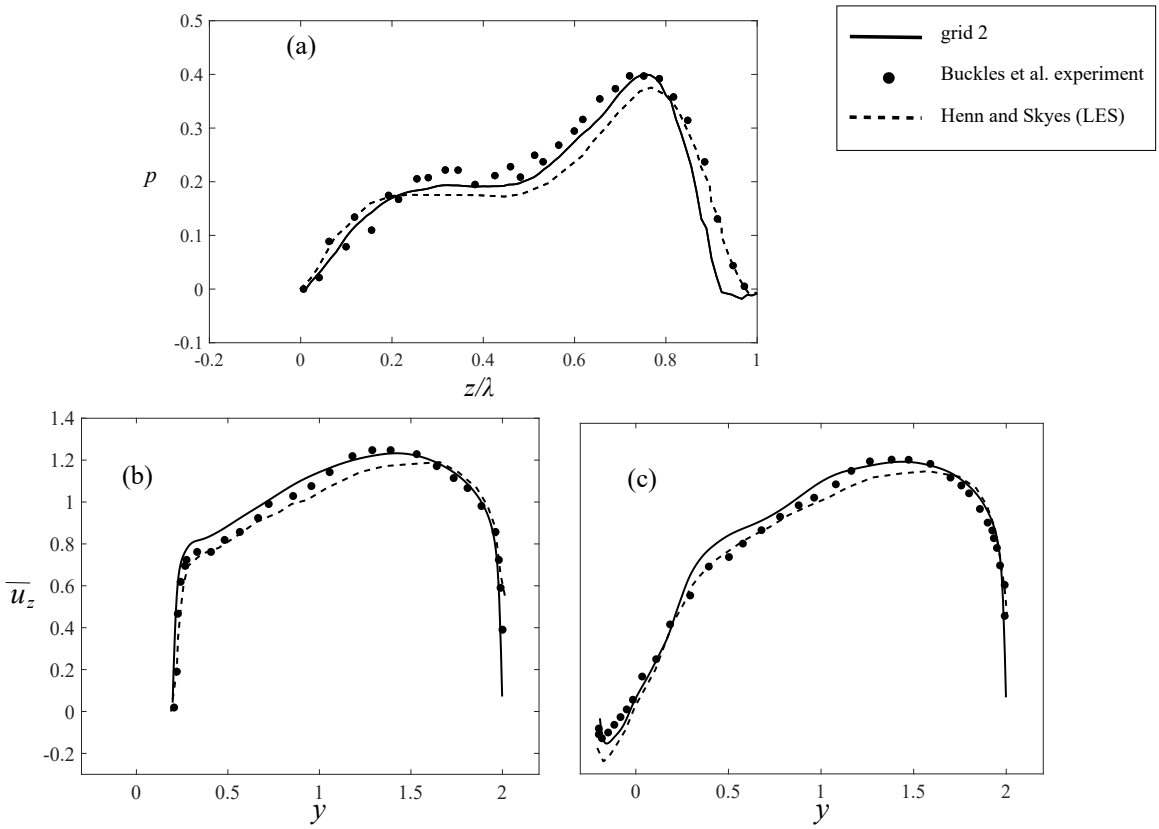

Figure 3.3: Validation for turbulent separated flow: (a) profile of the wall pressure along the wave, (b) profile of the mean streamwise velocity along the vertical direction at z=0, and (c) profile of the mean streamwise velocity along the vertical direction at $z = \lambda/2$. Reprinted from [167].

3.1.1.3 Turbulent channel with traveling wavy walls

The LES-IBM is further validated for traveling waves by carrying out LES simulation of a wavy channel in which its lower wall undergoes traveling waves deformations and comparing the forces against the DNS of Shen et al. [4]. The Reynolds number based on the mean velocity U of the external flow and wall motion wavelength λ is 10,170; the wave steepness is $2\pi a/\lambda = 0.04$ where a is the traveling wave amplitude. Simulations are performed for the static case and a traveling case with wave speed of $C/U = 1.0$. The simulation mesh is almost the same as grid 2 (3.1) except the channel half width, which is $H = 2\lambda/\pi$. The drag force of the waves are shown in Table 3.2. Herein, C_d is the total drag force consists of a form drag (C_p) and a friction drag (C_f), and the forces are normalized with $\rho U^2 A$, where A is the area of the flat plate. The results show about 18.2% discrepancy against DNS for the static case whereas a 7.3% for the traveling wave case.

Table 3.2: Comparison of force coefficients obtained from LES with DNS of Shen et al. [4] for wave speeds $C = 0$ and $C = 1.0$.

case	C	C_d	C_p	C_f
DNS	0	0.0055	0.0038	0.0017
LES	0	0.0065	0.0045	0.0020
DNS	1.0	0.0025	-0.0002	0.0025
LES	1.0	0.0027	-0.0005	0.0027

3.1.2 Inclined plate

To ensure that LES modeling can predict the aerodynamic performance of inclined plates, flow over a 2-D flat inclined plate was simulated at angles of attack ranging from $\theta = 0$ to 12^o with Re = 40,000, which is the same Re in the LES of [172]. The computational domain is presented in Fig.3.4a. As it is shown, the domain is a cube of $0.1L \times 15L \times 15L$ in x, y and z directions. The mesh is cuboid and has $21 \times 421 \times 401$ grid points along x, y, and z direction, respectively. The

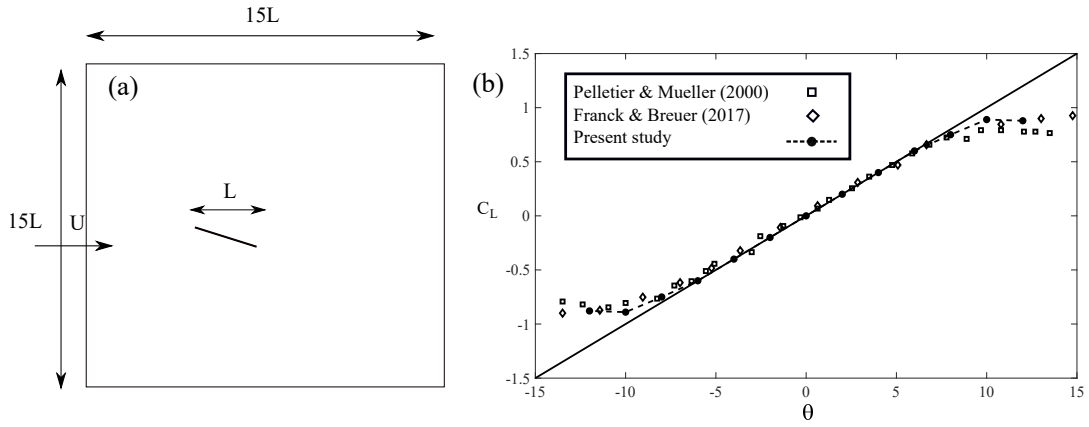

Figure 3.4: Time averaged lift coefficient for a flat inclined plate at various angles of attack θ. Solid line is the classic thin airfoil theory. Reprinted from [158].

grid is clustered in the vicinity of the plate, i.e., it is a rectangle of 0.34 with 280×200 grid points evenly distributed. The mesh is extended towards the boundary with a hyperbolic function. The boundary conditions are as follows: inlet is a uniform flow; in the y directions boundary conditions are slip walls, the outlet is Neumann, and the spanwise boundary condition is periodic since the plate is 2D. The plate is placed as an immersed boundary in the fluid domain centered in the refined zone. More details about the grid and setup can be found in section 4.2 and Table 4.3.

The time-averaged lift coefficient is plotted in Fig. 3.4, where the results for negative angles of attack are extrapolated due to the plate's symmetry, i.e., $C_L(-\theta) = -C_L(\theta)$. In addition, the lift coefficient for an inviscid thin plate is plotted where the lift coefficient is $C_L = \pi^2\theta/90$ (θ in degree). The results of this study agree well with the experimental data of [173] and LES results of [172]. Until angle of attack of 8^o the results follow exactly the experimental results, but there are small discrepancies with the experimental results for higher angles of attack ($\theta > 8$), which can be related to the effect of Reynolds number, as the Reynolds number in the experiment of [173] is $80,000$. Nevertheless, the agreement of our LES with the experimental results is similar to that of [172].

3.1.3 Pitching airfoil

To validate LES simulations for moving boundary with high (Re) we checked the thrust (C_t= -C_D) for a pitching NACA0012 airfoil at Re =12600. The airfoil pitching motion is given by:

$$\theta(t) = \theta_0 \sin(2\pi f^* t) \tag{3.2}$$

where $\theta_0 = 2^o$ is the amplitude of the pitching motion and the center of the rotation is at $0.25L$, same as previous experiments [174]. The computational grid used for this simulation is a $0.09L \times 15L \times 15L$ box in x, y and z directions, where L is the chord length, respectively. The airfoil is placed as an immersed body at $5L$ from the inlet boundary. The $x-y-z$ directions are discretized by $21 \times 401 \times 601 \simeq 5$ million nodes. The inlet is a uniform flow and boundary conditions in the x and y directions are slip walls and the outlet is Neumann. Figure 3.5a shows the variation of mean thrust coefficient ($C_T = -C_D$), with reduced frequency f^*. As it can be observed, the thrust coefficient in our simulations was in good agreement with the previous experimental and numerical results [175, 174, 176] for low reduced frequency ($f^* < 3$). However, there are discrepancies between our numerical results, the experimental results of Koochesfahani et al. [174] and numerical results of Lai and Platzer [175] and [176] for higher reduced frequency, i.e., our results underestimate the thrust reported by [175] about 10% at $f^* = 4$ and overestimate the thrust reported by [174] about 40% at $f^* = 3.5$. The reason for the discrepancy between our results and reported thrust of [175] and [176] can be the difference between the numerical methods, i.e., [176] used a DNS compressible flow solver for their two dimensional simulations, whereas ours is an incompressible LES flow solver for 3D simulation (there are 21 nodes in the spanwise direction to handle the 3D effects of the flow). The reason for the discrepancy between the experimental result of [174] and numerical results at high reduced frequency can be the uncertainties for estimating the forces as [174] estimated the thrust by applying the integral momentum theorem to a control volume surrounding the airfoil. Although they consider the effect of velocity fluctuations in their estimation, but even calculating the fluxes induced by velocity fluctuation has uncertainty

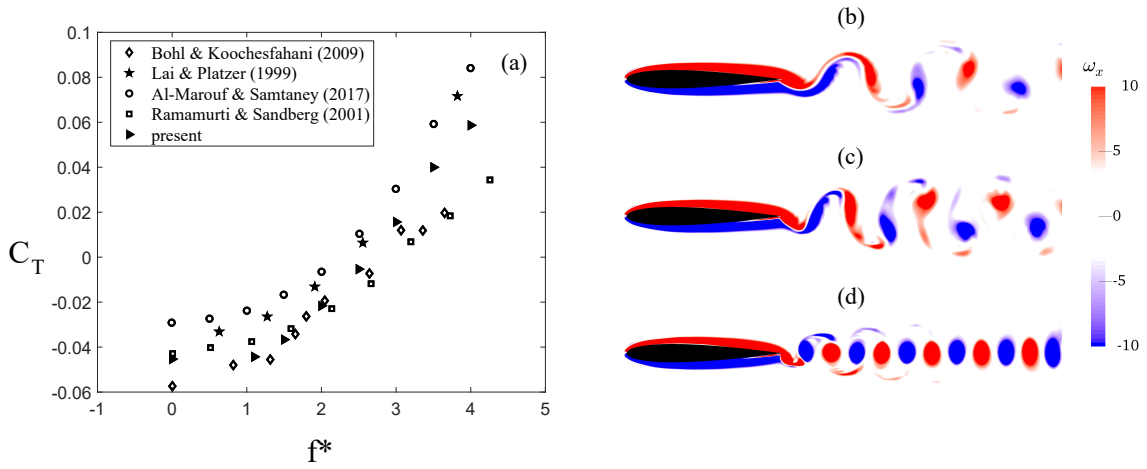

Figure 3.5: LES of a pitching airfoil, (a) Thrust coefficient for a pitching airfoil with nondimensional frequency (fl/U). (b) to (d) Wake visualization by spanwise vorticity; (b) $f^* = 1.5$, (c) $f^* = 2.0$, (d) $f^* = 3.5$. Reprinted from [158].

which increases by increasing f^* as reported by [174]. In addition, the the spanwise vorticity field is presented for three frequencies (figure 3.5(b,c,d)) which is similar to the vorticity distribution observed by [174], [177] and [176]. The streamwise spacing between vortices is proportional to $1/f^*$ as it is also reported by [174], i.e., the streamwise spacing was $0.65L$, $0.52L$, and $0.37L$ for reduced frequencies 1.5, 2.0, and 3.5, respectively.

3.2 Compressible LES

In this section the validations for the developed compressible LES are presented. First, the LES is validated against decaying isotropic turbulent flows. Afterwards, the validation of compressible channel flow, and shock diffraction by a cylinder are reported.

3.2.1 Decaying isotropic turbulent flow

To validate our computational scheme and our LES, large eddy simulations of isotropic decaying turbulence are performed with a dynamic C_s and the results are compared against the results of direct numerical simulations (DNS) of Samtaney et al. [178] and LES of Li et al. [179]. The computational details of this simulation are described as follows.

The computational domain is a cube of $[0, 2\pi] \times [0, 2\pi] \times [0, 2\pi]$ which is discretized evenly

with 64 grid points in each direction. The boundary conditions are periodic for every parameter at all boundaries. Here, the Mach number is $M_t = u'/c = 0.4$, where u' is the turbulent fluctuation velocity and c is the speed of sound. The Reynolds number is $Re_\lambda = \lambda u' \rho/\mu = 153$, defined based on u' and taylor length scale (λ). The turbulence fluctuation velocity is <$u_i^2/3$>, where <> is the volume average in the computational domain, u_i ($i = 1, 2, 3$) is the i-th component of the velocity vector, and Taylor length scale is defined as

$$\lambda^2 = \frac{u'^2}{< (\partial u_i/\partial x_i)^2 >}, \tag{3.3}$$

The simulation is initialized with a specified spectrum [178] for velocity which is divergence free initially and given by

$$E(k) = Ak^4 exp(-2k^2/k_0^2) \tag{3.4}$$

where k is the wave number, $k_0 = 6$ is the wave number at which the spectrum peaks, similar to study of Li et al. [179], and A is a constant chosen to get initial kinetic energy of 1.0. The turbulence decay is presented for different times (t/τ), where τ is the initial large-eddy turnover time, defined as

$$\tau = \sqrt{\frac{32}{A}} (2\pi)^{\frac{1}{4}} k_0^{\frac{-7}{2}} \tag{3.5}$$

The turbulence decay is presented in Fig. 3.6, which visualizes the magnitude of vorticity in computational domain at three different times $t/\tau = 1$, $t/\tau = 2$, and $t/\tau = 5$. The reduction of the magnitude of vorticity in time indicate the reduction of turbulence intensity of the flow. The plot of turbulent kinetic energy spectrum ($E(k)$) versus k is presented at 4 different times in Fig.3.6d. The computed plot for energy cascade at $t/\tau = 5$ reveals that the LES model can capture the inertial subrange as the energy spectrum follows the theoretical 5/3 power law. The validation of the study is performed by comparing the time history of turbulent kinetic energy (TKE) of the domain obtained from LES and DNS of Samtaney et al. [178] and LES of Li et al.[179] in Fig. 3.6e. The TKE is defined as TKE=$0.5 < u_i^2 >$. The plot for the time history of the TKE is in good agreement with the DNS at times $t/\tau > 2$, but there is a small discrepancy at $t/\tau < 2$, which can be due to

lower grid resolution compared to DNS because a similar discrepancy is also observed in LES of Li et al. [179] which had a similar grid resolution. Nevertheless, the good agreement between the history of the turbulence decay of our simulations and previous studies [179, 178] show that our LES deployed and the hybrid scheme can properly model the subgrid stress tensor.

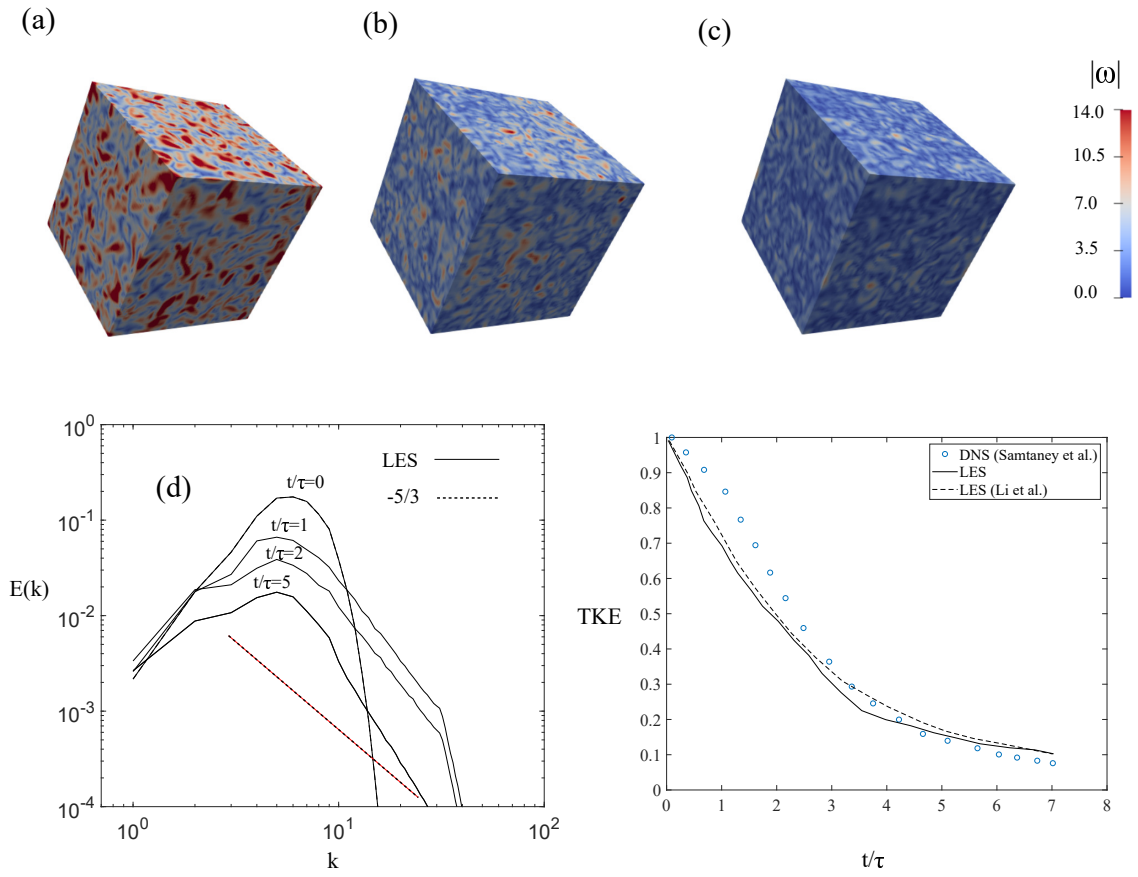

Figure 3.6: (a) The decay of vorticity at (a) $t/\tau = 1$, (b) $t/\tau = 2$, and (c) $t/\tau = 5$. (d) The decay of energy spectrum $E(k)$ in time, (e) the decay of turbulence kinetic energy (TKE)

3.2.2 Compressible channel

To validate our code and setup for turbulent wall bounded flows, LESs of a turbulent channel are performed for a subsonic flow with $M = 0.5$ and a supersonic flow with $M = 1.5$. The simulations are performed with two grids, which their details are shown in Table 3.3. The channel length and width of grids are $2\pi H$ and πH, respectively. The grid mesh is a cuboid (Fig. 3.1a)

Table 3.3: The details of grids of the simulations. Grid 1 (coarse) and 2 (fine) are used for grid sensitivity study in the flat channel. Grid 2 is the main grid of the simulations with wavy walls.

grid	N_x	N_y	N_z	Δx_{min}	Δy_{min}	Δz_{min}
1	48	48	48	0.0652	0.016	0.1308
2	120	112	240	0.0261	0.0035	0.0261

that is evenly spaced along x and z directions. In the y direction, the grid is clustered towards both walls with a hyperbolic function as shown in Fig. 3.1a. The grid spacing near the wall is ($\delta y = 0.0035H$) as expressed in Table 3.3. The wall normal resolution ($\delta y = 0.0035H$) is equivalent to $y^+ = u_\tau \delta y/\mu = 0.8$ which is enough for reconstructing the velocity of the IB nodes with a linear interpolation [165]. The non-dimensional time step ($\delta t^* = \delta t \bar{u}/H$) is set to $\delta t^* = 0.002$.

The results of subsonic and supersonic cases are compared against the results of direct numerical simulations (DNS) of Lee et al. [169] and Coleman et al. [180], respectively. Note that we compare the subsonic case against incompressible results because it has been demonstrated when the Mach number is lower than 0.6, the flow regime is expected to follow a quasi-incompressible pattern. The validation results are presented in Fig. 3.7. The mean streamwise velocity ($< u_z >$) is normalized with the friction velocity (u_τ), i.e., $< u >^+ = < u_z > /u_\tau$, and plotted against wall normalized distance (y^+) in Fig. 3.7a. It can be observed that the mean velocity is in good agreement with DNS of Lee et al.[169] for both grids. The mean velocity $< u >$ normalized by bulk velocity ($u_0 = \frac{1}{2H}\int_0^{2H} u_z dy$) and the mean density ($< \rho >$) normalized by the bulk density ($\rho_0 = \frac{1}{2H}\int_0^{2H} \rho dy$) are plotted along channel half width for case 2. It can be observed that by refining the grid, the profiles of mean velocity and density agree well with the DNS of Coleman et al. [181]. The results of the validation study indicate that our framework can properly resolve the turbulent boundary layer.

3.2.3 Shock diffraction

In this section, 2D simulation of the diffraction of a moving planar shock at Mach number M=2.81 with a stationary cylinder is presented. The simulations are performed with a hybrid scheme and C_s is 0.01. The domain size of the simulations is $25D \times 10D$, where D is the diameter

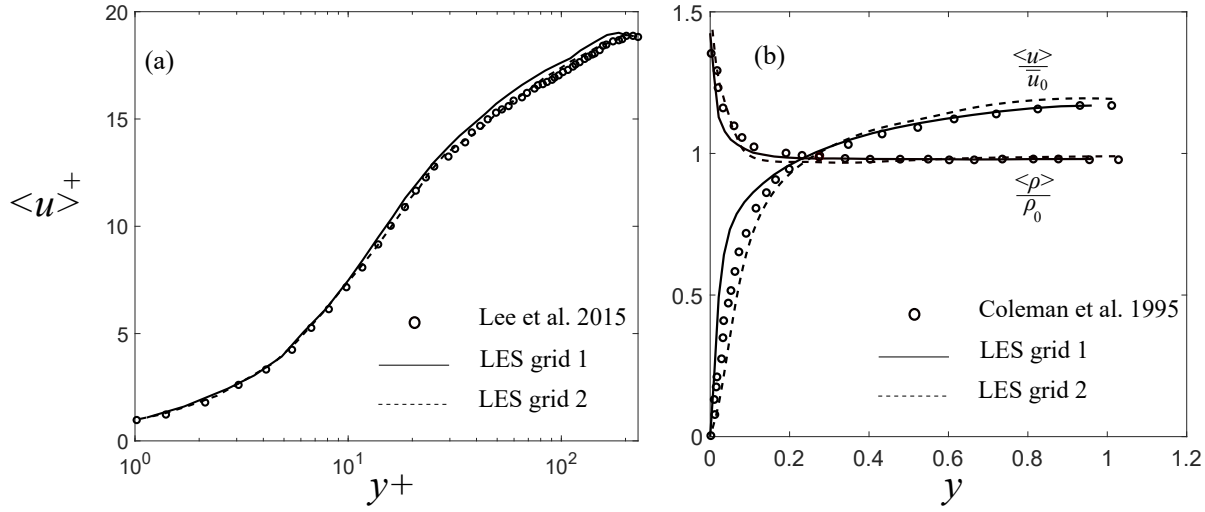

Figure 3.7: The comparison of LES with DNS for (a) case 1 ($M = 0.5$) and (b) case 2 ($M = 1.5$).

of the cylinder, and meshed evenly with 4400×1200 nodes. The time-step is chosen $0.001D/U$ that corresponds to Courant–Friedrichs–Lewy (CFL) number of 0.2. The simulation is carried out with no-slip conditions on the surface of the cylinder. The Reynolds number $UD\rho/\mu = 8700$ (where $U = \sqrt{(p/\rho)}$ is the velocity scale, and μ is the dynamic viscosity behind the undisturbed shock) which matches the Reynolds number of experiments of Bryson and Gross [3]. Figure 3.8 shows the interaction of a moving shock with a cylinder. The moving shock is reflected by the cylinder (Fig. 3.8b) and generates a reflected shock (R.S.), incident shock (I.S.), and a Mach shock (M.S.). The intersection of the R.S., M.S.1, and I.S. is called the first triple points (T.P.1). The interaction of M.S.1 from the top and the bottom of the symmetry plane creates M.S.2 and their intersection creates T.P.2 (Fig.3.8d). The contact discontinuity (C.D.2) is formed behind M.S.1 and M.S.2.

Figure 3.9a presents the comparison of the loci of the triple points, i.e., $x = 0$ and $y = 0$ corresponds to the center of the cylinder. As it can be observed in Fig. 3.8c, two triple points appear on either side of the plane of symmetry of the flow. The first one (T.P.1) starts at the front of the cylinder ($x/D = 0.0$), and the second one (T.P.2) at the plane of symmetry behind the cylinder ($x/D = 1.6$). The location of both triple point obtained from the simulation is in

good agreement with the experimental results [3], which reveal that the hybrid scheme and switch function can properly capture the shock waves for flows interacting with immersed boundaries. Moreover, the flow is visualized with the contours of out-of-plane vorticity (ω_z) in Fig. 3.9b. The flow visualization shows vortex shedding in the wake of the cylinder at about 8.6D upstream of the moving shock. The shedding occurs when the shear layer in the wake of the cylinder becomes unstable.

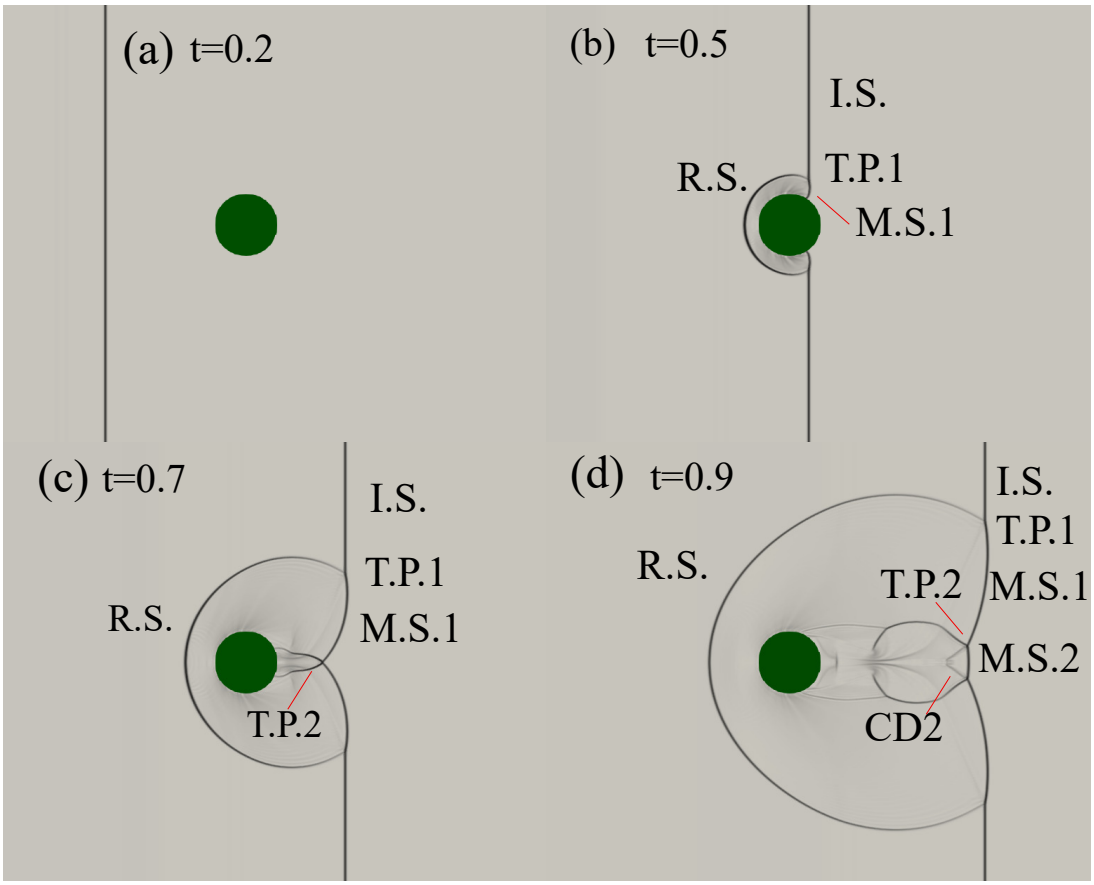

Figure 3.8: The interaction of a moving shock and a circular cylinder. R.S. reflected shock, M.S.1 Mach shock, I.S. incident shock, T.P.1 the first triple point, and T.P.2 is the second triple point.

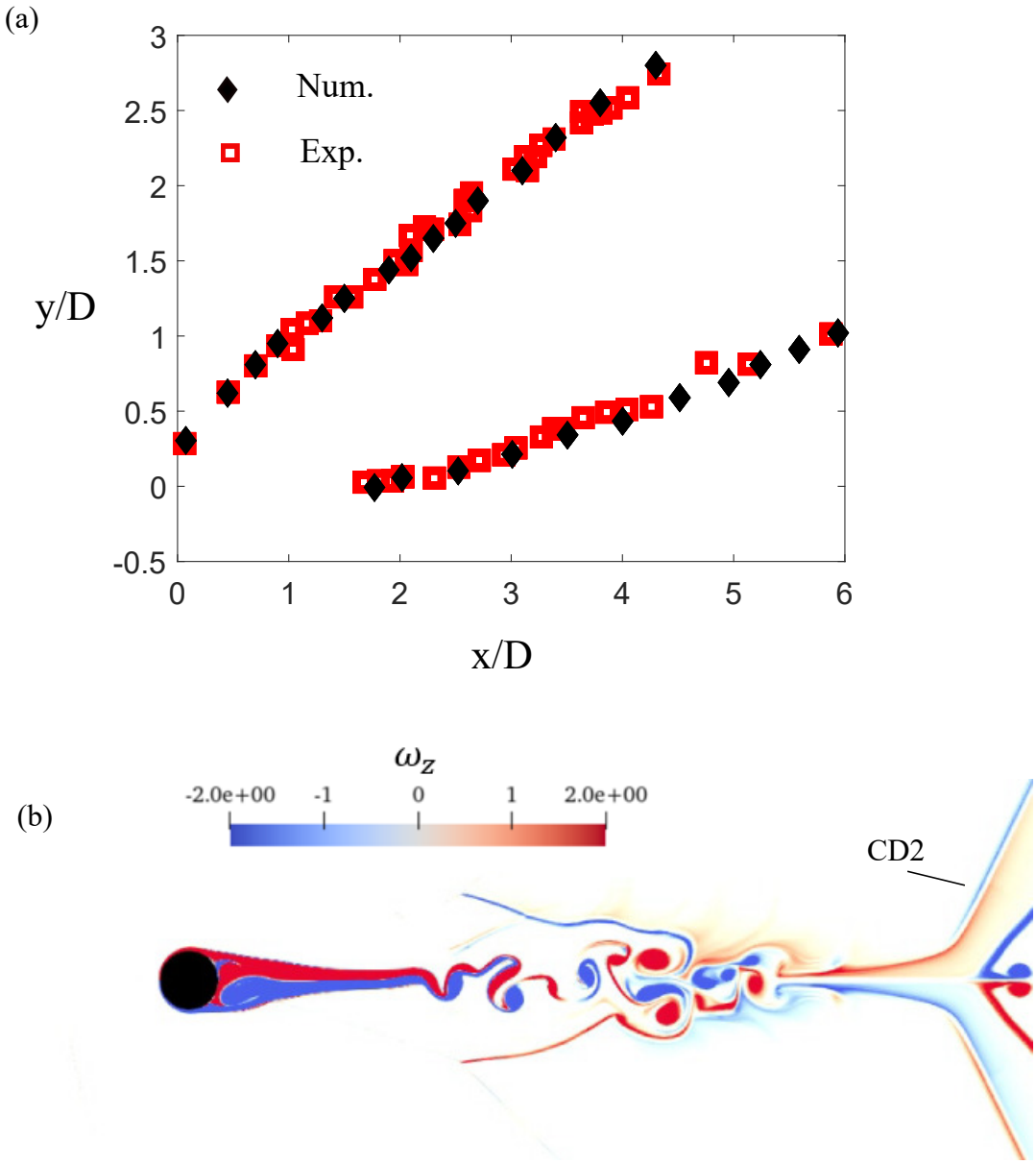

Figure 3.9: (a) The location of the T.P.1 (upper curve) and T.P.2 from the simulation (Num.) and experimental results of Bryson and Gross [3]. (b) Contours of the vorticity in the wake of the cylinder at $t = 2.7$.

4. TRAVELING WAVES FOR FLOW CONTROL OF INCOMPRESSIBLE FLOWS*

In this chapter, the results of simulations of active flow control by traveling wave surface morphing in turbulent flows are presented. First, the effect of traveling waves on a turbulent chaanel are presented in 4.1. The effects of traveling waves on flow separation for an inclined plate and airfoil are studied in §4.2 and §4.3. Part of these studies are now published in Akbarzadeh & Borazjani [167, 158, 182, 183].

4.1 Traveling wavy turbulent channel flow

In this section, LES of flow in turbulent channel with motionless wavy wall, and traveling wave walls are carried out. This chapter is organized as follows: a background on wavy incompressible channel and traveling wave is studied in §4.1.1. The details of the simulations are shown in §4.1.2. The results of the simulations are presented in §4.1.3. The discussion and conclusion are provided in §4.1.4 and finally the limitation and future work are presented in §4.1.5.

4.1.1 Background

Flow of a motionless wavy channel becomes separated from the crest of the wave as the flow over a concave surface is subject to a centrifugal instability that generates a Gortler vortex [184]. However, the separated flow over the wavy wall is removed when the wall undergoes a backward traveling wave [4]. In addition, it is found that backward traveling waves can reduce the pressure drag and turbulent kinetic energy [4]. Based on previous studies of traveling waves with a small steepness ($s = a/\lambda < 0.0625, a$: nondimensional wave amplitude, λ: nondimensional wavelength) [4], it is thought that the nondimensional wave-speed ($C^* = C/U$, C: dimensional wave-speed, U: mean channel velocity) is required to be more than one to have a zero net drag. In addition,

*Part of This chapter is reprinted with permission from "Large eddy simulations of a turbulent channel flow with a deforming wall undergoing high steepness traveling waves" by A.M. Akbarzadeh and I. Boazjani, 2019 Physics of Fluid 31 (12), 125107, copyright [2019] by authors, "Reducing flow separation on an inclined plate via backward traveling waves" by A.M. Akbarzadeh and I. Boazjani, 2019 JFM 880, 831-863, copyright [2019] by Cambridge University Press, and "Controlling Flow separation on a thick airfoil using backward traveling waves" by A.M. Akbarzadeh and I. Boazjani, 2020 AIAA journal 58 (9), 3799-3807, copyright [2020] by authors.

it has been reported that when $C > U$, the turbulence intensity highly reduces in the vicinity of the wavy surface, i.e., has its minimum value [185]. Nevertheless, most of the studies on traveling wavy channel focused on low wave-steepness ($s = a/\lambda \approx 0.05; a$: amplitude, λ : wavelength), and effect of waves with higher steepness has not been investigated. Our goal in this study is to investigate the effect of high wave steepness waves ($s > 0.1$) on mean flow and turbulence statistics, as many swimmers undulate their bodies with high wave steepness waves [186]. To achieve this goal, simulations of turbulent channels in which a wall was undergoing traveling wave deformations were carried out. In these simulations, the steepness ranges from $0.05 < s < 0.15$ and wave speed ranges from $-0.4U < C < 1.6U$.

4.1.2 Methods

In this study, we numerically investigate the turbulent flow of a channel in which a wall is undergoing traveling wave oscillations as shown in Fig. 4.1a. Flow is in the frame $x_i = (x, y, z)$ where x, y, z are spanwise, vertical and streamwise coordinates, respectively. Here, the characteristic length is the channel half width (H^*), which is same as the wavelength (λ^*), and the characteristic velocity is the mean velocity U^*. As shown in Fig. 4.1b, the lower wall is undergoing a vertical oscillation (y direction) in the form of a backward sinusoidal traveling wave in the streamwise direction (z) as follows:

$$h = a\, cos(\frac{2\pi}{\lambda}(C\, t - z)) \tag{4.1}$$

where $h = h^*/H^*$ is the non-dimensional vertical displacement of the lower wall, $a = a^*/H^* = s\lambda$ is the non-dimensional amplitude of the wave, $\lambda = \lambda^*/H^*$ is the non-dimensional wavelength, s is the wave steepness, C is the non-dimensional wave-speed, and $t = t^*H^*/U^*$ is the non-dimensional time. Here, the parameters with (*) symbol are dimensional. The simulation set-up configuration, including the domain size, grid size, and wave varying parameters are summarized in Table 4.1. The Reynolds number is chosen $Re = H^*U^*/\nu^* = 10,000$ based on the mean streamwise velocity (U^*), channel half height (H^*) and kinematic viscosity (ν^*), which is equivalent to $Re_{\tau^*} = u_\tau^* H^*/\nu^* = 570$, based on the friction velocity (u_τ^*) [169]. The simulations

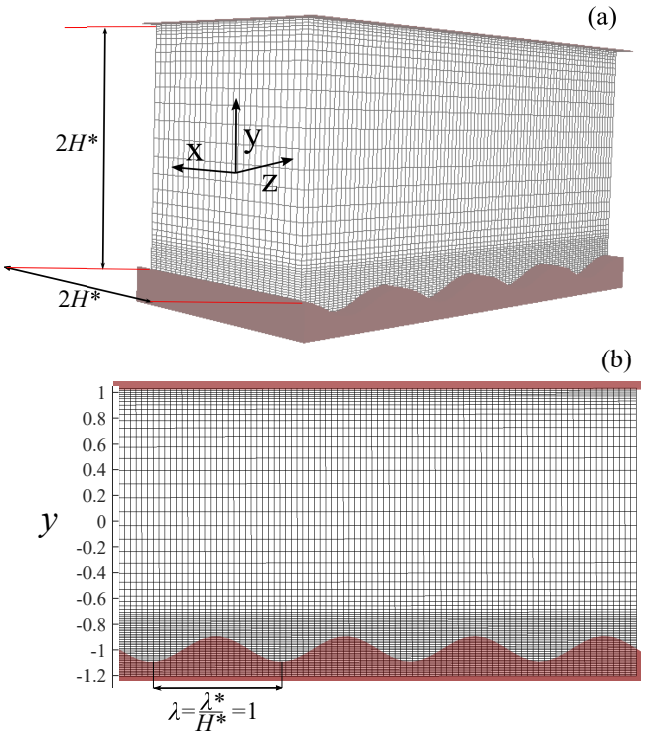

Figure 4.1: Flow simulation set-up: (a) 3D (b) 2D view of the simulation grid and the wavy channel wall. The fluid is discretized with a cartesian grid whose resolution increases near the walls. The bottom wall of the channel which moves with a traveling wave is discretized with triangular elements and placed as an immersed body onto the background mesh. Every third and fourth points, respectively, are shown in y and z directions, respectively, for the background grid. Reprinted from [167].

are performed using three grids presented in Table 4.1. Grid 1 is used only for validation and grid sensitivity studies. The undulatory simulations are performed using grid 2, and the domain sensitivity study of the undulating cases is performed using grid 3, in which the streamwise length is doubled but its resolution is kept the same as grid 2 (Table 4.1). The channel length and width of grid 2 are $4H^*$ and $2H^*$, respectively. The grid mesh is a cuboid (Fig. 4.1a) that is evenly spaced along x and z directions. In the y direction, the grid is clustered towards both walls with a hyperbolic function as shown in Fig. 4.1b. The grid spacing is kept constant in the vicinity of the wave, i.e., at $-1.2 < y < -0.8$ the grid spacing is ($\delta y = 0.0042$) as expressed in Table 4.1 and Fig. 4.1b. The wall normal resolution ($\delta y = 0.0042$) is equivalent to $y^+ = u_\tau^* \delta y^* / \nu^* = 2.5$ which

is enough for reconstructing the velocity of the IB nodes with a linear interpolation [165]. The non-dimensional time step ($\delta t = \delta t^* U^*/H^*$) is set to $\delta t = 0.004$, and $\delta t = 0.003$ for the motionless wavy wall and the traveling wave, respectively. The corresponding Courant-Friedrichs-Lewy (CFL=$U^*\delta t^*/\Delta z^{*_{min}}$) number for the motionless and traveling wavy simulations are 0.35 and 0.27, respectively. The time step of the motionless channel corresponds to the time-step in wall unit of $\delta t^+ = \delta t^* u_\tau^{*^2}/\nu^* = 0.13$ which is sufficient for capturing the turbulence statistics [168]. The boundary condition along the streamwise and spanwise direction is periodic.

In the traveling wave simulations, the varying parameters are C and $s = a/\lambda$ (changed by a) in Eqn. (4.6). Different case studies are presented in Table 4.2 which are classified by their amplitude into 4 rows. Case 4 is the validation case study, which has wavy motionless wall with amplitude and wavelength identical to Henn and Skyes [170] simulation. In cases 1-3, the non-dimensional wavelength is $\lambda = 1.0$ and the non-dimensional wave-speed (C) varies from -0.4 to 1.6, where the negative wave-speed represents a forward traveling wave. The non-dimensional amplitude ranges from $0.05 - 0.15$ which leads to the Strouhal number ($St = 2sC$) varies from 0.04-0.48. The LES simulations are first performed for a flat channel in §3.1 with grids 1 and 2 to further test the grids for LES. Afterwards, the validations for wavy channel are performed, which are presented in §3.1. The instantaneous results of the motionless wavy channel are used as the initial condition of the traveling wave simulations. It has been observed that the flow of the traveling wavy channel become quasi-steady after about 25 cycles. However, the averaging is performed after at least 30 cycles for 20 cycles. In fact, the flow over the oscillating wall becomes quasi steady-state in a shorter time than the flat channel and motionless wavy channel because the flow is dominated by the prescribed oscillations which will be shown later. To ensure that the averaging time was sufficient the sampling uncertainty of the forces is calculated using the procedure described by Oliver et al.[187] which is reported in appendix §B.1.

4.1.3 Results

The effect of undulatory oscillations with different wave-speeds at three wave steepness $s = 0.05, 075, 0.15$ (Table 4.2) on the mean flow, mean streamwise forces acting on the wave, and the

Table 4.1: The details of grids of the simulations. Grid 1 (coarse) and 2 (fine) are used for grid sensitivity study in the flat channel. Grid 2 is the main grid of the simulations with wavy (stationary and traveling) walls, and grid 3 is used for the domain sensitivity study. Reprinted from [167].

grid	N_x	N_y	N_z	Δx_{min}	Δy_{min}	Δz_{min}
1	48	48	48	0.0652	0.016	0.1308
2	61	201	361	0.0331	0.0041	0.0110
3	61	201	721	0.0331	0.0041	0.0110

Table 4.2: Undulating waves with different parameters, amplitudes, wavelength, steepness, and wave-speed. The traveling wave with a negative wave-speed represents a forward traveling wave. Reprinted from [167].

case	a/H	λ	s	C_{min}	C_{max}
1	0.05	1.0	0.05	-0.4*	1.6
2	0.075	1.0	0.075	-0.4	1.6
3	0.15	1.0	0.15	-0.4	1.6
4†	0.2	2.0	0.1	0.0	0.0

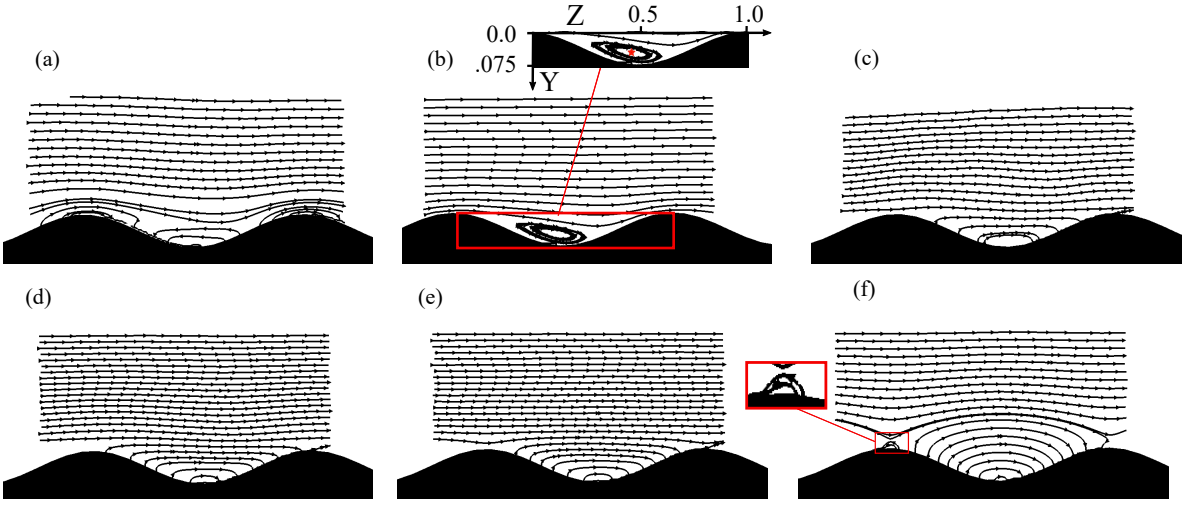

Figure 4.2: Streamlines of the velocity for case 2 ($s = 0.075$) with different wave-speeds: (a) forward traveling wave with $C = -0.4$, (b) motionless wavy channel ($C = 0.0$), (c) backward traveling wave with $C = 0.4$, (d) backward traveling wave with $C = 0.8$, (e) backward traveling wave with $C = 1.2$, and (f) backward traveling wave with $C = 1.6$. The inset of (b) shows the position of the separation bubble, and inset of (f) indicates the reverse flow on the crest of the wave. Reprinted from [167].

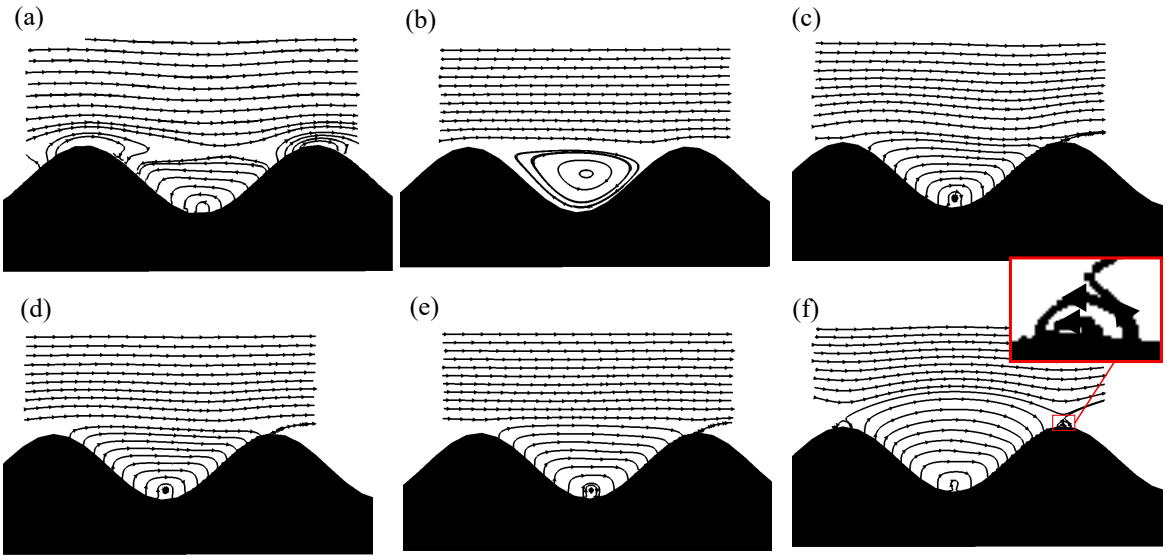

Figure 4.3: Streamlines of the velocity for case 3 ($s = 0.15$) with different wave-speeds: (a) forward traveling wave with $C = -0.4$, (b) motionless wavy channel ($C = 0.0$), (c) backward traveling wave with $C = 0.4$, (d) backward traveling wave with $C = 0.8$, (e) backward traveling wave with $C = 1.2$, and (f) backward traveling wave with $C = 1.6$. The inset shows the reverse flow on the crest of the wave. Reprinted from [167].

turbulence kinetic energy (TKE) is reported in this section. Because the surface oscillations are periodic, the velocity field and TKE of the traveling wave case are phase-averaged. Our observations reveal that the velocity field for cases 1 and 2 are similar. Therefore, to avoid repetition, only the flow visualization for case 2 is shown.

The structure of mean flow for waves with two steepness values is presented by the streamlines in Figs. 4.2 and 4.3 for cases 2 and 3, respectively. In each case, the mean flow is visualized for different non-dimensional wave-speeds of C = -0.4, 0.0, 0.4, 0.8, 1.2, and 1.6 in Figs. 4.2-4.3a, b, c, d, e, and f, respectively. When the wavy wall is motionless ($C = 0$) with a low steepness ($s = 0.05$ and 0.075), the flow becomes separated on the downslope of the wave and generates a separation bubble (a clockwise vortex) that reattaches on the uphill of the wave (Fig. 4.2b). The center of the separation bubble is at $Z = 0.37$ and $Z = 0.42$ for cases 1 and 2, respectively, where $Z = 0$ is at the crest of the wave (see the inset of Fig. 4.2b). The streamwise location of the

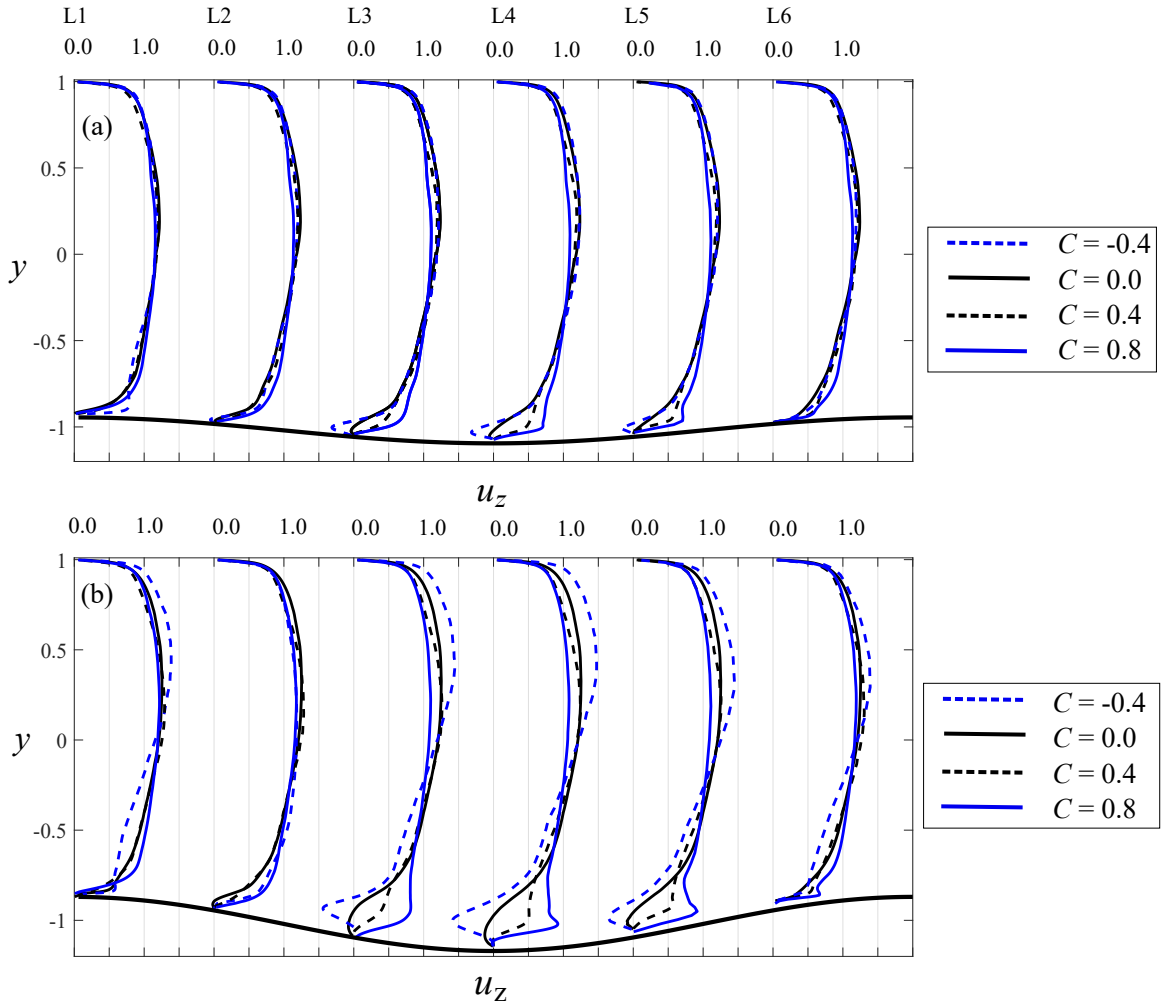

Figure 4.4: Streamwise velocity profile for a forward traveling wave with wave-speed $C = -0.4$, motionless wavy channel ($C = 0.0$), and backward traveling waves with wave-speeds $C = 0.4$ and $C = 0.8$ along six streamwise sections for two cases: (a) case 2 ($s = 0.075$), and (b) case 3 ($s = 0.15$). Reprinted from [167].

center of the sparation bubble is similar to the one reported in Shen et al. [4] in which the wave steepness was $s = 0.04$ and Z was about 0.38. When the wave steepness increases to $s = 0.15$ (Fig. 4.3b), the separation bubble grows such that it fills the whole trough of the wave, and the streamwise location of its center translates to $Z = 0.52$. The generated vortex (separation bubble) of the motionless wave (Fig. 4.3b) resembles the one observed by Henn and Skyes [170], and Ganju et al. [188]. As the wavy wall undulates with a forward traveling wave ($C = -0.4$), a

high reverse flow is generated in the trough of the wave (see the direction of streamlines in Figs. 4.2a and 4.3a), similar to the results of Shen et al. [4]. While a negative wave-speed increases the reverse flow in the troughs of the wave (Figs 4.3a), a positive one increases the streamwise velocity in that zone (Figs 4.3c-f). By increasing the wave-speed, the magnitude of the vertical velocity of the fluid adjacent to the surface increases monotonically because the velocity of the surface scales with $u_y = O(sC)$, which can be analytically obtained by taking the derivative of the vertical oscillations (h) with respect to the time (t) in Eqn. (4.6). As the vertical velocity of the fluid adjacent to the surface increases, the vertical velocity of the flow away from the surface increases, which can be observed by comparing the streamlines over the trough of the wave for high wave-speed case $C = 1.6$ (4.2f and 4.3f) and the rest of the cases. In fact, the size of the zone where the flow is influenced by the wave is larger for the high wave-speed waves (Figs. 4.2f and 4.3f). In addition, the traveling wave with a high wave-speed ($C = 1.6$) induces a reverse flow on the crest of the waves (Figs. 4.2f and 4.3f).

To see the effect of the wave steepness and the wave-speed on the streamwise velocity, the profiles of the mean streamwise velocity for cases 2 and 3 for a forward traveling wave with $C = -0.4$, a motionless wavy channel ($C = 0.0$), and two backward traveling waves with $C = 0.4, 0.8$ are plotted in Figs. 4.4a and b, respectively. Comparing the velocity profile of cases 2 and 3 for the motionless wavy channel demonstrates that the reverse flow has increased by increasing the wave steepness (sections L3, L4 and L5 in Fig. 4.4a,b). Figure 4.4 shows that the flow near the wavy wall is influenced by the wave-speed of the traveling wave. For both cases, in sections L3, L4, L5 and L6, when the wave-speed increases, the streamwise velocity near the wall increases and the forward traveling wave induces a reverse flow. The change of u_z with respect to the motionless wavy channel is higher for the high steepness waves (case 3) because they have a higher surface velocity ($u_y = O(sC)$) which increases the velocity of the fluid near the surface. The backward traveling waves increase the axial momentum of the fluid near the wavy surface, e.g., a local maximum is observed in Fig. 4.4b in case 3, for wave-speed $C = 0.8$ at $z = 0.5\lambda$ (section L4) and $z = 0.67\lambda$ (section L5). For case 3, the traveling waves also affect the streamwise velocity

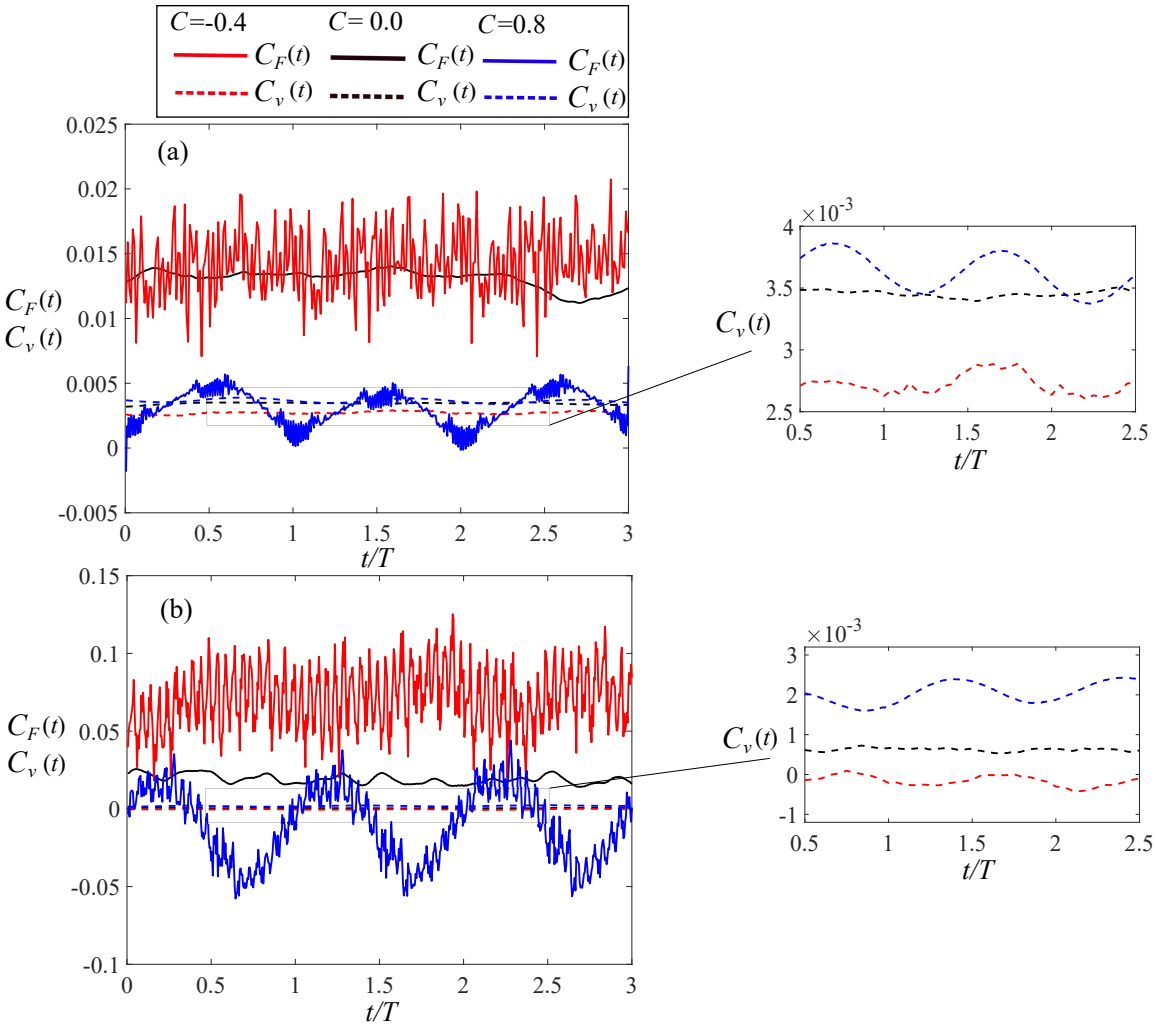

Figure 4.5: The profile of instantaneous forces including, total instantaneous force $C_F(t)$, and viscous force $C_v(t)$ for three cycles for waves with wave-speed of C=-0.4, 0.0, and 0.8, for two wave steepness: (a) case 1 ($s = 0.05$), and (b) case 3 ($s = 0.15$). Reprinted from [167].

of the fluid far away from the wavy wall, e.g., near the flat wall (Fig. 4.4b). It can be observed that at $y > -0.5$ at sections L2 to L6, the streamwise velocity decreases by the increase of wave-speed such that the maximum of u_z on section L4 of the motionless wavy channel decreases from $u_z = 1.22$ to $u_z = 1.14$, when C becomes 0.8. The reason for the decrease of u_z far away from the wavy wall is the increase of u_z in the vicinity of the wavy wall. The mass flux in each section of the channel remains almost constant due the conservation of mass ($\int_h^2 \bar{u_z} dy = 2 \pm 0.01$). Therefore, the reverse flow near the forward traveling wavy wall is canceled out with the increase of u_z around

the middle of the channel to keep the mass flux at a constant value (see sections L3, L4, and L5 of Fig. 4.4b).

Traveling waves affect the forces acting on the wavy surface. The instantaneous force acting on the wavy wall along stramwise direction (z) is composed of the pressure and viscous forces as follows (see[189] for more detail):

$$C_F(t) = \frac{1}{\frac{1}{2} \times A_{flat}} \int_A (-pn_3 + \tau_{3j}\, n_j) dA, \tag{4.2}$$

where all elements of Eqn. (4.2) are in their non-dimensional form, defined in §4.1.2. Here, the force coefficient is normalized the area of the flat surface $A_{flat} = 8$. The first term of the integral is the pressure force, and the second term is the viscous force. dA is the area of an element of the wavy surface, n_i is the ith component of the unit normal vector on dA, and τ_{ij} is the viscous stress tensor. The instantaneous normalized pressure and viscous forces are denoted, respectively, by $C_p(t)$ and $C_v(t)$. Depending on whether $C_F(t)$ is positive or negative, it is either drag- or thrust-type, respectively. The instantaneous forces are plotted for cases 1 and 3, for a forward traveling wave ($C = -0.4$), a motionless wavy channel, and a backward traveling wave with $C = 0.8$ in Fig. 4.5a,b. When the steepness increases from s = 0.05 (Fig. 4.5a) to s = 0.15 (Fig. 4.5b), the magnitude of the forces and their fluctuations increase for all wave-speeds. The total forces do not follow the trend of viscous forces for both s=0.05 and 0.15 (Fig. 4.5), i.e., the pressure force is the main contributor to the total force. Similar to the stationary channel, the pressure force is the dominant force for traveling wave channel regardless of their wave-speeds at high Reynolds numbers. It can be observed in Fig. 4.5 that by increasing the wave-speed from $C = 0.0$ to $C = 0.8$, the mean of the force coefficient decreases but the viscous force increases slightly similar to the viscous force of an undulatory swimmer[190, 48]. The time history of the force coefficient shows that the backward traveling wave generates a temporally periodic force on the wavy surface, but the forward traveling wave generates a randomly fluctuating force. When the steepness increases from $s = 0.05$ to $s = 0.15$, the amplitude of the fluctuations of the force coefficient increases for all wave-speeds.

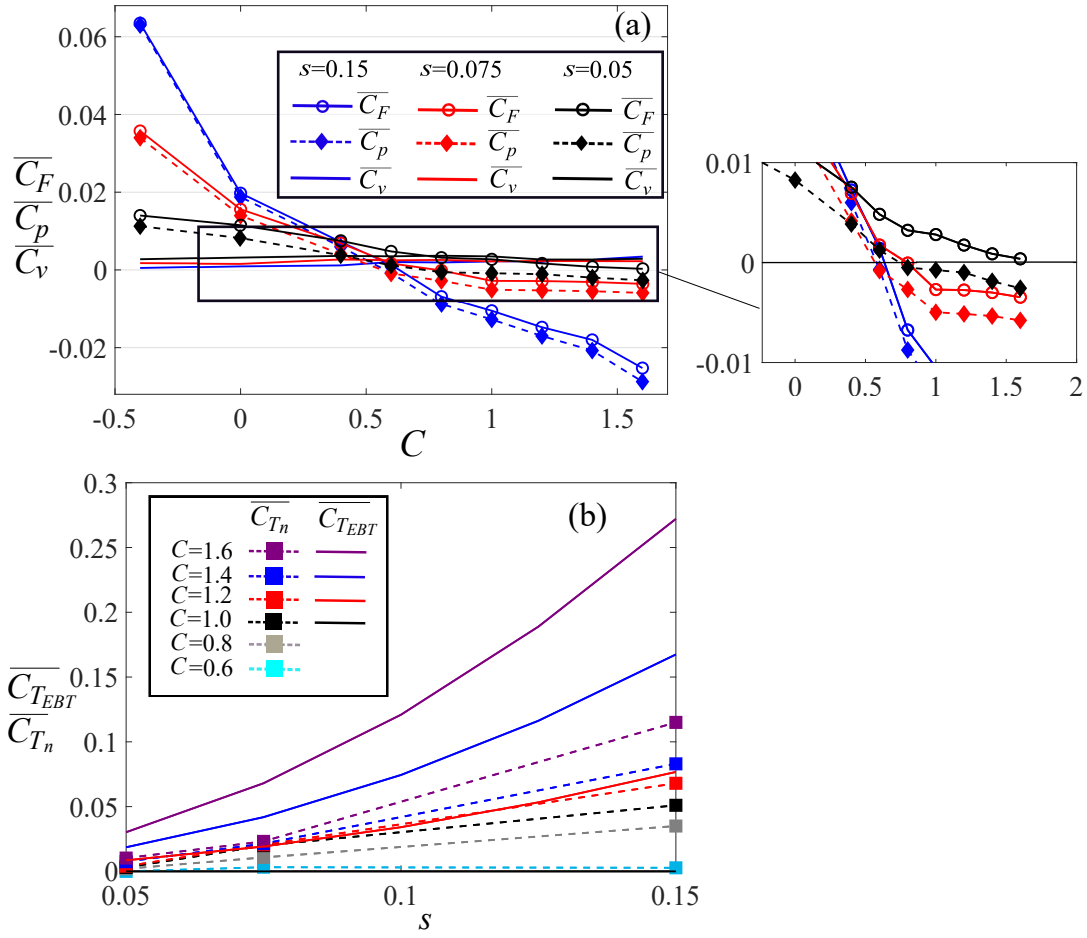

Figure 4.6: (a) The profile of mean forces including, mean force coefficient ($\overline{C_F}$), mean pressure coefficient ($\overline{C_p}$), and mean viscous coefficient ($\overline{C_v}$) along C, for cases 1 to 3. The inset indicates the wave-speed at which the forces become zero. (b) The variations of the numerical thrust ($\overline{C_{T_n}}$) and analytical thrust ($\overline{C_{T_{EBT}}}$) along with the wave steepness (s) for different wave-speeds. Reprinted from [167].

The mean forces are calculated by averaging the instantaneous forces over 10 cycles. The time-averaged normalized total, pressure, and viscous forces are denoted, respectively, by $\overline{C_F}$, $\overline{C_p}$, and $\overline{C_v}$. The forces are plotted for cases 1-3 (Table 4.2) for various C, ranging from -0.4 to 1.6, in Fig. 4.6a. Based on the mean force sign, the forces are classified into the net drag type ($\overline{C_F} > 0$) and the net thrust type ($\overline{C_F} < 0$). It can be observed that over the motionless wavy channel ($C = 0$) the force acting on the wavy channel is dominated by the pressure force and it increases by increasing the wave steepness, whereas the viscous force decreases by increasing the wave steepness, similar to the trend of the instantaneous force. In fact, $\overline{C_p}/\overline{C_v}$ of the motionless wavy channel increases from 2.5 to 18.8 as s increases form 0.05 to 0.15. When the wavy surface undulates with a backward traveling wave oscillation, the pressure force ($\overline{C_p}$) decreases monotonically by increasing the wave-speed, but the viscous force varies slightly which is negligible compared to the variations of the pressure force. Because the total force follows the trend of the pressure force, consequently, the total force ($\overline{C_F}$) decreases monotonically when C increases. On the other hand, comparing the plots of pressure force for different s shows that the slope of $\overline{C_p}$ increases by increasing the wave steepness. Therefore, the wave-speed at which the mean force ($\overline{C_F}$) becomes zero decreases by the increase of the wave steepness. For instance, for $s = 0.05$ the wave-speed at which $\overline{C_F}$ becomes zero is, approximately, at $C = 1.6$ (Fig. 4.6a) similar to the values reported by Shen et al. [4]. By increasing the wave steepness to $s = 0.075$ and $s = 0.15$ (cases 2 and 3) the total force ($\overline{C_F}$) becomes zero at wave-speeds 0.9 and 0.7 (Fig. 4.6a), respectively. Nevertheless, the wave-speed at which the pressure force goes to zero is in a smaller range, e.g., the mean pressure force ($\overline{C_p}$) is zero at wave-speeds 0.9, 0.6, 0.6 for cases 1 to 3 ($s = 0.05, 0.075, 0.15$), respectively. Note that these given wave-speeds are estimated from the plot of the force coefficient in the inset of Fig. 4.6a.

While backward traveling waves reduce the force coefficient, a forward one ($C < 0$) increases it as forward waves generate an axial momentum along the upstream direction. Similar to the backward traveling wave, the magnitude of the drag variation increases, even more intensely, by increasing the wave steepness for a forward traveling wave (Fig. 4.6a). For example, for case 3, a

forward traveling wave ($C = -0.4$) increases $\overline{C_F}$ about 400% compared to the motionless wavy channel, whereas a backward one with the same wave-speed ($C = 0.4$) decreases the mean force only by about 70%.

To better observe the effect of traveling waves on the mean forces, the variations of mean numerical thrust ($\overline{C_{T_n}}$) with respect to s for backward traveling waves are presented in Fig. 4.6b. The mean numerical thrust is defined as $\overline{C_{T_n}} = 0.5(-\overline{C_p} + |\overline{C_p}|)$, where $\overline{C_p}$ is the mean pressure coefficient. By this definition, only a mean negative pressure force (thrust type) accounts for the thrust force. The numerical thrust is compared with the thrust predicted by EBT[40] for an undulatory surface in the external flow. Based on EBT, the non-dimensional predicted thrust coefficient is:

$$\overline{C_{T_{EBT}}} = \frac{\pi}{4}(\pi s C)^2(1 - (\frac{1}{C})^2), \tag{4.3}$$

where $\overline{C_{T_{EBT}}}$ is the non-dimensional EBT thrust coefficient, and $\pi/4$ is the term appeared from the virtual mass term (see Akbarzadeh and Borazjani[158] for the derivation). Here, the virtual mass is assumed to be half of the virtual mass of an oscillating plate because only one side of the wavy surface is in contact with the fluid. In Fig. 4.6b, the analytical thrust is plotted for $C > 1$ because thrust is generated only when the wave-speed exceeds one ($C > 1$) based on Eqn. (4.3).

Figure 4.6b shows that the numerical thrust of waves at a constant wave-speed increases by increasing the wave steepness. Moreover, thrust increases for a given s by the increase of the wave-speed (Fig. 4.6b), e.g., for case 3, when C increases from 1.0 to 1.6, $\overline{C_{T_n}}$ increases from 0.05 to 0.27. Similarly, the EBT thrust ($\overline{C_{T_{EBT}}}$) follows the same trend as the numerical thrust ($\overline{C_{T_n}}$), i.e., the increase of thrust by the increase of the wave steepness (Eqn. 4.3). While EBT predicts thrust generation for waves with $C > 1.0$, Fig. 4.6b shows that waves with $C < 1$ can also generate thrust. For instance, a thrust is generated when the wave-speed is greater than 0.6 for cases 2 and 3 (Fig. 4.6b). The EBT thrust is close to the numerical thrust for wave-speed $C = 1.2$, but it overestimates the thrust for higher wave-speeds, e.g., $\overline{C_{T_{EBT}}}$ is three times larger than $\overline{C_{T_n}}$ for $C = 1.4$ and $C = 1.6$. The overestimation of thrust by EBT has also been observed in the

previous studies [191, 190, 192].

The traveling wave oscillations impact not only the mean flow but also turbulent intensities such as the turbulent kinetic energy (TKE). The effect of undulations on TKE for cases 2 and 3 ($s = 0.075$ and $s = 0.15$) are presented in Figs. 4.7 and 4.8, respectively, which plots the contours of TKE over lower half of the channel. Here, the TKE of the motionless wavy channel ($C = 0$) and traveling wavy channels ($C \neq 0$) is computed using, respectively, time-averaged and phase-averaged velocities. Over a motionless wavy wall with low steepness (Fig. 4.7b), the maximum TKE is generated over the trough of the wave, above the separation bubble (Fig. 4.2b). For the higher steepness (Fig. 4.8b), the maximum TKE is over the separation bubble (Fig. 4.3b) but with a smaller magnitude compared to case 2. For low amplitude case, TKE of the most region of the channel decreases monotonically by increasing the wave-speed from 0.4 to 1.2 as shown in Fig. 4.7c to f. From the decrease of TKE, it can be concluded that the traveling waves have relaminarized the flow as observed previously [185, 4]. The traveling wave oscillation on a high steepness wave, in contrast to the lower one, does not lead to a monotonic decrease. The TKE decreases substantially in the entire lower half of the channel by increasing the wave-speed from $C = 0$ to $C = 0.6$ (Fig. 4.8d). By increasing C further from 0.6 to 0.8 the TKE increases on the uphill of the wave (Fig. 4.8e) while the TKE decreases away from the wall at higher lateral positions, i.e., $y > -0.6$. When C increases to 1.2 (Fig. 4.8f), the TKE increases in the trough of the wave but decreases at higher lateral positions similar to $C = 0.8$ (Fig. 4.8e). Comparing the TKE for different wave-speeds of case 3, in Fig. 4.8, indicates that TKE over the trough and uphill of the wave, where have the highest TKE in the channel, is qualitatively minimum when $C = 0.6$, the wave-speed at which the drag is almost zero (Fig. 4.6a).

While a backward traveling wave ($C > 0$), in general, reduces TKE in the most of the channel, a forward traveling wave ($C < 0$) increases it. The negative wave-speed, $C = -0.4$, in both high and low amplitude waves (Figs. 4.7a, 4.8a) increases TKE in the entire lower half of the channel compared to motionless wavy channel. The increase of TKE is associated with the increase of mixing due to the interaction of the main flow and the reverse flow.

The effect of undulation on turbulent kinetic energy can also be observed qualitatively in the instantaneous flow field. Figure 4.23 shows the instantaneous vortical coherent structures visualized by the iso-surface of q-criterion (Q=20), colored by the magnitude of vorticity, and the streamwise velocity on a spanwise cross section of the channel. The results are presented for three wave-speeds $C = -0.4,\ 0.0$ and 0.8 in Fig. 4.23 for cases 2 and 3. The enhancement of TKE via a negative wave-speed, which was observed in Figs. 4.7a and 4.8a can also be detected in Figs. 4.23a, d. The number of vortical structures of an undulating wall with negative wave-speed is higher than the corresponding motionless one, e.g., compare Figs. 4.23a,b, which elucidates the enhancement of TKE that was observed in Figs. 4.7a, 4.8a. (The mechanism of production of vortical structures in the forward traveling wave which is equivalent to the increase of TKE can be visualized better via the movies which show that the vortical structures are produced over the troughs where the reverse flow interacts with the outer layer flow of the channel). Nevertheless, by increasing the wave-speed to a positive value such as $C = 0.8$, the vortical structures inside the channel decrease for both steepness $s = 0.15$ (Fig. 4.23f) and $s = 0.075$ (Fig. 4.23c) compared to the corresponding motionless ones. At this wave-speed ($C = 0.8$), the vortical structures are mostly visible in the troughs of the wave, which indicates that the vortical structures are more organized compared to the motionless wavy channel. In fact, the traveling wave relaminarizes the flow by decreasing the random component of the flow [193]. Note that the trend of variation of the coherent structures near the flat wall (upper wall) is similar to the wavy wall, i.e., the amount of vortical structures decreases as the wave-speed increases. The increase in the amount of coherent structures near the flat wall of a motionless wavy channel compared to a flat turbulent channel has also been reported previously [194].

4.1.4 Discussions and conclusions

Flow of a motionless wavy channel becomes separated from the crest of the wave as the flow over a concave surface is subject to a centrifugal instability that generates a Gortler vortex [184]. The separated flow increases by increasing the wave steepness [170] as observed in Figs. 4.2b and 4.3b. When the lower wall undergoes a backward traveling wave, the separated flow decreases

monotonically by increasing the wave-speed of the wave (Fig. 4.4) regardless of its steepness. The profile of the streamwise velocity demonstrates that the streamwise velocity (u_z) increases in the vicinity of the troughs of the wave when the wave steepness increases. The enhancement of the streamwise velocity in case 3 (high steepness) compared to case 2 implies the generation of a higher axial momentum near the traveling wavy wall when steepness increases.

High steepness traveling waves modify both pressure and viscous forces acting on the wavy surface. Backward traveling waves slightly increase the mean viscous force (Fig. 4.5a) and decrease the mean pressure force compared to a motionless wavy channel, but forward traveling waves act vice versa. The reason for the increase of the viscous forces with a backward traveling wave is the increase of the streamwise velocity in the vicinity of the wave (Fig. 4.4), which increases the term $1/Re(\partial u_z/\partial y)$ of the viscous force (Eqn. 4.2). The viscous force of the undulating surface with this range of steepness and wave-speed, however, is smaller than a flat channel. For example, the viscous force of the flat channel at this Re is $\overline{C_v} = 0.0065$ but the maximum viscous force of the traveling wavy surface is $\overline{C_v} = 0.00375$ for a backward traveling wave with $C = 1.6$ in case 3. Nevertheless, the change of the mean viscous force due to traveling waves is small compared to pressure forces (Fig. 4.5b) due to the high Re of the flow and the high steepness of the wave. The mean pressure force decreases monotonically by the increase of the wave-speed for waves with a constant steepness, similar to the previous studies [4, 48, 195]. Furthermore, both pressure and total force coefficients decrease monotonically by the increase of the wave steepness for a given wave-speed (Fig. 4.6). Consequently, the rate of change of the total force coefficient with respect to the change of the wave-speed (slope of C_F in Fig 4.6a) increases as the wave steepness increases. Therefore, the critical wave-speed, i.e., the wave-speed at which the net force is zero, is not constant. In fact, the critical wave-speed reduces from $C = 1.6$ to $C = 0.7$ as s increases from 0.05 to 0.15. These observations indicate that the wave-speed of one ($C = 1.0$), in contrast to common belief and EBT[196], is not the critical wave-speed in terms of thrust generation, specifically for waves with a high wave steepness ($s > 0.05$). In fact, the wave-speed at which a net thrust is generated reduces by increasing the wave steepness and it can be less than one.

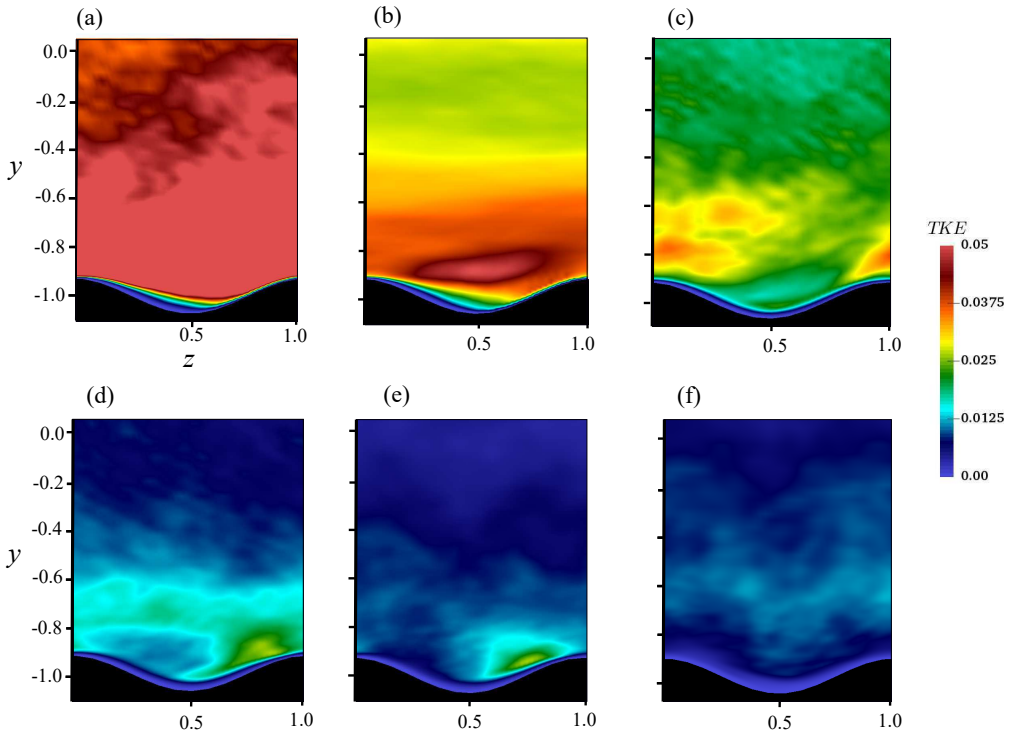

Figure 4.7: Distribution of the turbulent kinetic energy (TKE) for case 2 ($s = 0.075$) at six wave-speed, (a) forward traveling wave with $C = -0.4$, (b) motionless wavy channel ($C = 0.0$), (c) backward traveling wave with $C = 0.4$, (d) backward traveling wave with $C = 0.6$, (e) backward traveling wave with $C = 0.8$, and (f) backward traveling wave with $C = 1.2$. Reprinted from [167].

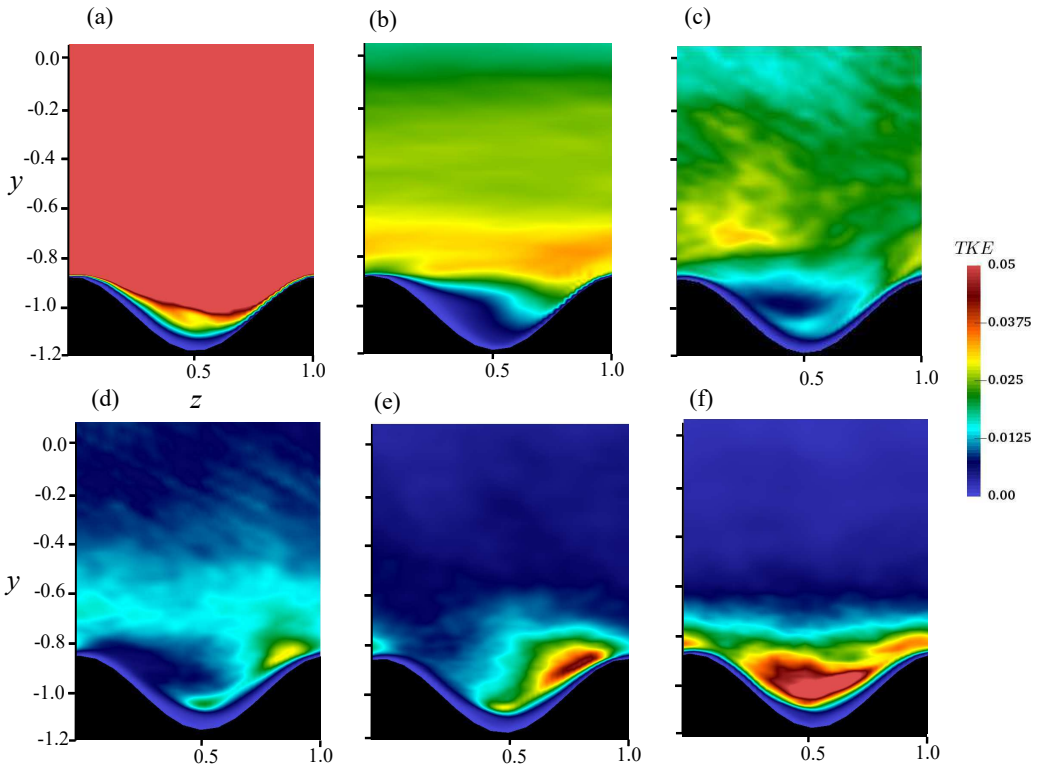

Figure 4.8: Distribution of the turbulent kinetic energy (TKE) for case 3 ($s = 0.15$) at six wave-speed, (a) forward traveling wave with $C = -0.4$, (b) motionless wavy channel ($C = 0.0$), (c) backward traveling wave with $C = 0.4$, (d) backward traveling wave with $C = 0.6$, (e) backward traveling wave with $C = 0.8$, and (f) backward traveling wave with $C = 1.2$. Reprinted from [167].

In this study, the backward traveling wave deformations of the lower wall have resulted in the reduction of the turbulence intensity in most of the region of the channel, including the vicinity of the wave and far away from that (Fig. 4.7, 4.8). In addition to the traveling wavy deformation, traveling wavy suction and blowing [197, 198, 199], and forcing [193] can also decrease turbulence intensity by reducing the turbulent shear stress. Mamori et al. [198] observed that relaminarization occurs when the maximum vertical speed, wave-speed and wavelength of the suction blowing wave are in the range of $u_y \approx 0.1$, $C \approx 1.5$ and $\lambda \approx 4$, respectively, for a traveling wavy suction and blowing channel with a low Reynolds number ($Re = 2000$). In fact, for traveling wavy forcing or suction and blowing walls, effects of the wall deformations are not taken into account as the wall was flat. In addition, in the previous studies at which the wall was deforming with a traveling wavy motion [4, 185], the wave steepness was $s \leq 0.04$ and the corresponding wave-speed at which a significant reduction of TKE, i.e., relaminarization, was observed was near one ($C \approx 1$). In this study, the wave-speeds at which the TKE of the flow near the wave is qualitatively minimized are $C = 1.2,\ 1.2$, and 0.6, respectively, for the wave steepness of $s = 0.05$, $s = 0.075$, and $s = 0.15$. In fact, the critical wave-speed for TKE, the wave-speed at which the TKE is qualitatively minimized, i.e., highly reduced in all regions of the channel, for cases 1 and 2 is similar to the study of [4], but, for case 3, the critical wave-speed has become less than 1 as the higher wave speeds increase the TKE near the traveling walls (Fig. 4.8). In summary, the critical wave-speed varies by increasing the wave steepness, i.e., it can be less than one.

4.1.5 Limitation and future work

The main finding of this work was finding the effective wave speed at which the flow separation was suppressed. The simulations were performed only for one Reynolds number. Therefore, main limitation of this work was Reynolds number. The other limitations are the range of steepness and wave speeds which can be a part of future work.

4.2 Controlling flow separation of inclined plates by using backward traveling waves

In this section, effects of low-amplitude traveling waves on controlling flow separation for an inclined plate at 10 degrees angle of attack is investigated. This section is organized as follows: a background on active flow control over bluff bodies is provided in §4.2.1. The methods of the simulations are presented in §4.2.2. The results of simulations are presented in §4.2.3 and discussed in §4.2.4. The conclusion is presented in §4.2.5, and finally the limitation and future work are presented in §4.2.6.

4.2.1 Background

It is known that traveling waves can reduce flow separation on flat plate at zero angle of attack [200], over a turbulent channel [4], or a swimmer's body. The traveling waves can reduce the pressure drag as they create thrust force on a swimmer's body or a wavy surface. Lighthill [40] derived a scaling for the thrust force acting on the swimmers using elongated body theory (EBT). Based on EBT, the instantaneous lift of an undulating slender body (low thickness) is scaled with the added-mass force (reactive force). The reactive force produced by the undulation generates a thrust force that increases as wave speed (C) is increased. The thrust generated by the waves can increase the momentum of the fluid adjacent to the wavy surface as it was observed in the previous study (see the profile of streamwise velocity near the wavy surface in Fig. 4.4a,b). The momentum enhancement might help reducing flow separation over bluff bodies, e.g., when a plate is at an angle of attack. This idea is tested by applying low-amplitude ($0.01L$) backward traveling waves on an inclined plate at angle of attack of 10^o, where the flow is massively separated. Effect of different wave parameters, such as reduced frequency, and wavelength on flow separation and aerodynamic performance were studied. The results of these simulations can be used as a guideline for applying traveling waves for flow control.

4.2.2 Methods

Numerical simulations are performed for an inclined, three dimensional plate of aspect ratio 2 at the angle of attack of 10^o. The angle of attack is chosen to be 10^o because it is high enough

to generate an unstable leading edge vortex (LEV) for a wing with an aspect ratio of 1.5 to 3 [173, 201]. The plate chord length is L, its thickness is $0.02L$, and the spanwise length is $2L$. The free stream velocity (U) and the chord length (L) are the reference velocity and length scales for nondimensionalization, respectively. As shown in Fig. (4.1a), flow is in the frame (x, y, z) where x, y, z are spanwise, vertical and streamwise coordinates, respectively. Simulations are performed for both flat and undulatory inclined plates. The prescribed undulatory motion is a backward traveling wave that starts from $0.1L$ of the leading edge with a linearly increasing amplitude toward the trailing edge. To calculate the new position of the inclined plate under motion in the flow frame, a local frame (X, Y, Z) is defined, which is rotated by the angle of attack (figure 4.1b). The undulations h are prescribed perpendicular to the plate, i.e., along Y direction in the rotated frame, based on the traveling wave equation:

$$h(Z,t) = a(Z)\sin(\Omega^* t^* - 2\pi Z^*/\lambda^*) \tag{4.4}$$

where h is the lateral undulation, $Z^* = Z/L$ is nondimensional chordwise length in local coordinates, respectively, and $a(Z)$ is the amplitude of the wave. The origin is at the top surface of leading edge such that $Z = 0$ and $Z = L$ are the leading edge and trailing edge, respectively. Frequency (f) and wavelength (λ) are the varying terms of the wave, where $\lambda^* = \lambda/L$ is nondimensionalized with L. The amplitude envelope of the traveling wave is $a(Z) = 0$ for $Z < 0.1L$ and $a(Z) = a_{max}(Z - 0.1L)/0.9L$ for $Z > 0.1L$, where $a_{max} = 0.01L$ is the dimensional maximum amplitude of the wave. The reduced frequency is $f^* = fL/U$, $\Omega^* = 2\pi f^*$, $\theta = 10^o$ is the angle of attack, and $t^* = tU/L$ is the nondimensional time where t is the dimensional time. The maximum amplitude a_{max} is chosen to be small because traveling waves generated by smart structures have small amplitudes [202]. Herein, $(*)$ symbol denotes nondimensional parameters including length, time, velocity, and vorticity. However, the notation for nondimensional pressure and Q-Criterion are p, and Q, respectively.

The Reynolds number in this study is $Re = LU/\nu = 20,000$, (ν: kinematic viscosity). Varying

parameters in these simulations are f^* and λ^* which have the range of $(0-30)$ and $(0.15-2.0)$, respectively. The Strouhal number, defined as $St = 2a_{max}f/U$ is in the range of $(0.0-0.6)$, which is close to the range typically observed in the nature $(0.2-0.7)$ [42]. More specifically, the simulations for undulating cases are carried out for three reduced frequencies, $f^* = (6, 20, 30)$ and six wavelengths $\lambda^* = (0.15, 0.2, 0.5, 1.0, 2.0, 1000.0)$. The different f^*, λ^* for each case is presented in Table 4.4. Case 1 is a flat inclined plate and case 9 ($\lambda = 1000.0$) is a pitching plate. It should be noted that when the wavelength is increased, the wave speed ($C/U = f^*\lambda^*$) increases and the wave steepness (a^*_{max}/λ^*) decreases.

To discuss the impact of undulations on the flow over the plate, scalings for velocity, vorticity and thrust are derived based on EBT [40] in appendix A. EBT is based on inviscid slender body theory, i.e., the flow perturbation in the lateral direction is much smaller than the axial direction. In addition, the pressure of the adjacent fluid to the swimmer scales with the reactive force that is related to the fluid acceleration. Although EBT is based on inviscid flow assumption and low velocity undulation, it will be demonstrated in section 4.2.3 that such scalings can predict the patterns of the simulations for flow characteristics such as lateral velocity, out of plane vorticity, and relative drag force compared to the flat inclined plate (thrust force) because the main mechanism for thrust generation in EBT, i.e., the added mass, is dominant in high frequency undulations.

The computational domain of the simulation (figure 4.1a) is a cuboid with dimensions $3L \times 15L \times 15L$, which is discretized with $81 \times 421 \times 301$ grid nodes in x, y and z directions, respectively. The thin plate is placed $5L$ from the inlet boundary and centered in the lateral (y) and spanwise (x) directions as shown in figure 4.1a. To resolve the flow near the thin plate, a curvilinear grid is built with a constant resolution of $0.0013L$ and $0.01L$ in a rectangle of $0.34L \times L$ in y and z directions, respectively, which contains the undulating plate and stretches out to the domain boundaries using a hyperbolic function as shown in figure 4.1b. The grid resolution is constant in the x direction and grid spacing normal to the wall is 1.5 wall units ($y^+ = u_\tau \delta/\nu = 1.5$, where u_τ is the friction velocity and δ is the normal distance of the IB node to the plate). The first grid point is within the viscous sublayer ($y^+ < 5$) of the turbulent boundary layer which is enough for reconstructing the

velocity of the IB nodes with a linear interpolation citepope. The nondimensional time step for the flat inclined plate is 0.0025 and for the rest of the cases is $\frac{1}{240f^*}$. The sensitivity of the simulations to the grid and time-step size is investigated in the next subsection.

The boundary condition on the lateral and spanwise boundaries is the slip wall, the inlet is uniform (plug) flow, and the outlet is a Neumann boundary with a correction to satisfy the conservation of mass. All simulations in which the plate is undulating are initialized by the flow field of the flat inclined plate where both leading and trailing edge vortices are shedding. Furthermore, the hydrodynamic forces (lift and thrust) are computed by integrating the pressure and viscous forces acting on the plate.

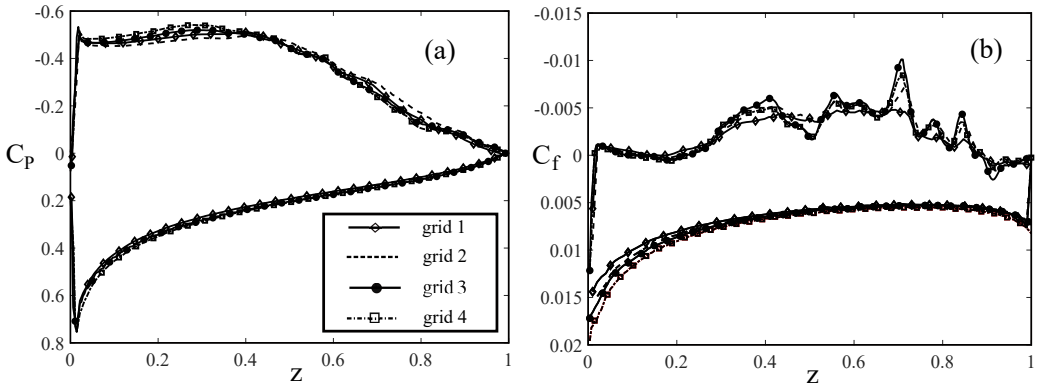

Figure 4.9: The (a) pressure and (b) skin friction coefficient along the chord on the midplane of the flat inclined plate for four different grids. The upper and lower curves are the coefficients on the suction and pressure side of the plate, respectively. Reprinted from [158].

4.2.2.1 Grid and time-step sensitivity studies

A grid sensitivity study is performed to investigate the effect of mesh size and domain spanwise size on the pressure distribution and skin friction for the flat inclined plate with four grids (figure 4.9a, b). In addition, a grid sensitivity study and a time-step sensitivity study are performed to ensure that the results of the simulations are time-step and grid independent for undulating cases. The details of grids, time-step, mean lift and drag coefficients with their corresponding root-mean-

case	grid	L_x	N_x	N_y	N_z	Δx_{min}	Δy_{min}	Δz_{min}	δt^*	C_D	C_L	$C_{D_{rms}}$	$C_{L_{rms}}$
(1)	1	3	81	421	301	0.0375	0.0013	0.010	0.0025	0.120	0.542	0.001	0.004
(1)	2	5	121	421	401	0.020	0.0013	0.005	0.0018	0.117	0.523	0.001	0.004
(1)	3	7	121	541	481	0.020	0.0009	0.0036	0.0012	0.115	0.514	0.001	0.005
(1)	4	3	105	541	481	0.020	0.0009	0.0036	0.0012	0.115	0.520	0.001	0.005
(4)	1	3	81	421	301	0.0375	0.0013	0.010	0.00020	0.060	0.631	0.492	1.732
(4)	2	5	121	421	301	0.020	0.0013	0.005	0.00020	0.063	0.611	0.451	1.623
(4)	1	3	81	421	301	0.0375	0.0013	0.010	0.00010	0.062	0.635	0.517	1.769

Table 4.3: The details of grid and time-step size for the grid sensitivity studies. A grid sensitivity study for a flat inclined plate (case 1) with four grids is performed. A grid sensitivity study with two grids as well as a time-step sensitivity study are performed for a high frequency undulating plate (case 4 ($f^* = 20, \lambda^* = 0.2$)). δt^* is the nondimensional time step size, L_x is the domain spanwise length, $C_{D_{rms}}$ and $C_{L_{rms}}$ are the rms of lift fluctuations for drag and lift coefficient, respectively, and all hydrodynamic forces are nondimensionalized with $\rho U^2 L^2$ as the spanwise length of the plate is $2L$ (plate area is L^2).

squared (rms) of fluctuations are presented in Table 4.3. Grid 2 has a higher resolution along the streamwise and spanwise directions, while grids 3 and 4 have a higher resolution in three directions, i.e., the grid spacing has decreased to 0.53, 0.69, and 0.33 of that of grid 1 in x, y, z directions, respectively. The spanwise length of the domain has increased from 3 for grid 1 to 5 and 7 for grids 2 and 3, respectively, whereas grid 4 has the same domain size as grid 1. In fact, grid 4 has the same grid resolution near the thin plate as grid 3, while the same domain size as grid 1. Consequently, comparing the results of grids 1 and 4 (same domain size) reveals the effect of grid resolution while comparing the results of grids 3 and 4 (same resolution) reveals the effect of the spanwise length of the numerical domain.

The grid sensitivity study for the flat inclined plate shows the drag coefficient as well as the rms of fluctuations vary less than 4% for all four grids (Table 4.3), and the lift coefficient decreases slightly (less than 6%) as the grid becomes finer. Nevertheless, even the lift coefficient of the coarsest grid (C_L=0.54 for grid 1) is within the range of $0.48 - 0.54$, reported for Reynolds numbers of $6 \times 10^4 - 20 \times 10^4$ [173, 203]. Figure 4.9a shows the time-averaged pressure coefficient ($C_p = 2p/\rho U^2$) on both sides of the plate for grids 1, 2, 3 and 4. As it can be observed, the pressure coefficient is similar between the four grids. Figure 4.9b shows the skin friction coefficient

$C_f = \frac{2}{Re}\frac{\partial u_z^*}{\partial y^*}$ along the plate on both sides of the plate, where u_z^* is the nondimensional streamwise velocity. As it can be observed in figure 4.9b, the curves of C_f for all of the grids on the pressure side of the plate are approximately identical, but there are some discrepancies on the suction side where the flow is separated. The C_f of grids 3 and 4 shows slightly higher fluctuations of the skin friction on the suction side as they have a higher resolution. These discrepancies, nevertheless, does not influence the force coefficients (see Table 4.3) because the friction force is significantly (an order of magnitude) smaller than the pressure force ($C_f \ll C_p$ as observed in Fig. 4.9) and also the magnitude of C_f on the suction side is small compared to the pressure side (see the profile of C_f on both sides of the plate in Fig. 4.9b). Based on these results, i.e., similarity of the pressure coefficients on the mid-plane for these grids (figure 4.9a), observing a very close lift coefficients (less than 6% difference), and the similarity between skin friction coefficients (figure 4.9b), the spatial and spanwise length are enough to capture the flow physics and forces.

Another grid sensitivity study is also carried out for an undulating case with grids 1 and 2 by comparing the lift and drag coefficients and their corresponding rms fluctuations. The difference between the aerodynamic performances of two grids are less than 6%, and the difference between their rms is less than 10%. Based on the averaged forces and their rms we conclude that the undulating simulations are grid insensitive as well. The time step sensitivity study is performed with a time step size $\delta t^* = 1/480 f^*$ which is half of the original time step size ($\delta t^* = 1/240 f^*$) used in this study. The averaged forces obtained from time step sensitivity study are similar and the difference between the rms of the forces is around 5% (Table 4.3) which shows that the time step is small enough to capture the correct physics.

4.2.3 Results

To see the effect of undulation on flow separation, time-averaged results, including mean flow field and turbulence intensity are presented in subsections §4.2.3.1 and §4.2.3.2. The mean and instantaneous aerodynamic forces are shown in §4.2.3.3 and compared with the scalings obtained using EBT. Afterward, the trends observed for mean flow separation and aerodynamic forces for different frequencies and wavelengths are discussed based on the phase-averaged flow in §4.2.3.4

to identify the mechanisms affecting flow reattachment by the traveling waves.

4.2.3.1 The effect of traveling waves on the flow separation of the mean flow

In this section, the mean flow is visualized to see the impact of both frequency and wavelength of traveling waves on flow separation. The impact of frequency and wavelength of the traveling wave on flow separation is reported quantitatively by defining a *reattachment length* for the separated flow. The reattachment length is defined here as the distance between the leading edge and the point where the time-averaged streamwise velocity becomes greater than zero ($u_z > 0$) on the midplane. For oscillating plates, the reattachment point is found over the buffer zone of motion, which contains all the points that the moving plate has passed through at least once in a cycle. This buffer zone is shown schematically by the gray region in figure 4.11a. This buffer zone is defined because the time averaging of values, e.g. velocities, is valid only for the fluid nodes and not the solid nodes. Therefore, the time-averaged values in this study, including the pressure and velocity values, are for the nodes which are out of this buffer zone. The reattachment point can be visually detected by the streamline normal to the plate as shown schematically in figure 4.11a. The exact reattachment length, denoted by R, is reported in Table 4.4.

To visualize the flow separation, the time-averaged streamlines and out-of-plane vorticity on the midplane of the nine cases (Table 4.4) are presented in figure 4.10. The left column of figure 4.10 shows the cases with similar wavelength but different frequency, i.e., the effect of frequency, while the right column shows the cases with similar frequency but different wavelength, i.e., the effect of wavelength. Due to the sharp leading edge of the plate, the flow separates from the leading edge for all cases and forms a clockwise recirculatory region near the leading edge (figure 4.10), which is depicted schematically in figure 4.11a. This recirculatory (separation) region is represented by the negative (clockwise) vorticity (figure 4.10).

Over the flat inclined plate (figure 4.10a), the separated shear layer, which is inviscidly unstable, transitions to turbulence and reattaches near the trailing edge ($0.93L$) as the turbulent flow energizes the near wall flow [204]. The traveling wave at low frequency f^*=6 does not affect the flow separation (figure 4.10b) and the reattachment length is similar to the flat inclined plate (Ta-

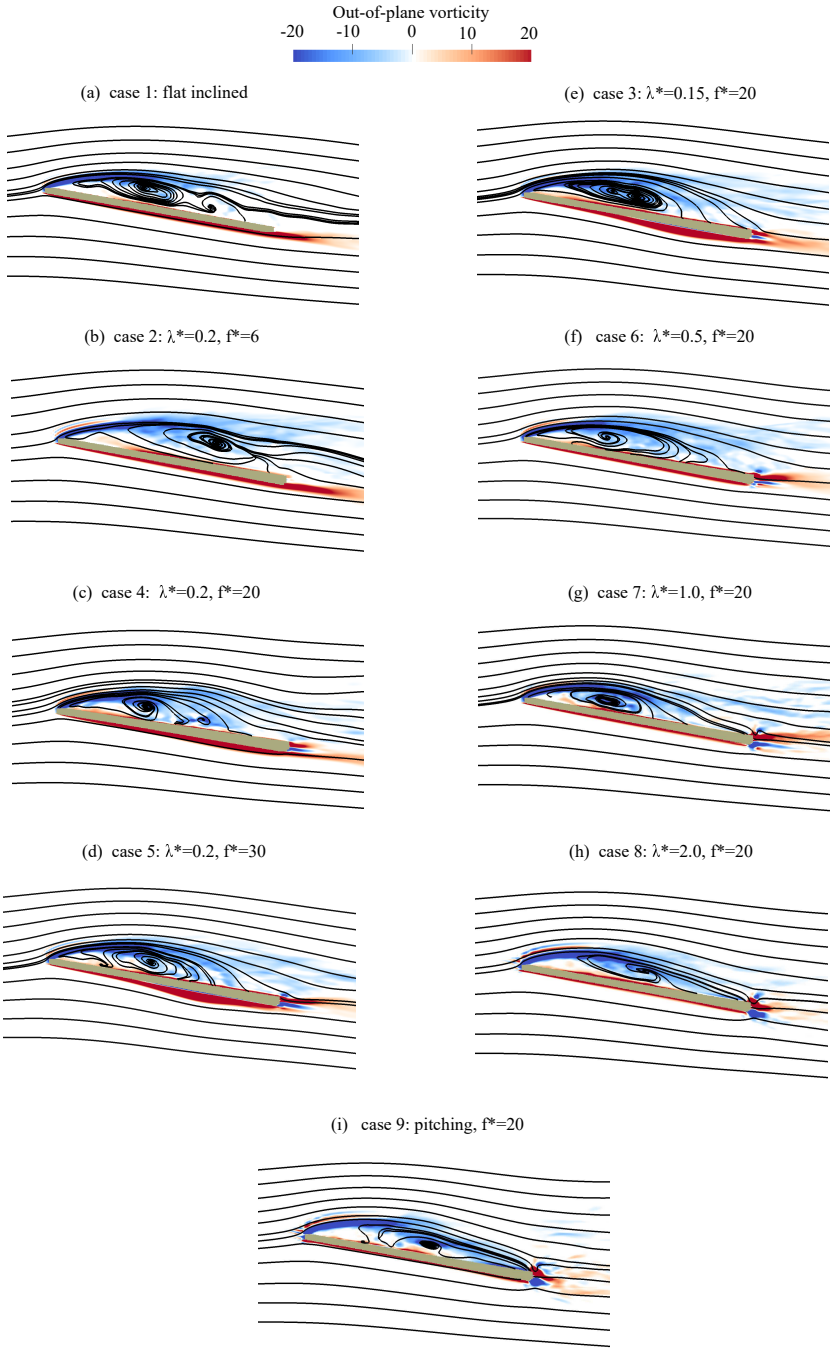

Figure 4.10: Out of plane vorticity contours and streamlines of the mean flow on the midplane for nine cases. The left and right columns show the effect of frequency and wavelength on flow separation, respectively.

ble 4.4). By increasing f^* from 6 to 20 and 30 (C/U from 1.2 to 4 and 6), however, the separated shear layer reattaches earlier at $0.78L$ and $0.70L$ from the leading edge (Table 4.4), respectively,

$case$	f^*	λ^*	C/U	C_D	C_{D_f}	C_{D_p}	$C_{D_{rel}}$	C_L	R	$C_{D_{rms}}$	$C_{L_{rms}}$
1	0	-	0	0.120	0.011	0.109	0.000	0.54	0.93L	0.001	0.004
2	6.0	0.2	1.2	0.118	0.009	0.109	0.002	0.54	0.92L	0.031	0.110
3	20.0	0.15	3.0	0.080	0.007	0.073	0.041	0.70	0.73L	0.471	1.752
4	20.0	0.2	4.0	0.060	0.008	0.052	0.060	0.63	0.78L	0.492	1.732
5	30.0	0.2	6.0	-0.023	0.008	-0.031	0.143	0.71	0.70L	1.170	4.104
6	20.0	0.5	10	0.029	0.007	0.022	0.090	0.60	0.89L	1.442	8.015
7	20.0	1.0	20	-0.008	0.015	-0.023	0.127	0.57	0.57L	4.500	25.420
8	20.0	2.0	40	-0.043	0.016	-0.059	0.163	0.55	0.68L	9.412	51.501
9	20.0	-	-	-0.070	0.016	-0.086	0.190	0.54	0.82L	11.761	66.890

Table 4.4: Values of the mean drag coefficient (C_D), relative drag coefficient $(C_{D_{rel}})$, viscous drag (C_{D_f}), form drag (C_{D_p}), relative drag $(C_{D_{rel}})$, lift coefficient (C_L), the reattachment length (R), and the rms values of drag and lift coefficients for different cases. The relative drag $(C_{D_{rel}})$ is defined as the drag reduction relative to case 1 (flat inclined) along the plate chord ($C_{D_{rel}} = (C_D^{flat\ inclined} - C_D^{undulating})/cos(\theta)$), which is a measure of the thrust force produced by the wave. All force coefficients are nondimensionalized with $\rho U^2 L^2$ since the area of the plate is $2L^2$. Case 1 is the non-moving flat inclined plate and case 9 is the pitching inclined plate for which the wave speed is not defined.

as observed in figure 4.10c,d. In fact, comparing the streamlines in the left column of figure 4.10 shows that increasing the wave speed by increasing the frequency in this range reduces flow separation monotonically.

The wavelength variation at constant frequency did not produce a monotonic pattern for decrease/increase of the flow separation (right column of figure 4.10). Increasing λ^* from 0.15 (case 3) to 0.2 (case 4) and 0.5 (case 6) at constant $f^* = 20$, i.e., increasing C/U from 3 to 4 and 10, increases the separation length from $0.73L$ to $0.78L$ and $0.89L$, respectively (Table 4.4 and compare figures 4.10e, c, and f). By increasing the wavelength further from 0.5 (case 6) to 1.0 (case 7) and 2.0 (case 8) (C/U from 10 to 20 and 40), however, the reattachment length reduces to $0.57L$ and then increases to $0.68L$ (Table 4.4), respectively, as observed in figure 4.10f, g, h. For the pitching plate (case 9), the flow separation increases compared to case 8 ($\lambda^* = 2.0$), i.e., reattachment length increases to $0.82L$ (Table 4.4 and figure 4.10h,i). In summary, when the wave speed increases by increasing the wavelength (left column of figure 4.10), in contrast to the trend

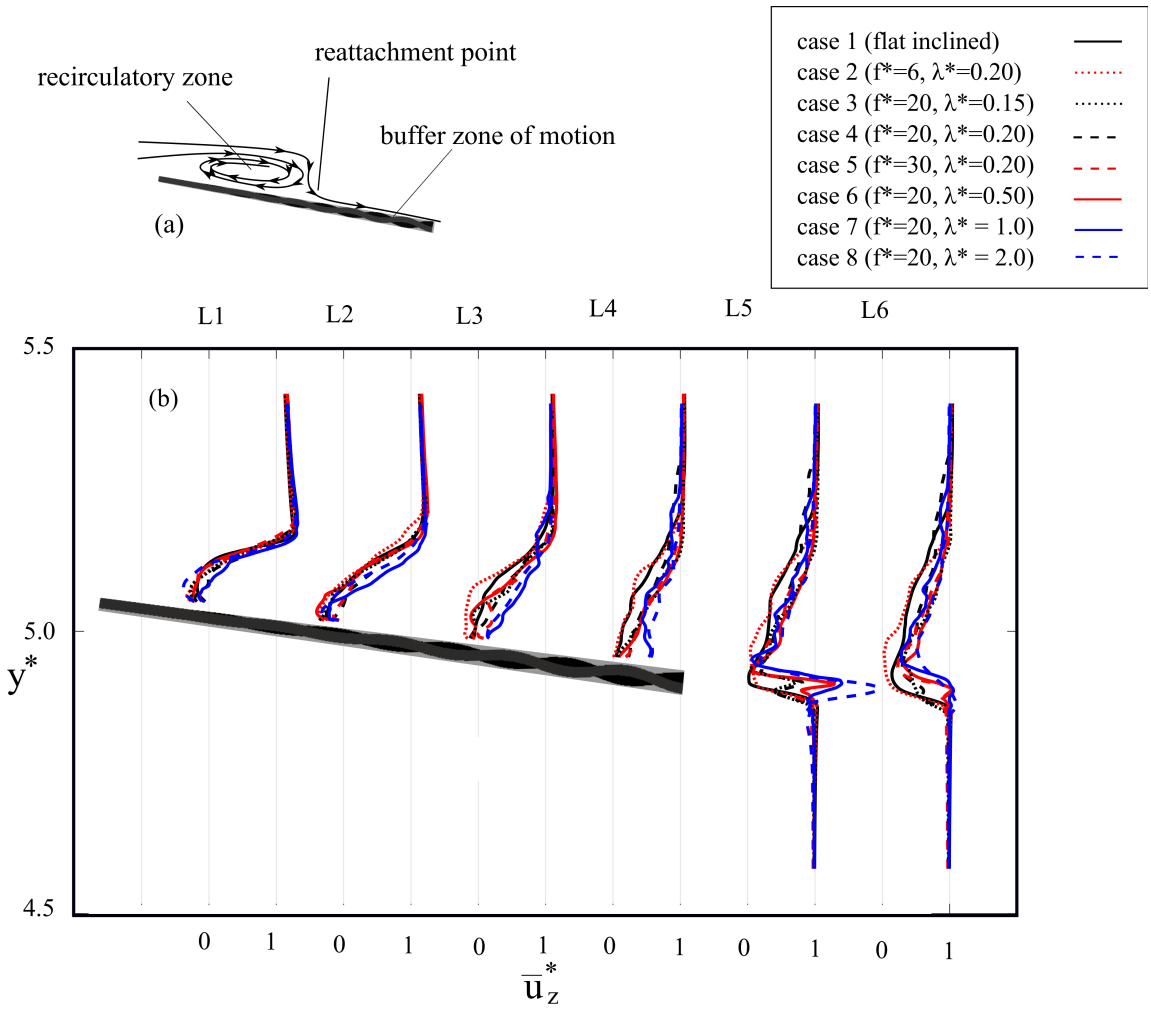

Figure 4.11: (a) Schematic of the average flow field. The gray zone is the buffer zone of the motion which includes all points the plate passes through at least once in a cycle. (b) The nondimensional time-averaged streamwise velocity profile $\overline{u_z^*}$ at midplane. Reprinted from [158].

observed for frequency (left column of figure 4.10), the flow reattachment length neither decreases nor increases monotonically.

To clearly show the reattaching and reverse flows, figure 4.11b presents the time-averaged streamwise velocity profile at six sections on the midplane. The time-averaged streamwise velocity profile of cases 1 and 2 are approximately identical in all sections of figure 4.11b, which agrees with the results of Table 4.4, indicating that low f^* (case 2) does not change the reattachment length compared to the flat inclined one (case 1). As f^* increases to 20, the reverse flow increases

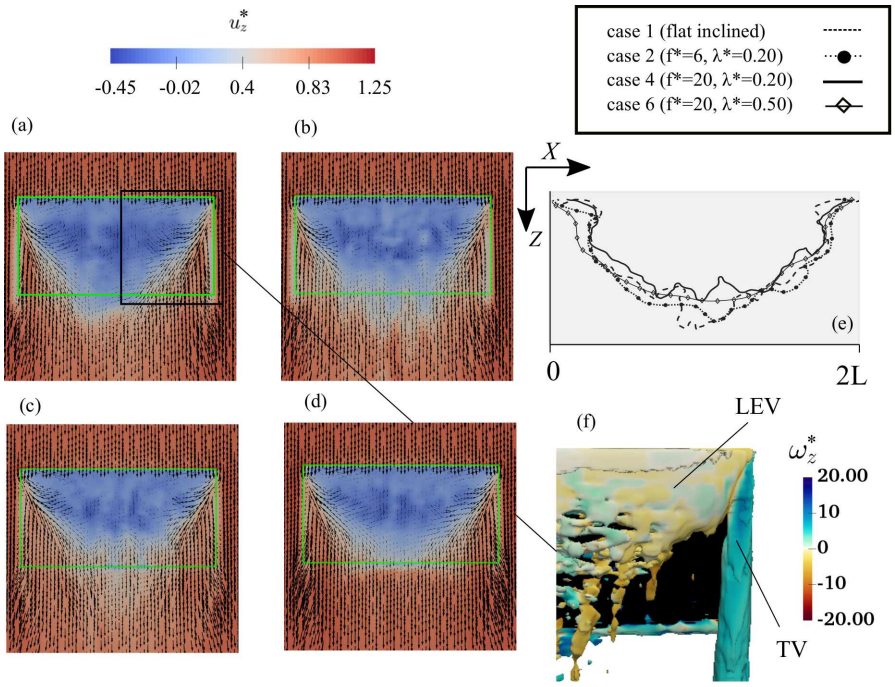

Figure 4.12: Streamwise velocity field over the plane adjacent to the top surface of the buffer zone of the motion. (a) flat inclined plate, (b) undulating plate case 2 ($f^* = 6, \lambda^* = 0.2$), (c) undulating plate case 4 ($f^* = 20, \lambda^* = 0.2$), and (d) undulating plate case 6 ($f^* = 20, \lambda^* = 0.5$). The green rectangle is the plate. (e) The corresponding reattachment line plotted along the span of the plate by detecting the zero streamwise velocity for these cases. $x = 0$ and $x = 2L$ are tips, and $x = L$ is the midplane of the plate. (f) Time-averaged vortices on the suction side, including LEV, tip vortex (TV) identified by Q-criterion with Q=10 and colored with nondimensional streamwise vorticity (ω_z^*). Reprinted from [158].

slightly near the leading edge, in sections L1 and L2 of figure 4.11b, for cases 6 and 8, whereas it decreases in section L2 for case 7 which has the minimum reattachment length (Table 4.4). Near the trailing edge, at section L4 of figure 4.11b, the time-averaged streamwise velocity of cases 3 to 8 is higher than cases 1 and 2 as the flow has reattached earlier for cases 3 to 8 (Table 4.4).

To investigate the flow reattachment at different spanwise locations, the time-averaged streamwise velocity field on the plane that is adjacent to the top surface of the buffer zone of the motion is shown for cases (1, 2, 4, 6) in figure 4.12(a, b, c, d). The velocity vectors in figure 4.12(a, b, c, d) are the projected velocity field to this plane. It can be observed in figure 4.12(a, b, c, d) that the reverse flow is higher near the midplane ($x = L$) for all cases and decreases towards the tips of the plate as the spanwise velocity increases. Figure 4.12e shows the reattachment lines of cases (1, 2,

4, 6), which are plotted by detecting the boundary of zero streamwise velocity of figure 4.12(a, b, c, d), and the time averaged tip vortex (TV) and LEV of the flat inclined plate are visualized using Q-criterion in figure 4.12f. The profile of the reattachment length (figure 4.12e) shows that the flow reattaches earlier as we move toward the tips from the midplane due to the impact of the tip vortex. The tip vortex, which has a higher streamwise vorticity compared to the LEV, induces a spanwise velocity near the tips (figure 4.12(a, b, c, d)) which contributes to the earlier flow reattachment near the tips of the plate [205].

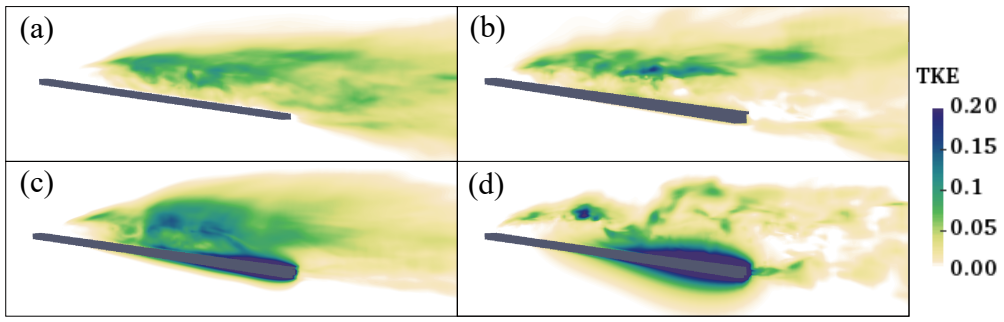

Figure 4.13: Distribution of nondimensional turbulent kinetic energy in (a) flat inclined plate, (b) undulating plate case 2 ($f^* = 6$, $\lambda^* = 0.2$), (c) undulating plate case 4 ($f^* = 20$, $\lambda^* = 0.2$), and (d) undulating plate case 6 ($f^* = 20$, $\lambda^* = 0.5$). The undulations increase the TKE over the plate, but decrease it in the wake downstream of the trailing edge. Reprinted from [158].

4.2.3.2 The effect of traveling waves on turbulence intensity

Traveling waves are known to reduce the turbulence intensity of turbulent boundary layers, e.g., turbulent channel flows [4, 185, 198], by decreasing the random component of the flow [198]. However, the effect of traveling waves on the turbulent intensity in external flows, e.g., flow over an inclined plate, where the boundary layer is not fully turbulent, is unknown. Here, we investigate the effect of traveling waves on turbulence intensity of the flow.

To investigate the effects of traveling waves on turbulence intensity, turbulent kinetic energy (TKE) is shown for case (1, 2, 4, 6) in figure 4.13(a,b,c,d), respectively. The TKE of the flat inclined plate is non-zero on the plate's suction side where the separated shear layer mixes with

reverse flow near the wall, but zero on the pressure side. Similarly, TKE is non-zero only on the suction side of the low frequency case (case 2) (figure 4.13b). The TKE of the flow adjacent to the both sides of the undulating plate increases as f^* and λ^* increase (figure 4.13c,d). However, in case 4 which has the lowest reattachment length among these cases, the TKE over the plate at the separation zone is higher than other cases (figure 4.13c). In addition, the TKE is lower in the wake on the downstream of the plate for case 4 and 6 compared to the flat incline plate.

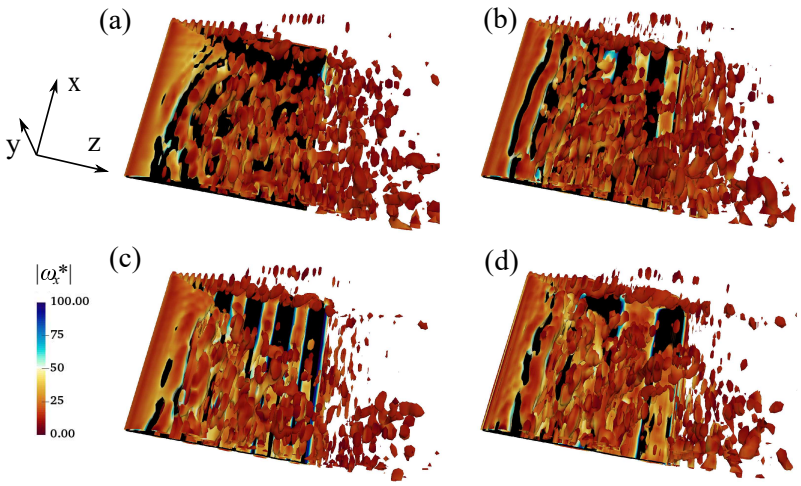

Figure 4.14: 3D vortical structures visualized by the instantaneous isosurfaces of Q-criterion ($Q = 20$) from mid-plane to the tip. (a) flat incline plate, (b) undulating plate case 2 ($f^* = 6$, $\lambda^* = 0.2$), (c) undulating plate case 4 ($f^* = 20$, $\lambda^* = 0.2$), and (d) undulating plate case 6 ($f^* = 20$, $\lambda^* = 0.5$). Reprinted from [158].

The decrease of TKE in the downstream wake for high frequency undulatory cases (figure 4.13c,d) can also be observed by the instantaneous three dimensional vortical structures. Figure 4.14 shows the 3-D vortical structures visualized by the isosurface of Q-criterion. Comparing the wake of cases 4 and 6 with the flat inclined one (figure 4.14a, c, d) reveals that the number of vortical structures have decreased for cases 4 and 6 compared to case 1, which confirms the decrease of turbulence intensity in the wake (figure 4.13a,c,d). Furthermore, it can be observed that the shear layer separates from the sharp leading edge and breaks down into small vortices as it

becomes unstable. The vortical structures of the flat inclined plate resemble the vortices visualized by [201] whose plate had the same aspect ratio (=2) but the angle of attack was 8^o. It can also be observed that the flow is more spread laterally at the midplane compared to the regions near the tips of the plate.

4.2.3.3 The effect of traveling waves on the aerodynamic performance

The flow visualizations in the previous section showed that traveling waves can reduce flow separation, which can impact both of the drag and lift forces. A reduction in drag force is expected because backward traveling waves are known to generate thrust which propels aquatic swimmers forward [40, 206, 207]. However, the effect of traveling waves on the lift coefficient cannot be predicted purely based on the thrust generation because traveling waves completely change the pressure field by creating a low pressure region on both sides of the plate at high frequencies as will be discussed below. In addition, the effects of traveling waves on the mean and instantaneous aerodynamic forces are discussed by comparing the trend of computed forces and the analytically derived ones using EBT [40].

To quantify the aerodynamic performance, the drag (C_D), relative drag ($C_{D_{rel}}$), lift (C_L) coefficients, and the root-mean-square (rms) of fluctuations of drag and lift coefficients are reported in Table 4.4. Drag coefficient is the total nondimensional drag force ($C_D = F_{drag}/(\rho U^2 L^2)$) that consists of the viscous (C_{D_f}) and form (C_{D_p}) drag acting on the plate along the incoming flow (z direction), and lift coefficient ($C_L = F_{lift}/(\rho U^2 L^2)$) is the total nondimensional force acting normal to the incoming flow in the y direction. The relative drag coefficient for each case is defined as the drag reduction relative to the flat inclined case along the plate ($C_{D_{rel}} = (C_D^{flat\ inclined} - C_D^{undulating})/cos(\theta)$) which is almost equivalent to the thrust force produced by the oscillations. The time-averaged results for the oscillating plates are averaged over 60 cycles and the averaging is started after 50 cycles.

Table 4.4 shows that the viscous drag is about 10% of the form (pressure) drag. When the plate undulates at a high reduced frequency ($f^* \geq 20$), e.g., cases (3-8), the ratio of the viscous to the form drag increases because the form drag is reduced by the undulations (undulations generate

thrust) while viscous drag is negligibly changed. In fact, the change in the viscous drag with respect to the flat inclined plate is less than 0.005 for all cases ($|\Delta C_{D_f}| < 0.005$, where $\Delta C_{D_f} = C_{D_f}^{flat\ inclined} - C_{D_f}^{undulating}$ is the difference between the viscous drag of the flat inclined plate and an undulating one). Consequently, the reduction in form drag accounts for the majority of the reduction in drag coefficient (C_D).

Comparing the time-averaged values, Table 4.4 shows that in case 2 (f^*=6, C/U=1.2), the traveling wave does not improve the aerodynamic performance compared to the flat inclined plate. However, increasing the wave speed by increasing the reduced frequency to f^*=20 (C/U=4) and f^* =30 (C/U=6) increases the lift force by 16.7% and 31.4% and decreases the drag force by 50% and 119.2% (generates thrust), respectively. It is interesting to note that when the traveling wave generates thrust (positive relative drag in Table 4.4) at high f^*, e.g., cases 3-8, a jet-like profile velocity is observed in the wake (sections L5 of figure 4.11b). In addition, the thrust produced in case 5, 7, 8 and 9 is high such that the drag (C_D) is negative (thrust-type). In these cases a streamwise flow can be observed in the middle of plate (section L3 of figure 4.11b), i.e., jet-like profile is initiated earlier (closer to the leading edge).

When the frequency is kept the same ($f^* = 20$), increasing the wave speed by increasing the wavelength from λ^*=0.15 (C/U=3) in case 3 to λ^*=0.2 (C/U=4) in case 4 decreases the lift by 10% (case 3 is 29% higher than the flat inclined plate) but increases the relative drag by 33%. Similarly, when the wave speed is further increased by increasing the wavelength to 0.5 in case 6 (f^*=20, C/U=10), lift decreases but thrust (relative drag) increases compared to case 4. Nevertheless, C_L is still 9.2% higher than the lift of the flat inclined plate. Similar results such as the increase of thrust (relative drag) and the decrease of lift are observed by increasing the wavelength to 1.0 and 2.0 in cases 7 and 8, respectively. It can also be observed that the pitching motion (case 9) produces the maximum relative drag but it does not change the lift compared to the flat inclined case.

Theoretically, the time-averaged thrust (relative drag) increases by both frequency and wave-

length as wave speed C increases according to EBT [40]—see appendix A for the derivation:

$$C_T = 0.11\pi(2\pi f^* a^*_{max})^2(1 - (\frac{1}{\lambda^* f^*})^2) \tag{4.5}$$

Note that $1/(\lambda^* f^*) = U/C$. The calculated relative drag (Table 4.4) follows the trend predicted by EBT, i.e., the thrust (relative drag) increases by increasing wave speed through increasing f^* and/or λ^*. However, the lift force does not follow the same trend.

The lift force of cases (3-7) (undulating at high f^*) has increased compared to the flat inclined plate (case 1) as observed in Table 4.4. A simple explanation is that the traveling waves on the plates generate thrust along the Z direction (figure 4.1b) which has a component in the lift (y) direction, i.e., enhances lift. The contribution of thrust force, generated by traveling waves, to the lift coefficient (denoted by ΔC_L here) can be approximated by the component of the thrust force in the lift (y) direction, i.e., $\Delta C_L = C_T \sin(\theta)$ where θ is the angle of attack (the angle between Z and y direction in figure 4.1). Therefore, for case 3, $\Delta C_L = (0.06) \times (sin(10^o)) \approx 0.005$. This is two orders of magnitude smaller than the lift enhancement of cases (3-6) (≈0.1) relative to the flat inclined plate (Table 4.4). Therefore, the y component of the generated thrust is not the main reason for such lift enhancement. The lift enhancement is due to the modification of the pressure distribution around the plate, which is further investigated below.

To see how the lift force along the plate is modified by the traveling waves, the mean spanwise averaged lift distribution along the plate for the flat inclined plate and three undulating case (2, 4, 6) is presented in figure 4.15a. To see the spatial dependency of the lift force, the spanwise averaged are shown along with the lift coefficient at three sections across the span of the plate, $X = 0.1L, X = 0.3L, X = L$, where X is the spanwise distance between the section and the tip of the plate (see figure 4.12e). It can be observed that the range of spanwise variation of the lift is higher in the recirculatory (separated) zone (see the error bars (vertical lines) in figure 4.15a) because the lift is high on the midplane but decreases more near the tips of the plate ($X = 0.1L$) due to the tip vortex (figure 4.12f) [205, 208]. In addition, it can be observed that these variations

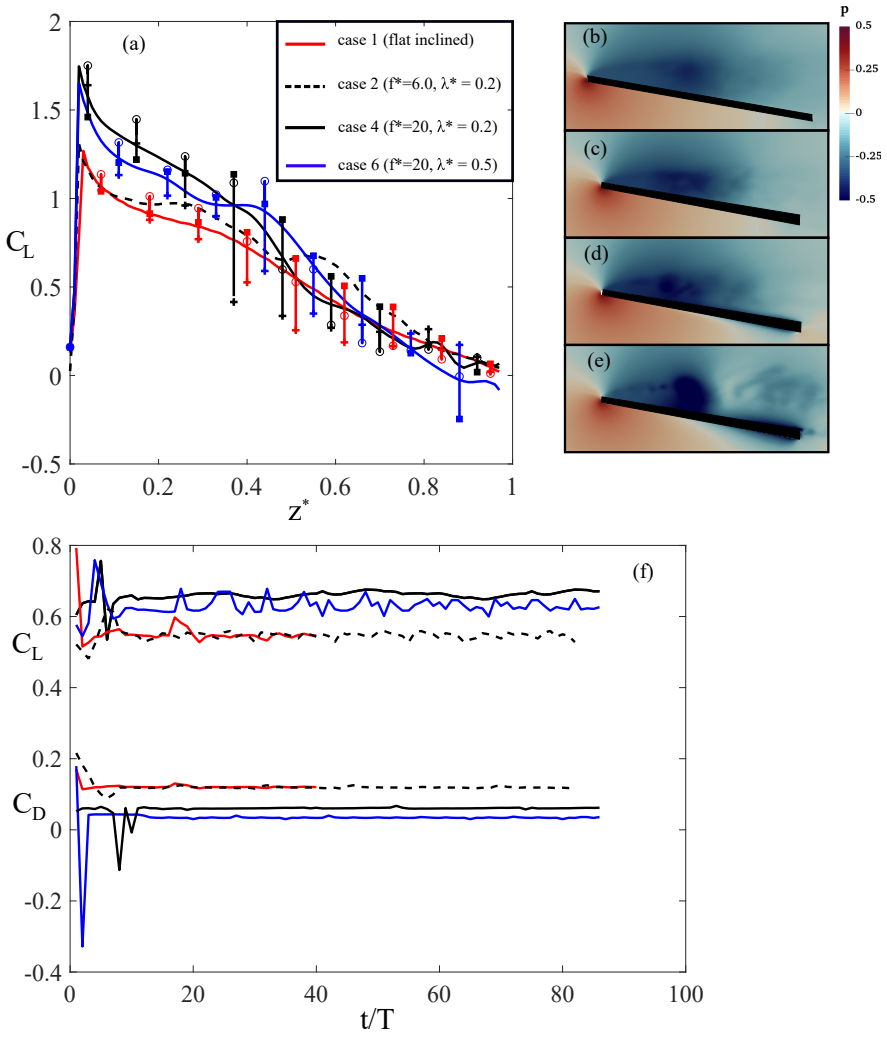

Figure 4.15: (a) spanwise averaged distribution of the lift coefficient along the plate with three points along the span of the plate. ∘, ■ and + symbols are the lift coefficient at $0.3L$, L (mid plane) and $0.1L$ from the tip of the plate, respectively, for cases (1, 4, 6). (b) to (e) Time-averaged pressure field at midplane for cases (1, 2, 4, 6), respectively. (f) Time history of cycle averaged lift (upper curve) and drag coefficient (lower curve), for cases (2, 4 and 6). Here, T is the period time of the wave for undulating cases which is $1/f$, and T is defined as $T = L/U$ for flat inclined plate. Reprinted from [158]

are higher for the undulating cases.

To show that the lift force along the plate has reached quasi-steady state, the time histories of the cycle averaged lift and drag coefficients for flat inclined and three undulating case (1, 2, 4, 6) are shown in (figure 4.15f). Figure 4.15f shows that the cycle averaged forces for undulating cases become steady after about 12 cycles. The lift forces of undulating cases (2, 4 and 6) plotted in

figure 4.15a are averaged over 20 cycles, and averaging is started after 50 cycles as the forces are steady as shown in figure 4.15f. The time averaging for flat inclined plate is performed for $10t/T$ which is equivalent to 4000 iterations.

Comparing the mean spanwise averaged lift coefficient of undulating plates with the flat inclined one (figure 4.15a) shows that C_L does not change significantly for the low frequency undulating case (case 2), but it becomes higher near the leading edge and slightly decreases near the trailing edge for high frequency undulatory cases. This indicates that the total lift of case 4 and 6 has increased compared to the lift of the flat inclined plate (case 1) due to the increase of the generated lift near the leading edge. In fact, case 4 that has the largest C_L near the leading edge (figure 4.15a) has the highest total lift coefficient among these four cases (Table 4.4).

The lift of high f^* cases (case 4 and 6) has increased near the leading edge because of the lower pressure in the recirculatory zone relative to the pressure side (figure 4.15d,e). The reason for the slightly lower lift coefficient of the high f^* cases in the vicinity of the trailing edge (figure 4.15a), is the symmetric time-averaged pressure distribution (figure 4.15d,e). It can be observed in figures 4.15d,e that a low pressure exists on both suction and pressure sides of the undulating plate near the trailing edge area, which can be explained by the scaling of pressure on an undulating surface at high frequency. The pressure on an undulating inclined plate is generated by two mechanisms: (a) the angle of plate which pushes the incoming flow downward (downwash) generating a higher pressure on the lower surface and a lower pressure on the upper surface; and (b) the pressure created by the undulations of the plate which accelerates the fluid near the plate (appendix A.2). The pressure due to undulations (undulating pressure) increases as frequency increases. In fact, for the undulating pressure, the normal component of the time-averaged pressure gradient along the lateral direction pointing outwards from the plate $\partial\bar{p}/\partial n$, near the trailing edge, scales with $(a^*_{max})^2(f^* - 1/\lambda^*)^2$, which is derived by simplifying the time-averaged Navier-Stokes equations (see appendix A.2). Note that the positive $\partial\bar{p}/\partial n$ indicates that the pressure increases as we move away from the plate in the normal direction, i.e., a low pressure near the undulating plate. At high frequencies (case 3 to 8), the undulating component dominates the pressure created by downwash

(flat inclined plate). In fact, the magnitude of pressure near the trailing edge of an undulating plate at higher frequencies is one order of magnitude larger than the pressure over the trailing edge of the flat inclined plate (case 1). Therefore, the pressure near the trailing edge on both sides of the plate becomes similar at high f^*, i.e., results in a low symmetric time-averaged pressure distribution (figure 4.15d,e), because (a) the pressure at the trailing edge is dominated by the undulating pressure at high f^* and (b) the undulating pressure is similar (low) on both sides of the plate.

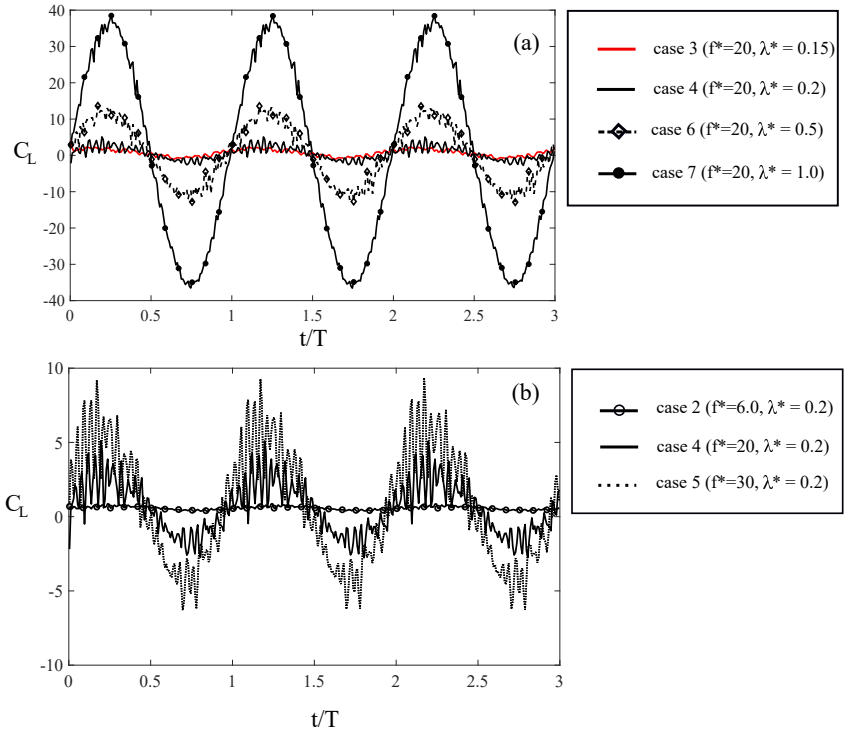

Figure 4.16: (a) The effect of wavelength on the instantaneous lift coefficient: instantaneous lift coefficients for three cycles at quasi steady state for four oscillating cases with the same $f^* = 20$, case 3 ($f^* = 20, \lambda^* = 0.15$), case 4 ($f^* = 20, \lambda^* = 0.2$), case 6 ($f^* = 20, \lambda^* = 0.5$), and case 7 ($f^* = 20, \lambda^* = 1.0$). (b) The effect of frequency on instantaneous lift coefficient: instantaneous lift coefficient for three cycles at quasi steady state for three undulating cases with the same $\lambda^* = 0.2$ and different f^*, case 2 ($f^* = 6, \lambda^* = 0.2$), case 4 ($f^* = 20, \lambda^* = 0.2$), and case 5 ($f^* = 30, \lambda^* = 0.2$). Here, $T = 1/f$ is the period time of the wave for undulating cases. Reprinted from [158]

Although EBT does not predict any mean lift generation when the plate is undergoing an undulatory oscillation, it predicts a sinusoidal profile for instantaneous lift and thrust, similar to aquatic

swimmers [42, 189], which increases the rms of the forces. The rms values of lift and drag coefficient are presented in Table 4.4. It can be observed that the (rms) values for fluctuations of both lift and drag coefficient are small for the flat inclined plate ($C_{L_{rms}} = 0.004, C_{D_{rms}} = 0.001$). When the plate undulates with a low frequency (case 2: $f^* = 6, \lambda^* = 0.2$), the rms values increase compared to the flat inclined plate, but the rms values are still less than mean values ($C_{L_{rms}}/C_L \approx 0.2$ and $C_{D_{rms}}/C_D \approx 0.25$). By increasing the reduced frequency, however, in case 4 ($f^* = 20, \lambda^* = 0.2$), $C_{L_{rms}}/C_L$ and $C_{D_{rms}}/C_D$ increase approximately to 3 and 6, respectively. It can be observed that when the wavelength increases, the rms values increase more intensely, e.g., in case 6 ($f^* = 20, \lambda = 0.5$) $C_{L_{rms}}/C_L$ increases to 50. The high rms of the forces in high frequency oscillating cases (3-9) can be explained by the instantaneous forces. The effect of λ^* and f^* on the instantaneous lift coefficient after reaching quasi steady state is shown in figure 4.16a and b, respectively. When the frequency increases, the intensity of the fluctuations increases (figure 4.16b) and consequently the rms of the forces increases as well (Table 4.4). Increasing the wavelength, however, increases the amplitude of the forces more intensely (figure 4.16a), e.g., the amplitude of the lateral force has increased from 14 to 37 by increasing the wavelength from 0.5 to 1.0. It can be noted that although the net reduced drag generated by the wave is higher for case 5 than cases 6 and 7 (Table 4.4), but the amplitude of the fluctuation is higher for cases 6 and 7. The observed trends are consistent with the theoretical trend for the amplitude of instantaneous lateral (reactive) force, according to EBT [40]. In fact, the amplitude of the lateral force of an undulating plate scales with $O(\lambda^*(f^* - 1/\lambda^*)^2)$, according to equation A.26 derived in appendix A.

4.2.3.4 Traveling waves and the mechanisms of flow reattachment

Traveling waves were shown to reduce turbulence intensity in the wake but increase it near the plate (section 4.2.3.2). In addition, they were shown to reduce flow separation of the mean flow at high frequency while the wavelength effect was not monotonic (section 4.2.3.1). To explain the effect of wave parameters on turbulence intensity, reattachment, and detachment of the flow, the phase averaged flow along with their corresponding scalings, e.g., lateral velocity (u_Y), are investigated in this section, which will reveal the main mechanisms governing flow reattachment

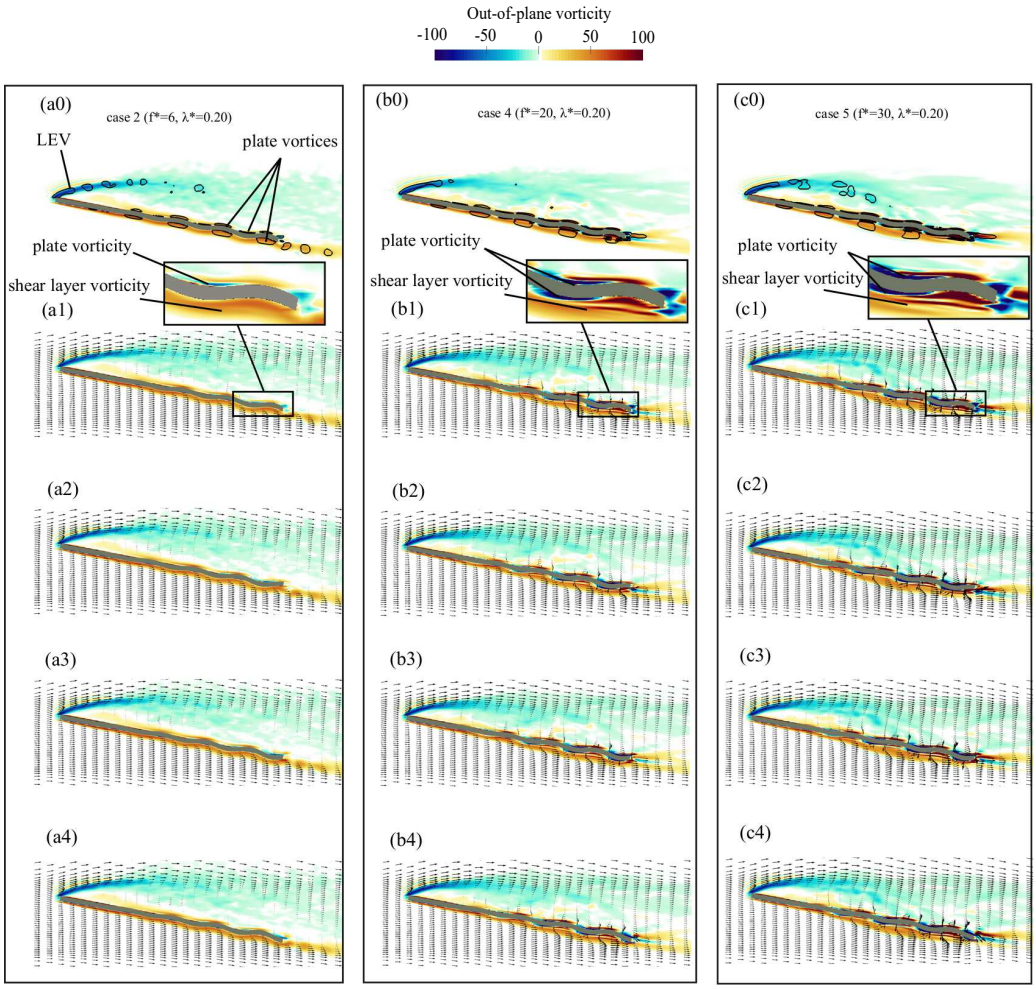

Figure 4.17: The effect of frequency on the phase-averaged flow field of undulating cases with similar wavelength ($\lambda^* = 0.2$) on the midplane. The first row for each case visualizes the contours of out-of-plane vorticity and the footprint of Q-criterion ($Q = 40$) by black lines for phase angle $t/T = 0$. The second to fifth rows for each case visualize the vorticity and velocity vectors of the flow close to the plate for four phase angles (a0-a4) is the undulating plate case 2 ($f^* = 6$, $\lambda^* = 0.2$), (b0-b4) is the undulating plate case4 ($f^* = 20$, $\lambda^* = 0.2$), and (c0-c4) is the undulating plate case 5 ($f^* = 30$, $\lambda^* = 0.5$). The inset shows the shear layer vorticity over the pressure side, and the plate vorticity over the pressure and suction sides of the plate. The visualizations of the second to the fifth rows of each case is for phase-angle of (1) t/T=0.0; (2) t/T=0.25; (3) t/T=0.5; and (4) t/T=0.75, respectively. $T = 1/f$ is the period of each case.

by traveling waves.

Figures 4.17 and 4.18 represent the effect of frequency and wavelength, respectively, on the phase-averaged flow field visualized by out-of-plane vorticity and velocity vectors for four phase angles. The first row of each case (figures 4.17,4.18) shows the contours of vorticity and the

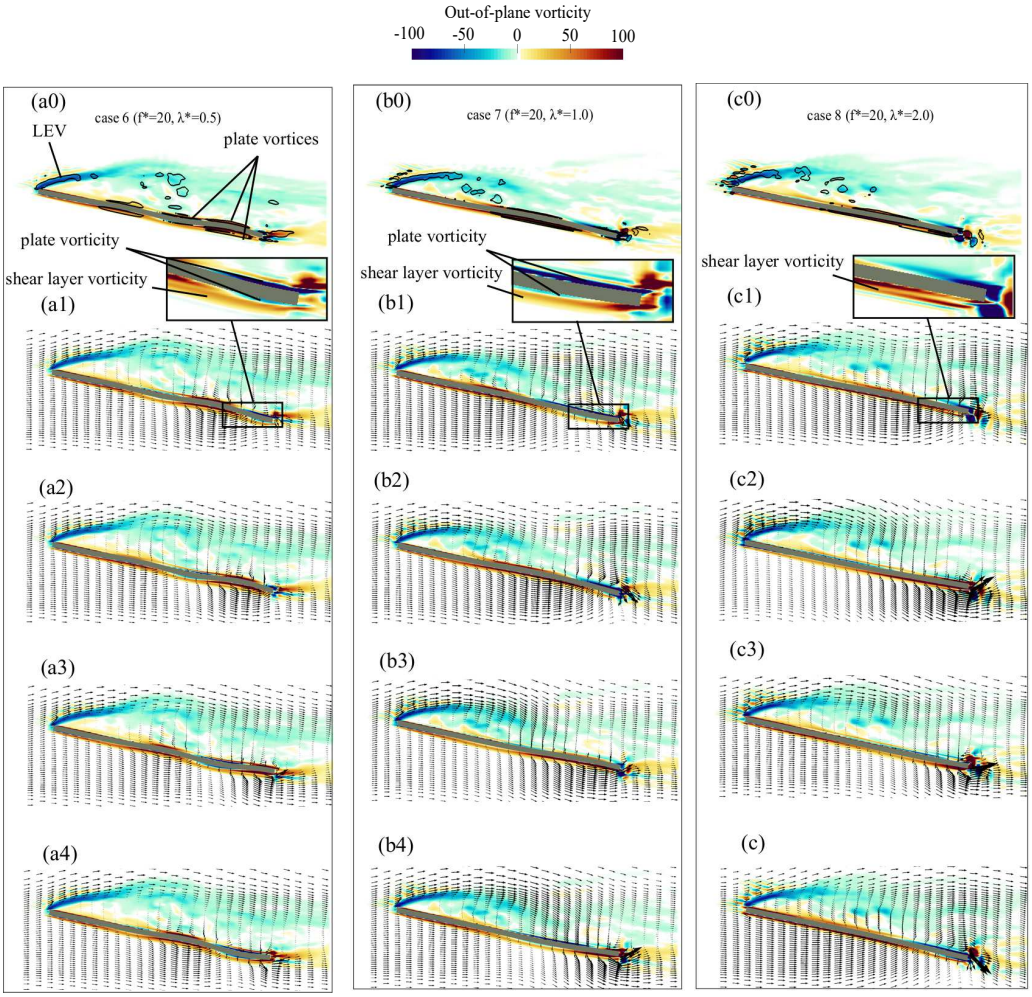

Figure 4.18: The effect of wavelength on the phase-averaged flow field of undulating cases with similar frequency ($f^* = 20$) on the midplane. The first row for each case visualizes the contours of out-of-plane vorticity and the footprint of Q-criterion ($Q = 40$) by black lines for phase angle $t/T = 0$. The second to fifth rows for each case visualize the vorticity and velocity vectors of flow close to the plate for four phase angles (a0-a4) is the undulating plate case 6 ($f^* = 20$, $\lambda^* = 0.5$), (b0-b4) is the undulating plate case 7 ($f^* = 20$, $\lambda^* = 1.0$), and (c0-c4) is the undulating plate case 8 ($f^* = 20$, $\lambda^* = 2.0$). The inset shows the shear layer vorticity over the pressure side, and the plate vorticity over the pressure and suction sides of the plate. The visualizations of the second to fifth rows of each case is for phase-angle of (1) t/T=0.0; (2) t/T=0.25; (3) t/T=0.5; and (4) t/T=0.75, respectively. $T = 1/f$ is the period of each case. Reprinted from [158]

footprints of the 3D vortices identified by the isolines of Q-criterion for the first phase angle ($t/T = 0$). The four rows below it show the velocity vectors and vorticity contours near the plate at four other time instants in the cycle. In all cases, an attached and a separated shear layer is formed on

the pressure and suction sides of the plate, respectively. The shear layer on the suction side, which has been separated at the leading edge, forms an LEV that sheds into the wake.

In addition to the vortices shed to the wake by the LEV, there are vortices on the plate that travel by the traveling wave along the plate and into the wake (see figure 4.17a0). The vorticity of these vortices (the nondimensional out-of-plane vorticity of the fluid on the plate) is composed of the plate vorticity ($\frac{\partial u_Y^*}{\partial Z^*}$) and the shear layer vorticity ($\frac{\partial u_Z^*}{\partial Y^*}$), i.e., out-of-plane vorticity= $-$ in-plane vorticity= $-\omega_x^* = -(\frac{\partial u_Y^*}{\partial Z^*} - \frac{\partial u_Z^*}{\partial Y^*})$. The plate vorticity is obtained by taking the derivative of the lateral velocity with respect to the streamwise length ($\frac{\partial u_Y^*}{\partial Z^*}$) because the plate has no streamwise motion ($u_Z = 0$). The plate vorticity scales with $O((a_{max}^*/\lambda^*)(f^* - 1/\lambda^*))$ while the shear layer vorticity scales with O($\sqrt{Re}$) for an attached boundary layer of the plate based on Blasius skin friction coefficient [209]—see appendix A.

If the flow is separated, e.g., on the suction side, the shear layer vorticity is low and the plate vorticity dominates. Consequently, the vorticity of the fluid near the plate follows the same trend as the plate vorticity on the suction side as observed in figures 4.17 and 4.18, e.g., the vorticity on the suction side is counter-clockwise (positive) and clockwise (negative) on the peaks and valleys of the wave, respectively, similar to the plate vorticity for all cases (figures 4.17 and 4.18). On the pressure side, however, the shear layer is attached and creates a counter-clockwise (positive) vorticity. The shear layer vorticity is approximately $0.3\sqrt{Re} \approx 45$, which is much higher than the plate vorticity at low frequency (case 2) that is approximately $4\pi^2(a_{max}^*/\lambda^*)(f^* - 1/\lambda^*) \approx 2$. Similarly, for case 8 which has a high wavelength (λ^*) the approximation of plate vorticity ($\partial u_Y^*/\partial Z^* \approx 4\pi^2(a_{max}^*/\lambda^*)(f^* - 1/\lambda^*) \approx 5$) is much smaller than shear layer vorticity ($\partial u_Z^*/\partial Y^* \approx 0.3\sqrt{Re} \approx 45$). Therefore, no clockwise (negative) vorticity is observed on the valleys on the pressure side for case 2 (figure 4.17a0-a4) and case 8 (figure 4.18c0-c4). For other cases (4, 5, and 6), however, the clockwise (negative) vorticity is observed on the pressure side for cases 4, 5 and 6 on the valleys of the wave close to the plate while the counter-clockwise (positive) shear layer is still present and stretches from the leading to the trailing edge on the pressure side (figure 4.17b,c and figure 4.18a). This agrees with the trend predicted by the scaling because the

order of plate vorticity increases by the increase of f^* and the decrease of λ^* (cases 4, 5, 6) and becomes similar to the order of the shear layer vorticity on the pressure side.

The counter-clockwise and clockwise vortices, which are on the suction side for case 2 and on both sides for cases 4 to 8, travel on the peaks and valleys of the traveling wave, respectively, to the wake (figure 4.17a0). The counter-clockwise (positive) vortices, identified by the isolines of Q-criterion, are visible in the wake of case 2 (figure 4.17(a0)), but neither the clockwise nor the counter-clockwise vortices are observed in the wake (after the trailing edge) of cases 4 to 8 (figure 4.17(b,c), figure 4.18(a,b,c)). The reason for the annihilation of these vortices in the wake of cases 4 to 8 is the interaction of the clockwise and counter-clockwise vortices due to the sudden reduction in their speed in the wake. In fact, these vortices are convected on the peaks and valleys of the wave toward the wake with the wave speed C. However, their speed suddenly reduces when they reach the wake as the speed in the wake is much smaller ($U \ll C$). Therefore, shortly after a clockwise vortex enters the wake and slows down, the adjacent counter-clockwise one (traveling with the wave speed C) reaches the wake as well. Due to the short distance of these vortices, afterwards, they interact and cancel out each other. For case 2, the clockwise (negative) vortices are dissipated in the wake due to the interaction with the turbulent flow of the wake. However, the attached shear layer on the pressure side amplifies the counter-clockwise (positive) ones, so they are still visible in the wake (figure 4.17(a0)). Note that, for values of Q> 10 at which the coherent structures can be distinguished, the annihilation of these vortices is found to be independent of the value of Q used for the visualization (Q=40 in figures 4.17 and 4.18). The cancellation of these vortices in the wake for $C \gg U$ is the main reason for the observed lower turbulence intensity in the wake of traveling waves (§4.2.3.2).

The flow reattachment can better be observed by the phase-averaged velocity field, which is shown for four phase angles in figures 4.17 and 4.18. The velocity and vorticity above the trailing edge and into the wake of case 2 is very small (figure 4.17a), which indicates that the plate does not impart enough momentum into the flow because of its low frequency ($f^* = 6$). By increasing the frequency to $f^* = 20$ in case 4 both the velocity in the wake above the trailing edge and the

plate vorticity (figure 4.17b1-b4) are much higher than case 2 (figure 4.17a1-a4), which indicates a higher momentum transfer into the wake because of higher f^* of the plate. By increasing the frequency further to $f^* = 30$ in case 5, the streamwise velocity increases near the trailing edge (figure 4.17c1-c4) compared to case 4 (figure 4.17b1-b4), but the streamwise flow does not change near the leading edge, i.e., the reverse flow can be observed in all phase angles near the leading edge (figure 4.17). However, increasing the wavelength from 0.5 to 1.0 or 2.0 (figure 4.18) totally removes the reverse flow near the leading edge in case 7 (figure 4.18b3) and case 8 (figure 4.18c2) which is probably due to the high instantaneous reactive force generated at high wavelengths (figure 4.16 and eqn. A.26) that changes the flow field from the leading to the trailing edge. In addition, by increasing the wavelength, both the lateral and streamwise velocities increase at the trailing edge (figure4.18b,c) where the increase of streamwise velocity was also observed as a jet-like profile of the time-averaged velocities in figure 4.11b at section L5.

When f^* increases from 6 to 20 or 30 in cases 3 to 8, considerable thrust is generated by the wave (see $C_{D_{rel}}$ in Table 4.4) and flow reattaches earlier compared to cases 1 and 2 (see R Table 4.4). Note that the increase in thrust is equivalent to the increase in the axial momentum of the wake here (eqn. A.30) as shown by a simple control volume analysis in Appendix A. Such a reduction in flow separation by increasing the frequency is, therefore, due to the increase in the transfer of axial momentum to the fluid by the undulations similar to the steady blowing technique in flow control [6]. Nevertheless, higher axial momentum is not the only consideration for reducing flow separation based on our results. Case 8 compared to case 7 and also in case 6 compared to case 4 have a higher λ^* (similar f^*) but a higher separation as well (Table 4.4). Higher λ^* indicates a higher momentum transfer to the fluid according to Eqns. 4.5 and A.30 as well as the results of relative drag in Table 4.4, i.e., the lower axial momentum is not the reason for larger reattachment length for case 8 compared to case 7 and also for case 6 compared to case 4 (Table 4.4). It is probably due to the higher lateral velocity as it affects the spreading of the wake.

Based on EBT, the lateral velocity of a fluid particle over an undulating plate scales with $O(a^*_{max}(f^* - 1/\lambda^*))$—see appendix A for details. This scaling shows that at a given reduced fre-

quency and amplitude, the magnitude of lateral velocity increases as wavelength increases. When the magnitude of the lateral velocity increases, the lateral spreading of the flow increases which tends to increase the separation. Here, the spreading of the wake is approximated as the ratio of the height (H) of the wake at the trailing edge to the chord length. The height (H) is defined as the distance between the plate trailing edge and the point above the trailing edge (y-direction) at which the out-of-plane vorticity is close to zero. The spreading of the wake is $0.44, 0.48$ and 0.51 for cases 2, 4 and 6, respectively, which confirms that the spreading of the wake increases as the lateral velocity is increased by either wavelength or frequency. Herein, the vorticity threshold used for distinguishing the height of the wake is a small value (out-of-plane vorticity $= 1.0$) to filter out the vorticity produced by numerical perturbations. Our observation reveals that choosing a higher threshold such as out-of-plane vorticity $= 3.0$ does not change the pattern observed above, i.e., the spreading of the wake increases by the increase of either wavelength or frequency.

4.2.4 Discussion

Previous studies on flow control using surface morphing actuators on airfoils [210, 7] explained reattachment mechanism as follows: the oscillation amplifies the Kelvin-Helmholtz instability, which leads to the earlier roll up of the vortices and generation of a spanwise large coherent structure (LCS). Finally, the break-up of the LCS energizes the near wall flow and improve flow reattachment. They also reported that the reverse flow near the leading edge of the airfoil will be reduced gradually by transferring the high momentum flow of the shear layer to the surface. Here, there is no such a vortex roll-up as flow separates from the sharp leading edge. In addition, there is no such an LCS over the plate as observed in figure 4.14a-d for the instantaneous flow of cases 1, 2, 4 and 6. Also, the presence of a jet-like streamwise velocity adjacent to the plate and the fast transition of reverse flow to streamwise flow near the trailing edge has not been reported in surface morphing studies. In this study, therefore, the reattachment is due to the momentum transfer into the flow by the traveling waves, and the amplification of the Kelvin-Helmholtz instability near the leading edge does not contribute to flow reattachment.

Studies on aquatic swimmers have reported that the viscous force increases due to undulation,

i.e., viscous force of a swimming fish is higher than a translating fish stretched straight [211, 190, 48]. However, it can be observed in Table 4.4 that the viscous drags of cases 2 to 6 are smaller than the flat inclined plate (case 1), whereas cases 7 and 8 are higher, i.e., high frequency undulations have decreased the viscous drag in cases 3-6. The reason for the reduction of the viscous drag in cases 3 to 6 compared to case 1 might be the stronger clockwise vortices on the plate whose (negative) vorticity is much higher than the shear layer vorticity on the pressure side as discussed in the previous section (figures 4.17,4.18). These clockwise vortices may reduce the wall shear stress on the peaks of the wave on the pressure side, which may consequently decrease the C_{D_f} for these cases. Nevertheless, such changes in the viscous drag C_{D_f} are negligible compared to the variations of the pressure drag C_{D_p} as observed in Table 4.4. In fact, the thrust generated by the undulations ($C_{D_{rel}}$) mainly reduces the pressure drag (Table 4.4).

Thrust increases by increasing the wave speed $C/U = f^*\lambda^*$ according to EBT (Eqn. 4.5). Taking into account that the increase in thrust is equivalent to the increase of axial momentum in the wake (see Eqn. A.30 in Appendix A), therefore, the axial momentum exerted by a traveling wave on a fluid increases by increasing the wave speed. The higher axial momentum by increasing C/U is thought to decrease flow separation. However, the higher separation of flow in case 6 compared to cases 3 and 4, and in case 8 compared to case 7 shows that separation cannot be decreased just by increasing C/U as the waves with $C/U = 3$ (case 3) and $C/U = 4$ (case 4) have lower separation than the waves with $C/U = 10$ (case 6). These observations are in contrast to the observation of flow reattachment over wavy walls [200, 4] or aquatic swimmers [48, 189] for $C/U > 1$. This is probably due to the fact that the nature of flow separation and reattachment over an inclined plate is different from that of a plate at zero angle of attack. Over a wavy plate at zero angle of attack [4, 200], flow separates over the valleys of the waves. In this study, however, flow separates from the leading edge due to the plate angle of attack ($AOA = 10^o$) and the sharp leading edge of the plate. Increasing λ^* increases the wave speed (C/U) and decreases the wave steepness (a^*_{max}/λ^*). Increasing the wave speed and decreasing the wave steepness reduces flow separation over the valleys of the waves [4] but does not necessarily reduces flow separation at the

leading edge of an inclined plate.

As discussed above, C/U is not the only parameter that affects flow separation on an inclined plate. In fact, both f^* and λ^* impact the flow separation in highly separated flows. Increasing frequency f^* from 6 to 20 and 30 reduces flow separation (Table 4.4). Increasing λ^*, however, does not result in monotonic reduction in flow separation, e.g., increasing the wavelength from 0.5 to 1 reduces flow separation, but increasing it from 0.2 to 0.5 increases flow separation (Table 4.4). This indicates that flow separation is not directly related to the thrust generated by an undulating inclined plate because thrust increases by increasing f^* and λ^* as shown by Eqn. 4.5 or the computed relative drag in Table 4.4. In fact, based on our results (figures 4.17, 4.18 and Table 4.4), both the generated thrust and the lateral velocity influence flow reattachment: thrust tends to reduce flow separation by increasing the axial momentum (see Eqn. A.30 and related derivation in Appendix A), whereas the lateral velocity increases flow separation by spreading the wake. Therefore, in some cases, e.g., case 4, 5 and 7, the effect of axial momentum on flow separation dominates the lateral velocity, and in some cases vice versa, e.g., cases 6 and 8. Note that it is impossible to generate thrust without lateral undulations with a traveling wave because a traveling wave by definition (Eqn. 4.4) only vibrates in the lateral direction. As discussed previously, the lateral velocity scales with $O(f^* - 1/\lambda^*)$ (Eqn. A.23) which also appears in scaling of thrust, i.e., $O(f^{*2} - 1/\lambda^{*2}) = O(f^* - 1/\lambda^*)(f^* + 1/\lambda^*)$ according to Eqn. 4.5. Due to the non-linearity of flow separation and the interdependence of lateral velocity and thrust, it might not be possible to predict the flow separation just by the scalings of lateral velocity and thrust *a priori*. Nevertheless, these scalings provide insights and general guidelines for reducing flow separation.

As a final note, low-amplitude traveling waves, which are recently generated by piezoelectric actuators [202], are used in this investigation. It is expected that such low-amplitude traveling waves reduce flow separation on an inclined plate for angles of attack lower than 10 degrees because separation is known to decrease with the decrease of angle of attack for flat inclined plates [173]. For higher angles of attack ($AOA > 10^o$), however, flow separation and drag coefficient are higher. Therefore, these low-amplitude traveling waves might not reattach the flow. For higher

angles of attack, nevertheless, waves with higher amplitudes might reattach the flow.

4.2.5 Conclusions

The impact of low-amplitude traveling waves on flow separation and aerodynamic performances of a thin plate at the angle of attack of 10^o is investigated numerically. In addition, the scaling of lateral velocity, thrust, and vorticity are derived based on EBT to support and provide insight into the numerical results.

The results of simulations show that flow separation, drag, and lift are not changed via a traveling wave with a reduced frequency $f^* = 6$ and wavelength $\lambda^* = 0.2$, whereas the drag decreases by 50% and the flow reattaches earlier when the reduced frequency and consequently the wave speed increases ($f^* = 20; \lambda^* = 0.2$). Further increase of wave speed by increasing frequency from 20 to 30 reduces flow separation further and decreases drag such that the wave produces a net thrust. Increasing the wavelength to 0.5 from 0.2 with frequency $f^* = 20$ increases the flow separation, although the drag decreases 75% compared to the flat inclined plate. Similarly, reducing wavelength from $\lambda^* = 0.2$ to $\lambda^* = 0.15$ reduces flow separation and decreases drag by 33% compared to the flat inclined plate. Increasing the wave speed considerably by increasing wavelength from $\lambda^* = 0.5$ to $\lambda^* = 1.0 - 2.0$, interestingly, decreases flow separation and the drag such that a net thrust is generated. Based on these results, the wave speed, which depends on f^* and λ^* according to $C/U = f^*\lambda^*$, should be high enough to reduce flow separation and drag. However, increasing the wave speed does not necessarily reduce flow separation. Consequently, it can be concluded that the wave speed is not the main parameter for flow reattachment, but both f^* and λ^* individually impact the flow separation.

4.2.6 Limitation and future work

The limitations of this section are the Reynolds number and AOA. The future work can be focused on effect of these waves on flow separation at higher AOA.

4.3 Controlling flow separation of a NACA0018 airfoil by backward traveling waves

In this section the application of traveling waves for controlling flow separation for a NACA0018 airfoil at stall angle of attack is studied. This section is organized as follows: A background of active flow control with surface morphing is provided in §4.3.1. The numerical setup is described in §4.3.2. Results are explained in §4.3.3 and the conclusion is brought in §4.3.4. Finally, the limitation and future work are presented in §4.3.5.

4.3.1 Background

Flow control via surface morphing has been investigated in several studies [28, 29, 37, 36]. Munday et al. [36, 39] reported up to 60% decrease in flow separation. Recently, Jones et al. [23] reported a delay in the onset of stall by morphing the suction side of a NACA4415 airfoil in which the fibers of piezoelectric materials covered about 80% of the whole suction side. In these studies, the oscillations of the surface were in the form of a standing wave [23] or a simple vibration [36], which accelerates the fluid adjacent to the surface along its normal direction. These types of surface morphing reduce flow separation by triggering the boundary layer instability and increasing the mixing of high momentum fluid of the separated shear layer to the low momentum fluid of the reverse flow zone [23, 18], similar to other periodic excitation methods. Nevertheless, the morphing can increase the boundary layer momentum directly if the surface vibrations be in the form of backward traveling waves because traveling waves can increase the fluid momentum along their propagation direction [4, 41], e.g., backward traveling waves, in which the wave is propagated from the leading edge toward the trailing edge, can increase the streamwise momentum. Previous studies [52, 167, 41] has shown that backward traveling wave deformations can reduce flow separation.

Using traveling waves to control flow separation is inspired from aquatic swimmers as they propel themselves by undulations in the form of backward traveling waves [200, 212]. It has been observed that traveling waves can reduce flow separation in different flow regimes and applications, including the turbulent boundary layer of a turbulent channel [4, 41] and bluff bodies such as

a circular cylinder [52] and an inclined plate [167]. Recently, Akbarzadeh and Borazjani [182] performed large eddy simulations (LES) of flow over a NACA0018 airfoil at prestall angle of attack of 10^o to investigate the role of traveling oscillations on the suction side. They observed that the lift coefficient might increase up to 4% by backward traveling wave oscillations. However, flow control is more effective at higher angles of attack, i.e., near the stall angle [17]. Inspired from the impact of traveling waves on reducing flow separation over bluff bodies and recent developments in smart materials [213, 214, 8], which have facilitated the generation of such low-amplitude traveling waves [215], our previous work is extended to investigate the impact of oscillations on the suction side with different waveforms, including backward/forward traveling and standing waves for NACA0018 at the stall angle of attack ($AOA = 15^o$).

Previous studies on surface morphing with standing waves [23, 29, 37] have shown that the amplitude and frequency of the oscillations are the main parameters affecting flow separation. However, when the oscillations are in the form of traveling waves, wavelength and wave speed (product of wavelength and frequency) can also influence the flow separation [200, 167]. For example, it is found that increasing the wave speed by increasing the frequency decreases the flow separation [200, 4, 41], but increasing the wave speed by increasing the wavelength does not necessarily decrease the flow separation [167]. Here, the effect of amplitude, frequency, and wave speed of traveling waves at a constant wavelength ($\lambda = 0.2L; L$: chord length) is studied.

4.3.2 Methods

The simulation set-up, including the fluid mesh and the airfoil geometry, is presented in Fig. 4.19. The flow is in a Cartesian frame (Fig. 4.19), in which x, y and z are along streamwise, vertical and spanwise directions, respectively. The suction side of the airfoil undergoes an actuation which can be either a traveling or standing wave deformation, as it is shown in Fig. 4.19b. To calculate the new position of the suction side of the airfoil under motion in the original Cartesian frame (x, y, z), a local frame (X, Y, Z) is defined, i.e., its origin is at the leading edge and is rotated by the angle of attack (Fig. 4.19b). The backward traveling wave oscillation ($h(X, t)$) prescribed along Y

direction, is:

$$h^*(X,t) = a^*(X)\sin(2\pi(f^*t^* - X^*/\lambda^*)), \tag{4.6}$$

where $h^* = h/L$ is the nondimensional displacement of the suction-side, $f^* = fL/U$ is the reduced frequency, $\lambda^* = \lambda/L$ is the nondimensional wavelength, and $t^* = tU/L$ is the nondimensional time, $X^* = X/L$ is the nondimensional streamwise length that starts from the leading edge, and $a^*(X) = a(X^*)/L$ is the amplitude of the wave which starts from $X = 0.1L$ to $X = 0.85L$. The amplitude is constant and equal to its maximum value $a^* = a/L$ from $X = 0.2L$ to $X = 0.8L$ and decreases linearly toward leading and trailing edges. Here, the parameters with (*) symbol are nondimensional. The schematic of a backward traveling wave, in which the wave propagates with wave speed C^* from the leading edge toward the trailing edge is depicted in Fig. 1.1. To investigate the effect of actuation type, a standing and a forward traveling wave actuation have also been employed on the suction side. The corresponding equation for a forward traveling wave, in which the wave propagates towards upstream, is:

$$h^*(X,t) = a^*(X)\sin(2\pi(f^*t^* + X^*/\lambda^*)), \tag{4.7}$$

and the standing wave oscillation has the following deformation:

$$h^*(X,t) = a^*(X)\sin(2\pi f^*t^*)\sin(2\pi X^*/\lambda^*), \tag{4.8}$$

where the parameters of Eqns.4.7 and 4.8 are same as Eqn. 4.6.

The Reynolds number, in the entire study, is chosen $Re = LU/\nu = 50,000$ based on the free flow velocity (U), airfoil chord length (L) and kinematic viscosity (ν). The fluid grid is an O-type grid (Fig. 4.19b) generated in the curvilinear frame (ξ, η, ζ), where η is normal to the airfoil surface, and ξ is parallel to the airfoil surface. This two dimensional domain is extruded in the $\zeta = z$ direction for $0.1L$ to generate a 3D domain. Note that, in regular body fitted grids $\eta = 0$ is attached to the surface of the airfoil, but here it is inside the immersed airfoil to capture the motion of the surface, i.e., $\eta = 0$ has a minimum normal distance of 0.012 from the surface of the

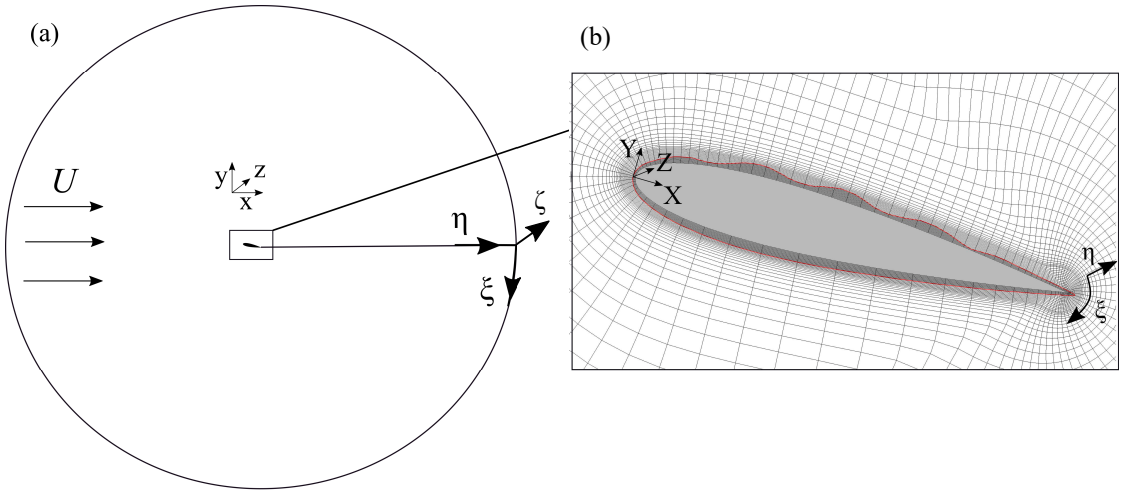

Figure 4.19: The simulation set-up configuration, (a) flow and airfoil in the curvilinear and Cartesian coordinates, (b) representation of an undulating airfoil as an immersed boundary (red line) within the O-grid mesh. Every 10th point , and every 5th point in η and ξ directions are presented, respectively. Reprinted from [183]

airfoil (see the grids inside the immersed boundary in Fig. 4.19b). The boundary condition along ξ, ζ is periodic, and it is defined on $\eta(N_\eta)$ (outer boundary) as follows: It is inlet ($u_x = U$) in the upstream, (x<0), and it is Newman with a mass flux correction in the downstream (x>0). Note that the span size of the domain is chosen to be small to reduce computational costs. Therefore, the focus of this work is on spanwise-averaged results due to the limitation for capturing three-dimensional effects with this span size.

Table 4.5: The details of grid and time-step size of the simulation. R is the approximate radius of the O-type grid in Fig. 4.19a. N_ξ, N_η, and N_ζ are the number of points along ξ, η, and ζ directions, respectively. Δl_ξ^{min}, Δl_η^{min}, and Δl_ζ^{min} are the minimum grid spacing along ξ, η, and ζ directions, respectively.

grid	R	N_ξ	N_η	N_ζ	Δl_ξ^{min}	Δl_η^{min}	Δl_ζ^{min}
1	$15L$	421	281	21	$0.001L$	$0.0003L$	$0.005L$

The simulation set-up configuration, including the domain size and grid size are summarized in

Table 4.5. The grid resolution is maintained $0.0003L$ along the η direction in the vicinity of the airfoil surface which is equivalent to a wall unit spacing of $\eta^+ = 0.9$, where $\eta^+ = \delta l_\eta u_\tau/\nu$, δl_η is the normal distance between the surface and first fluid node, and u_τ is the friction velocity. With this resolution, the viscous sublayer ($\eta^+ < 11.0$) of the boundary layer has at least 12 grid points along wall normal direction (η). The grid spacing remains constant up to $\eta = 0.022$, then it increases with a hyperbolic function to the boundaries. Using the curvilinear O-type grid in conjunction with the immersed boundary is suitable for low amplitude morphing simulations since it can capture the low amplitude oscillations with a lower computational cost compared to a Cartesian mesh. The time step is $0.0005L/U$ for the unactuated case and it ranges from $0.00032L/U$ to $0.00048L/U$ for the actuated cases, which corresponds to Courant-Friedrichs-Lewy numbers (CFL=$U\delta t/\Delta x$) less than 0.5.

Table 4.6: The case studies, including unactuated airfoil, standing wave, forward traveling wave and backward traveling wave actuation with various frequencies and amplitudes. $\overline{C_L}$, $\overline{C_D}$, and $\overline{C_{Po}}$ are nondimensional, lift, drag and power coefficients, respectively. The wavelength is $\lambda^* = 0.2$ for all cases. Reprinted from [183]

case	actuation type	f^*	a^*	C^*	$\overline{C_L}$	$\overline{C_D}$	$\overline{C_L}/\overline{C_D}$	$\overline{C_{Po}}$
1	unactuated	–	–	-	0.676	0.279	2.42	0.0
2	backward traveling wave	2.0	0.002	0.4	0.730	0.221	3.53	0.00012
3	backward traveling wave	4.0	0.002	0.8	0.886	0.096	9.23	0.00017
4	backward traveling wave	8.0	0.002	1.6	0.935	0.088	10.62	0.00027
5	backward traveling wave	4.0	0.008	0.8	0.824	0.125	6.59	0.00035
6	forward traveling wave	4.0	0.002	-0.8	0.807	0.276	2.92	0.00019
7	standing wave	4.0	0.002	-	0.817	0.206	3.96	0.00017

The case studies are presented in Table 4.6. The first case is an unactuated airfoil and the wavelength of the actuated cases is $\lambda^* = 0.2$. Cases 2 to 4 are backward traveling wave actuated airfoils with constant amplitude and different reduced frequency (f^*) ranging from $f^* = 2.0$ to $f^* = 8$, i.e., corresponding to wave speeds $C^* = 0.4$ to $C^* = 1.6$. Case 5 is a high amplitude traveling wave actuation ($a^* = 0.008$, $f^* = 4.0$, and $C^* = 0.8$), case 6 is the forward traveling

wave actuation ($a^* = 0.002$, $f^* = 4.0$, and $C^* = -0.8$), and case 7 is a standing wave actuation ($a^* = 0.002$, $f^* = 4.0$). Note that the positive and negative signs of the wave speeds correspond to forward and backward traveling waves, respectively.

4.3.3 Results

The mean lift, drag, lift to drag, and power coefficients for all cases are presented in Table 4.6. Lift coefficient is $\overline{C_L} = \overline{F_L}/(0.5\rho U^2 L)$, where $\overline{F_L}$ is the mean dimensional per unit of the span of the airfoil force acting on the airfoil along the y direction, and the mean drag coefficient is $\overline{C_D} = \overline{F_D}/(0.5\rho U^2 L)$, where $\overline{F_D}$ is the mean dimensional per unit of the span of the airfoil force acting on the airfoil along the x direction. The power coefficient is the mean power required to accelerate the fluid near the oscillating surface which is calculated as follows:

$$\overline{C_{Po}} = \frac{1}{(0.5\rho U^3) A\, T} \int_T \left(\int_A -p n_Y \dot{h} dA \right) dt. \tag{4.9}$$

where $\dot{h}$ is the time derivative of the lateral displacement (Y direction), i.e., the velocity of the surface oscillation, n_Y is the Y component of the surface normal, p is the fluid pressure on the oscillating surface, dA is the area of the surface element, A is the actuated area of the airfoil's suction side, and T is the integration time which is equivalent to about 80 cycles for the actuated cases and 35 nondimensional time (L/U) for the unactuated case.

The mean lift coefficients ($\overline{C_L}$) and drag coefficient ($\overline{C_D}$) are presented in Table 4.6, which shows that the lift coefficient increases and the drag coefficient decreases by any actuation. The lowest lift increase (7.4%) is for case 2 which has the lowest f^*, and the highest lift enhancement (38.3%) is for case 4, which has a high frequency backward traveling wave. Comparing the lift and drag coefficients of cases 2 to 4, which have a constant amplitude with different frequencies, indicates that the lift coefficient increases and the drag coefficient decreases by increasing the frequency, e.g., C_L has increased by 16.4%, 31.0%, and 38.3% compared to the unactuated airfoil and C_D has decreased by 20.7%, 65.5%, and 68.4% compared to the unactuated airfoil, in cases 2, 3, and 4, respectively. By increasing the amplitude from 0.002, in case 3, to 0.008, in case 5, the lift

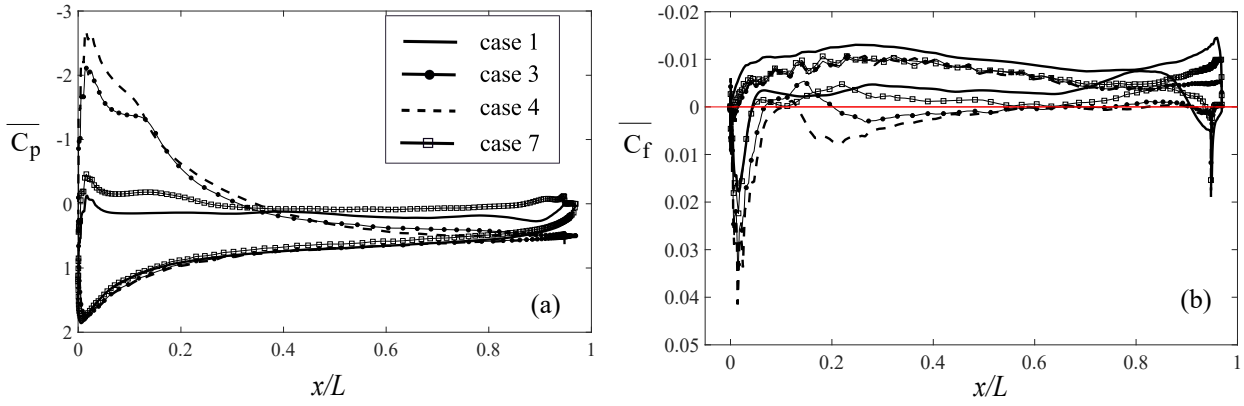

Figure 4.20: The (a) mean spanwise-averaged pressure and (b) skin friction coefficients of the unactuated airfoil (case 1), the morphing airfoil with backward traveling wave actuations of $\mathbf{f}^* = \mathbf{4.0}$, $\mathbf{a}^* = \mathbf{0.002}$ (case 3) and $\mathbf{f}^* = \mathbf{8.0}$, $\mathbf{a}^* = \mathbf{0.002}$ (case 4), and a standing wave actuation $\mathbf{f}^* = \mathbf{4.0}$, $\mathbf{a}^* = \mathbf{0.002}$ (case 7). Reprinted from [183]

coefficient has decreased and the drag coefficient has increased compared to the lower amplitude case, i.e., C_L has increased by 21.4% and C_D has decreased by 55.2% compared to the unactuated airfoil. Table 4.6 shows that the backward traveling wave actuation is more effective than either a forward traveling wave or a standing wave actuation in terms of improving the aerodynamic performance. The lift coefficient of case 3 is higher than cases 6 (forward traveling wave) and 7 (standing wave). The lift coefficient of cases 3, 6 and 7 has increased 31.0%, 19.3% and 20.4% compared to the unactuated case, respectively. In addition, C_D of these cases have reduced by 65.5%, 1.1%, and 26.1%, respectively, compared to the unactuated airfoil. Among these cases, case 4 has the highest lift to drag ratio, e.g., $\overline{C_L}/\overline{C_D} = 10.62$ which is about 4 times greater than the unactuated case (Table 4.6). In addition, among the cases with the same frequency but different actuation type, i.e., cases 3, 5, 6 and 7, the low amplitude traveling wave actuation (case 3) has the highest $\overline{C_L}/\overline{C_D}$ of 9.23 and the forward traveling wave actuation (case 6) has the lowest one, i.e., it is only 20.6% higher than the unactuated case. In fact, based on the aerodynamic performance observed in Table 4.6, the low-amplitude traveling wave actuations are more effective than either forward traveling wave or standing wave actuations. The required power for these oscillations is small compared to the drag power loss ($U \times C_D$). For instance, the C_{Po} is less than 0.0004 for all

cases while the drag loss power is O(0.1).

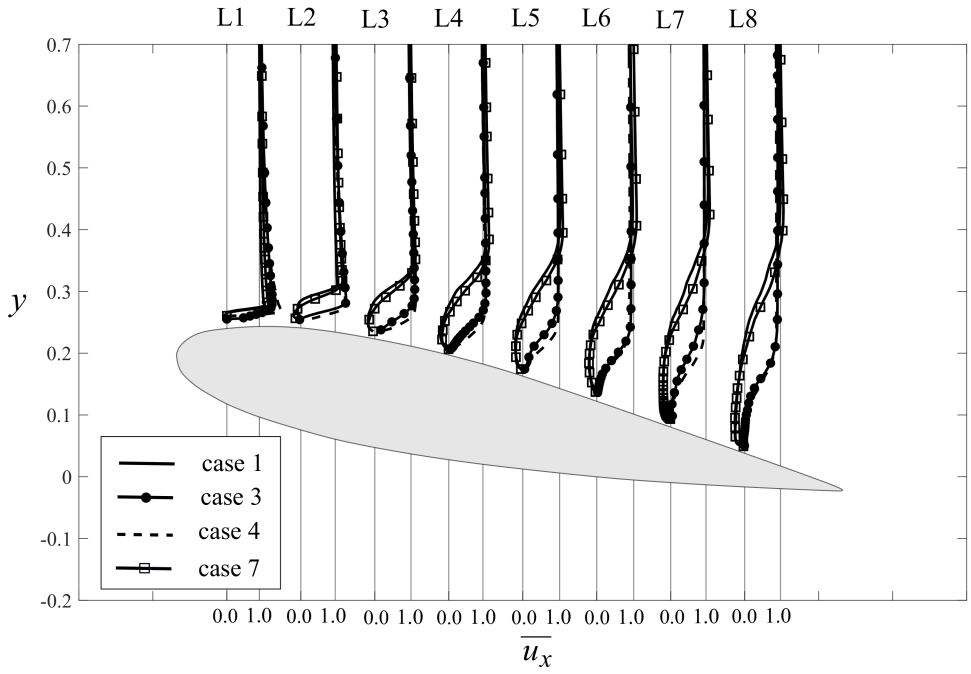

Figure 4.21: The profile of the mean spanwise-averaged streamwise velocity ($\overline{u_x}$) for cases 1, 3, 4, and 7 at 8 different sections spaced by $0.1L$, starting from L1 at $0.1L$ to L8 at $0.8L$ of the airfoil's leading edges. Reprinted from [183]

The enhancement of lift coefficient by the actuations in Table 4.6 can better be observed by the distribution of the mean pressure coefficient around the circumference of the airfoil. The pressure coefficient can be expressed as $C_p = 2p/(\rho U^2)$, where the reference pressure (zero pressure) is pressure at leading edge $(X, Y = 0)$. The mean pressure coefficient ($\overline{C_p}$) is computed by averaging the pressure of the grid point adjacent to the surface. The mean pressure coefficient is plotted for cases 1, 3, 4, and 7 in Fig. 4.20a. The profile of $\overline{C_p}$ (Fig. 4.20a) shows that the lift coefficient of the actuated airfoil increases because $\overline{C_p}$ of the suction side of the airfoil decreases in the vicinity of the leading edge, i.e., the negative C_p contributes to lift. The profile of the pressure coefficient of the unactuated case shows the stall condition. For instance, on the suction side of the unactuated airfoil, the $\overline{C_p}$ decreases from the leading edge, i.e., it has a peak at $x = 0.03$, then it has a flat-

like profile at $0.05 < x < 0.83$, and finally, it decreases again near the trailing edge, similar to the $\overline{C_p}$ profile reported by Puri et al. [31]. When a backward traveling wave actuation (cases 3 and 4) is applied, the peak of $\overline{C_p}$ increases substantially (pressure decreases) compared to the unactuated airfoil, i.e., lift coefficient increases. In case 4, there is a pressure recovery from the peak ($x = 0.03$) up to the trailing edge. However, for cases 3, there is a plateau from $x = 0.10$ to $x = 0.18$, and then the pressure recovery occurs toward the trailing edge. When a standing wave actuation (case 7) is applied, the peak is higher than the unactuated airfoil but it is lower than the one generated by the traveling wave actuations (cases 3 and 4).

Flow over an airfoil at the stall angle of attack becomes separated from the leading edge [216]. By using a flow control technique, the flow separation might decrease either by delaying the separation to further backward or reattaching the separated flow further backward. The flow separation and reattachment is an unsteady process and, consequently, the separation/reattachment location varies with time. Here, to quantify the effect of actuations on the flow separation, the separation/reattachment is defined based on the mean skin friction ($\overline{C_f}$). The mean skin friction is the mean spanwise-averaged of instantaneous skin friction on the points adjacent to the surface, where the instantaneous skin friction is $C_f = 2/Re(\partial u_x^*/\partial y^*)$ and the velocity gradient in the curvilinear coordinates is $\partial u_x^*/\partial y^* = (\partial u_x^*/\partial \xi)(\partial \xi/\partial y^*) + (\partial u_x^*/\partial \eta)(\partial \eta/\partial y^*))$. Based on the mean skin friction, the separation and reattachment location on the suction side are defined as the points where the mean skin friction ($\overline{C_f}$) becomes negative and positive, respectively. The distribution of $\overline{C_f}$ indicates a high positive value on the suction side near the trailing edge, e.g., $x > 0.9L$. However, this positive value does not account for a flow reattachment. In fact, the positive C_f at those locations e.g., $x/L > 0.9$ is due to a strong trailing edge vortex which is present in the mean flow similar to the instantaneous ones (Fig. 5a). The C_f plot indicates that the traveling wave actuations moves the separation point further backward toward the trailing edge. Based on Fig. 4.20b, the flow of the unactuated airfoil becomes separated from $x = 0.05L$ without reattachment. The skin friction of case 7 is similar to case 1, i.e., flow separates from the leading edge without reattachment. In case 3, flow separates at $x = 0.1L$, and reattaches at $x = 0.18L$, where the plateau region

for pressure coefficient is created (Fig. 4.20a). Afterwards, flow becomes separated at $x = 0.78L$. Nevertheless, in case 4, flow remains attached from the leading edge up to $x = 0.75L$. The flow attachment for cases 3 and 4 results in a lower pressure coefficient at those sections as it was shown in Fig. 4.20a.

In addition to the location of the separation point, the profile of the mean streamwise velocity can demonstrate effects of the actuations on flow separation by quantifying the reverse flow on the suction side. The profile of the mean spanwise-averaged streamwise velocity ($\overline{u_x}$) for the unactuated airfoil and actuated cases 3, 4, and 7 are presented in Fig. 4.21. As it can be observed in Fig. 4.21, there is a strong reverse flow at section L2 to L6 for the unactuated and standing wave cases, whereas there is no reverse flow at that locations for the traveling cases (cases 3 and 4). Note that the standing wave actuation does not suppress the flow separation similar to the traveling wave one, but it reduces the reverse flow relative to the unactuated case. Flow becomes separated for cases 3 and 4 near the trailing edge (section L8) while the reverse flow is less than the unactuated and standing wave cases, as it was also observed in Fig. 4.20b.

To visualize the instantaneous flow separation and attachment more clearly, the spanwise-averaged instantaneous out-of-plane vorticity of the seven cases (Table 4.6) at four different time instants are presented in Fig. 4.22. Flow is fully separated over the suction side of the unactuated airfoil, i.e., the shear layer separates from the leading edge and sheds to the wake, and on the trailing edge an unstable counter clockwise vortex (trailing edge vortex) is generated (Fig. 4.22a3). Both the shear layer and trailing edge separation decrease when any type of actuation is applied. Similar to the mean flow (Fig. 4.21), the separation reduction is more significant when a traveling wave actuation with $f^* \geq 4$ (cases 3 and 4) is applied, i.e., the shear layer is closer to the airfoil's surface near the leading edge.

When the low frequency traveling actuation (case 2) is applied, the flow separates from the leading edge. Nevertheless, the separated shear layer is closer to the airfoil surface, and the trailing edge vortex is smaller compared to the unactuated airfoil (compare Fig. 4.22b3 and Fig. 4.22a3). By increasing the frequency to 4 and 8, the shear layer separation decreases (Fig. 4.22c1 to c4

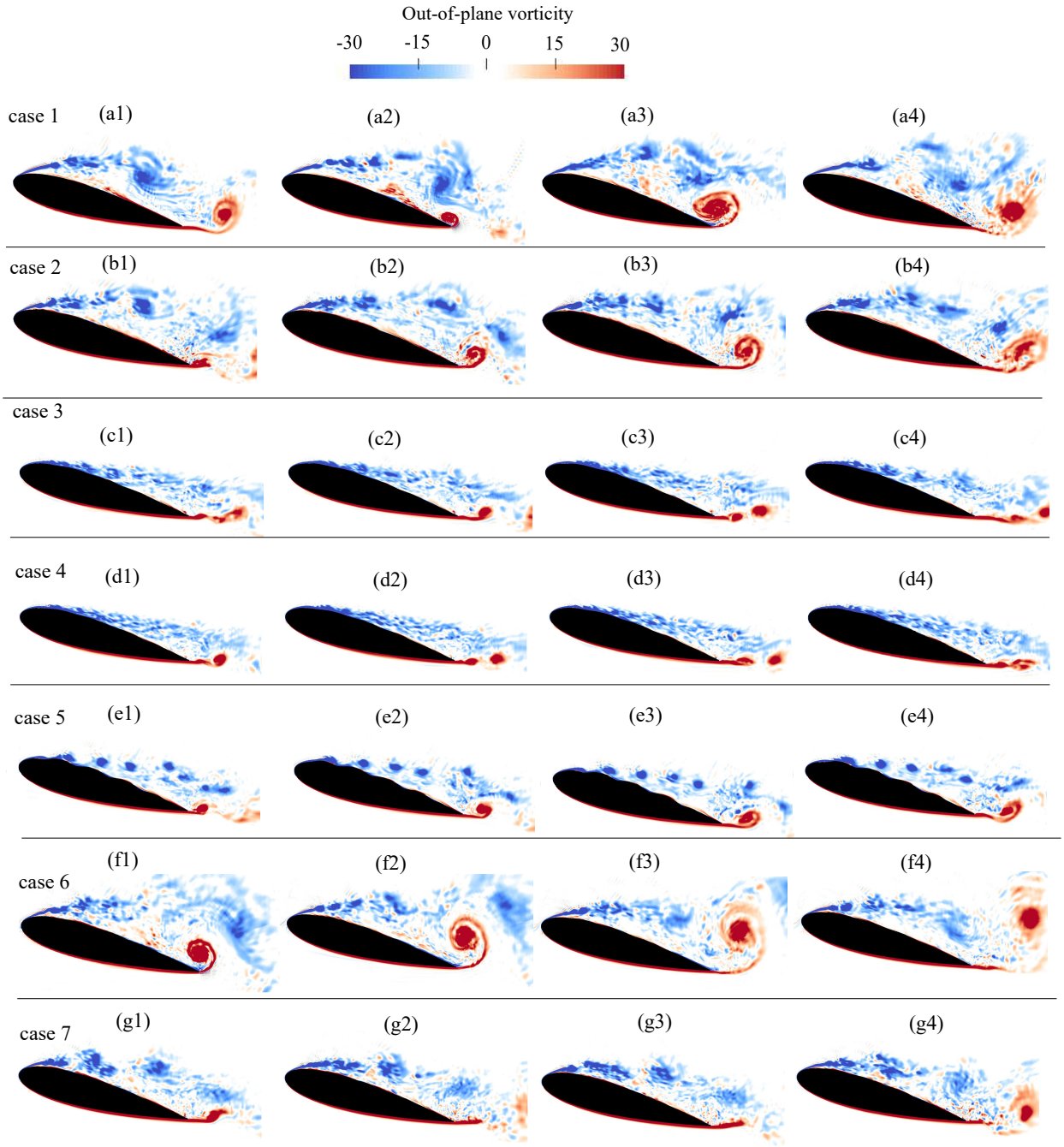

Figure 4.22: Instantaneous flow field visualized by the contours of out-of-plane vorticity (ω_z). Reprinted from [183]

and Fig. 4.22d1 to d4), and size of the trailing edge vortex decreases due to delayed separation. By increasing the amplitude to 0.008 in case 5, the shear layer becomes unstable near the actuation point ($x > 0.1$). The higher amplitude traveling wave oscillations generates large coherent

structures that become separated from the airfoil surface and shed periodically with the oscillations frequency into the wake. Nevertheless, the traveling wave oscillations increase the axial momentum and reduce the flow separation near the trailing edge. The generation of the coherent structures by the traveling waves have also been reported in the previous studies [167, 52]. The forward traveling wave actuation (case 6), in contrast to the backward traveling wave one does not reduce flow separation (Fig. 4.22f). In case 6, the shear layer is fully separated while a large trailing edge vortex is generated at the trailing edge, similar to the unactuated case (Fig 4.22a). The standing wave actuation brings the shear layer closer to the airfoil surface (Fig. 4.22g) but not as closer as the traveling wave one (Fig. 4.22c).

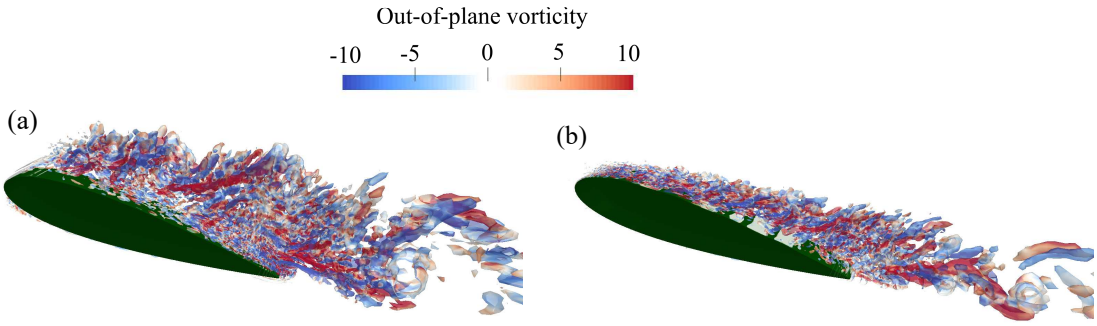

Figure 4.23: Three dimensional vortical structures visualized by the instantaneous isosurfaces of the Q-Criterion (Q=20) colored by the out-of-plane vorticity for (a) case 1 (unactuated airfoil) and, (b) case 4 (traveling wave morphing airfoil with $\mathbf{f^* = 8.0, a^* = 0.002}$). Reprinted from [183]

Figure 4.23 presents the three dimensional turbulent flow structure (vortices) visualized using iso-surface of Q-criterion that colored by out-of-plane vorticity for unactuated airfoil (case 1) and morphing airfoil with $f^* = 8.0, a^* = 0.002$ (case 4). By comparing Fig. 4.23a and Fig. 4.23b, it can be observed that the low amplitude traveling wave morphing reduces the flow separation, similar to the observation of 2D flow field in Fig. 4.22.

4.3.4 Discussion and Conclusion

Previous studies [158, 41, 40] have shown that backward traveling waves can increase the streamwise fluid momentum and decrease the drag force, which theoretically scales with $(a^* f^*)^2(1-1/C^{*2})$ [40, 167]. Recently, Akbarzadeh and Borazjani [167] observed that traveling wave oscillations with significantly higher amplitudes ($a^* = 0.01$) and frequency ($f^* = 20$) but the same wavelength ($\lambda^* = 0.2$) as of this study on an inclined plate could reduce the flow separation and drag coefficient but they could not postpone the stall and reattach the flow to the leading edge because of the plate's sharp leading edge. However, in this study, it was shown that a surface morphing in the form of backward traveling waves can suppress the static stall and delay separation. The results of our LES show that a low amplitude traveling wave ($a = 0.002L$) with reduced frequencies 4.0 and 8.0, and $\lambda^* = 0.2$ can suppress the stall and increases the lift coefficient by about 34%. The lift enhancement is high compared to our previous study for this airfoil at $AOA = 10^o$ in which the lift increased only by about 4% [158] because flow control is, typically, more effective at stall and post stall angles where the flow is massively separated [17].

The flow visualizations (Figs. 4.21 and 4.16) indicate that the backward traveling wave actuations are more effective than other actuations because they accelerate the fluid adjacent to the surface along the streamwise direction [167], i.e., increase the momentum of the fluid near the surface directly, similar to a swimming fish [40]. While the backward traveling waves with frequency greater than 4, e.g., cases 3 and 4, suppress the stall, a lower frequency of $f^* = 2$ (case 2) does not influence the flow separation significantly. Based on the results of cases 2, 3 and 4, it can be concluded that the frequency needs to be high enough to control the flow separation because, theoretically, the axial force created by traveling waves scales with $((af)^2(1 - 1/(\lambda f)^2))$ [40, 167]. However, by increasing the wave amplitude in case 6, the shear layer is only attached up to the actuation point and it becomes unstable after that point. Afterwards, the unstable shear layer sheds into the wake in the form of large periodic coherent structures. Therefore, the flow separation has increased in case 6 compared to case 3, although the amplitude has increased. The reason for the shear layer destabilization in case 6 is, probably, the high wave steepness (a/λ) as

the shear layer separates from the first trough of the traveling wave (Fig. 4.16e). In fact, a steep surface deformation can destabilize an attached shear layer and enhance the separation [41, 171]. In contrast to the backward traveling waves, the forward traveling wave actuation is the least effective actuation because it increases the reverse flow near the wavy surface [4, 41]. Finally, the standing wave actuation (case 7) reduced the flow separation though it does not increase the boundary layer's streamwise momentum directly. Standing waves reduce the flow separation by triggering the Kelvin-Helmholtz instability [23] and enhancing the mixing of the separated shear layer with the low momentum flow of near the surface similar to periodic excitation flow control mechanism [17]. Note that this mixing occurs for other actuations, including backward and forward traveling waves, because the airfoil surface oscillates. The oscillating surface induces a normal velocity that scales with $0.05U < u_Y = O(2\pi f\, a) < 0.1U$ which is close the velocity induced by the surface in previous studies [23].

4.3.5 Limitation and future work

One of the limitation of this work is the number of test cases due to computational cost. Therefore, we could only investigate a low range of frequencies and amplitude. Because of the same reason, the effect of Reynolds number, and AOA has not been studied yet. Investigating the role of higher range of amplitudes, frequencies, and AOA, and higher Reynolds number can be a part of future work. Moreover, we found that traveling wave actuations reduce flow separation by two mechanisms, (i) increasing the axial momentum induced to the flow and (ii) the triggering of instabilities to increase mixing. Nevertheless, understanding the effect of each of these two terms, i.e., axial momentum induced to the flow versus triggering the instabilities, on the flow separation, or investigating the effects of wavelength at the stall and post stall angles of attack can be an interesting topic for future studies.

5. NREL PHASE VI WIND TURBINE SIMULATIONS

Owing to the potential severity of climate change as a result of global warming, every country in the world is taking an active interest in the development of renewable energy. In particular, the installation of wind power generation systems, which are economically feasible and environmentally friendly, has shown a sharp increase since the 1990s with an average rate of 20% [217]. According to the department of energy report (DOE) [217], the wind energy will generate about 20% of the United States total energy production by 2030, and it is expected that its share increases to 35% by 2050. One of the fundamental technological field in the wind power system is the blade design. The blades are typically designed for low wind speeds $4m/s < U < 7m/s$ and they lose their efficiency by increasing the wind speed and will not rotate at lower wind speed. This decrease in efficiency is due to flow separation, which we try to reduce through active flow control. In this chapter, large eddy simulations of NREL phase VI wind turbine's blade and the full-scale turbine are performed. This chapter is organized as follows: a background about NREL Phase VI wind turbine and active flow control methods for wind turbines are presented in 5.1. Section 5.2 provides the detail of the computational set-up, and overset grids. Section 5.3 presents the results of the simulations for baseline and pitching blade. The conclusions are presented in section 5.4, and finally, the limitations and future work are explained in section 5.5.

5.1 Background

Most blades for wind power generation require an optimized aerodynamic design, and rotor blade designs must predict the flow field in order to improve the aerodynamic performance. To optimize the blade design parameters, it is necessary to study flow field and aerodynamic performance from reliable experiments. However, the experiments are expensive due to the large size of wind turbines and issues associated with the measurements, e.g., they are often contaminated by varying wind speeds, changes in wind direction, etc. Therefore, various numerical studies have been performed to investigate flow around the blade and full-scale wind turbines [218, 112]. Dif-

ferent CFD models such as finite element method [218], finite volume[112] and finite difference methods [219] have been utilized to simulate flow over a NREL Phase VI wind turbine which is a benchmark case as its flow parameters have been measured comprehensively in the wind tunnel of NASA Ames [220].

The wind turbines are designed for wind speed of $5m/s < U < 7m/s$ and they lose their efficiency out of this range due to flow separation. To mitigate this problem several passive and active flow control techniques are employed. For passive flow control, vortex generators (VG) and rigid trailing edge flap are used [221, 222]. The VGs are attached on the suction side near the leading edge on a radius at which flow becomes separated [223]. They create coherent structures that energize the boundary layer, and consequently delay flow separation and enhance the overall lift coefficient. Flaps are typically attached near the trailing edge and they augment the power and reduce the turbine load by varying the airfoil camber [224]. For active flow control, suction blowing, steady blowing, plasma actuator, active camber control, surface morphing, and active pitch control are utilized [225, 226]. Previous studies have shown that there is an optimum pitch angle for every wind speed [227]. However, the effect of a sinusoidal dynamic pitch on the aerodynamic performance of a blade is not understood. A dynamic pitch might act as a vibration and trigger boundary layer instabilities to enhance boundary layer transition and reduce flow separation.

In this study, we perform LES of NREL Phase VI wind turbine for two different wind speeds of $U = 7m/s$ and $U = 15m/s$. First, the framework is validated by comparing the results against experimental measurements with fixed pitch. Next, we investigate the effect of a low amplitude dynamic pitch on the performance of a NREL Phase VI wind turbine for both wind speeds.

5.2 Material and Method

In this chapter, simulations of a NREL Phase VI wind turbine are performed using our dynamic overset framework. NREL phase VI is a modified Grumman Windstream turbine with full-span pitch control and a power rating of 18 kW. It has 2 blades, with s809 tapered and twisted blade profile as shown in Fig. 5.1. The rotor diameter is $D = 2R$ =10.058 m, its height is 12.19 m, and the blade's maximum chord length is L =0.72m which is at 0.25R as shown in Fig. 5.1. Three

different types of simulations are performed. First, LES of flow over rotating blade was performed to validate the framework. Afterwards, simulations of a full-scale turbine that includes nacelle, and tower were performed to investigate the effect of tower and nacelle on flow. Finally, the simulations of rotating blades with a low amplitude sinusoidal pitch are carried out. The turbine has an upwind configuration, the blade tip pitch angle is 3^o, the yaw and cone angles are 0^o, and the rotational speed is $72rpm$.

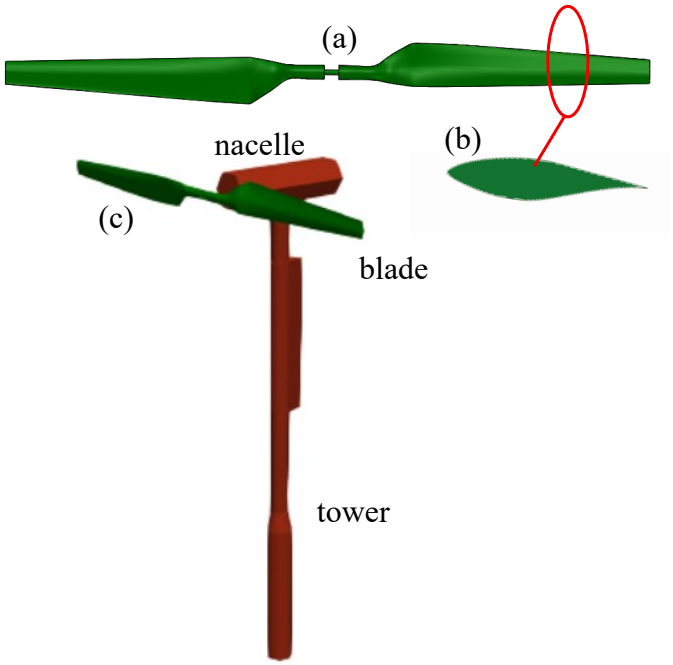

Figure 5.1: The wind turbine configuration: (a) blade, (b) its airfoil profile (s809), and (c) complete turbine geometry.

The simulations setup is presented in Fig. 5.2. The turbine has an upwind configuration, and the wind blows along z direction. The setup has three cuboid blocks where block 1 is the background domain, block 2 captures the turbines wake, nacelle, and the tower, and block 3 resolves the flow around the blade (Fig. 5.2c). Blocks 1, 2, and 3 have a size of $112L \times 112L \times 140L$, $20L \times 20L \times 24L$, and $16L \times 1.8L \times 2L$, respectively. Blocks 1 and 2 are static while block 3 rotates with the rotating blade. Because block 3 should capture the blade's boundary layer, the validation

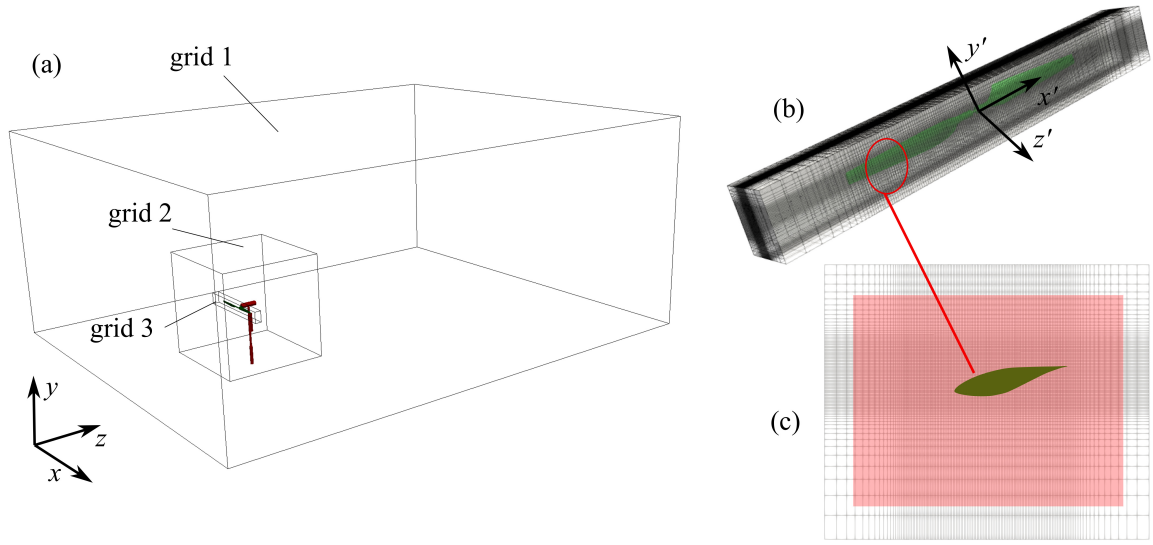

Figure 5.2: The wind turbine simulation set-up. (a) overset is consisted of three blocks; block 1 is the background domain, block 2 includes the tower and nacelle, and block 3 includes the rotor and rotates with the blades. (b) mesh grid of block 3 and its frame, and (c) a cross section of blade (every four grid points along y' and z' are presented).

and grid sensitivity studies are performed by changing the resolution of block 3. Therefore, four sets of block 3 are generated while girds 1 and 2 are similar in all set-ups. The details of blocks' mesh sizes are presented in Table 5.1. The total number of mesh ranges from 30 million in setup 1 to 122 millions in setup 3. The Reynolds number based on the wind speed, blade's maximum chord length (L), and the kinematic viscosity of air ($\nu = 1.48 \times 10^{-5}$) is 345,000 and 739,000, for low and high wind speed cases, respectively. Moreover, the Reynolds number based on the blade's velocity and diameter is in the range of 10^7.

Flow is incompressible turbulent, which is simulated with our CURVIB chimera framework. The turbulent flow is modeled with LES model explained in section2.1. The flow in blocks 1 and 2 is solved in an inertial frame while block 3 is solved in a non-inertial frame as it rotates with the blade. By using a non-inertial frame the simulation cost reduces significantly because the metrics of the curvilinear coordinates are only calculated once and the search algorithm for identifying the fluid, solid, and immersed nodes are only called once. The overset framework is explained in

detail in [108, 228], however, to complete this part the method is explained here briefly. Using the overset framework, the velocities on the boundaries of blocks 3 and 2 are interpolated from blocks 2 and 1, respectively, via a second-order interpolation. Moreover, the velocities of the overlapping zones of blocks 1 and 2 needs to be interpolated from finer blocks. To perform the interpolation of velocities for girds 1 and 2 from grids 2 and 3, respectively, some of the overlapping grid points are blanked out to transfer the information from the inner block to the outer block. For example, the pink area in Fig. 5.2c represents the blank of block 2. The velocities of the grid points over the blank are interpolated from overlapped grid points of block 3. The blank of grid 1 is a cube of $16L \times 1.5L \times 1.4L$ that has been cut by a cube of $2L \times 1.5L \times .4L$ from the surface that faces the nacelle and centered with the blade rotating center. Herein, the flow of block 3 is solved in a non-inertial frame (Fig. 5.2) while the flow in block 2 is solved in the inertial frame. Therefore, after each interpolation, the interpolated velocity on the boundary of block 3 is transformed to the non-inertial frame by a rotation. The interpolation of variables within the overlapped zone requires finding the suitable grid points in each iteration since the blanking zone and block 3 change due to rotation. The search for the suitable grid points and interpolation of variables are performed using our parallel overset framework developed by Hedayat et al. [108]. The blade, tower, and nacelle are placed as immersed bodies, where the blade is in blocks 3, the tower is in block 2, and the nacelle is in both blocks. The grid points are categorized into fluid, immersed, blank, and solid points, by ray tracing algorithms [229]. Here, the velocity of the immersed points is interpolated by Cabot wall modeling [220] because the boundary layer is turbulent and grid normalized wall spacing along the normal direction is $z^+ = u_{tau}\delta_{z_{min}}/\nu = O(500)$, where u_{tau} is the friction velocity.

The flow is initialized with a uniform velocity, $u_z = 1.0$. The inflow of block 1 is a uniform (plug) flow, the outlet of block 1 is a Neumann boundary with a correction to satisfy the conservation of mass. The ground, which is along $-y$ boundary has a no-slip boundary condition on both grids 1 and 2. Each cycle of the turbine rotation has 8000 iterations for setup 1, 10000 iterations for setup 2, and 20000 iterations for set-ups 3 and 4. The CFL number for these cases ranges from

0.28 to 0.72, respectively. The simulations with set-up 3 and 4 are performed for only one cycle, where the averaging was performed for a half cycle due to high computational cost. Note that, the aerodynamic torque becomes quasi-steady after about one quarter of a cycle and it has been observed that a half a cycle averaging is sufficient for reporting the mean values.

Table 5.1: The simulations setup and their corresponding grids. Grids 1 and 2 are the same for all set-ups.

setup	block	N_x	N_y	N_z	$\delta_{x_{min}}$	$\delta_{y_{min}}$	$\delta_{z_{min}}$
1	1	201	157	281	0.29L	0.32L	0.3L
1	2	241	241	321	0.11L	0.11L	0.015L
1	3	149	157	133	0.12L	0.008L	0.0057L
2	3	301	273	201	0.06L	0.004L	0.0039L
3	3	401	401	361	0.04L	0.003L	0.002L
4	3	401	481	501	0.12L	0.0026L	0.0016L

5.3 Results

In this section, first, the results of the baseline simulations are presented in §5.3.1. To validate the simulations, the rotor torque and pressure coefficient are compared against the experiments with different set-ups. Afterwards, the effect of low-amplitude dynamic pitch is investigated in section 5.3.2.

5.3.1 Baseline

Flow over the turbine's blade becomes separated at wind speeds greater than $U = 10m/s$. Figure 5.3 shows the vortical structures identified by iso-surfaces of Q-Criteria at $Q = 2$ for the rotor both simulation and entire turbine simulation at wind speeds $U = 7m/s$ and $U = 15m/s$. While strong tip vortices are generated in the wake of the low wind speed case, these tip vortices are not observed for high wind speed cases due to flow separation. Nevertheless, strong vortices can be observed along the nacelle and tower for entire turbine simulation for both wind speeds (Fig. 5.3c,d).

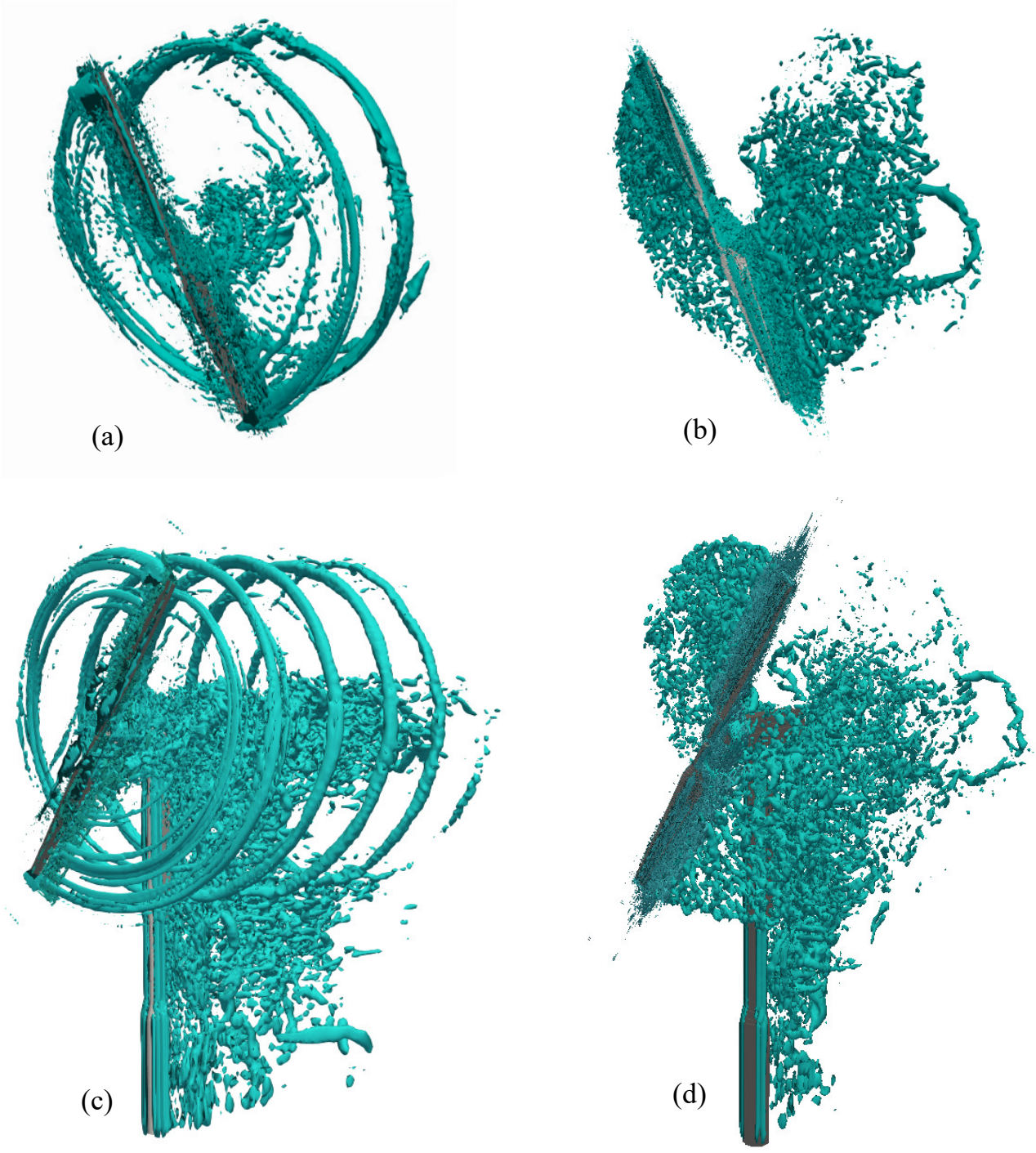

Figure 5.3: The wind turbine rotor torque for four simulation set-ups.

The flow separation can be observed more clearly by visualizing the flow at different cross sections. Figure 5.4 presents the contours of instantaneous out-of-plane vorticity and velocity

vectors at three different radius, $r/R = 0.3$, $r/R = 0.80$, and $r/R = 0.95$. The velocity vectors represent the relative velocity of the air with respect to the blade. As it is shown in Fig 5.4, the flow is attached for all cross sections at low wind speed case but it is separated from the leading edge at high wind speed case as the angle of attack of the incoming air with the blade increases. Especially, the separation is higher at $r/R = 0.3$ since it has the highest angle of attack.

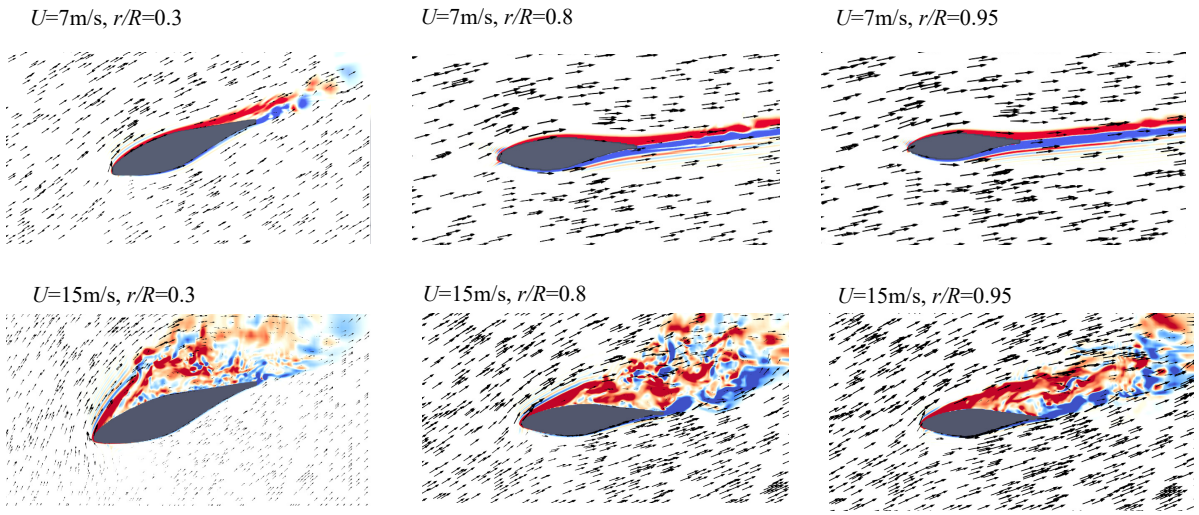

Figure 5.4: The contours of out-of-plane vorticity and velocity vectors.

Time-averaged aerodynamic torque is shown for both wind speeds in Fig. 5.5. The rotor torque of low wind speed case is plotted for set-ups 1, 2, and 3, while it is plotted for set-ups 2, 3, and 4 for the high wind speed case. The torque values are compared against NREL experiments [220]. The simulation results and experimental data match remarkably well at the low wind speed case for set-ups 2 and 3, however, the simulation results for seup 1 underpredicts the torque. The predicted torque of the high wind speed case for set-up 3 and 4 is in good agreement with the experimental data but set-up 2 underestimates the torque due to lower grid resolution. To extend the validations and grid sensitivity studies, the pressure coefficient over the blades is compared against the experimental measurements. The pressure coefficient is the pressure of the fluid points

adjacent to the blade surface that is defined as follows:

$$C_p = \frac{p - p_0}{\frac{1}{2}\rho(U^2 + (r\omega)^2)} \tag{5.1}$$

where r is the blade's radius, ω is the rotor speed, U is the wind speed, and p_0 is the reference pressure, which is the pressure on the leading edge. The pressure coefficient is presented in Fig. 5.6 for two set-ups, i.e., set-ups 2 and 3 for low wind speed case and set-ups 3 and 4 for high wind speed case at three blade's radius, $r/R = 0.3$, $r/R = 0.8$, and $r/R = 0.95$. While C_p for the low wind speed case agrees well with the experimental data on the pressure side for all radius, it has some discrepancy with the experiments on the suction side near the leading edge. For higher wind speed case, C_p matches with the experimental data on the pressure side, however, it has some discrepancy on the suction side for all radius near the leading edge but it follows the trend well. The discrepancy against experiments at $r/R = 0.3$ is greater than other radii which has been observed in the previous numerical studies [218, 112]. Nevertheless, the turbine's torque and C_p plots (Figs. 5.5 and 5.6) are in good agreement with the experiments and it can also be observed that simulations are grid independent when set-ups 2 and 3 are chosen for low wind speed case, and set-ups 3 and 4 are chosen for the high wind speed case.

5.3.2 Pitching blade

In this part, the effect of low-amplitudes sinusoidal dynamic pitch is investigated. The dynamic pitch is applied as a prescribed motion on the turbine's blade which its equation is as follows:

$$\theta(t) = 3.0 + \theta_0 * sin(2\pi f t) \tag{5.2}$$

where θ is the blade's pitch angle, θ_0 is the amplitude of the oscillation, and f is the frequency of oscillations. Here, the frequency is $3.6Hz$, and θ_0 is 3 and 0.5 degrees for low and high wind speed cases, respectively. The amplitude of pitching for high wind speed case is chosen to be small due to computational cost and difficulty associated with high amplitude oscillations in a refined mesh, the pitching blade simulations are performed with set-up 2 and 3 for low and high wind speed

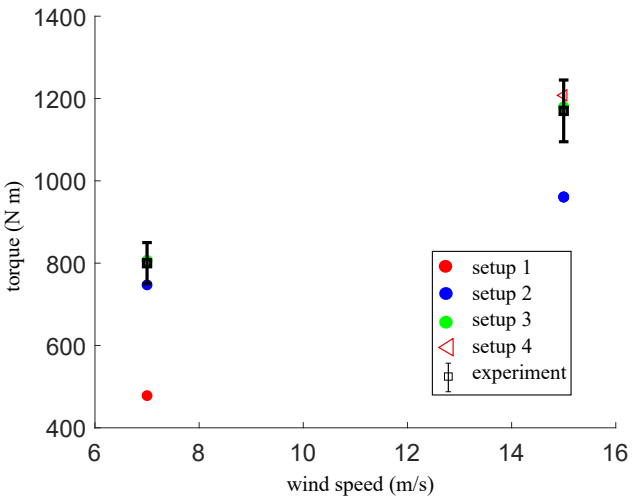

Figure 5.5: The wind turbine wake vortices identified by the iso-surface of Qcriteria with $Q = 2$ for (a) a low wind speed case ($U = 7m/s$), and (b) a high wind speed case ($U = 15m/s$).

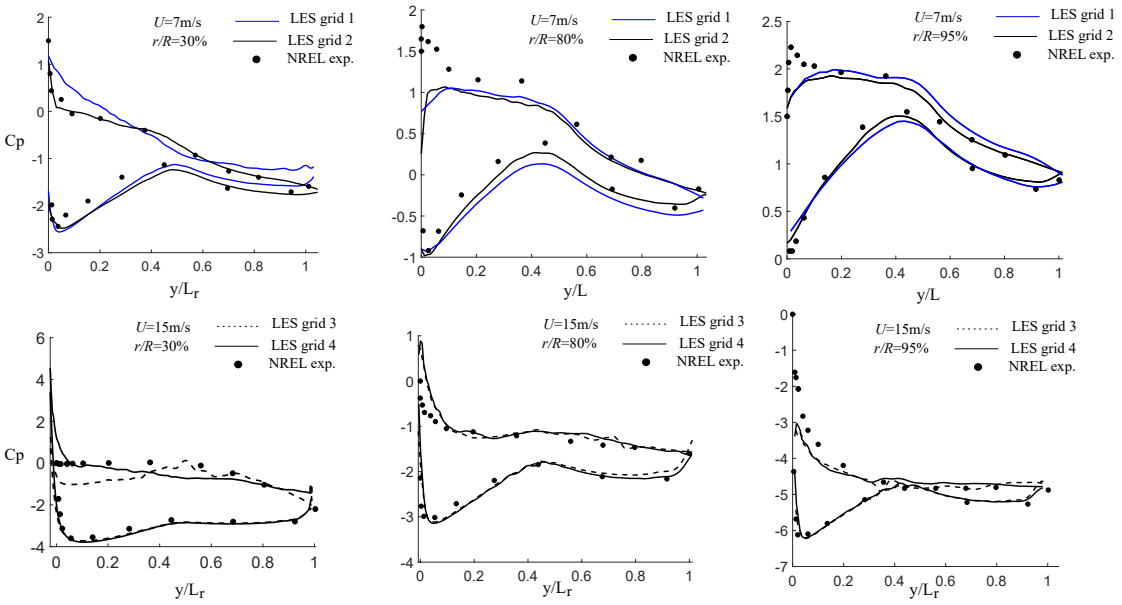

Figure 5.6: The pressure coefficient at 30%, 80%, and 95% of

cases, respectively. Moreover, the simulations are performed for rotating blades without the tower and nacelle to reduce the computational cost. The mean torque for pitching cases are $827N.m$ and $1223N.m$, at wind speeds $U = 7m/s$ and $U = 15m/s$, respectively, which are similar to the

baseline's values (Fig 5.5). The instantaneous aerodynamic torque is plotted for both wind speeds in Fig. 5.7. It can be observed that the dynamic pitch increases the torque fluctuations for both wind speeds. In fact, the results of the simulations suggest that these low amplitude dynamic pitch not only does not improve the mean aerodynamics but also increases the shaft oscillations which can generate noise and damage the rotor.

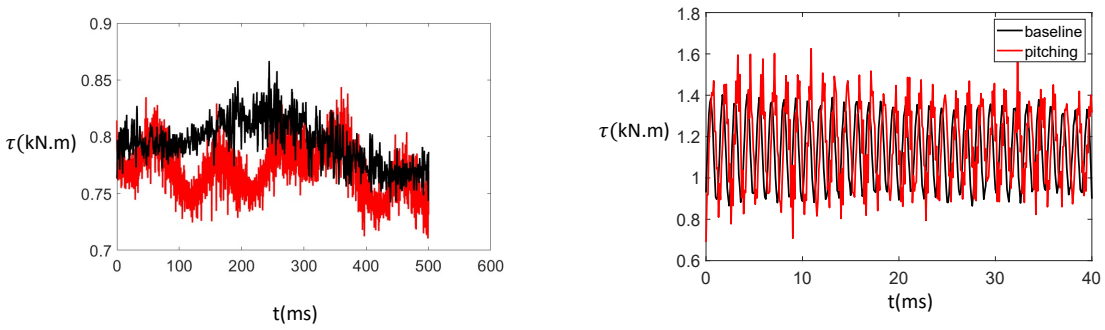

Figure 5.7: The instantaneous torque coefficient for baseline and pitching blade for (a) $U = 7m/s$ and (b) $U = 15m/s$.

Although, the dynamic pitch tested here did not influence the mean torque, but higher amplitude/frequency oscillations might work which need to be tested further as a future work. The pitching motion can modify the tip vortex dynamics. Figure 5.8 compares the wake structure of the rotating blade with a dynamic pitch for low wind speed case with the baseline. It can be observed that tip vortex is still generated but it has been deformed due to the blade pitching motion. However, since the pitch angle was small, flow did not separate and strong tip vortices are present (Fig. 5.8).

5.4 Conclusion

Large-eddy simulations of the full-scale wind turbine are performed using our sharp-interface immersed boundary framework. The simulation are carried out for wind speeds $U = 7m/s$ and $U = 15m/s$. Simulation mesh consists of 3 cuboid blocks that contain the background, wake, and blade. The results of simulations were validated against the experimental measurements by

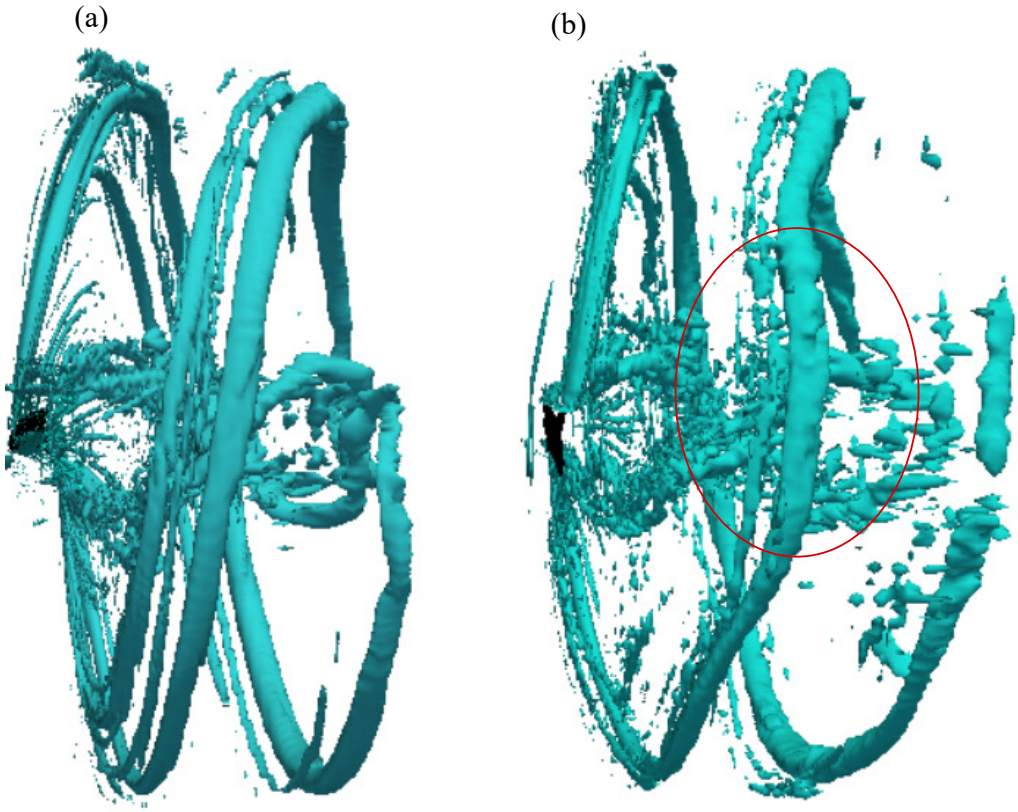

Figure 5.8: The countours of is-surface Q-criteria for blade at wind speed of $U = 7m/s$(a) baseline, (b) pitching.

comparing the mean torque and pressure coefficients, and a good agreement with the experiments was observed. The effect of low-amplitude sinusoidal dynamic pitch on the torque and flow was investigated. For both cases, the pitching did not change the mean torque but increased the torque fluctuations. Moreover, it was observed that the dynamic pitch can deform the tip vortex of the low-wind speed case.

5.5 Limitation and future work

In this study, a cuboid mesh was used that increased the simulation cost significantly compared to body-conformed and unstructured grids. Due to this limitation, only two wind speeds were tested where one pitching case was tested for each wind speed. For the future, simulation of wind

turbines with curvilinear grids which can capture the boundary layer more accurately with fewer computational cost can be performed. The other limitation was on the amplitude of pitch angle for high wind speed case. Due to the complexity of the flow, e.g., high velocity of the tip of the blade, the flow-solver become unstable at higher amplitude. Therefore, the effect of higher frequency and amplitude pitching can be tested later by fixing the instability issues as a future work.

6. TRAVELING WAVES IN TURBULENT COMPRESSIBLE FLOWS

The main application of flow control is in aeronautical flows to reduce flow separation and improve the aerodynamic performance of flying vehicles. Our previous studies on flow control with traveling waves (see section 4) were performed for incompressible flows, where Mach number (M) should be less than 0.2 for the comprehensibility of the air to be negligible. However, many flying vehicles such as commercial aircraft, UAVs, and miltary aircraft fly at high Mach numbers, ranging from $0.5 < M < 1.5$. At this high-velocity flight, flow surrounding the aircraft is compressible and the effectiveness of the traveling wave morphing for flow control needs to be restudied. Therefore, in this chapter, we study the effect of traveling waves on flow separation and the physics of compressible boundary layer. First, the effects of wavy surfaces on the turbulent boundary layer for both subsonic and supersonic flows are investigated. Afterwards, the effect of traveling waves is studied. This chapter is organized as follows: a brief introduction on turbulent flow in wavy compressible channel is provided in 6.1. The material and methods is presented in 6.2. Section 6.3 reports the results and discussion. Finally, the conclusion, limitation and future work are presented in 6.4.

6.1 Background

One of the main applications of wavy surface roughness is passive flow control. The surface roughness can accelerate the transition to turbulence and enhance the lift coefficient of wings [230]. The role of wavy roughness has been investigated for incompressible turbulent boundary layer comprehensively [231, 171, 170, 167]. For example, previous studies of incompressible turbulent wavy channel have demonstrated that the wave steepness, i.e., the ratio of wave amplitude to the wavelength, is an important factor on turbulent boundary layer physics [232, 231]. It has been observed that a wave steepness of 0.05 can separate the turbulent boundary layer of an incompressible flow within a Reynolds number of $180 < Re_\tau < 570$ [231, 171, 167]. Nevertheless, the effect of wave steepness on flow separation for compressible wavy turbulent channels has not

been investigated yet.

The fluid compression can modify the temperature and density near the wall of a flat channel with a negligible effect on turbulence statistics and mean velocities [181]. The effect of Mach number is more significant for wavy channels as the crest of the wave can compress the flow and create shock waves at supersonic Mach numbers. For example, the direct numerical simulation (DNS) study of Tyson and Sandham [11] for wavy channel at three different Mach numbers of of M = 0.3, 1.5, and 3 suggested strong alternation of mean and turbulence statistics due to the shock patterns associated with the sinusoidal wavy roughness at $M = 3.0$. Muppidi & Mahesh [233] found that counter-rotating vortices, generated by the roughness elements, break the shear layer and trigger boundary layer transition. Jouybari et al. [234] investigated the effect of 2D and 3D sinusoidal wavy roughness in a supersonic turbulent channel at M=1.5. They found strong modifications of mean and turbulence statistics by roughness geometries. They observed strong oblique shock waves by 2D surface waves at M =1.5, in contrast to the result of Tyson and Sandham [11] in which the strong shock waves were only observed at $M = 3.0$. This discrepancy in the literature indicates that the effect of compressibility and surface wavy roughness is not understood well for turbulent boundary layers.

The problem of the turbulent wavy channel becomes more complicated when the wavy wall channel undergoes deformations, similar to our study in section 4.1. In particular, when shock waves interact with the turbulent boundary layer. However, there are not many studies on controlling turbulent separated flows at supersonic Mach numbers due to the complexity and variety of shock wave boundary layer interaction (SWBLI) problems. In fact, the properties of SWBLIs depend on flow as well as geometric parameters, including Mach and Reynolds numbers, and the nature of the shock generator. Nevertheless, the effects that surface deformation has on SWLBI has been investigated recently by Shinde et al. [124]. They demonstrated that vertical surface oscillations can reduce the separated flow that is induced by SWBLI. However, to best of our knowledge, there is no study on the interaction of traveling wave deformations on compressible turbulent boundary layers. As mentioned above, at high M, the wavy wall might create weak

shocks, and the possible effect of wall deformation on physics is unknown.

In this study, first, the role of wave steepness on the mean and turbulence statistics of turbulent boundary layer is studied for a quasi-compressible ($M = 0.5$) and supersonic ($M = 1.5$) wavy channel by our compressible LES sharp-interface immersed boundary solver. Afterwards, we will investigate the role of traveling wave deformations on the instantaneous and mean flow.

6.2 Methods

The numerical method and validations have already been reported in §2. Here, the numerical setup is presented.

The computational setup is shown in Fig. 6.1a. Flow is in the frame $x_i = (x, y, z)$ where x, y, z are spanwise, vertical, and streamwise coordinates, respectively. Here, the characteristic length is the channel half width (H) and the characteristic velocity is the bulk velocity $U = \frac{1}{2\pi H \times 2H \times \pi H} \int u \; dxdydz$. The lower wall undergoes a streamwise traveling wave as shown in Fig. 6.1b. The lower wall motion is:

$$h = a \, sin(\frac{2\pi}{\lambda} z - Ct) \tag{6.1}$$

where h is the vertical location of the lower wall with respect to the flat wall, a is the amplitude of the wave, λ is the wavelength, which is $\lambda = \frac{\pi}{2} H$, and $C = f\lambda$ is the wave speed, where f is the frequency of the wave. Here, $C = 0$ leads to a wavy channel and positive wave speed ($C > 0$) means a streamwise traveling wave. In this study, the spatial averaging is performed along the homogeneous direction (x), and mean spanwise-averaged terms are denoted by <>.

The simulations are performed with a cuboid grid, which its details are presented in Table 6.1. The domain size is same as the validation test case in §3, i.e., a cube of $\pi H \times 2H \times 2\pi H$. The grid mesh is shown in Fig. 6.1a. The grid mesh is evenly spaced along x and z directions. In the y direction, the grid is clustered towards both walls with a hyperbolic function as shown in Fig. 6.1b. The grid spacing is kept constant in the vicinity of the wave, i.e., at $-0.1 < y < 0.1$ the grid spacing is ($\delta y = 0.0035H$) as expressed in Table 4.1 and Fig. 6.1b. The wall normal

Table 6.1: The details of computational setup.

grid	N_x	N_y	N_z	Δx_{min}	Δy_{min}	Δz_{min}
1	120	112	240	0.0261	0.0035	0.0261

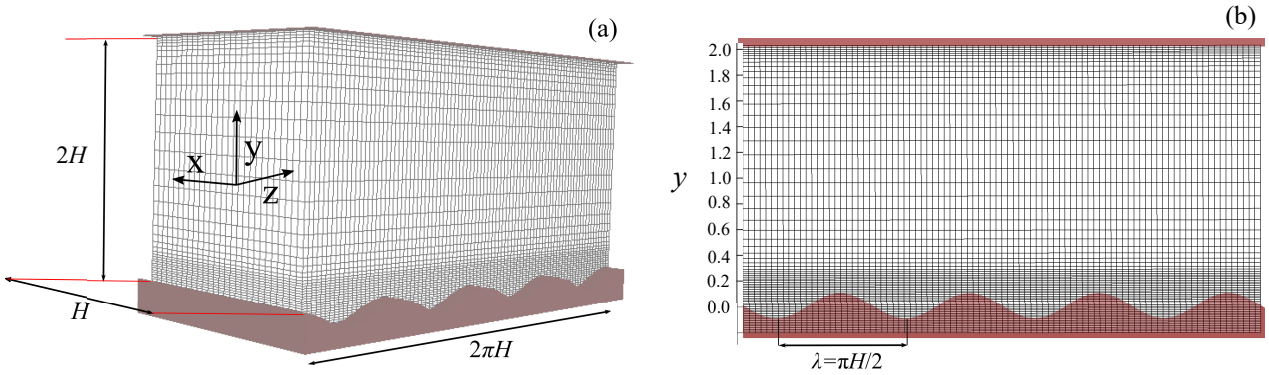

Figure 6.1: Flow simulation set-up: (a) 3D (b) 2D view of the simulation grid and the wavy channel wall. The fluid is discretized with a cartesian grid whose resolution increases near the walls. The walls of the channel are discretized with triangular elements and placed as an immersed body onto the background mesh.

resolution ($\delta y = 0.0035H$) is equivalent to $y^+ = u_\tau \delta y/\mu = 0.8$ which is enough for reconstructing the velocity of the IB nodes with a linear interpolation [165]. The non-dimensional time step ($\delta t^* = \delta t \bar{u}/H$) is set to $\delta t^* = 0.002$ for the wavy case and for the traveling wave case it is $\delta t^* = 0.001$. The LES simulations are validated for a flat channel in §3.

The physical parameters, including wave amplitude, the Mach number (M), the Prandtl number (Pr), the ratio of specific heats (γ), the viscosity exponent (n) where $\mu \propto T^n$ are presented in Table 6.2. The Reynolds number based on the bulk velocity and channel half width is $Re = \rho U H/\mu = 3000$. The simulations are performed for a subsonic ($M = 0.5$) and a supersonic Mach number ($M = 1.5$). Cases 1 and 2 in Table 6.2 are for the stationary wavy channel, and cases 3 and 4 represent the traveling wave simulations. The traveling wave simulations are performed for only one nondimensional frequency $f^* = fH/U = 0.5$.

The boundary condition along the streamwise and spanwise direction is periodic, and the walls

Table 6.2: Physical parameters of the simulations.

case	a/H	fH/U	M	Pr	γ	μ
1	0.05	0.0	0.5	0.7	1.4	$T^{0.7}$
2	0.05	0.0	1.5	0.7	1.4	$T^{0.7}$
3	0.05	0.5	0.5	0.7	1.4	$T^{0.7}$
4	0.05	0.5	1.5	0.7	1.4	$T^{0.7}$

are no-slip adiabatic $\partial T/\partial n = 0$, where n is the surface normal and $T = p/(R\rho)$ where R is the ideal gas constant. Here, the adiabatic boundary condition is applied by imposing a zero pressure gradient along the wall normal. Afterwards, ρ is updated from the adiabatic boundary condition (see §3.2.2 for more details). The simulations are initialized with nondimensional values $u_z/U = 1.0$, $\rho/\bar{\rho} = 1.0$ and $p = \frac{1}{2}\gamma M^2(\bar{\rho}U^2)$, where $\bar{\rho}$ is the bulk density.

6.3 Results and discussion

The mean flow for the supersonic channel is presented in Fig. 6.3b. The results of wavy cases are time-averaged for $150H/U$, and for traveling wave channel are averaged for 5 cycles.

The contours of instantaneous streamwise velocity u_z are presented in Fig. 6.2. It can be observed that there is a reverse flow in the vicinity of the troughs of the wave for both wavy stationary cases (case 1 and case 2). However, by applying the traveling waves the reverse flow is removed by increasing the fluid momentum in the vicinity of the wave. The role of the wavy surface and the traveling wave can be observed more clearly by visualizing the mean flow. The profile of the mean streamwise velocity $\bar{u}_z$ is presented in 6.3. It can be observed that flow separates from the downhill of the wave for both stationary cases (case 1 and 2) and reattaches near the uphill. A comparison between the mean flow profile of stationary subsonic and supersonic channels reveals that the reverse flow is stronger in the vicinity of the wave trough for the supersonic case. Nevertheless, when a traveling wave is applied on the lower wall of the channel, the flow separation is removed for both Mach numbers, which implies that traveling waves have a similar effect on mean velocities regardless of the fluid compression, i.e., increase the fluid momentum in the vicinity of the wave and reduce flow separation. Nevertheless, the effect of wavy roughness and traveling

waves on other flow parameters such as pressure and temperature will be discussed below.

The wavy surface and traveling waves can have significant effects on flow physics for the supersonic case due to higher fluid compression and shock generation. Figure 6.4 presents the effect of wavy roughness and traveling waves on shock waves for the supersonic cases. The shock waves are visualized with the contours of the pressure gradient ($|\nabla p|$). It can be observed that the wavy surface imparts strong shock patterns that go all from the peak of the wave to the upper surface and reflect from the upper wall to the domain. These shock patterns exhibit the same wavelength of wavy surface and impact the flow properties in the entire channel. However, these shock patterns become weaker when the traveling waves are applied, in particular near the wavy surface. Previous studies on wavy supersonic channels [155] explained that the shock waves are generated due to fluid compression on the peaks of the wave. When the wall undergoes a traveling wave, the peak and trough of the wave move along the streamwise direction with wave speed ($C = \lambda f$), which means that flow has a lower relative speed and consequently, a lower Mach number with respect to the wave. In fact, the lower surface has a wave speed of ($C = \lambda f = \pi/4$). Therefore, the relative velocity of the incoming flow is $1 - \pi/4 \approx 0.22U$ which corresponds to a Mach number of $M = 0.33$. Because the relative velocity of the wave to the flow becomes subsonic, the shock waves that have been generated in a wavy channel (Fig. 6.4a) are disappeared (Fig. 6.4b).

The profile of spanwise-averaged mean and phase-averaged temperature ($< T >$) and density ($< \rho >$) at peak and trough of the wave of the supersonic channel are plotted along the channel width (y/H) in Fig. 6.5. The shock waves in the wavy supersonic channel have created a significant variation in density and temperature along the streamwise direction (Fig 6.5). For example, the mean temperature is about 0.3 higher along the trough of the wave near the wavy wall, and this high temperature difference is observed up to the top wall. In contrast, when the traveling waves are applied, the profiles of $< \rho >$ and T at the peak and trough of the wave become similar as the shock is disappeared.

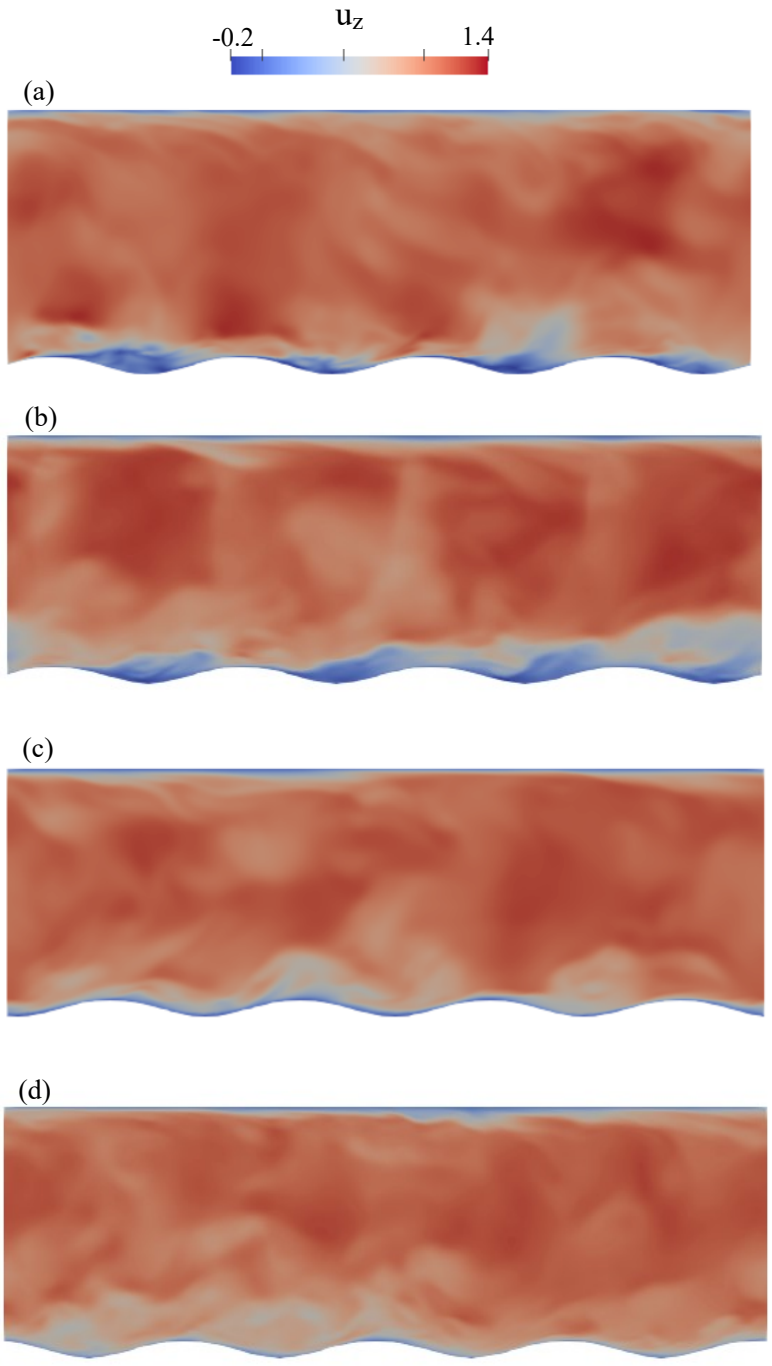

Figure 6.2: The contour of instantaneous streamwise velocity for (a) case 1 (wavy subsonic channel), (b) case 2 (wavy supersonic channel), (c) case 3 (traveling wave subsonic channel), and (d) case 4 (traveling wave supersonic channel).

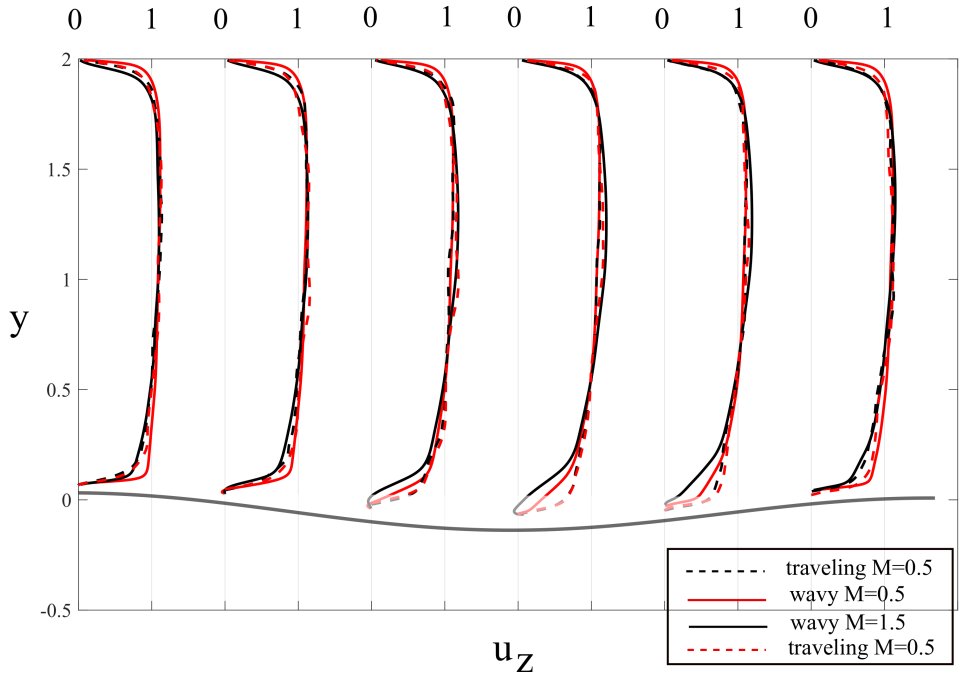

Figure 6.3: The profile of mean streamwise velocity at 6 location along the wave.

6.4 Conclusion, limitation, and future work

The results of the wavy stationary channel reveal the generation of reverse flow in the vicinity of the trough of the waves for both supersonic and subsonic flows, similar to the incompressible simulations. However, the reverse flow is slightly higher near the trough of the wave when the flow is supersonic. Moreover, shock waves were observed near the lower and upper walls of the supersonic channel due to fluid compression near the peaks of the wave. In fact, the higher reverse flow in the vicinity of the wave of the supersonic case can be due to the generation of these shock waves. Nevertheless, when the lower wall undergoes a backward traveling wave that propagates along the mainstream with a wave speed $C = \frac{\pi}{4}U$ the reverse flow is disappeared for both cases, and more importantly, the shock waves of the supersonic case were disappeared. One of the limitations of this work is the low range of test cases, e.g., the simulations have been performed for a small number of amplitudes and wave speeds. Moreover, there are not many studies in the literature on wavy supersonic channels, even, there is a discrepancy in literature regarding the wavy

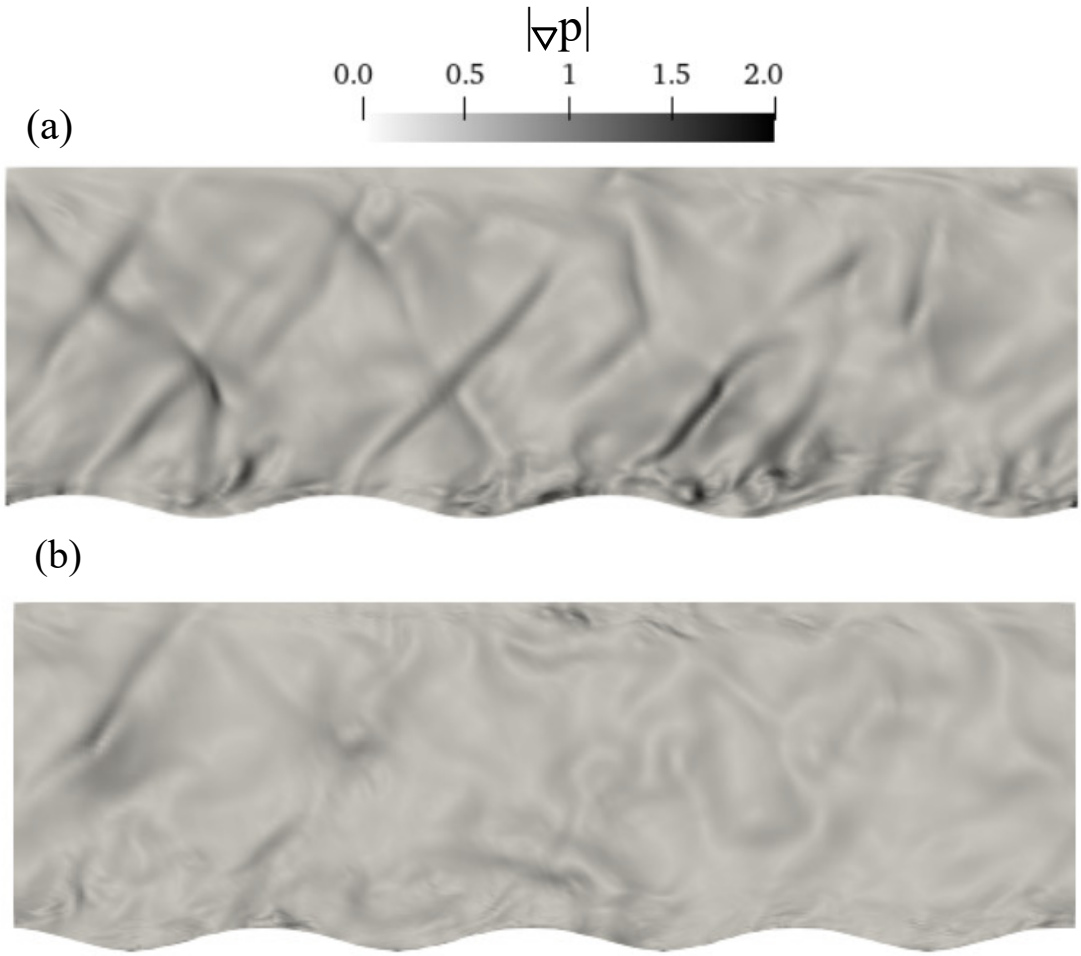

[!hbt]

Figure 6.4: The shock visualization with instantaneous pressure gradient for the supersonic channel, (a) case 2 and (b) case 4.

channel simulations which makes the validation and discussion more challenging. To overcome this problem, simulations with finer grids and larger domain size should be performed as a future work to ensure that the domain size and grid resolution is sufficient.

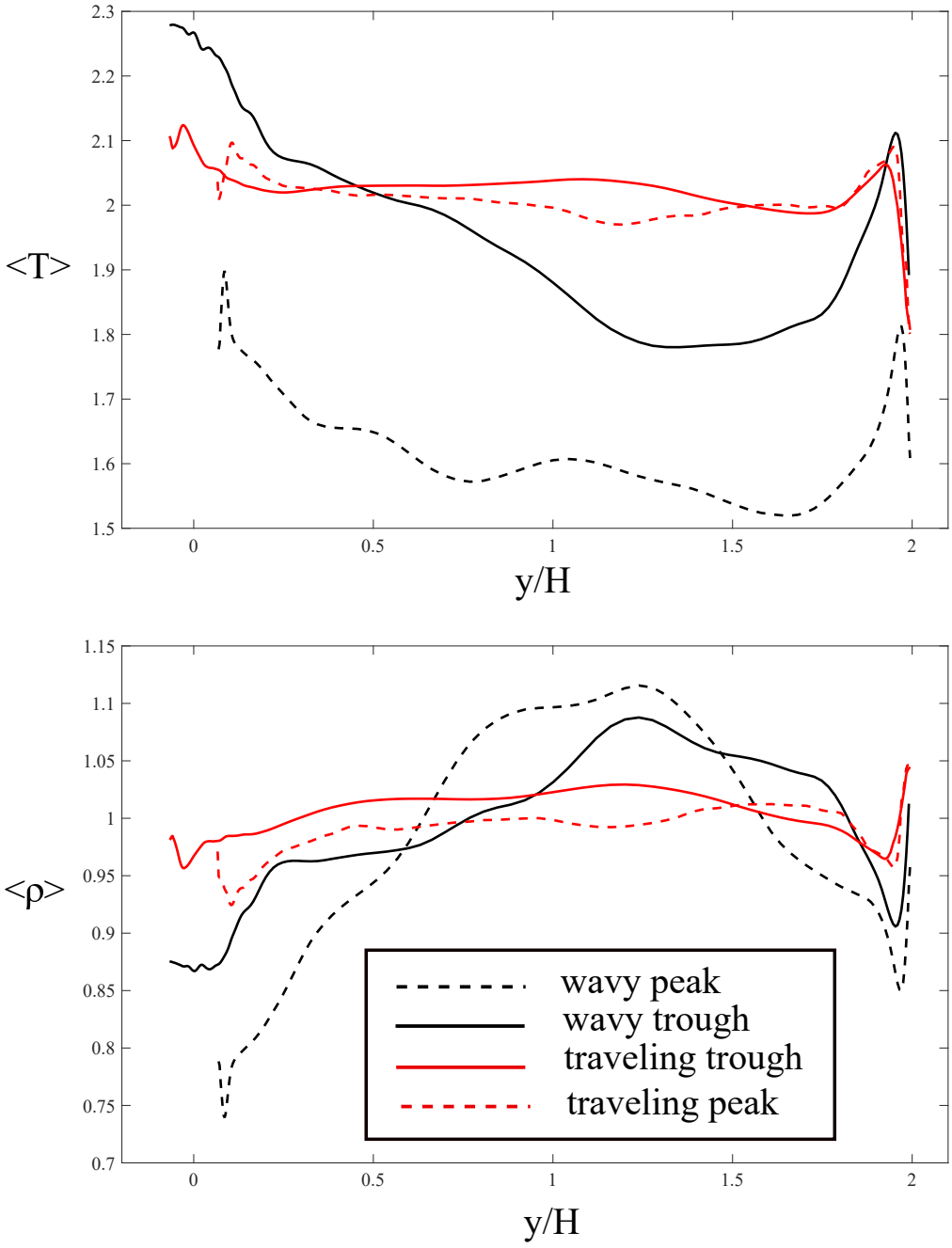

Figure 6.5: The plots of mean and phase-averaged (a) temperature and (b) density, at peak and trough of the wave for cases 2 and 4.

7. SUMMARY AND OUTLOOK

Flow separation is associated with aerodynamic loss. To solve this problem, several techniques have been used to remove flow separation, referred as flow control, in engineering applications. Flow control strategies can be classified based on the mechanism of reattachment into: (i) direct injection of momentum to the boundary layer, e.g., steady blowing or (ii) indirect transfer of momentum by periodic excitations which trigger flow instabilities that form large coherent structures (LCS) to entrain high momentum fluid into the near-wall flow. Knowing that traveling waves can directly inject momentum to the boundary layer and also can trigger boundary layer instabilities similar to other surface morphing actuations, the feasibility of controlling flow separation with backward traveling waves was studied for a turbulent channel, inclined plate, and a NACA0018 airfoil at stall. For the first time, it has been shown that traveling waves can control massively separated flows over bluff bodies such as inclined plates and airfoils. The other major finding of this work was uncovering that traveling wave actuations are more effective for flow control than other types of actuation, e.g., standing wave and pitching motion. It was shown that the critical wave speed, i.e., the wave speed at which flow is attached and TKE is minimized can be less than one and it changes with the wave steepness. The simulations of traveling waves for a NACA0018 airfoil at $AOA = 15^o$ showed that surface morphing in the form of backward traveling waves can suppress the static stall and delay separation. It was observed that a low amplitude traveling wave ($a = 0.002L$, L : chord length) with reduced frequencies $fL/U = 4.0$ and $fL/U = 8.0$, and $\lambda = 0.2L$ can suppress the stall and increases the lift coefficient by about 34% and reduce the drag by 67% compared to the baseline (section 4).

The role of different parameters of traveling waves on the flow separation was studied. It has been shown for the first time that in contrast to common belief, wave speed is not the only critical parameter for controlling flow separation. In fact, both wavelength and frequency influence the flow separation individually. These observation were further studied by investigating the flow control mechanisms of traveling waves and analyzing them with EBT (in §4.2.3.4). The travel-

ing wave deformations can control flow separation by directly increasing the momentum of the fluid surrounding the wave and triggering the boundary layer instabilities. The direct momentum enhancement mechanism occurs by accelerating the fluid particles along the axial direction (added mass mechanism) which can creates a thrust force that was observed as a jet flow in the wake of inclined plate and near the trough of the wave. Based on EBT, the thrust force (C_T), which tends to attach the flow, scales with O$((a^*_{max})(f^* - 1/\lambda^*)(f^* + 1/\lambda^*))$ and the lateral velocity of a fluid particle (u_Y) over an undulating plate, which tends to detach the flow, scales with $O(a^*_{max}(f^* - 1/\lambda^*))$—see appendix A for details. Therefore, just increasing the wave speed to enhance the thrust $C = f^*\lambda^*$ does not necessarily reattach the flow because the lateral velocity will also increase.

The surface morphing was further applied in more complex flows. Low-amplitude pitching surface morphing were applied on the blade of a NREL PHASE VI wind turbine to increase the torque. To validate the framework, the simulations of a full-scale NREL PHASE VI wind turbine at wind speeds $U = 7m/s$ and $U = 15m/s$ were performed using overset-CURVIB. To the best of our knowledge, it was the first wind turbine simulation with a cuboid mesh and immersed boundary method. The validation performed by comparing the mean torque and pressure coefficients, and a good agreement with the experiments was observed. The pitching blade simulations show that the tested dynamic pitch cannot enhance the aerodynamic performance but it can modify the turbine's wake (section 5).

The effect of traveling waves on flow separation in wavy channels was investigated for compressible flows by developing a dynamic sub-grid stress LES for the CURVIB framework. The inviscid fluxes of compressible flow equations in curvilinear coordinates are discretized with a hybrid discretization comprising a fourth-order central scheme and a third-order weighted essentially non-oscillatory (WENO) scheme. The framework is validated extensively by performing simulations for isotropic decay, subsonic and supersonic turbulent channel, and shock diffraction by a cylinder (section 2). The results of a wavy stationary compressible channel reveal the generation of reverse flow in the vicinity of the trough of the waves for both supersonic and subsonic flows,

similar to the incompressible simulations. However, the reverse flow is slightly higher near the trough of the wave when the flow is supersonic. Moreover, shock waves were observed near the lower and upper walls of the supersonic channel due to fluid compression near the peaks of the wave. Nevertheless, when the lower wall undergoes a backward traveling wave that propagates toward the downstream with a wave speed $C = \frac{\pi}{4}U$, (U: bulk channel velocity) the reverse flow is disappeared for both cases, and more importantly, the shock waves of the supersonic case were disappeared (section 6).

7.1 Limitations and Future work

One of the limitations of this work is the number of test cases due to computational cost. Therefore, we could only investigate a low range of frequencies and amplitude. Because of the same reason, the effect of Reynolds number, and AOA has not been studied yet. Investigating the role of a higher range of amplitudes, frequencies, and AOA, and higher Reynolds number can be a part of future work. Moreover, we found that traveling wave actuations reduce flow separation by two mechanisms, (i) increasing the axial momentum induced to the flow and (ii) the triggering of instabilities to increase mixing. Nevertheless, the impact of each of these mechanisms was not studied here. Therefore, understanding the effect of each of these two terms, i.e., axial momentum induced to the flow versus triggering the instabilities, on the flow separation can be an interesting topic for future studies (section 4).

The simulations of the wind turbine were performed by a cuboid mesh, which increased the simulation cost significantly compared to body-conformed and unstructured grids. Due to this limitation, only two wind speeds were tested where one pitching case was tested for each wind speed. For the future, simulation of wind turbines with curvilinear grids which can capture the boundary layer more accurately with fewer computational cost can be performed. The other limitation was on the amplitude of pitch angle for the high wind speed cases. Due to the complexity of the flow, e.g., high velocity of the tip of the blade, the flow-solver becomes unstable at a higher amplitude. Therefore, the effect of higher frequency and amplitude pitching can be tested later by fixing the instability issues as future work.

One of the main limitations of this work is the low range of test cases for compressible simulations, e.g., the simulations have been performed for a small number of amplitude and wave speeds. Moreover, there are not many studies in the literature on wavy supersonic channels and the two studies in the literature regarding the wavy channel simulations [11, 234] are not in full agreement which makes the validation and discussion more challenging. To overcome this problem, more simulations and/or experiments are needed. The other important future work is performing more validation studies for shock wave turbulent boundary layer (SWBLI) problems to ensure that our framework can handle these interactions properly, in particular, in the vicinity of the immersed boundaries. To this aim, the WENO scheme might need to have further modifications. In this study, a third-order WENO is used near discontinuities. In the WENO implementation, the inviscid fluxes are computed directly from the reconstructed variables, i.e., pressure, velocity, and density that are computed using WENO scheme. This WENO implementation can add diffusion near the discontinuities, in particular at high Mach numbers. To solve this problem, the following three steps need to be performed: (I) the inviscid fluxes should be calculated directly from the variables, (II) the computed fluxes will be modified by a flux limiter, and (III) the final inviscid fluxes at half points will be approximated by the WENO scheme. Moreover, a fifth-order WENO can be deployed to reduce the numerical dissipation.

REFERENCES

[1] I. Borazjani, L. Ge, and F. Sotiropoulos, "Curvilinear immersed boundary method for simulating fluid structure interaction with complex 3d rigid bodies," *Journal of Computational physics*, vol. 227, no. 16, pp. 7587–7620, 2008.

[2] L. Ge and F. Sotiropoulos, "A numerical method for solving the 3d unsteady incompressible navier–stokes equations in curvilinear domains with complex immersed boundaries," *Journal of Computational Physics*, vol. 225, no. 2, pp. 1782–1809, 2007.

[3] A. Bryson and R. Gross, "Diffraction of strong shocks by cones, cylinders, and spheres," *Journal of Fluid Mechanics*, vol. 10, no. 1, pp. 1–16, 1961.

[4] L. Shen, X. Zhang, D. K. P. Yue, and M. S. Triantafyllou, "Turbulent flow over a flexible wall undergoing a streamwise travelling wave motion," *Journal of Fluid Mechanics*, vol. 484, pp. 197–221, jun 2003.

[5] S. Aubrun, J. McNally, F. Alvi, and A. Kourta, "Separation flow control on a generic ground vehicle using steady microjet arrays," *Experiments in Fluids*, vol. 51, pp. 1177–1187, jun 2011.

[6] J. Donovan, L. Kral, and A. Cary, "Active flow control applied to an airfoil," in *36th AIAA Aerospace Sciences Meeting and Exhibit*, American Institute of Aeronautics and Astronautics, jan 1998.

[7] G. Jones, M. Santer, M. Debiasi, and G. Papadakis, "Control of flow separation around an airfoil at low reynolds numbers using periodic surface morphing," *Journal of Fluids and Structures*, vol. 76, pp. 536–557, 2018.

[8] A. Seifert, S. Eliahu, D. Greenblatt, and I. Wygnanski, "Use of piezoelectric actuators for airfoil separation control," *AIAA Journal*, vol. 36, pp. 1535–1537, aug 1998.

[9] L. N. Cattafesta and M. Sheplak, "Actuators for active flow control," *Annual Review of Fluid Mechanics*, vol. 43, pp. 247–272, jan 2011.

[10] A. Olivett, P. Corrao, and M. A. Karami, "Flow control and separation delay in morphing wing aircraft using traveling wave actuation," *Smart Materials and Structures*, vol. 30, no. 2, p. 025028, 2021.

[11] C. Tyson and N. Sandham, "Numerical simulation of fully-developed compressible flows over wavy surfaces," *International journal of heat and fluid flow*, vol. 41, pp. 2–15, 2013.

[12] I. W. Ekoto, R. D. Bowersox, T. Beutner, and L. Goss, "Supersonic boundary layers with periodic surface roughness," *AIAA journal*, vol. 46, no. 2, pp. 486–497, 2008.

[13] A. Gopalarathnam, B. A. Broughton, B. D. McGranahan, and M. S. Selig, "Design of low reynolds number airfoils with trips," *Journal of aircraft*, vol. 40, no. 4, pp. 768–775, 2003.

[14] J. C. Lin, "Review of research on low-profile vortex generators to control boundary-layer separation," *Progress in Aerospace Sciences*, vol. 38, no. 4-5, pp. 389–420, 2002.

[15] A. Abbas, J. De Vicente, and E. Valero, "Aerodynamic technologies to improve aircraft performance," *Aerospace Science and Technology*, vol. 28, no. 1, pp. 100–132, 2013.

[16] P. K. Chang, *Separation of flow*. Elsevier, 2014.

[17] D. Greenblatt and I. J. Wygnanski, "The control of flow separation by periodic excitation," *Progress in aerospace Sciences*, vol. 36, no. 7, pp. 487–545, 2000.

[18] A. Seifert, A. Darabi, and I. Wyganski, "Delay of airfoil stall by periodic excitation," *Journal of Aircraft*, vol. 33, pp. 691–698, jul 1996.

[19] J.-Z. Wu, X.-Y. Lu, A. G. Denny, M. Fan, and J.-M. Wu, "Post-stall flow control on an airfoil by local unsteady forcing," *Journal of Fluid Mechanics*, vol. 371, pp. 21–58, sep 1998.

[20] A. Glezer and M. Amitay, "Synthetic jets," *Annual review of fluid mechanics*, vol. 34, no. 1, pp. 503–529, 2002.

[21] M. Amitay, D. R. Smith, V. Kibens, D. E. Parekh, and A. Glezer, "Aerodynamic flow control over an unconventional airfoil using synthetic jet actuators," *AIAA Journal*, vol. 39, pp. 361–370, mar 2001.

[22] N. A. Buchmann, C. Atkinson, and J. Soria, "Influence of ZNMF jet flow control on the spatio-temporal flow structure over a NACA-0015 airfoil," *Experiments in Fluids*, vol. 54, feb 2013.

[23] G. Jones, M. Santer, M. Debiasi, and G. Papadakis, "Control of flow separation around an airfoil at low reynolds numbers using periodic surface morphing," *Journal of Fluids and Structures*, vol. 76, pp. 536–557, jan 2018.

[24] Y. W. Park, S.-G. Lee, D.-H. Lee, and S. Hong, "Stall control with local surface buzzing on a NACA 0012 airfoil," *AIAA Journal*, vol. 39, pp. 1400–1402, jul 2001.

[25] G. Jodin, V. Motta, J. Scheller, E. Duhayon, C. Döll, J. Rouchon, and M. Braza, "Dynamics of a hybrid morphing wing with active open loop vibrating trailing edge by time-resolved PIV and force measures," *Journal of Fluids and Structures*, vol. 74, pp. 263–290, oct 2017.

[26] Y. Katz, B. Nishri, and I. Wygnanski, "The delay of turbulent boundary layer separation by oscillatory active control," *Physics of Fluids A: Fluid Dynamics*, vol. 1, pp. 179–181, feb 1989.

[27] Z. Lyu and J. R. R. A. Martins, "Aerodynamic shape optimization of an adaptive morphing trailing-edge wing," *Journal of Aircraft*, vol. 52, pp. 1951–1970, nov 2015.

[28] G. Jones, M. Santer, and G. Papadakis, "Control of low reynolds number flow around an airfoil using periodic surface morphing: A numerical study," *Journal of Fluids and Structures*, vol. 76, pp. 95–115, jan 2018.

[29] S. Kang, "An improved near-wall modeling for large-eddy simulation using immersed boundary methods," *International Journal for Numerical Methods in Fluids*, vol. 78, pp. 76–88, feb 2015.

[30] D. You, M. Wang, and P. Moin, "Large-eddy simulation of flow over a wall-mounted hump with separation control," *AIAA Journal*, vol. 44, pp. 2571–2577, nov 2006.

[31] K. Puri, M. Laufer, H. Müller-Vahl, D. Greenblatt, and S. H. Frankel, "Computations of active flow control via steady blowing over a NACA-0018 airfoil: Implicit LES and RANS validated against experimental data," in *2018 AIAA Aerospace Sciences Meeting*, American Institute of Aeronautics and Astronautics, jan 2018.

[32] D. P. Rizzetta, M. R. Visbal, and P. E. Morgan, "A high-order compact finite-difference scheme for large-eddy simulation of active flow control," *Progress in Aerospace Sciences*, vol. 44, no. 6, pp. 397–426, 2008.

[33] A. Krzysiak and J. Narkiewicz, "Aerodynamic loads on airfoil with trailing-edge flap pitching with different frequencies," *Journal of Aircraft*, vol. 43, pp. 407–418, mar 2006.

[34] C. Abdessemed, Y. Yao, A. Bouferrouk, and P. Narayan, "Aerodynamic analysis of a harmonically morphing flap using a hybrid turbulence model and dynamic meshing," in *2018 Applied Aerodynamics Conference*, American Institute of Aeronautics and Astronautics, jun 2018.

[35] T. Lee and P. Gerontakos, "Unsteady airfoil with dynamic leading- and trailing-edge flaps," *Journal of Aircraft*, vol. 46, pp. 1076–1081, may 2009.

[36] D. Munday and J. Jacob, "Active control of separation on a wing with oscillating camber," *Journal of Aircraft*, vol. 39, pp. 187–189, jan 2002.

[37] G. Di, Z. Wu, and D. Huang, "The research on active flow control method with vibration diaphragm on a NACA0012 airfoil at different stalled angles of attack," *Aerospace Science and Technology*, vol. 69, pp. 76–86, oct 2017.

[38] P. R. Ashill, J. L. Fulker, and K. C. Hackett, "A review of recent developments in flow control," *The Aeronautical Journal*, vol. 109, pp. 205–232, may 2005.

[39] D. Munday, J. Jacob, T. Hauser, and G. Huang, "Experimental and numerical investigation ofAerodynamic flow control using oscillating adaptive surfaces," in *1st Flow Control Conference*, American Institute of Aeronautics and Astronautics, jun 2002.

[40] M. J. Lighthill, "Note on the swimming of slender fish," *Journal of Fluid Mechanics*, vol. 9, no. 2, p. 305–317, 1960.

[41] A. Akbarzadeh and B. Iman, "Video: Controlling flow separation using traveling wave actuation," in *72th Annual Meeting of the APS Division of Fluid Dynamics - Gallery of Fluid Motion*, American Physical Society, nov 2019.

[42] M. S. Triantafyllou, G. Triantafyllou, and D. Yue, "Hydrodynamics of fishlike swimming," *Annual review of fluid mechanics*, vol. 32, no. 1, pp. 33–53, 2000.

[43] M. H. Dickinson and K. G. Gotz, "Unsteady aerodynamic performance of model wings at low reynolds numbers," *Journal of Experimental Biology*, vol. 174, no. 1, pp. 45–64, 1993.

[44] D. Lentink and H. M. Dickinson, "Rotational accelerations stabilize leading edge vortices on revolving fly wings," *J. Expl Bio.*, vol. 212, pp. 2705–2719, 2009.

[45] R. Bottom II, I. Borazjani, E. Blevins, and G. Lauder, "Hydrodynamics of swimming in stingrays: numerical simulations and the role of the leading-edge vortex," *Journal of Fluid Mechanics*, vol. 788, pp. 407–443, 2016.

[46] I. Borazjani and M. Daghooghi, "The fish tail motion forms an attached leading edge vortex," *Proceedings of the Royal Society B*, vol. 280, p. 20122071, 2013.

[47] D. Lentink and M. H. Dickinson, "Biofluiddynamic scaling of flapping, spinning and translating fins and wings," *Journal of Experimental Biology*, vol. 212, no. 16, pp. 2691–2704, 2009.

[48] I. Borazjani and F. Sotiropoulos, "Numerical investigation of the hydrodynamics of carangiform swimming in the transitional and inertial flow regimes," *Journal of Experimental Biology*, vol. 211, no. 10, pp. 1541–1558, 2008.

[49] U. E. Ogunka, M. Daghooghi, A. M. Akbarzadeh, and I. Borazjani, "The ground effect in anguilliform swimming," *Biomimetics*, vol. 5, p. 9, mar 2020.

[50] T. Y.-T. Wu, "Swimming of a waving plate," *Journal of Fluid Mechanics*, vol. 10, no. 3, pp. 321–344, 1961.

[51] S. Taneda, "Visual study of unsteady separated flows around bodies," *Progress in Aerospace Sciences*, vol. 17, pp. 287–348, 1976.

[52] C.-j. Wu, L. Wang, and J. Wu, "Suppression of the von kármán vortex street behind a circular cylinder by a travelling wave generated by a flexible surface," *Journal of Fluid Mechanics*, vol. 574, p. 365–391, 2007.

[53] P. F. Musgrave and P. A. Tarazaga, "Turbulent boundary layer over a piezoelectrically excited traveling wave surface," in *AIAA Scitech 2019 Forum*, American Institute of Aeronautics and Astronautics, jan 2019.

[54] M. Lighthill, "Hydromechanics of aquatic animal propulsion," *Annual review of fluid mechanics*, vol. 1, no. 1, pp. 413–446, 1969.

[55] L. E. Kinsler, A. R. Frey, H. B. Coppens, J. V. Sanders, and H. Saunders, "Fundamentals of acoustics (3rd ed.)," *Journal of Vibration and Acoustics*, vol. 105, pp. 269–270, jul 1983.

[56] R. Mittal and G. Iaccarino, "Immersed boundary methods," *Annual Review of Fluid Mechanics*, vol. 37, pp. 239–261, 2005.

[57] M. Lesoinne and C. Farhat, "Geometric conservation laws for flow problems with moving boundaries and deformable meshes, and their impact on aeroelastic computations," *Computer methods in applied mechanics and engineering*, vol. 134, no. 1, pp. 71–90, 1996.

[58] A. Masud and T. J. Hughes, "A space-time galerkin/least-squares finite element formulation of the navier-stokes equations for moving domain problems," *Computer Methods in Applied Mechanics and Engineering*, vol. 146, no. 1, pp. 91–126, 1997.

[59] P. Thomas and C. Lombard, "Geometric conservation law and its application to flow computations on moving grids," *AIAA journal*, vol. 17, no. 10, pp. 1030–1037, 1979.

[60] C. Hirt, A. Amsden, and J. Cook, "An arbitrary lagrangian-eulerian computing method for all flow speeds," *Journal of Computational Physics*, vol. 14, pp. 227–253, mar 1974.

[61] J. Donea, S. Giuliani, and J. Halleux, "An arbitrary lagrangian-eulerian finite element method for transient dynamic fluid-structure interactions," *Computer Methods in Applied Mechanics and Engineering*, vol. 33, pp. 689–723, sep 1982.

[62] J. Waltz, N. Morgan, T. Canfield, M. Charest, L. Risinger, and J. Wohlbier, "A three-dimensional finite element arbitrary lagrangian–eulerian method for shock hydrodynamics on unstructured grids," *Computers & Fluids*, vol. 92, pp. 172–187, mar 2014.

[63] O. Hassan, K. Sørensen, K. Morgan, and N. Weatherill, "A method for time accurate turbulent compressible fluid flow simulation with moving boundary components employing local remeshing," *International journal for numerical methods in fluids*, vol. 53, no. 8, pp. 1243–1266, 2007.

[64] T. A. Helgedagsrud, Y. Bazilevs, A. Korobenko, K. M. Mathisen, and O. A. Øiseth, "Using ale-vms to compute aerodynamic derivatives of bridge sections," *Computers & Fluids*, 2018.

[65] V. K. Lakshminarayan and C. Farhat, "Nonlinear aeroelastic analysis of highly flexible flapping wings using an ale formulation of embedded boundary method," in *52nd Aerospace Sciences Meeting*, p. 0221, 2014.

[66] C. Farhat and V. K. Lakshminarayan, "An ALE formulation of embedded boundary methods for tracking boundary layers in turbulent fluid–structure interaction problems," *Journal of Computational Physics*, vol. 263, pp. 53–70, apr 2014.

[67] C. Farhat, "Cfd-based nonlinear computational aeroelasticity," *Encyclopedia of Computational Mechanics Second Edition*, pp. 1–21, 2017.

[68] D. M. Espino, D. E. Shepherd, and D. W. Hukins, "Evaluation of a transient, simultaneous, arbitrary lagrange–euler based multi-physics method for simulating the mitral heart valve,"

Computer Methods in Biomechanics and Biomedical Engineering, vol. 17, pp. 450–458, may 2012.

[69] S. S. Abbas, M. S. Nasif, and R. Al-Waked, "State-of-the-art numerical fluid–structure interaction methods for aortic and mitral heart valves simulations: A review," *SIMULATION*, p. 00375497211023573, 2021.

[70] S. S. Abbas, M. S. Nasif, R. Al-Waked, and M. A. Meor Said, "Numerical investigation on the effect of bileaflet mechanical heart valve's implantation tilting angle and aortic root geometry on intermittent regurgitation and platelet activation," *Artificial organs*, vol. 44, no. 2, pp. E20–E39, 2020.

[71] S. S. Abbas, M. S. Nasif, R. Al-Waked, and M. A. M. Said, "Numerical investigation on the effect of bileaflet mechanical heart valve's implantation tilting angle and aortic root geometry on intermittent regurgitation and platelet activation," *Artificial Organs*, vol. 44, aug 2019.

[72] A. Abdehkakha, A. L. Hammond, T. R. Patel, A. H. Siddiqui, G. Dargush, and H. Meng, "Cerebral aneurysm flow diverter modeled as a thin inhomogeneous porous medium in hemodynamic simulations," *arXiv preprint arXiv:2106.05994*, 2021.

[73] S. Ragani and A. Bahrami, "Numerical investigation of a copper—water nanofluid flowing in a parallel plate channel," *Heat Transfer Research*, vol. 50, no. 7, 2019.

[74] R. J. Damiano, V. M. Tutino, S. R. Lamooki, N. Paliwal, G. F. Dargush, J. M. Davies, A. H. Siddiqui, and H. Meng, "Improving accuracy for finite element modeling of endovascular coiling of intracranial aneurysm," *PloS one*, vol. 14, no. 12, p. e0226421, 2019.

[75] R. Ghias, R. Mittal, and H. Dong, "A sharp interface immersed boundary method for compressible viscous flows," *Journal of Computational Physics*, vol. 225, no. 1, pp. 528–553, 2007.

[76] M. D. de Tullio, P. De Palma, G. Iaccarino, G. Pascazio, and M. Napolitano, "An immersed boundary method for compressible flows using local grid refinement," *Journal of Computational Physics*, vol. 225, no. 2, pp. 2098–2117, 2007.

[77] A. Piquet, O. Roussel, and A. Hadjadj, "A comparative study of brinkman penalization and direct-forcing immersed boundary methods for compressible viscous flows," *Computers & Fluids*, vol. 136, pp. 272–284, 2016.

[78] B. Muralidharan and S. Menon, "A high-order adaptive cartesian cut-cell method for simulation of compressible viscous flow over immersed bodies," *Journal of Computational Physics*, vol. 321, pp. 342–368, 2016.

[79] L. Schneiders, D. Hartmann, M. Meinke, and W. Schröder, "An accurate moving boundary formulation in cut-cell methods," *Journal of Computational Physics*, vol. 235, pp. 786–809, 2013. simulated oscillating sphere.

[80] M. Uhlmann, "An immersed boundary method with direct forcing for the simulation of particulate flows," *Journal of Computational Physics*, vol. 209, pp. 448–476, nov 2005.

[81] T. Kempe and J. Fröhlich, "An improved immersed boundary method with direct forcing for the simulation of particle laden flows," *Journal of Computational Physics*, vol. 231, pp. 3663–3684, may 2012.

[82] A. Gilmanov and F. Sotiropoulos, "A hybrid cartesian/immersed boundary method for simulating flows with 3d, geometrically complex, moving bodies," *Journal of Computational Physics*, vol. 207, no. 2, pp. 457 – 492, 2005.

[83] C. S. Peskin, *Flow patterns around heart valves: a digital computer method for solving the equations of motion*. PhD thesis, Sue Golding Graduate Division of Medical Sciences, Albert Einstein College of Medicine, Yeshiva University, 1972.

[84] C. S. Peskin, "Flow patterns around heart valves: A numerical method," *Journal of Computational Physics*, vol. 10, pp. 252–271, 1972.

[85] C. Peskin, "Numerical Analysis of Blood Flow in the Heart," *Journal of Computational Physics*, vol. 25, p. 220, 1977.

[86]

[87] F. Sotiropoulos and X. Yang, "Immersed boundary methods for simulating fluid–structure interaction," *Progress in Aerospace Sciences*, vol. 65, pp. 1–21, feb 2014.

[88] B. Griffith, R. Hornung, D. McQueen, and C. Peskin, "An adaptive, formally second order accurate version of the immersed boundary method," *Journal of Computational Physics*, vol. 223, no. 1, pp. 10–49, 2007.

[89] B. Griffith, "Immersed boundary model of aortic heart valve dynamics with physiological driving and loading conditions," *International Journal for Numerical Methods in Biomedical Engineering*, vol. 28, no. 3, pp. 317–345, 2012.

[90] R. Van Loon, P. Anderson, J. De Hart, and F. Baaijens, "A combined fictitious domain/adaptive meshing method for fluid–structure interaction in heart valves," *International journal for numerical methods in fluids*, vol. 46, no. 5, pp. 533–544, 2004.

[91] R. J. LeVeque and Z. Li, "The immersed interface method for elliptic equations with discontinuous coefficients and singular sources," *SIAM Journal on Numerical Analysis*, vol. 31, pp. 1019–1044, aug 1994.

[92] E. Fadlun, R. Verzicco, P. Orlandi, and J. Mohd-Yusof, "Combined immersed-boundary finite-difference methods for three-dimensional complex flow simulations," *Journal of computational physics*, vol. 161, no. 1, pp. 35–60, 2000.

[93] I. Borazjani and F. Sotiropoulos, "Why don't mackerels swim like eels? the role of form and kinematics on the hydrodynamics of undulatory swimming," *Physics of Fluids*, vol. 21, p. 091109, 2009.

[94] R. Bottom II, I. Borazjani, E. Blevins, and G. Lauder, "Hydrodynamics of swimming in stingrays: numerical simulations and the role of the leading-edge vortex," *Journal of Fluid Mechanics*, vol. 788, pp. 407–443, 2016.

[95] M. Daghooghi and I. Borazjani, "Self-propelled swimming simulations of bio-inspired smart structures," *Bioinspiration & biomimetics*, vol. 11, no. 5, p. 056001, 2016.

[96] I. Borazjani, "Fluid-structure interaction, immersed boundary-finite element method simulations of bio-prosthetic heart valves," *Computer Methods in Applied Mechanics and Engineering*, vol. 257, no. 0, pp. 103–116, 2013.

[97] I. Borazjani, J. Westerdale, E. McMahon, P. K. Rajaraman, J. Heys, and M. Belohlavek, "Left ventricular flow analysis: Recent advances in numerical methods and applications in cardiac ultrasound.," *Computational and Mathematical Methods in Medicine, Special Issue: Computational Analysis of Coronary and Ventricular Hemodynamics*, vol. 2013, pp. 395081–11 DOI:10.1155/2013/395081, 2013.

[98] M. Hedayat and I. Borazjani, "Comparison of platelet activation through hinge vs bulk flow in bileaflet mechanical heart valves," *Journal of biomechanics*, vol. 83, pp. 280–290, 2019.

[99] M. Hedayat, H. Asgharzadeh, and I. Borazjani, "Platelet activation of mechanical versus bioprosthetic heart valves during systole," *Journal of Biomechanics*, vol. 56, pp. 111–116, may 2017.

[100] Z. Song and I. Borazjani, "The role of shape and heart rate on the performance of the left ventricle," *Journal of biomechanical engineering*, vol. 137, no. 11, p. 114501, 2015.

[101] I. Borazjani, "A review of fluid-structure interaction simulations of prosthetic heart valves," *Journal of Long-term Effects of Medical Implants, Special Issue on Heart Valves*, vol. In Press, 2014.

[102] I. Borazjani, *Numerical simulations of fluid/structure interaction problems in biological flows*. PhD thesis, University of Minnesota, June 2008.

[103] H. Asgharzadeh, H. Asadi, H. Meng, and I. Borazjani, "A non-dimensional parameter for classification of the flow in intracranial aneurysms. II. patient-specific geometries," *Physics of Fluids*, vol. 31, p. 031905, mar 2019.

[104] T. B. Le, I. Borazjani, and F. Sotiropoulos, "Pulsatile flow effects on the hemodynamics of intracranial aneurysms," *Journal of biomechanical engineering*, vol. 132, p. 111009, 2010.

[105] M. Daghooghi and I. Borazjani, "The influence of inertia on the rheology of a periodic suspension of neutrally buoyant rigid ellipsoids," *Journal of Fluid Mechanics*, vol. 781, pp. 506–549, 2015.

[106] M. Daghooghi and I. Borazjani, "The effects of irregular shape on the particle stress of dilute suspensions," *Journal of Fluid Mechanics*, vol. 839, pp. 663–692, feb 2018.

[107] S. Kang, I. Borazjani, J. A. Colby, and F. Sotiropoulos, "Numerical simulation of 3d flow past a real-life marine hydrokinetic turbine," *Advances in Water Resources*, vol. 39, pp. 33 – 43, 2012.

[108] M. Hedayat and I. Borazjani, "A parallel dynamic overset grid framework for immersed boundary methods," *arXiv preprint arXiv:1910.09315*, 2019.

[109] I. Borazjani, "Sharp-interface immersed-boundary method for compressible flows with shock–particle interaction," *AIAA Journal*, vol. 59, no. 4, pp. 1169–1183, 2021.

[110] D. C. Wilcox *et al.*, *Turbulence modeling for CFD*, vol. 2. DCW industries La Canada, CA, 1998.

[111] S. B. Pope, *Turbulent flows*. Cambridge university press, 2000.

[112] N. N. Sørensen, J. Michelsen, and S. Schreck, "Navier–stokes predictions of the nrel phase vi rotor in the nasa ames 80 ft$\times$ 120 ft wind tunnel," *Wind Energy: An International Journal for Progress and Applications in Wind Power Conversion Technology*, vol. 5, no. 2-3, pp. 151–169, 2002.

[113] M.-C. Hsu, I. Akkerman, and Y. Bazilevs, "Wind turbine aerodynamics using ALE–VMS: validation and the role of weakly enforced boundary conditions," *Computational Mechanics*, vol. 50, pp. 499–511, feb 2012.

[114] M.-C. Hsu, I. Akkerman, and Y. Bazilevs, "Finite element simulation of wind turbine aerodynamics: validation study using NREL phase VI experiment," *Wind Energy*, vol. 17, pp. 461–481, mar 2013.

[115] B. Nugroho, J. Brett, B. Bleckly, and R. Chin, "Numerical study of geometric morphing wings of the 1303 UCAV," *The Aeronautical Journal*, pp. 1–17, mar 2021.

[116] H. K. Jawahar, Q. Ai, and M. Azarpeyvand, "Experimental and numerical investigation of aerodynamic performance of airfoils fitted with morphing trailing-edges," in *23rd AIAA/CEAS Aeroacoustics Conference*, American Institute of Aeronautics and Astronautics, jun 2017.

[117] O. Gabor, A. Koreanschi, R. M. Botez, M. Mamou, and Y. Mebarki, "Numerical simulation and wind tunnel tests investigation and validation of a morphing wing-tip demonstrator aerodynamic performance," *Aerospace Science and Technology*, vol. 53, pp. 136–153, jun 2016.

[118] M. L. Shur, P. R. Spalart, M. K. Strelets, and A. K. Travin, "A hybrid rans-les approach with delayed-des and wall-modelled les capabilities," *International Journal of Heat and Fluid Flow*, vol. 29, no. 6, pp. 1638–1649, 2008.

[119] Y. Wang, G. Yuan, Y.-K. Yoon, M. G. Allen, and S. A. Bidstrup, "Large eddy simulation (les) for synthetic jet thermal management," *International Journal of Heat and Mass Transfer*, vol. 49, no. 13-14, pp. 2173–2179, 2006.

[120] J. Dandois, E. Garnier, and P. Sagaut, "Numerical simulation of active separation control by a synthetic jet," *Journal of Fluid Mechanics*, vol. 574, p. 25, 2007.

[121] E. Asgari and M. Tadjfar, "Active control of flow over a rounded ramp by means of single and double adjacent rectangular synthetic jet actuators," *Computers & Fluids*, vol. 190, pp. 98–113, 2019.

[122] C. Abdessemed, A. Bouferrouk, and Y. Yao, "Aerodynamic and aeroacoustic analysis of a harmonically morphing airfoil using dynamic meshing," in *Acoustics*, vol. 3, pp. 177–199, Multidisciplinary Digital Publishing Institute, 2021.

[123] D. P. Rizzetta and M. R. Visbal, "Large-eddy simulation of supersonic cavity flowfields including flow control," *AIAA journal*, vol. 41, no. 8, pp. 1452–1462, 2003.

[124] V. J. Shinde, J. J. McNamara, and D. V. Gaitonde, "Shock wave turbulent boundary layer interaction over a flexible panel," in *AIAA Scitech 2021 Forum*, p. 0488, 2021.

[125] J. Winkler, S. Moreau, and T. Carolus, "Airfoil trailing-edge blowing: Broadband noise prediction from large-eddy simulation," *AIAA journal*, vol. 50, no. 2, pp. 294–303, 2012.

[126] D. J. Garmann and M. R. Visbal, "Numerical investigation of transitional flow over a rapidly pitching plate," *Physics of Fluids*, vol. 23, no. 9, p. 094106, 2011.

[127] A. Akbarzadeh, I. Borazjani, and U. Ogunka, "The role of amplitude on controlling flow separation using traveling wave morphing," in *AIAA Scitech 2021 Forum*, American Institute of Aeronautics and Astronautics, jan 2021.

[128] J.-P. Bonnet and N. Qin, "Active flow control strategies and tools for turbulent flows," in *Advances in Effective Flow Separation Control for Aircraft Drag Reduction*, pp. 1–26, Springer International Publishing, oct 2019.

[129] J. Smagorinsky, "General circulation experiments with the primitive equations: I. the basic experiment," *Monthly Weather Review*, vol. 91, no. 3, pp. 99–164, 1963.

[130] M. Germano, U. Piomelli, P. Moin, and W. H. Cabot, "A dynamic subgrid-scale eddy viscosity model," *Physics of Fluids A: Fluid Dynamics (1989-1993)*, vol. 3, no. 7, pp. 1760–1765, 1991.

[131] D. K. Lilly, "A proposed modification of the germano subgrid-scale closure method," *Physics of Fluids A: Fluid Dynamics*, vol. 4, no. 3, pp. 633–635, 1992.

[132] R. A. Clark, J. H. Ferziger, and W. C. Reynolds, "Evaluation of subgrid-scale models using an accurately simulated turbulent flow," *Journal of fluid mechanics*, vol. 91, no. 1, pp. 1–16, 1979.

[133] C. Fureby and F. F. Grinstein, "Large eddy simulation of high-reynolds-number free and wall-bounded flows," *Journal of Computational Physics*, vol. 181, pp. 68–97, sep 2002.

[134] A. Hamzehloo, D. J. Lusher, S. Laizet, and N. D. Sandham, "On the performance of WENO/TENO schemes to resolve turbulence in DNS/LES of high-speed compressible flows," *International Journal for Numerical Methods in Fluids*, vol. 93, pp. 176–196, aug 2020.

[135] L. G. Margolin, W. J. Rider, and F. F. Grinstein, "Modeling turbulent flow with implicit LES," *Journal of Turbulence*, vol. 7, p. N15, jan 2006.

[136] K. Duraisamy, G. Iaccarino, and H. Xiao, "Turbulence modeling in the age of data," *Annual Review of Fluid Mechanics*, vol. 51, pp. 357–377, 2019.

[137] P. Moin, K. Squires, W. Cabot, and S. Lee, "A dynamic subgrid-scale model for compressible turbulence and scalar transport," *Physics of Fluids A: Fluid Dynamics*, vol. 3, no. 11, pp. 2746–2757, 1991.

[138] B. Vreman, B. Geurts, and H. Kuerten, "Subgrid-modelling in les of compressible flow," *Applied scientific research*, vol. 54, no. 3, pp. 191–203, 1995.

[139] D. Levy, G. Puppo, and G. Russo, "Central weno schemes for hyperbolic systems of conservation laws," *ESAIM: Mathematical Modelling and Numerical Analysis*, vol. 33, no. 3, pp. 547–571, 1999.

[140] C.-W. Shu, "Essentially non-oscillatory and weighted essentially non-oscillatory schemes for hyperbolic conservation laws," in *Advanced numerical approximation of nonlinear hyperbolic equations*, pp. 325–432, Springer, 1998.

[141] S. Pirozzoli, "Numerical methods for high-speed flows," *Annual review of fluid mechanics*, vol. 43, pp. 163–194, 2011.

[142] S. Lee, S. K. Lele, and P. Moin, "Eddy shocklets in decaying compressible turbulence," *Physics of Fluids A: Fluid Dynamics*, vol. 3, no. 4, pp. 657–664, 1991.

[143] S. Pirozzoli, "Conservative hybrid compact-weno schemes for shock-turbulence interaction," *Journal of Computational Physics*, vol. 178, no. 1, pp. 81–117, 2002.

[144] W. Xiaoshuai and Z. Yuxin, "A high-resolution hybrid scheme for hyperbolic conservation laws," *International Journal for Numerical Methods in Fluids*, vol. 78, no. 3, pp. 162–187, 2015.

[145] Y. Hasegawa, M. Quadrio, and B. Frohnapfel, "Numerical simulation of turbulent duct flows with constant power input," *Journal of Fluid Mechanics*, vol. 750, pp. 191–209, jun 2014.

[146] I. Borazjani, L. Ge, T. Le, and F. Sotiropoulos, "A parallel overset-curvilinear-immersed boundary framework for simulating complex 3d incompressible flows," *Computers and Fluids*, vol. 77, pp. 76–96, 2013.

[147] M. Germano, U. Piomelli, P. Moin, and W. H. Cabot, "A dynamic subgrid-scale eddy viscosity model," *Physics of Fluids A: Fluid Dynamics (1989-1993)*, vol. 3, no. 7, pp. 1760–1765, 1991.

[148] V. Armenio and U. Piomelli *Flow, Turbulence and Combustion*, vol. 65, no. 1, pp. 51–81, 2000.

[149] S. Balay, S. Abhyankar, M. F. Adams, J. Brown, P. Brune, K. Buschelman, L. Dalcin, A. Dener, V. Eijkhout, W. D. Gropp, D. Karpeyev, D. Kaushik, M. G. Knepley, D. A. May, L. C. McInnes, R. T. Mills, T. Munson, K. Rupp, P. Sanan, B. F. Smith, S. Zampini, H. Zhang, and H. Zhang, "PETSc users manual," Tech. Rep. ANL-95/11 - Revision 3.15, Argonne National Laboratory, 2021.

[150] M. Samiee, A. Akhavan-Safaei, and M. Zayernouri, "A fractional subgrid-scale model for turbulent flows: Theoretical formulation and a priori study," *Physics of Fluids*, vol. 32, p. 055102, may 2020.

[151] A. Akhavan-Safaei, S. H. Seyedi, and M. Zayernouri, "Anomalous features in internal cylinder flow instabilities subject to uncertain rotational effects," *Physics of Fluids*, vol. 32, p. 094107, sep 2020.

[152] R. Jahromi, M. Rezaei, S. H. Samadi, and H. Jahromi, "Biomass gasification in a downdraft fixed-bed gasifier: Optimization of operating conditions," *Chemical Engineering Science*, p. 116249, oct 2020.

[153] F. De Vanna, M. Cogo, M. Bernardini, F. Picano, and E. Benini, "Unified wall-resolved and wall-modeled method for large-eddy simulations of compressible wall-bounded flows," *Physical Review Fluids*, vol. 6, no. 3, p. 034614, 2021.

[154] S. Hickel, C. P. Egerer, and J. Larsson, "Subgrid-scale modeling for implicit large eddy simulation of compressible flows and shock-turbulence interaction," *Physics of Fluids*, vol. 26, no. 10, p. 106101, 2014.

[155] N. Sandham, Y. Yao, and A. Lawal, "Large-eddy simulation of transonic turbulent flow over a bump," *International Journal of Heat and Fluid Flow*, vol. 24, no. 4, pp. 584–595, 2003.

[156] R. D. Moser, S. W. Haering, and G. R. Yalla, "Statistical properties of subgrid-scale turbulence models," *Annual Review of Fluid Mechanics*, vol. 53, 2021.

[157] F. Ducros, F. Laporte, T. Soulères, V. Guinot, P. Moinat, and B. Caruelle, "High-order fluxes for conservative skew-symmetric-like schemes in structured meshes: application to compressible flows," *Journal of Computational Physics*, vol. 161, no. 1, pp. 114–139, 2000.

[158] A. M. Akbarzadeh and I. Borazjani, "Reducing flow separation of an inclined plate via travelling waves," *Journal of Fluid Mechanics*, vol. 880, pp. 831–863, oct 2019.

[159] I. Borazjani, F. Sotiropoulos, E. D. Tytell, and G. V. Lauder, "Hydrodynamics of the bluegill sunfish c-start escape response: three-dimensional simulations and comparison with experimental data," *Journal of Experimental Biology*, vol. 215, no. 4, pp. 671–684, 2012.

[160] H. Asgharzadeh and I. Borazjani, "A newton–krylov method with an approximate analytical jacobian for implicit solution of navier–stokes equations on staggered overset-curvilinear

grids with immersed boundaries," *Journal of Computational Physics*, vol. 331, pp. 227–256, 2017.

[161] S. S. Abbas, B. A. Zambrano, and I. Borazjani, "Analysis of the coagulation kinetics under prosthetic heart valve flows," *Bulletin of the American Physical Society*, 2020.

[162] H. Asadi, H. Asgharzadeh, and I. Borazjani, "On the scaling of propagation of periodically generated vortex rings," *Journal of Fluid Mechanics*, vol. 853, pp. 150–170, 2018.

[163] M. Hedayat, T. R. Patel, T. Kim, M. Belohlavek, K. R. Hoffmann, and I. Borazjani, "A hybrid echocardiography-CFD framework for ventricular flow simulations," *International Journal for Numerical Methods in Biomedical Engineering*, vol. 36, jun 2020.

[164] H. Asgharzadeh and I. Borazjani, "A non-dimensional parameter for classification of the flow in intracranial aneurysms. i. simplified geometries," *Physics of Fluids*, vol. 31, p. 031904, mar 2019.

[165] S. B. Pope, *Turbulent flows*. Cambridge university press, 2000.

[166] M. Wang and P. Moin, "Dynamic wall modeling for large-eddy simulation of complex turbulent flows," *Physics of Fluids*, vol. 14, no. 7, pp. 2043–2051, 2002.

[167] A. M. Akbarzadeh and I. Borazjani, "Large eddy simulations of a turbulent channel flow with a deforming wall undergoing high steepness traveling waves," *Physics of Fluids*, vol. 31, p. 125107, dec 2019.

[168] H. Choi and P. Moin, "Effects of the computational time step on numerical solutions of turbulent flow," *Journal of Computational Physics*, vol. 113, no. 1, pp. 1–4, 1994.

[169] M. Lee and R. D. Moser, "Direct numerical simulation of turbulent channel flow up to Re_τ=5200," *Journal of Fluid Mechanics*, vol. 774, pp. 395–415, jun 2015.

[170] D. S. Henn and R. I. Sykes, "Large-eddy simulation of flow over wavy surfaces," *Journal of Fluid Mechanics*, vol. 383, pp. 75–112, mar 1999.

[171] J. Buckles, T. J. Hanratty, and R. J. Adrian, "Turbulent flow over large-amplitude wavy surfaces," *Journal of Fluid Mechanics*, vol. 140, p. 27, mar 1984.

[172] J. A. Franck and K. S. Breuer, "Unsteady high-lift mechanisms from heaving flat plate simulations," *International Journal of Heat and Fluid Flow*, vol. 67, pp. 230–239, 2017.

[173] A. Pelletier and T. J. Mueller, "Low reynolds number aerodynamics of low-aspect-ratio, thin/flat/cambered-plate wings," *Journal of Aircraft*, vol. 37, no. 5, pp. 825–832, 2000.

[174] D. G. Bohl and M. M. Koochesfahani, "Mtv measurements of the vortical field in the wake of an airfoil oscillating at high reduced frequency," *Journal of Fluid Mechanics*, vol. 620, pp. 63–88, 2009.

[175] J. Lai and M. Platzer, "Jet characteristics of a plunging airfoil," *AIAA journal*, vol. 37, no. 12, pp. 1529–1537, 1999.

[176] M. Al-Marouf and R. Samtaney, "A versatile embedded boundary adaptive mesh method for compressible flow in complex geometry," *Journal of Computational Physics*, vol. 337, pp. 339–378, 2017.

[177] P. R. Hammer, *Computational study of the effect of Reynolds number and motion trajectory asymmetry on the aerodynamics of a pitching airfoil at low Reynolds number*. PhD thesis, Michigan State University, 2016.

[178] R. Samtaney, D. I. Pullin, and B. Kosović, "Direct numerical simulation of decaying compressible turbulence and shocklet statistics," *Physics of Fluids*, vol. 13, no. 5, pp. 1415–1430, 2001.

[179] Z. Li, Y. Ju, and C. Zhang, "Hybrid central–weno scheme for the large eddy simulation of turbulent flows with shocks," *Numerical Heat Transfer, Part B: Fundamentals*, vol. 72, no. 2, pp. 170–189, 2017.

[180] G. N. Coleman, J. Kim, and R. D. Moser, "A numerical study of turbulent supersonic isothermal-wall channel flow," *Journal of Fluid Mechanics*, vol. 305, pp. 159–183, 1995.

[181] G. N. Coleman, J. Kim, and R. Moser, "A numerical study of turbulent supersonic isothermal-wall channel flow," *Journal of Fluid Mechanics*, vol. 305, pp. 159–183, 1995.

[182] A. Akbarzadeh and I. Borazjani, "A numerical study on controlling flow separation via surface morphing in the form of backward traveling waves," in *AIAA Aviation 2019 Forum*, p. 3589, 2019.

[183] A. M. Akbarzadeh and I. Borazjani, "Controlling flow separation on a thick airfoil using backward traveling waves," *AIAA Journal*, vol. 58, pp. 3799–3807, sep 2020.

[184] W. S. Saric, "Görtler vortices," *Annual Review of Fluid Mechanics*, vol. 26, no. 1, pp. 379–409, 1994.

[185] R. Nakanishi, H. Mamori, and K. Fukagata, "Relaminarization of turbulent channel flow using traveling wave-like wall deformation," *International Journal of Heat and Fluid Flow*, vol. 35, pp. 152–159, jun 2012.

[186] P. W. Webb, "'steady'swimming kinematics of tiger musky, an esociform accelerator, and rainbow trout, a generalist cruiser," *Journal of Experimental Biology*, vol. 138, no. 1, pp. 51–69, 1988.

[187] T. A. Oliver, N. Malaya, R. Ulerich, and R. D. Moser, "Estimating uncertainties in statistics computed from direct numerical simulation," *Physics of Fluids*, vol. 26, p. 035101, mar 2014.

[188] S. Ganju, J. Davis, S. C. Bailey, and C. Brehm, "Direct numerical simulations of turbulent channel flows with sinusoidal walls," in *AIAA Scitech 2019 Forum*, p. 2141, 2019.

[189] I. Borazjani and F. Sotiropoulos, "Numerical investigation of the hydrodynamics of anguilliform swimming in the transitional and inertial flow regimes," *Journal of Experimental Biology*, vol. 212, no. 4, pp. 576–592, 2009.

[190] E. J. Anderson, W. R. Mcgillis, and M. A. Grosenbaugh, "The boundary layer of swimming fish," *Journal of Experimental Biology*, vol. 204, no. 1, pp. 81–102, 2001.

[191] D. B. Quinn, G. V. Lauder, and A. J. Smits, "Scaling the propulsive performance of heaving flexible panels," *Journal of Fluid Mechanics*, vol. 738, pp. 250–267, 2014.

[192] M. J. Lighthill, "Aquatic animal propulsion of high hydromechanical efficiency," *Journal of Fluid Mechanics*, vol. 44, no. 2, pp. 265–301, 1970.

[193] H. Mamori and K. Fukagata, "Drag reduction effect by a wave-like wall-normal body force in a turbulent channel flow," *Physics of Fluids*, vol. 26, p. 115104, nov 2014.

[194] M. Marquillie, J.-P. Laval, and R. Dolganov, "Direct numerical simulation of a separated channel flow with a smooth profile," *Journal of Turbulence*, vol. 9, p. N1, jan 2008.

[195] I. Borazjani and F. Sotiropoulos, "Numerical investigation of the hydrodynamics of anguilliform swimming in the transitional and inertial flow regimes," *Journal of Experimental Biology*, vol. 212, pp. 576–592, feb 2009.

[196] F. M.J Lighthill, "Large-amplitude elongated-body theory of fish locomotion," *Proceedings of the Royal Society of London. Series B. Biological Sciences*, vol. 179, pp. 125–138, nov 1971.

[197] T. Min, S. M. Kang, J. L. Speyer, and J. Kim, "Sustained sub-laminar drag in a fully developed channel flow," *Journal of Fluid Mechanics*, vol. 558, p. 309, jul 2006.

[198] H. Mamori, K. Iwamoto, and A. Murata, "Effect of the parameters of traveling waves created by blowing and suction on the relaminarization phenomena in fully developed turbulent channel flow," *Physics of Fluids*, vol. 26, p. 015101, jan 2014.

[199] R. Moarref and M. R. Jovanović, "Controlling the onset of turbulence by streamwise travelling waves. part 1. receptivity analysis," *Journal of Fluid Mechanics*, vol. 663, pp. 70–99, sep 2010.

[200] S. Taneda, "Visual study of unsteady separated flows around bodies," *Progress in Aerospace Sciences*, vol. 17, pp. 287–348, 1976.

[201] M. Visbal, "Three-dimensional flow structure on a heaving low-aspect-ratio wing," in *49th AIAA Aerospace Sciences Meeting including the New Horizons Forum and Aerospace Exposition*, p. 219, 2011.

[202] M. A. Bani-Hani and M. A. Karami, "Analytical structural optimization and experimental verifications for traveling wave generation in self-assembling swimming smart boxes," *Smart Materials and Structures*, vol. 24, no. 9, p. 094005, 2015.

[203] J. D. Anderson Jr, *Fundamentals of aerodynamics*. Tata McGraw-Hill Education, New York, US, 1985.

[204] T. J. Mueller and S. M. Batil, "Experimental studies of separation on a two-dimensional airfoil at low reynolds numbers," *AIAA journal*, vol. 20, no. 4, pp. 457–463, 1982.

[205] D. Kim and M. Gharib, "Experimental study of three-dimensional vortex structures in translating and rotating plates," *Experiments in Fluids*, vol. 49, no. 1, pp. 329–339, 2010.

[206] F. Fish and G. Lauder, "Passive and active flow control by swimming fishes and mammals," *Annu. Rev. Fluid Mech.*, vol. 38, pp. 193–224, 2006.

[207] I. Borazjani and F. Sotiropoulos, "On the role of form and kinematics on the hydrodynamics of self-propelled body/caudal fin swimming," *Journal of Experimental Biology*, vol. 213, no. 1, pp. 89–107, 2010.

[208] H. R. Beem, D. E. Rival, and M. S. Triantafyllou, "On the stabilization of leading-edge vortices with spanwise flow," *Experiments in fluids*, vol. 52, no. 2, pp. 511–517, 2012.

[209] H. Schlichting and K. Gersten, *Boundary-layer theory*. Springer, 2016.

[210] E. P. DeMauro, H. Dell'Orso, S. Zaremski, C. M. Leong, and M. Amitay, "Control of laminar separation bubble on naca 0009 airfoil using electroactive polymers," *AIAA Journal*, vol. 53, no. 8, pp. 2270–2279, 2015.

[211] R. Godoy-Diana and B. Thiria, "On the diverse roles of fluid dynamic drag in animal swimming and flying," *Journal of The Royal Society Interface*, vol. 15, no. 139, p. 20170715, 2018.

[212] I. Borazjani and F. Sotiropoulos, "Numerical investigation of the hydrodynamics of carangiform swimming in the transitional and inertial flow regimes," *Journal of Experimental Biology*, vol. 211, pp. 1541–1558, 2008.

[213] S. Barbarino, O. Bilgen, R. M. Ajaj, M. I. Friswell, and D. J. Inman, "A review of morphing aircraft," *Journal of Intelligent Material Systems and Structures*, vol. 22, pp. 823–877, jun 2011.

[214] A. J. Lee, A. Moosavian, and D. J. Inman, "A piezoelectrically generated bistable laminate for morphing," *Materials Letters*, vol. 190, pp. 123–126, mar 2017.

[215] M. A. Bani-Hani and M. A. Karami, "Analytical structural optimization and experimental verifications for traveling wave generation in self-assembling swimming smart boxes," *Smart Materials and Structures*, vol. 24, p. 094005, aug 2015.

[216] R. Mittal, R. Kotapati, and L. Cattafesta, "Numerical study of resonant interactions and flow control in a canonical separated flow," in *43rd AIAA Aerospace Sciences Meeting and Exhibit*, p. 1261, 2005.

[217] M. Wiser, R.; Bolinger, "Wind technologies market report," tech. rep., U.S. Department of Energy, http://energy.gov/eere/wind/downloads/2013-wind-technologies-market-report, 2013.

[218] M.-C. Hsu, I. Akkerman, and Y. Bazilevs, "Finite element simulation of wind turbine aerodynamics: validation study using NREL phase VI experiment," *Wind Energy*, vol. 17, pp. 461–481, mar 2013.

[219] F. Zahle, "Wind turbine aerodynamics using an incompressible overset grid method," 2006.

[220] M. Hand, D. Simms, L. Fingersh, D. Jager, J. Cotrell, S. Schreck, and S. Larwood, "Unsteady aerodynamics experiment phase vi: wind tunnel test configurations and available data campaigns," tech. rep., National Renewable Energy Lab., Golden, CO.(US), 2001.

[221] S. Aubrun, A. Leroy, and P. Devinant, "A review of wind turbine-oriented active flow control strategies," *Experiments in Fluids*, vol. 58, no. 10, pp. 1–21, 2017.

[222] M. Akhter, F. K. Omar, *et al.*, "Review of flow-control devices for wind-turbine performance enhancement," *Energies*, vol. 14, no. 5, p. 1268, 2021.

[223] M. S. Genc, K. Kemal, and H. H. Acikel, "Investigation of pre-stall flow control on wind turbine blade airfoil using roughness element," *Energy*, vol. 176, pp. 320–334, 2019.

[224] A. Ebrahimi and M. Movahhedi, "Wind turbine power improvement utilizing passive flow control with microtab," *Energy*, vol. 150, pp. 575–582, 2018.

[225] T. Macquart, A. Maheri, and K. Busawon, "Microtab dynamic modelling for wind turbine blade load rejection," *Renewable Energy*, vol. 64, pp. 144–152, 2014.

[226] A. Leroy, C. Braud, S. Baleriola, S. Loyer, P. Devinant, and S. Aubrun, "Comparison of flow modification induced by plasma and fluidic jet actuators dedicated to circulation control around wind turbine airfoils," in *Journal of Physics: Conference Series*, vol. 753, p. 022012, IOP Publishing, 2016.

[227] A. Rezaeiha, I. Kalkman, and B. Blocken, "Effect of pitch angle on power performance and aerodynamics of a vertical axis wind turbine," *Applied energy*, vol. 197, pp. 132–150, 2017.

[228] M. Hedayat, *Platelet Activation in Artificial Heart Valves*. PhD thesis, 2020.

[229] I. Borazjani, L. Ge, and F. Sotiropoulos, "Curvilinear immersed boundary method for simulating fluid structure interaction with complex 3d rigid bodies," *Journal of Computational physics*, vol. 227, no. 16, pp. 7587–7620, 2008.

[230] G. V. Lachmann, *Boundary layer and flow control: its principles and application*. Elsevier, 2014.

[231] J. D. Hudson, L. Dykhno, and T. J. Hanratty, "Turbulence production in flow over a wavy wall," *Experiments in Fluids*, vol. 20, pp. 257–265, feb 1996.

[232] P. Huang, G. Coleman, and P. Bradshaw, "Compressible turbulent channel flows: Dns results and modelling," *Journal of Fluid Mechanics*, vol. 305, pp. 185–218, 1995.

[233] S. Muppidi and K. Mahesh, "Direct numerical simulations of roughness-induced transition in supersonic boundary layers," *Journal of Fluid Mechanics*, vol. 693, no. 2, pp. 28–56, 2012.

[234] M. A. Jouybari, J. Yuan, G. J. Brereton, and F. A. Jaberi, "Supersonic turbulent channel flows over two and three dimensional sinusoidal rough walls," *arXiv preprint arXiv:2012.02852*, 2020.

[235] M. Vinokur, "An analysis of finite-difference and finite-volume formulations of conservation laws," *Journal of computational physics*, vol. 81, no. 1, pp. 1–52, 1989.

[236] J. Yang and E. Balaras, "An embedded-boundary formulation for large-eddy simulation of turbulent flows interacting with moving boundaries," *Journal of Computational Physics*, vol. 215, pp. 12–40, jun 2006.

[237] T. I. Józsa, E. Balaras, M. Kashtalyan, A. G. L. Borthwick, and I. M. Viola, "Active and passive in-plane wall fluctuations in turbulent channel flows," *Journal of Fluid Mechanics*, vol. 866, pp. 689–720, mar 2019.

[238] A. Lozano-Durán and J. Jiménez, "Effect of the computational domain on direct simulations of turbulent channels up to $re_\tau = 4200$," *Physics of Fluids*, vol. 26, p. 011702, jan 2014.

[239] K. Fukagata, S. Kern, P. Chatelain, P. Koumoutsakos, and N. Kasagi, "Evolutionary optimization of an anisotropic compliant surface for turbulent friction drag reduction," *Journal of Turbulence*, vol. 9, p. N35, jan 2008.

[240] P. R. Payne, "The virtual mass of a rectangular flat plate of finite aspect ratio," *Ocean Engineering*, vol. 8, no. 5, pp. 541–545, 1981.

[241] M. Piñeirua, R. Godoy-Diana, and B. Thiria, "Resistive thrust production can be as crucial as added mass mechanisms for inertial undulatory swimmers," *Physical Review E*, vol. 92, no. 2, p. 021001, 2015.

[242] U. Ehrenstein and C. Eloy, "Skin friction on a moving wall and its implications for swimming animals," *Journal of Fluid Mechanics*, vol. 718, pp. 321–346, 2013.

APPENDIX A

DERIVATIONS

In this appendix derivations of this study are presented. In section **??** a different derivation of the conservative form of momentum equations in a non-inertial frame of reference is presented. In [108], the same equations were derived by transforming the conservative form of the momentum equation in Cartesian coordinates to curvilinear ones. In section A the scalings for lateral velocity, spanwise vorticity, thrust coefficient, instantaneous reactive coefficient of an undulating plate are derived using EBT [40]. In section A.2 the derivation of pressure is presented.

In this appendix a different derivation of the the conservative form of momentum equations in a non-inertial frame of reference is presented. In [108], the same equations were derived by transforming the conservative form of the momentum equation in Cartesian coordinates to curvilinear ones. Here, the starting point is the momentum equations in curvilinear coordinates in an inertial frame of reference, and the non-inertial form is derived from the inertial one (both in curvilinear coordinates).

The continuity and momentum equations in an inertial frame of reference in strong conservative form after introducing a general time dependent curvilinear coordinate transformation $(x_1', x_2', x_3', t) \rightarrow (\xi_1, \xi_2, \xi_3, \tau)$ are [235]:

$$J' \frac{\partial}{\partial \xi_r}(U_r' - V_r') = 0, \tag{A.1}$$

$$\frac{\partial u_i'}{\partial t} = -C_1'(u_i') - G_i'(p) + \frac{1}{Re} D'(u_i') \tag{A.2}$$

Here, $\tau = t$, $i = 1, 2, 3$, $(')$ denotes term in the inertial frame (Fig. 2.1), and C_1', G', and D' are

the convective, gradient, and viscous operators in curvilinear coordinates

$$C_1'(*) = J' \frac{\partial}{\partial \xi_r} \Big[\Big(U_r' - V_r' \Big) * \Big], \tag{A.3}$$

$$G_i'(*) = J' \frac{\partial}{\partial \xi_r} \Big(\frac{\xi_{ri}'}{J'} * \Big), \tag{A.4}$$

$$D'(*) = J' \frac{\partial}{\partial \xi_r} \Big(\frac{g_{rm}'}{J} \frac{\partial}{\partial \xi_m} * \Big), \tag{A.5}$$

where J' is the determinant of the Jacobian of the transformation, $J' = |\partial(\xi_1, \xi_2, \xi_3)/\partial(x_1', x_2', x_3')|$, $\xi_{ri}' = \frac{\partial \xi_r}{\partial x_i'}$, g_{rm}' is the contravariant metric tensor, $g_{rm}' = \xi_{rq}' \xi_{mq}'$, U_q' and V_q' are the contravariant velocity components, which are correlated with the Cartesian velocity components as follows:

$$U_r' = u_i' \frac{\xi_{ri}'}{J'}, \; and \; V_r' = v_i' \frac{\xi_{ri}'}{J'} \tag{A.6}$$

where u_i' and v_i' are Cartesian fluid and frame grid velocity in inertial frame. Equation A.2 is valid for grids with any arbitrary deformation. However, using this equation requires updating the metrics of transformation ξ_{ri}' at each time-step, which is computationally expensive.

To avoid computing the metrics at each time step, for a grid undergoing a rigid body motion (translation and/or rotation), Eq. A.2 can be transformed to a non-inertial frame of reference. In fact, for a given rotation with a rotation matrix $\mathbf{Q}$, the transformation becomes $(x_1', x_2', x_3', t) \rightarrow (x_1, x_2, x_3, \tau) \rightarrow (\xi_1, \xi_2, \xi_3, \tau)$. Using this rotation, the velocity and contravariant metrics will be

$$u_i = Q_{ir} u_r' \tag{A.7}$$

$$\xi_{ij} = Q_{jr} \xi_{ir}' \tag{A.8}$$

where ξ_{ij} is the initial contravariant metric that does not change in a non-inertial frame of reference. In fact, ξ_{ij} represents the j_{th} component of vector $\xi_{\mathbf{i}}$. Similarly, u_r' can be obtained by $\mathbf{Q}^{-1}$, i.e., inverse of rotation matrix. Furthermore, the following relation is always valid for dot product of

any two arbitrary vectors $\mathbf{a}$ and $\mathbf{b}$:

$$\mathbf{Q^{-1}a}.\mathbf{Q^{-1}b} = \mathbf{a}.\mathbf{b} \tag{A.9}$$

Equation A.9 is the key equation in deriving the non-inertial terms. For example, the fact that contravariant velocity U_r, which is the flux passing through a cell surface in ξ_r direction, does not change due to frame rotation ($U = U'$) can be shown by mathematically by using the above equation and Eqns. A.7-A.9 as follows

$$U'_r = u'_i \frac{\xi'_{ri}}{J'} = Q^{-1}_{ik} u_k Q^{-1}_{in} \frac{\xi_{rn}}{J} = u_i \frac{\xi_{ri}}{J} = U_r, \tag{A.10}$$

Similarly, it can be shown that $V = V'$. Moreover, J is inverse of the volume of a grid cell. Therefore, $J = J'$ because the volume of the grid cell does not change due to rigid motion. By a similar approach (Eqn. A.10) it can be shown that operators $C'_1(u'_i) = Q^{-1}_{ij} C_1(u_j)$, $D'(u'_i) = Q^{-1}_{ij} D(u_j)$, and $G'_i(p) = Q^{-1}_{ij} G_j(p)$ where C_1, D, and G_i are operators in Eqns. A.3-A.5 with the non-inertial terms.

$$C_1(*) = J \frac{\partial}{\partial \xi_r} \Big[\Big(U_r - V_r \Big) * \Big], \tag{A.11}$$

$$G_i(*) = J \frac{\partial}{\partial \xi_r} \Big(\frac{\xi_{ri}}{J} * \Big), \tag{A.12}$$

$$D(*) = J \frac{\partial}{\partial \xi_r} \Big(\frac{g_{rm}}{J} \frac{\partial}{\partial \xi_m} * \Big), \tag{A.13}$$

On the other hand, by replacing u' with u and applying rotation matrix (Eqn. A.7), the left hand side of the momentum Eqn. A.2 becomes

$$\frac{\partial u'_i}{\partial t} = Q^{-1}_{ij} \frac{\partial u_j}{\partial t} + u_j \frac{\partial Q^{-1}_{ij}}{\partial t}, \tag{A.14}$$

where $\partial Q^{-1}_{ij} / \partial t = \partial v_i / \partial x_j$ is the rate of change of rotation of the frame. Applying the continuity equation, the last term of Eqn. A.14 becomes $\frac{\partial}{\partial x_j}(u_j v_i)$, which is similar to the convective term of

the Navier-Stokes equation that can be obtained in the curvilinear form using metrics as

$$\frac{\partial}{\partial x_j}(u_j v_i) = J\frac{\partial}{\partial \xi^r}\Big(v_i U^r\Big) \tag{A.15}$$

By multiplying the momentum equations (Eqn. A.2 by metric tensor ($Q_{ij}^{-1}\frac{\xi_{rj}}{J}$), and replacing the inertial term with non-inertial terms it becomes

$$Q_{ij}^{-1}\frac{\xi_{rj}}{J}Q_{im}^{-1}\frac{\partial u_m}{\partial t} = -Q_{im}^{-1}\frac{\xi_{rm}}{J}Q_{ij}^{-1}\Big(C_1(u_j) + C_2(v_j) + G_j(p) - \frac{1}{Re}D(u_j)\Big) \tag{A.16}$$

$$C_2(*) = J\frac{\partial}{\partial \xi^r}\Big(U_r\Big) \tag{A.17}$$

where the left hand side becomes $\frac{\partial U_r}{\partial t}$,and its final form is:

$$\frac{\partial U_r}{\partial t} = \frac{\xi_{rj}}{J}\Big(- C_1(u_j) - C_2(v_j) - G_j(p) + \frac{1}{Re}D(u_j)\Big) \tag{A.18}$$

When the grid undergoes a rigid body motion, its volume is constant. Therefore, $\frac{\partial V_r}{\partial \xi_r} = 0$ and the continuity equation becomes

$$J\frac{\partial}{\partial \xi_r}(U_r) = 0 \tag{A.19}$$

The frame velocity $\mathbf{v}$ is composed of a rotational term $\mathbf{w}$ and a transnational term $\mathbf{v}_t$. Using Eqn. A.19 and knowing that all spatial derivatives of $\mathbf{v}_t$ are zero, Eqn. A.18 will be simplified as follows:

$$\frac{\partial U_i}{\partial t} = \frac{\xi_{ij}}{J}\Big(- C_1(u_j) - C_2(w_j) - G_j(p) + \frac{1}{Re}D(u_j)\Big) \tag{A.20}$$

A.1 Velocity, vorticity, time averaged thrust, and instantaneous reactive force scalings

The scalings for lateral velocity, spanwise vorticity, thrust coefficient and instantaneous reactive coefficient of an undulating plate are derived using EBT [40]. In the derivations, the effect of angle of attack is neglected because the angle of attack is small ($cos(10^o) \approx 1$) and to simplify the derivations, i.e., the scalings are for an undulating plate at zero angle of attack. The lateral velocity

of fluid adjacent to the plate is composed of plate velocity ($\partial h/\partial t$) and a velocity induced by the curvy shape of a plate creating an angle of attack with the incoming flow ($U\partial h/\partial Z$) [40]:

$$u_Y = \frac{Dh}{Dt} = \frac{\partial h}{\partial t} + U\frac{\partial h}{\partial Z} \tag{A.21}$$

where u_Y is the fluid lateral velocity and h is the lateral undulations along the plate. Using Eqn. 4.4 for $h = h(Z,t)$, and nondimensionalizing Eqn. A.21 by U, the nondimensional lateral velocity (u_Y^*) becomes:

$$u_Y^* = a_{max}^* \frac{Z^* - 0.1}{0.9}(2\pi f^* - 2\pi/\lambda^*)\cos(2\pi(f^* t^* - Z^*/\lambda^*)) + \frac{a_{max}^*}{0.9} sin(2\pi(f^* t^* - Z^*/\lambda^*)) \tag{A.22}$$

Near the trailing edge, the first term in the above equation is dominant because $2\pi(f^* - 1/\lambda^*) \gg 1$ for the test cases here with $f^* \gg 1$. Therefore, the lateral velocity at the trailing edge is approximated by:

$$u_Y^* \approx 2\pi a_{max}^*(f^* - 1/\lambda^*)\cos(2\pi(f^* t^* - Z^*/\lambda^*)) \tag{A.23}$$

According to the above equation, the magnitude of lateral velocity of fluid near the trailing edge scales with $a_{max}^*(f^* - 1/\lambda^*)$.

The instantaneous reactive force F_R is the rate of change of lateral momentum, for which the dimensional form is given as follows [40]:

$$F_R(Z,t) = \frac{D(mu_Y)}{Dt} = -m(\rho, L)a_{max}(2\pi(f - 1/\lambda))^2 \sin(2\pi(ft - Z/\lambda)) \tag{A.24}$$

where $F_R(Z,t)$ is the reactive force per unit of length in axial (Z) direction at distance Z from leading edge. $m = m(\rho, L)$ is the virtual (added) mass per unit of length in axial direction which is approximated by $m = 0.25\rho\pi s^2$, where s is the span of the plate, according to EBT. Nevertheless, it has been shown by [240] and [241] that this equation is good only for low aspect ratio plates $(s/L < 0.4)$, and for plates with higher aspect ratio $(s/L > 0.5)$, equation given in the following

can be used [240]:

$$m = \frac{\pi/4\rho L s}{(1+(L/s)^n)^{1/n}} \tag{A.25}$$

where n is real number which has been reported typically greater than one [241, 240]. Here, the virtual mass is approximated by $m = 0.44\rho\pi L^2$ by setting n=2 in equation A.25.

Because the local reactive force (Eqn. A.24) acts along Y direction and the angle of attack is small, it can be an approximation of the local lateral momentum [40]. The sum (integral) of the local reactive force on the chord provides the total instantaneous reactive force $F_{RT}(t)$. The nondimensional form of the total reactive force F^*_{RT} is derived by integrating Eqn. A.24 along Z direction as follows:

$$\begin{aligned} F^*_{RT}(t^*) &= \frac{1}{\rho U^2 L^2}\int_{Z=0.1L}^{Z=L} F_R(Z,t)dZ \\ &= \int_{Z^*=0.1}^{Z^*=1} -m^* a^*_{max}(Z^*-.1)/0.9(2\pi(f^*-1\lambda^*))^2\sin(2\pi(f^*t^*-Z^*/\lambda^*))dZ^* \\ &= -0.11m^*a^*_{max}\lambda^*(f^*-1/\lambda^*)^2[\sin(2\pi f^*t^*-2\pi/\lambda^*) \\ &- \cos(2\pi f^*t^*-2\pi/\lambda^*)+\cos(2\pi f^*t^*-0.2\pi/\lambda^*)] \end{aligned} \tag{A.26}$$

Equations A.23 and A.24 show that the velocity and lateral force are periodic, hence their time-averaged value is zero. [40] derived thrust T_R by subtracting kinetic energy of flow due to lateral motion and work it has done by lateral motion:

$$T_R = \frac{1}{2}m[(\overline{\frac{\partial h}{\partial t}^2}) - U^2(\overline{\frac{\partial h}{\partial Z}^2})]_{Z=L} \tag{A.27}$$

where the quadratic terms in equation A.27 are time-averaged that can be conveniently calculated using equation 4.4 at the trailing edge (Z=L). Now substituting m from Eqn. A.25 into Eqn. A.27, and nondimensionalizing it with ρU^2L^2, the nondimensional thrust coefficient C_T is obtained conveniently as:

$$C_T = [0.11\pi(2\pi f^* a^*_{max})^2(1-(\frac{1}{f^*\lambda^*})^2)] \tag{A.28}$$

This equation shows that thrust scales with $C_T = O((f^*a^*_{max})^2(1-(\frac{1}{f^*\lambda^*})^2))$ irrespective of

how the added mass m is approximated.

The relation of thrust (the external force, assuming pressures cancel out) and the axial momentum for a control volume (CV) is given by the Reynolds transport theorem as follows:

$$T_R = \frac{\partial}{\partial t}\int_{CV} \rho u_Z dV + \int_{CS} \rho u_Z \vec{u}.\hat{n} dS \tag{A.29}$$

where ρu_Z is the axial momentum per unit volume, $\vec{u}$ is the velocity vector, dV is the volume differential within CV, dS is the area differential on the CV surfaces, i.e., the control surface (CS), and $\hat{n}$ is the outward normal of dS. By averaging the above equation over a cycle, the derivative of the volume integral goes to zero because we reach a quasi-steady (periodic) state. If we consider a cubic CV that is far away from the plate in the lateral and spanwise direction, then the net flux on the lateral and spanwise faces of the CS will be zero. Consequently, the above equation will reduce to only the axial direction:

$$\bar{T_R} = (\rho \bar{u}_Z^2 S)_{outlet} - (\rho \bar{u}_Z^2 S)_{inlet} \tag{A.30}$$

which indicates that the average thrust is the difference between the time-averaged axial momentum flux at the outlet and inlet. Because u_Z at the inlet (upstream of the plate) is uniform, the inlet momentum is constant. Consequently, the change in the thrust is directly related to the change in the mean axial momentum at the outlet (wake). Therefore, we have used thrust (force) and the mean axial momentum interchangeably in this manuscript, e.g., we have used increase in thrust as an equivalent to increase in the mean axial momentum in the wake.

The nondimensional plate vorticity ($\omega_x^* = \partial u_Y^*/\partial Z^*$) is approximated by calculating the derivative of equation A.23 with respect to Z

$$\omega_x^* \approx 4\pi^2 a_{max}^* \frac{(f^* - 1/\lambda^*)}{\lambda^*} \sin(2\pi(f^* t^* - Z^*/\lambda^*)) \tag{A.31}$$

The scaling of the shear layer vorticity on pressure side of a flat inclined plate can be obtained

using the friction coefficient for a laminar boundary layer based on the Blasius solution. The nondimensional friction coefficient at trailing edge is $C_f = 0.332/\sqrt{Re_L}$ based on the Blasius profile [209]. Using the Blasius friction coefficient and $C_f = 1/Re_L \frac{\partial u_Z^*}{\partial Y^*}$, the nondimensional shear layer vorticity scaling becomes:

$$\frac{\partial u_Z^*}{\partial Y^*} = 0.332\sqrt{Re_L} \tag{A.32}$$

However, it has been observed that the skin friction of a moving plate is greater than the skin friction of a Blasius boundary layer [211, 242]. Therefore, we also extract the skin friction scaling for the undulating plate using the drag coefficient derived by [242] and then we compare it with the one derived by Blasius friction coefficient (Eqn. A.32). The drag force based on [242] is:

$$D = 1.4\mu U Re_s^{1/2}\sqrt{\frac{u_Y}{U}} \tag{A.33}$$

where $Re_s = Us/\nu$ is the Reynolds number based on the span $s = 2L$. Nondimensionalizing D (Eqn. A.33) by $s\rho U^2$, and replacing s by $2L$, gives the nondimensional skin friction by:

$$C_f = 1.4\frac{\sqrt{u_Y^*}}{\sqrt{2Re_L}} = 1/Re_L \frac{\partial u_Z^*}{\partial Y^*} \tag{A.34}$$

Equation A.34 shows that $\frac{\partial u_Z^*}{\partial Y^*}$ is proportional to $\sqrt{u_y^*}\sqrt{Re_L}$. The maximum nondimensional lateral velocity (u_Y^*) does not exceed 1.6 according to Eqn. A.22 even for the high frequency cases. Therefore, this relation also provides a scaling of $O(\sqrt{Re_L})$ similar to the Blasius relation. For simplicity, we use the Blasius skin friction for the approximation of shear layer vorticity on the pressure side of the plate, which leads the shear layer vorticity to be approximately $\frac{\partial u_Z^*}{\partial Y^*} \approx 45$.

A.2 Pressure gradient scaling due to undulations

The lateral averaged pressure gradient over an undulationg plate at zero angle of attack is estimated by 2D Reynolds-averaged Navier-Stokes equation in the nondimensional form (A.35):

$$\overline{u_z^*}\frac{\partial\overline{u_y^*}}{\partial z^*} + \overline{u_y^*}\frac{\partial\overline{u_y^*}}{\partial y^*} = -\frac{\partial\overline{p}}{\partial y^*} + \frac{1}{Re}(\frac{\partial^2\overline{u_y^*}}{\partial y^{*2}} + \frac{\partial^2\overline{u_y^*}}{\partial z^{*2}}) - \frac{\partial\overline{u_y'^* u_z'^*}}{\partial z^*} - \frac{\partial\overline{u_y'^* u_y'^*}}{\partial y^*} \tag{A.35}$$

where overbar terms are time-averaged, $\overline{u_y'^* u_y'^*}$ and $\overline{u_y'^* u_z'^*}$ are the nondimensional Reynolds stresses. Because velocity of an undulating plate is periodic, the time-averaged lateral velocity over a period is zero. The lateral velocity fluctuation scales with instantaneous lateral velocity expressed in A.23.

$$u_y'^* = u_y^* - \overline{u_y^*} \approx (2\pi a_{max}^*(f^* - 1/\lambda^*))cos(2\pi(f^* t^* - Z^*/\lambda^*)) \tag{A.36}$$

In fact, the assumption of negligible mean lateral velocity is correct in this study, though it is valid for turbulent boundary layer of a flat plate, because $(u_y'^* = u_y'/U) \approx 1$, and u_y' is oscillatory, which implies that $u_y'^* \gg \overline{u_y^*}$. By this assumption, the lateral velocity fluctuation $\overline{u_y'^* u_y'^*}$ is the dominant term in equation A.35 because left hand side and viscous terms become zero as $\overline{u_y^*} \approx 0$. Therefore, the pressure gradient term can be simplified as:

$$\begin{aligned}\frac{\partial\overline{p}}{\partial y^*} &\approx -\frac{\partial\overline{u_y'^* u_y'^*}}{\partial y^*} \approx -\frac{1}{\Delta y^*}[-\frac{1}{T}\int_0^T (2\pi a_{max}^*(f^* - 1/\lambda^*))^2 cos^2(2\pi(f^* t^* - Z^*/\lambda^*))dt^*] \\ &= \frac{(2\pi a_{max}^*)^2(f^* - 1/\lambda^*)^2}{\Delta y^*}\end{aligned} \tag{A.37}$$

The right hand side of equation A.37 is obtained by assuming that u_y' is negligible at nondimensional distance Δy^* from the plate ($\Delta y^* = \Delta y/L$), and, consequently the Reynolds stress is negligible ($\overline{u_y'^* u_y'^*} \approx 0$) at $\Delta y = L$. It is also assumed that the Reynolds stress is decreasing linearly and $\Delta y = O(L)$. Note that, the assumption of zero velocity fluctuation ($u_y' \approx 0$) at $\Delta y \approx L$ is based on the assumption for the boundary layer of a flat plate, in which $u_y' \approx 0$ at $\Delta y = O(L)$. Similar arguments are applicable to the other (lateral) side of the undulating body, i.e., $-y$ direction, because velocity fluctuations decrease on the other side as well when we move away from the

body. Therefore, the order of nondimensional pressure gradient based on Eqn. A.37 in the lateral direction n, pointing outwards from the body, and assuming zero velocity fluctuation at $O(L)$ from the body, is:

$$\frac{\partial \overline{p}}{\partial n} = O((a^*_{max})^2(f^* - 1/\lambda^*)^2) \tag{A.38}$$

Positive $\frac{\partial \overline{p}}{\partial n}$ requires the pressure to increase as we move away from the plate, i.e., low average pressure near the plate.

APPENDIX B

DOMAIN SENSITIVITY AND COMPUTATIONAL BUDGET

In this appendix the domain sensitivity study and computational budget of different studies are presented.

B.1 Domain sensitivity and sampling error for turbulent channel simulation

During the LES of the channel flow, different types of numerical errors might be introduced which can be originated from the domain size, data sampling, time-step size and grid size. Our validation and grid sensitivity studies presented in §3.2.2 and previous numerical studies of channel flows [168] and turbulent traveling wave simulations [158, 236] indicate that our grid and time step size were sufficient. However, a sampling error for calculating the averaged parameters such as mean force coefficients (Fig. 4.6) might be introduced due to the insufficiency of the data used for averaging, e.g. the mean forces of the traveling wavy channel are computed by taking the average of 20 cycles of the forces. Therefore, the sampling uncertainty of the forces is quantified to ensure that the averaging is performed for a sufficient number of cycles. The sampling uncertainty of the mean forces is quantified using the method described by Oliver et. al. [187], which has been used by Jozsa et al. [237] for turbulent channel with compliant walls. It has been observed that the sampling uncertainty for the mean force coefficient of the motionless wavy channel is less than 1.0×10^{-5}, when the averaging is performed for a non-dimensional time of t =75 which corresponds to 18,800 time-steps (data samples). When the channel's wall undulates, the sampling uncertainty of the forces increases, i.e., it increases by the increase of either C or s as the amplitude of the instantaneous forces increases as shown in Fig. 4.5. Hence, the highest sampling uncertainty of $\overline{C_F}$ is observed for the traveling wave channel with $C = 1.6$. The sampling uncertainty is 0.00028 which corresponds to 0.59% of the drag reduction with respect to the motionless wavy channel. The previous studies have reported that the change of the domain size can affect the force of a turbulent channel with either a motionless flat wall (baseline) [238] or a deforming

wall [237, 239]. To calculate the error generated by the domain size, another LES simulation is performed for a traveling wave channel with C =0.8 and s=0.15. The simulation is performed using grid 3 (Table 4.1) which its streamwise length is $8H^*$, twice of grid 2, but its resolution is same as grid 2. Similar to the previous simulations, the traveling wave simulation is initialized with a motionless wavy channel simulation and the averaging is performed for 20 cycles. Using grid 3, the mean force coefficient of this case is $\overline{C_F} = -0.0067$ whereas the $\overline{C_F}$ of the same simulation with grid 2 is -0.0069. The change of mean force coefficient due to domain size corresponds to %2.9 decrease in the drag reduction with respect to the motionless wavy channel (C =0.0). Such a small difference in the mean values and drag-reduction does not affect the conclusions of this work.

B.2 Computational budget

All simulations in this work are performed using Texas A&M university cluster (Terra) computing nodes where each node has 28 cores, i.e., Intel Xeon E5-2680 v4 (Broadwell), 2.40GHz, 14-core, with 64GB. By doing many simulations, it was found that the optimum speed-up can be obtained with 228 CPUs for plate and channel flow simulations whereas the wind turbine simulations require at least 336 cores where the maximum speed-up was obtained with the same number of CPUs. In fact, it was obtained that no speed-up can be achieved by increasing the number of CPUs by having more than 336 cores due increase in the data-communication (send and receive) cost. The details of computational cost is described in Table B.1. The total number of mesh (N_{tot}), number of CPUs, time of the simulation, and the number of time-steps per SU, i.e., SU= CPU (core) $\times$ time (hour), are presented. The compressible simulations have the maximum timestep/CPU. In contrast, the wind turbine simulation has the lowest time-step/SU due to having overset and, rotating grid, and high Reynolds number of the flow.

Table B.1: The details of computational cost.

simulation	N_{tot} (Million)	N_{CPU}	time (hr)	time-step/SU
Incompressible Channel	4.4	228	144	8.18
Inclined plate	10.2	228-280	128	1.12
Wind turbine	112.5	336-448	720	0.2
Compressible channel	24.7	228	28	32.5